HETEROGENEOUS CATALYTIC EVALUATION AND ADSORPTION CHARACTERIZATION OF THE LA2CUO4/YSZ/PT POTENTIOMETRIC COUPLE

By

FREDERICK MARTIN VAN ASSCHE IV

A DISSERTATION PRESENTED TO THE GRADUATE SCHOOL
OF THE UNIVERSITY OF FLORIDA IN PARTIAL FULFILLMENT
OF THE REQUIREMENTS FOR THE DEGREE OF
DOCTOR OF PHILOSOPHY

UNIVERSITY OF FLORIDA

2008

©2008

by

Frederick Martin Van Assche IV

To my whole family, for teaching me:

Vita non est vivere sed valere vita est

ACKNOWLEDGMENTS

A strange thing that learning does is to teach you how much you do not know. Odder still is the realization that you desire to know exactly how much more you do not know! Whatever I learned (and learned what I want to learn) in my time here has been due to the help of a great many people.

I would like to take the opportunity to thank:

Dr. Jiho Yoo and Dr. Briggs White. Without their tireless assistance with equipment, and limitless patience for discussion, I could not have progressed this far;

My 3rd years, Bryan Blackburn, Cynthia Kan, and Eric Armstrong, for your enthusiasm and demands;

Everyone in the Wachsman research group, for color and support;

Dr. Eric Wachsman, for the resources and advice to make my tenure at the University a fruitful and enlightening one;

Drs. Scott Perry, Wolfgang Sigmund, and Juan Nino, for serving as my supervisory committee. Their guidance has been helpful, and it is greatly appreciated;

Dr. Jason Weaver, for serving as the external member of my committee, and for his continued support and direction throughout my many years at UF;

Dr. Merle Battiste, for helping me acquire a diligent scientific method and a formidable research skill set;

Eric Lambers and Dr. Susan Sinnott, for useful discussion;

The Major Analytical Instrumentation Center and the Engineering Research Center, for use of the facilities.

Research is an activity that requires great cooperation to accomplish. Behind every achievement stand ten people who made it happen. Thus, I would be remiss in my

acknowledgement without mentioning the individuals whose work on my behalf made this dissertation possible. Dr. Suman Chattergee and Dr. Jiho Yoo developed the early synthesis procedures for autoignition La_2CuO_4 powder used in Chapters 3 and 4. Sean Bishop, Jin Soo Ahn, Tak-keun Oh, and Dong-Jo Oh provided fabrication techniques for pellet synthesis performed in Chapter 6.

In early 2007, during sensor experiments utilizing a potentiometric gas sensor with heating elements, Bryan Blackburn noticed large sensor responses to small applied heater voltages after a crack formed in one of the heaters. The voltages caused changes in the potential of the sensor, and after testing the effect of the voltage gap, approached me to help him determine the causes of this behavior. Our discussions resulted in the possibility that the electric field had an effect on adsorption/desorption and or chemical/electrochemical reactions taking place at the electrodes. Thus began our collaborative research involving these external electric-field modifications to the sensor and measurements with the mass spectrometer that is included in Chapter 6 of my dissertation. Bryan and I worked closely on the testing procedures, utilizing my experience with the mass spectrometer and as a chemical engineer/materials scientist and his experience with sensors and as an electrical engineer/materials scientist. We constructed two new reactors for testing the sensors and this initial work has opened new avenues for investigating this phenomenon. My best wishes go to him as he continues it.

Special thanks go out to Dr. Heesung Yoon, for his contributions to keeping the labs running, and his assistance with equipment repair. Jennifer Tucker deserves my thanks for her diligent management of orders, reservations, supplies, and everything else keeping the group chugging along. My roommates Alan, Eric, and Henry, though they will never read these words, deserve my thanks and gratitude for the use of their 50 ft^2.

Success on any scale requires a curious combination of love, apprehension, support, intimidation, persistence, tenacity, larceny, and a bit of abject terror. For all those effects and more, I have a few people to thank. My fiancée, Christine has provided the continual impetus to persevere in my quest for the doctorate, and is just as happy as I to see it completed. My mother, Jeri, has been (and continues to be) a source of confidence, reason, temperance, and encouragement, and for that I thank her with all my heart. Finally, I thank my father, Fred, for impressing upon me a motto that has always served me well, and my tribute to him; *Aut viam inveniam aut faciam.*

TABLE OF CONTENTS

page

ACKNOWLEDGMENTS 4

LIST OF TABLES 10

LIST OF FIGURES 12

ABSTRACT 19

CHAPTER

1: INTRODUCTION 21

1.1 NO_X? 21
1.2 Advantages of the Potentiometric Sensor 22
1.3 Barriers to Commercialization 22

2: BACKGROUND 24

2.1 The Nernstian Sensor 24
2.2 The Non-Nernstian Sensor 25
2.3 Initial Theories for Non-Nerstian Behavior 26
2.4 Mixed Potential 27
2.5 Differential Electrode Equilibria 28
2.6 The Semiconducting Response 30
2.7 Materials of Sensing 32
2.8 Gas Phase NO_x and CO Chemistry 33
2.9 La_2CuO_4 Background 34

3: INITIAL TPD/TPR STUDIES OF LA2CUO4 AND PT 39

3.1 Introduction 39
3.2 Experimental 41
3.2.1 Synthesis of La_2CuO_4 41
3.2.2 Powder Characterization 41
3.2.3 TPD/TPR Setup 42
3.2.4 TPD/TPR Procedure 42
3.3 Results and Discussion 44
3.3.1 Powder Characterization Results 44
3.3.2 TPD/TPR Results of NO Gas Exposure 44
3.3.3 TPD/TPR Results of NO_2 Gas Exposure 50
3.3.4 TPD/TPR Results of CO_x /NO_x Gas Mixture Exposure 51
3.4 Summary 53

4: ADSORBATE STUDIES ON LA2CUO4 USING INFRARED SPECTROSCOPY AND X-RAY PHOTOEMISSION SPECTROSCOPY 63

4.1 Introduction 63
4.2 Experimental 64
4.2.1 Sample Preparation 64
4.2.2 Infrared Characterization 65
4.2.3 XPS Characterization 66
4.3 Results and Discussion 67
4.3.1 IR Results for NO_x Adsorption 67
4.2.2 XPS Results for NO_x Adsorption 70
4.4 Conclusions 77

5: ISOTOPICALLY LABELED OXYGEN STUDIES OF THE EXCHANGE BEHAVIOR OF NOx OVER LA2CUO4 85

5.1 Introduction 85
5.2 Experimental 93
5.2.1 Powder Preparation 93
5.2.2 Isotopically Labeled TPR/ TPD 93
5.3 Results and Discussion 95
5.3.1 $^{18}O_2$ Temperature Programmed Reaction 95
5.3.2 Determination of NO_x Adsorption via TPD/TPR 96
5.4 Summary 108

6: MASS SPECTROMETRY AND ELECTRICAL ANALYSIS OF A LA2CUO4/YSZ/PT FIELD MODIFIED DESORPTION SENSOR 122

6.1 Introduction 122
6.2 Reactor Construction 124
6.3 Experimental 125
6.3.1 Sample Preparation 125
6.3.2 Testing Setup 127
6.3.3 Electric-field Effect on Desorption 127
6.3.4 Electric-Field Effect on Sensing Behavior 128
6.4 Results and Discussion 128
6.4.1 Testing of La_2CuO_4 Capacitor-Type Sample 128
6.4.2 Testing of External Electric-Field Sensor 132
6.5 Summary 136

7: CONCLUSIONS 148

APPENDIX

A: CALIBRATION AND CORRECTION OF MASS SPECTROMETRY DATA 152

B: TEMPERATURE PROGRAMMED DESORPTION DATA FOR RELEVANT GAS COMBINATIONS 155

C: SILICA CONTAMINATION OF THE SENSOR ELECTRODE INTERFACE 163

D: ADSORPTION XPS OF NO/NO2/CO ON LA2CUO4 POWDER 169

E: DECONVOLUTED MASS SPECTRA OF ISOTOPICALLY LABELED NOX/LA2CUO4 TPD EXPERIMENTS.....182

LIST OF REFERENCES 202

BIOGRAPHICAL SKETCH 230

LIST OF TABLES

Table page

2-1. Metal oxides commonly used as resistance-type and potentiometric gas sensors and relevant publications. 37

3-1. TPD experiments 55

3-2. TPR experiments 55

3-3. Desorption energies of products resulting from NO adsorption on La_2CuO_4. 57

3-4. Desorption energies of products resulting from NO_2 adsorption on La_2CuO_4. 59

4-1. IR Peak assignments of the NO/NO_2 adsorbed samples of La_2CuO_4....78

5-1. List of Experiments Performed....112

6.1 NO adsorption TPD of device....140

6.2. NO_2 adsorption TPD of device 141

A-1. Primary and secondary ions found in Chapter 3 experiments 152

B-1. Temperature programmed desorption characteristics of 1% NO on La_2CuO_4 for the 30 ^oC per minute desorption 155

B-2. Temperature programmed desorption characteristics of 1% NO_2 on La_2CuO_4....156

B-3. Temperature programmed desorption characteristics of 0.67% NO and 0.33% CO on La_2CuO_4 157

B-4. Temperature programmed desorption characteristics of 500 ppm NO, 500 ppm CO, and 1% O_2 on La_2CuO_4....159

B-5. Temperature programmed desorption characteristics of 500 ppm NO_2, 250 ppm CO and 1000 ppm O_2 on La_2CuO_4. 161

B-6. Temperature programmed desorption characteristics of 500 ppm NO and 1000 ppm CO_2 on La_2CuO_4. 162

E-1: Desorption energy of peaks for 1% NO and 1% $^{16}O_2$ adsorption on $La_2Cu^{16}O_4$....182

E-2: Desorption energy and adsorption capacity for 1% NO and 1% $^{18}O_2$ adsorption on $La_2Cu^{16}O_4$ partially substituted with ^{18}O 184

E-3: Desorption energy and adsorption capacity of $La_2Cu^{18}O_4$ for adsorption of 1% NO and 1% $^{16}O_2$ 186

E-4: Desorption energy and adsorption capacity for 1% NO_2 and 1% $^{18}O_2$ adsorption on $La_2Cu^{16}O_4$ 189

E-5: Desorption energy of peaks for 1% NO_2 and 1% $^{18}O_2$ adsorption on $La_2Cu^{16}O_4$ partially substituted with ^{18}O.....192

E-11: Desorption energy and adsorption capacity for 1% NO_2 and 1% $^{16}O_2$ adsorption on $La_2Cu^{18}O_4$ 197

LIST OF FIGURES

Figure page

2-1. Diagram of the space charge layer at the surface of the electrode. Opposing charges build up inside the material to compensate for the charge established on the surface. The depth of this charged layer is dependant on the material (taken from Vayenas)[147] 36

2-2. Surface band model of a p-type semiconductor involving positive surface charge. The total work function (Φ) consists of the external work function (χ) combined with the Fermi energy (ε_v) and the contribution of the surface charge from adsorption (Φ_S)(taken from Vayenas)[147] 37

2-3. Plot of equilibrium mole fractions of exhaust gas consisting of 3% O_2, 15% CO_2, 3% H_2O, 650 ppm NO, and balance N_2 versus temperature in ^oC 38

3-1. Pipeline diagram of the Mass Spectrometer gas system....54

3-2. X-ray diffraction spectrum of La_2CuO_4 powder synthesized via the auto-ignition technique. Circles marked on the spectrum correspond to copper oxide impurities. 56

3-3. SEM image of the La_2CuO_4 powder generated via auto-ignition. 56

3-4. Temperature Programmed Desorption of 1% NO on La_2CuO_4. 57

3-5. Temperature Programmed Desorption of 500 ppm NO + 0.95% O_2 on La_2CuO_4. 57

3-6. Temperature Programmed Reaction of 500 ppm NO (a.)/ Temperature Programmed Reaction of 500 ppm NO and 1000 ppm O_2 (b.) on La_2CuO_4. 58

3-7. Temperature Programmed Reaction of 1000 ppm NO / 1000 ppm O_2 over (a.) Pt on YSZ and (b.) 500 ppm / 1000 ppm O_2 in the gas phase. 58

3-8. Temperature Programmed Desorption of 500 ppm NO_2 on La_2CuO_4. (a.)/ Temperature Programmed Reaction (b.) of 400 ppm NO_2 on La_2CuO_4. 59

3-9. Temperature Programmed Reaction of (a) 1200 ppm NO_2+ 1800 ppm O_2 over Pt/YSZ plate (b) 500 ppm NO_2 Temperature Programmed Reaction in the gas phase. 59

3-10. Temperature Programmed Desorption of 0.67% NO and 0.33% CO on La_2CuO_4. (a.)/ Temperature Programmed Reaction (b.) of 250 ppm NO and 1000 ppm CO on La_2CuO_4. 60

3-11. Temperature Programmed Desorption of 500 ppm NO, 500 ppm CO, and 1% O_2 on La_2CuO_4. (a.)/ Temperature Programmed Reaction (b.) of 500 ppm NO, 500 ppm CO, and 1000 ppm O_2 on La_2CuO_4. 60

3-12. Temperature Programmed Reaction of 1000 ppm NO, 1000 ppm CO, and 2000 ppm O_2 on Pt/YSZ and 500 ppm NO, 500 ppm CO, and 1000 ppm O_2 in blank reactor.....61

3-13. Temperature Programmed Desorption of 250 ppm CO, 500 ppm NO_2 and 1000 ppm O_2 on La_2CuO_4. (a.)/ Temperature Programmed Reaction (b.) of 500 ppm CO, 500 ppm NO_2 and 1000 ppm O_2 on La_2CuO_4. 61

3-14. Temperature Programmed Reaction of 1000 ppm NO_2, 1000 ppm CO, and 2000 ppm O_2 on Pt/YSZ and 500 ppm NO_2, 500 ppm CO, and 1000 ppm O_2 in blank reactor. 62

3-15. Temperature Programmed Desorption of 500 ppm NO and 1000 ppm CO_2 on La_2CuO_4. (a.)/Temperature Programmed Reaction (b.) of 500 ppm NO and 1000 ppm CO_2 on La_2CuO_4. 62

4-1a. IR spectra of La_2CuO_4/KBr mulled mixture after NO adsorption.....79

4-1b. IR spectra of La_2CuO_4/KBr mulled mixture after NO_2 adsorption 79

4-2a. Fourier Deconvolution of 1550-1200 cm^{-1} spectrum of NO-adsorbed La_2CuO_4 (Labeled line corresponds to the Fourier deconvolution) 80

4-2b. Fourier Deconvolution of 1550-1200 cm^{-1} spectrum of NO_2 – adsorbed La_2CuO_4 (Labeled line corresponds to the Fourier deconvolution) 80

4-3. Full range XPS spectra of solid La_2CuO_4 samples in the (a) freshly sintered case and (b) after 3 weeks of exposure to sensor testing conditions.....81

4-4. O1s XPS spectra of NO adsorbed La_2CuO_4 versus the unadsorbed case.....82

4-5. O1s XPS spectra of NO_2 adsorbed La_2CuO_4 versus the unadsorbed case.....82

4-6. Flowchart of proposed NO adsorption mechanism 83

4-7. Flowchart of proposed NO_2 adsorption mechanism.....84

5.1 Flowchart of possible isotopic oxygen exchange mechanisms during NO adsorption on La_2CuO_4. 110

5.2 Flowchart of possible oxygen exchange mechanisms during NO_2 adsorption on La_2CuO_4. 111

5-3. Temperature programmed reaction of 1000 ppm $^{18}O_2$ over $La_2Cu^{16}O_4$.....113

5-4 (a). 1% NO+ 1% $^{18}O_2$ TPD over $La_2Cu^{16}O_4$ Lattice, (b) Low Concentration Detail, (c).TPD of aged La_2CuO_4 sample.....113

5-5. (a) 1% NO+ 1% $^{16}O_2$ TPD over heavily enriched $La_2Cu^{18}O_4$ Lattice; (b) 1% NO+ 1% $^{18}O_2$ TPD over lightly enriched $La_2Cu^{18}O_4$ Lattice.....114

5-6. Gaussian Analysis of (a) Desorption Peak of $N^{16}O$; (b) Desorption Peak of $N^{18}O$; (c) Desorption Peak of $^{16}O_2$; (d) Desorption Peak of $^{16}O^{18}O$; (e) Desorption Peak of $^{18}O_2$.....114

5-7. (a) 1% NO_2 + 1% $^{18}O_2$ TPD over $La_2Cu^{16}O_4$ Lattice; (b) 1% NO_2 + 1% $^{16}O_2$ TPD over $La_2Cu^{16}O_4$ Lattice; (c) 1% NO_2 + 1% $^{16}O_2$ TPD over heavily enriched $La_2Cu^{18}O_4$ Lattice; (d) 1% NO_2 + 1% TPD over lightly enriched $La_2Cu^{18}O_4$ Lattice.....116

5-8. Gaussian Analysis of: (a) Desorption Peak of $N^{16}O_2$; (b) Desorption Peak of $N^{16}O^{18}O$; (c) Desorption Peak of $N^{18}O$; (d) Desorption Peak of $^{16}O_2$; (e) Desorption Peak of $^{18}O_2$; (f) Desorption Peak of $^{16}O^{18}O$; (g) Desorption Peak of $N^{16}O$ 118

5-9. (a). 700 ppm $N^{16}O$+600 ppm $^{16}O_2$ TPR over $La_2Cu^{18}O_4$ Lattice 119

(b). 700 ppm NO+ 300 ppm $^{16}O_2$ TPR over partially substituted $La_2Cu^{18}O_4$ Lattice. 119

5-11. Formation of nitrito via nitrosyl ion/ chelated nitrite intermediate 120

5-12. Nitrogen-down bonding to ^{16}O surface to form one-step nitrito charged complex. 120

5-13. Simplified Mechanism for NO Adsorption on La_2CuO_4. 120

5-14. Reversible rearrangement of the nitrite to nitrate formed by NO_x adsorption.....121

5-15 .Simplified Mechanism for NO_2 Adsorption on La_2CuO_4. 121

6.1 Tubular reactor for sensor reference studies 137

6.2 La_2CuO_4 capacitor device for determining E-field effects on desorption 138

6.3 NO desorption from the La_2CuO_4 capacitor following NO adsorption 138

6.4 NO desorption from La_2CuO_4 powder following NO adsorption 139

6.5 NO_2 desorption from the La_2CuO_4 capacitor following NO adsorption.....139

6.6. NO desorption from the La_2CuO_4 capacitor following NO_2 adsorption.....140

6.7. NO_2 desorption from the La_2CuO_4 capacitor following NO_2 adsorption. 141

6-8. Sensitivity plot of NO for the sensor 142

6-9. R^2 values of data fitting to linear plots for NO.....142

6-10. Sensitivity plot of NO_2 for the sensor.....143

6-11. R^2 values of data fitting to linear plots for NO_2 143

6-12. Mass spectrometry comparison of NO in reactor effluent from forward biased sensor testing.....144

6-13. Mass spectrometry comparison of NO_2 in reactor effluent from forward biased sensor testing.....145

6-14. Mass spectrometry comparison of NO in reactor effluent from reverse biased sensor testing.....146

6-15. Mass spectrometry comparison of NO_2 in reactor effluent from reverse biased sensor testing.....147

B-1. Temperature Programmed Desorption of 1% NO on La_2CuO_4 at 30 ^oC per minute (a.) and 5 ^oC per minute (b.).....155

B-2. Temperature Programmed Desorption of 500 ppm NO_2 on La_2CuO_4.....156

B-3. Temperature Programmed Desorption of 0.67% NO and 0.33% CO on La_2CuO_4. 157

B-4. Temperature Programmed Desorption of 500 ppm NO, 500 ppm CO, and 1% on La_2CuO_4. 158

B-5. Temperature Programmed Desorption of 500 ppm NO_2, 250 ppm CO and 1000 ppm O_2 on La_2CuO_4. 160

B-6. Temperature Programmed Desorption of 500 ppm NO and 1000 ppm CO_2 on La_2CuO_4. .162

C-1. La_2CuO_4 electrode on 8% YSZ substrate used for heat and gas cycling tests. 164

C-2. XPS of La_2CuO_4 electrode surface following 3 weeks of cycling under sensor testing conditions. After 3 weeks in a thermally cycled environment and exposure to NO, NO_2, CO, and CO_2 gas mixtures, the structure and composition of the La_2CuO_4 electrode remains constant according to XPS, indicating no silica deposition from siloxane occurs in the short term. 165

C-3. XPS spectra of YSZ electrolyte on the just-sintered sample. Some trace peaks of the La_2CuO_4 electrode can be seen due to slurry wetting during the screen printing process.....166

C-4. XPS spectra of the YSZ electrolyte after thermal cycling in sensor testing conditions. The peak for the Si 2p3 orbital was seen to increase due to diffusion of Si to the grain boundaries of the YSZ. 166

C-5. XPS spectra of the YSZ electrolyte below the La_2CuO_4 electrode after thermal cycling. The Si 2p3 peak was observed to increase over the uncycled sample, but remained lower than the uncovered and cycled YSZ sample. 167

C-6. SEM photograph of the electrode/electrolyte interface after sintering at 800 ^oC for 10 hours. The La_2CuO_4/YSZ interface was well-adhered, and showed no sign of auxiliary phases.....167

C-7. The surface of the La_2CuO_4 electrode shows no visible deposits of silica products after 3 weeks of thermal cycling under sensor testing conditions.....168

D-1. C1s XPS spectra for unadsorbed (blue) and NO adsorbed (green) La_2CuO_4 powder.....169

D-2. La3d5 XPS spectra of unadsorbed (blue) and NO adsorbed (green) La_2CuO_4 powder. 170

D-3. C1s XPS spectra of unadsorbed (blue) and NO_2 adsorbed (red) La_2CuO_4 powder.....170

D-4. La3d5 XPS spectra of unadsorbed (blue) and NO_2 adsorbed (red) La_2CuO_4 powder.....171

D-5. O1s XPS spectra of unadsorbed (blue) and NO+CO adsorbed (purple) La_2CuO_4 powder.....172

D-6. C1s XPS spectra of unadsorbed (blue) and NO+CO adsorbed (purple) La_2CuO_4 powder.....173

D-7. La3d5 XPS spectra of unadsorbed (blue) and NO+CO adsorbed (purple) La_2CuO_4 powder.....174

D-8. O1s XPS spectra of unadsorbed (blue) and NO_2+NO adsorbed (dark blue) La_2CuO_4 powder.....175

D-9. C1s XPS spectra of unadsorbed (blue) and NO_2+NO adsorbed (dark blue) La_2CuO_4 powder.....176

D-10. La3d5 XPS spectra of unadsorbed (blue) and NO_2+NO adsorbed (dark blue) La_2CuO_4 powder.....177

D-11. O1s XPS spectra of unadsorbed (blue) and CO adsorbed (orange) La_2CuO_4 powder. 178

D-12. C1s XPS spectra of unadsorbed (blue) and CO adsorbed (orange) La_2CuO_4 powder. 178

D-13. La3d5 XPS spectra of unadsorbed (blue) and CO adsorbed (orange) La_2CuO_4 powder. .179

D-14. Full range XPS comparison spectra of unadsorbed and adsorbed La_2CuO_4 powder samples.....180

D-15. O1s XPS comparison spectra of unadsorbed and adsorbed La_2CuO_4 powder samples. ...180

D-16. C1s XPS comparison spectra of unadsorbed and adsorbed La_2CuO_4 powder samples. ...181

D-17. La3d5 XPS comparison spectra of unadsorbed and adsorbed La_2CuO_4 powder samples.....181

E-1. Desorption Peak of $N^{16}O$ after NO adsorption on $La_2CuO_4{}^{16}$ with Gaussian Analysis 182

E-2. Desorption Peak of $^{16}O_2$ after NO adsorption on $La_2Cu^{16}O_4$ with Gaussian Analysis.....183

E-3. Desorption Peak of $^{18}O^{16}O$ after NO adsorption on $La_2Cu^{16}O_4$ with Gaussian Analysis.....183

E-4. Desorption Peak of $N^{16}O$ after NO adsorption on partially substituted $La_2Cu^{18}O_4$ with Gaussian Analysis.....184

E-5. Desorption Peak of $^{16}O_2$ after NO adsorption on partially substituted $La_2Cu^{18}O_4$ with Gaussian Analysis.....185

E-6. Desorption Peak of ^{16}O ^{18}O after NO adsorption on partially substituted $La_2Cu^{18}O_4$ with Gaussian Analysis.....185

E-7. Desorption Peak of $^{18}O_2$ after NO adsorption on partially substituted $La_2Cu^{18}O_4$ with Gaussian Analysis.....186

E-8. Desorption Peak of $N^{16}O$ after NO adsorption on $La_2Cu^{18}O_4$ with Gaussian Analysis 187

E-9. Desorption Peak of $N^{18}O$ after NO adsorption on $La_2Cu^{18}O_4$ with Gaussian Analysis 187

E-10. Desorption Peak of $^{16}O_2$ after NO adsorption on $La_2Cu^{18}O_4$ with Gaussian Analysis.....188

E-11. Desorption Peak of ^{16}O ^{18}O after NO adsorption on $La_2Cu^{18}O_4$ with Gaussian Analysis..188

E-12. Desorption Peak of $^{18}O_2$ after NO adsorption on $La_2Cu^{18}O_4$ with Gaussian Analysis.....189

E-13. Desorption Peak of $N^{16}O$ after NO_2 adsorption on $La_2Cu^{16}O_4$ with Gaussian Analysis....190

E-14. Desorption Peak of $N^{16}O_2$ after NO_2 adsorption on $La_2Cu^{16}O_4$ with Gaussian Analysis...190

E-15. Desorption Peak of $^{16}O_2$ after NO_2 adsorption on $La_2Cu^{16}O_4$ with Gaussian Analysis 191

E-16. Desorption Peak of ^{16}O ^{18}O after NO_2 adsorption on $La_2Cu^{16}O_4$ with Gaussian Analysis.....191

E-17. Desorption Peak of $^{18}O_2$ after NO_2 adsorption on $La_2Cu^{16}O_4$ with Gaussian Analysis 192

E-18. Desorption Peak of $N^{16}O$ after NO_2 adsorption on partially substituted $La_2Cu^{18}O_4$ with Gaussian Analysis.....193

E-19. Desorption Peak of $N^{16}O_2$ after NO_2 adsorption on partially substituted $La_2Cu^{18}O_4$ with Gaussian Analysis.....193

E-20. Desorption Peak of $N^{16}O^{18}O$ after NO_2 adsorption on partially substituted $La_2Cu^{18}O_4$ with Gaussian Analysis.....194

E-21. Desorption Peak of $N^{18}O$ after NO_2 adsorption on partially substituted $La_2Cu^{18}O_4$ with Gaussian Analysis.....194

E-22. Desorption Peak of $^{16}O_2$ after NO_2 adsorption on partially substituted $La_2Cu^{18}O_4$ with Gaussian Analysis.....195

E-23. Desorption Peak of $^{16}O^{18}O$ after NO_2 adsorption on partially substituted $La_2Cu^{18}O_4$ with Gaussian Analysis.....195

E-24. Desorption Peak of $^{18}O_2$ after NO_2 adsorption on partially substituted $La_2Cu^{18}O_4$ with Gaussian Analysis.....196

E-25. Desorption Peak of $N^{16}O$ after NO_2 adsorption on $La_2Cu^{18}O_4$ with Gaussian Analysis....198

E-26. Desorption Peak of $N^{16}O_2$ after NO_2 adsorption on $La_2Cu^{18}O_4$ with Gaussian Analysis...198

E-27. Desorption Peak of $N^{16}O^{18}O$ after NO_2 adsorption on $La_2Cu^{18}O_4$ with Gaussian Analysis.....199

E-28. Desorption Peak of $N^{18}O$ after NO_2 adsorption on $La_2Cu^{18}O_4$ with Gaussian Analysis....199

E-29. Desorption Peak of $^{16}O_2$ after NO_2 adsorption on $La_2Cu^{18}O_4$ with Gaussian Analysis 200

E-30. Desorption Peak of $^{16}O^{18}O$ after NO_2 adsorption on $La_2Cu^{18}O_4$ with Gaussian Analysis .200

E-31. Desorption Peak of $^{18}O_2$ after NO_2 adsorption on $La_2Cu^{18}O_4$ with Gaussian Analysis 201

Abstract of Dissertation Presented to the Graduate School
of the University of Florida in Partial Fulfillment of the
Requirements for the Degree of Doctor of Philosophy

HETEROGENEOUS CATALYTIC EVALUATION AND ADSORPTION CHARACTERIZATION OF THE LA2CUO4/YSZ/PT POTENTIOMETRIC COUPLE

By

Frederick Martin Van Assche IV

May 2008

Chair: Eric D. Wachsman
Major: Materials Science and Engineering

The problem of scarce resources has advanced the development of more efficient lean-burn engine technology for power generation and transportation. Thus, the issue of NO_x production and the need to monitor that production becomes increasingly important. To better understand NO_x sensing, the potentiometric couple of La_2CuO_4 and platinum across a yttrium-stabilized zirconia (YSZ) substrate was studied.

Temperature programmed reaction and desorption studies were performed on powder samples to determine desorption strength and catalysis of NO_x on La_2CuO_4. A mass spectrometer with one part per billion resolution collected spectra for the experiments. NO gas proved non-reactive in both oxygen-rich and oxygen-lean conditions. NO_2 gas desorbed in multiple gas-phase products, and its reaction was catalytically activated by La_2CuO_4.

Adsorption of NO_x was studied by X-ray photoelectron spectroscopy and infrared spectroscopy in diffuse reflection configuration. Results indicated the presence of ionic nitrate and nitrite complexes providing substantial electronic charge separation in large quantities. Photoelectron peak splitting of the O1s oxygen orbital verified NO caused oxygen deprivation and increased resistivity, while NO_2 adsorption resulted in creation of electron holes and an overall decrease in resistivity.

Oxygen isotope exchange was performed to determine the adsorption mechanism of NO_x. Temperature programmed experiments using $^{18}O_2$ gas over $La_2Cu^{16}O_4$ and $La_2Cu^{18}O_4$ identified bonding behavior and adsorption/desorption sequence of NO_x. Formation surface complexes were found to occur exclusively with solid phase oxygen, but substitution of the primary oxygen in the complex was dependent on available thermal energy. It could be concluded that the oxygen exchange is a very important component of the overall sensor response, and that the adsorptive component plays a large role in the establishment of the potential between the electrodes.

To adjust the adsorption equilibrium and modify sensor response, desorption experiments under external electric field bias were performed on a La_2CuO_4 pellet. Initial bias, aging effects and increases in field strength were shown to change the desorption profile of NO and NO_2 gases from the surface of the La_2CuO_4 pellet. A sensor utilizing a La_2CuO_4 pellet with similar field generating structures was also constructed. It displayed sensitivity changes to NO_x gases with changes in field voltage and bias.

CHAPTER 1
INTRODUCTION

1.1 NO_x?

The last 25 years have seen increased technological modernization of the world, and with it, a massive demand for energy. This demand coincides with economic and societal pressures for cleaner and more efficient power generation for transportation and electricity. While these influences provide a significant impetus to develop alternate sources of energy for future needs, current methods of power generation (such as combustion of oil, coal, or natural gas) will remain the most widely utilized processes for many years. As such, it is in the best interests of the world at large to optimize these processes.

The simplest and most effective method to increase the yield and efficiency of these combustion processes is to combust fuel in an excess of oxygen. This allows for complete conversion of the fuel and maximum heat liberation. Unfortunately, the excess oxygen has the undesired effect of producing oxides of nitrogen (NO_x).[1]

NO_x is a problematic by-product for a number of reasons. First, NO_x gases are biological irritants, and can react with airborne organics to produce smog and ozone (O_3). In concentrated urban areas, NO_x and smog cause respiratory problems after extended exposure.[2] NO_x can react with atmospheric water to form acids, which precipitate out as acid rain. Additionally, since this rain can migrate away from the cities, even rural areas are impacted by urban NO_x generation.[3]

In stationary (e.g. power generation, industrial heating) applications, treatments are available to eliminate the NO_x, but require bulky and delicate equipment in order to monitor the treatment process. In mobile applications, this equipment is unavailable to monitor NO_x. This

fact, combined with the multitude of demands placed on engines, results in transportation applications producing the majority of NO_x emissions.[4]

NO_x production from transportation can only grow, as more cars fill the roads and consumer pressure for greater fuel efficiency pushes the limits of lean-burn combustion. Thus, treatment of these mobile sources will become essential in order to decrease pollution. A compact NO_x sensor package would enable the application of pollution removal technology to mobile sources of NO_x generation.

1.2 Advantages of the Potentiometric Sensor

Solid state potentiometric sensors have key advantages for NO_x detection under lean-burn combustion conditions. These devices, based on the classic O_2 sensor design, have excellent resistance to high temperature, vibration, and corrosion. They require no external power source or complicated electronics to obtain a signal.

Potentiometric sensors for NO_x detection have some flexibility in design, and so can be constructed as either planar or tubular devices, depending on which electrodes are exposed to the sensed gas. Planar construction allows the sensor fabrication using simple ceramic processing techniques such as tape casting and screen printing. This allows for excellent control of the electrode microstructure, as well as construction of a multi-layered structure that can integrate heaters, temperature sensors, and other elements.

1.3 Barriers to Commercialization

At present, there are no commercial potentiometric sensors available for specific NO_x monitoring, instead estimating NO_x concentrations indirectly via multiple measurement of total pollutant concentration. This is due to the complicated response of current sensor technology to NO_x and other combustion products such as CO, water, and unburned hydrocarbons. Sensors of

this type tend to exhibit cross-sensitivity to mixtures of exhaust products, and so the signal generated must be deconvoluted in order to provide a useful value. This presents a substantial challenge, as the mechanism for sensing has not been deciphered for individual gases, and the interaction between the gases is not well established. Thus, the contribution from each component of the mixture cannot be accurately assigned and the total signal cannot be reliably determined under all conditions.

Some resistive NO_x sensors have been commercialized, though these devices suffer the same cross-sensitivity of NO_x to other exhaust products. This limits their use to applications where the analyte mixture can be treated to remove products that may interfere with NO_x sensing, such as stationary power generation.

CHAPTER 2
BACKGROUND

2.1 The Nernstian Sensor

It is impossible to discuss sensors in any depth without first discussing the qualities that compose a good example. The key attributes of a good sensor are sensitivity, selectivity, stability, and quick response. Sensitivity (S) can be expressed in a potentiometric sensor as the change in voltage across the electrolyte with a given change in gas concentration, represented below in Equation 2-1.

$$S(gas) = \frac{\Delta V(gas)}{\Delta[gas]} \qquad [2\text{-}1]$$

Selectivity to a component gas is the ratio of the sensitivity of a desired sensate over the sensitivity of the device to an undesired sensate. Quick response from a sensor means that the time required to achieve a stable value is short, and a sensor with good stability will repeatedly deliver that value over time.

The most widely used and best known example of a solid electrolyte sensor is the λ-sensor, "lambda sensor," named for its use in measuring the air/fuel ratio (denoted λ) during combustion. This sensor consists of two metal electrodes separated by a solid electrolyte layer capable of conducting O^{2-} ions, usually a doped ZrO_2. One electrode remains exposed to a reference concentration of oxygen, and the other submerged in an unknown concentration of O_2.

The difference in potential between these electrodes is sufficient to calculate the concentration of oxygen at the electrode in the unknown atmosphere, referred to as the sensing electrode. The voltage between the electrodes can be related to the difference in concentration between the unknown and reference atmospheres by the use of the Nernst equation, assuming

that the oxygen atmosphere is in equilibrium with the individual electrodes, shown in Equation 2-2.

$$\Delta V = \frac{RT}{4F} \ln \frac{[P_{O_2}(Unknown)]}{[P_{O_2}(Reference)]} \qquad [2\text{-}2]$$

Since the behavior of these sensors is governed by the Nernst equation, they are known as Nernstian sensors.

2.2 The Non-Nernstian Sensor

Nernstian behavior does not apply to all sensors or conditions. When the gas mixture does not establish oxygen equilibrium with the sensing electrodes, it is possible to see a shift from these Nernstian values, making the potential generated across the electrolyte a "non-Nernstian" potential. Fleming observed in 1977 that the presence of several thousand parts per million CO in the exhaust atmosphere region of an oxygen sensor caused a 100-200 mV shift in the sensor response.[5,6] If the Nernstian response to an order of magnitude change in oxygen concentration from 1% to 10% at 800 ^{o}C is examined, the result can be seen in Equation 2-3.

$$\Delta V = \frac{RT}{4F}\left(\ln \frac{[P_{O_2}(.1)atm]}{[P_{O_2}(.21)atm]} - \ln \frac{[P_{O_2}(.01)atm]}{[P_{O_2}(.21)atm]}\right) \cong 50mV \qquad [2\text{-}3]$$

The sensitivity can be calculated using Equation 2-4.

$$S(O_2) = \frac{\Delta V(O_2)}{\Delta[O_2]} = \frac{50mV}{100{,}000 - 10{,}000\,ppm} \cong 555\,\mu V/ppm \qquad [2\text{-}4]$$

This value can be compared to the sensitivity of CO on the oxygen sensor,[7] which responds to a change from 100 ppm CO to 500 ppm CO with a 30 mV non-Nernstian response, seen in Equation 2-5.

$$S(CO) = \frac{\Delta V(CO)}{\Delta[CO]} = \frac{30mV}{500 - 100\,ppm} = 75 \times 10^3\,\mu V/ppm \qquad [2\text{-}5]$$

This was a much larger shift than a corresponding shift from a change in oxygen concentration. If the selectivity of the two gases is compared, the sensitivity can be evaluated. (Equation 2-6)

$$\frac{S(CO)}{S(O_2)} = \frac{75\times10^3\ \mu V/ppm}{555\ \mu V/ppm} = 135 \qquad [2\text{-}6]$$

This means that the sensitivity is 135 times higher for CO than for O_2, and so the oxygen sensor is quite selective for CO over oxygen. This non-Nernstian behavior occurs in the presence of NO_x and other exhaust products as well, and so the need to understand the factors behind this behavior becomes readily apparent.

2.3 Initial Theories for Non-Nerstian Behavior

The non-Nernstian effect has been studied for many types of sensors. NO_x has been studied the most intensely,[7-79] but other exhaust products such as hydrocarbons,[13-15,80-87] hydrogen sulfide,[88] SO_x,[89-91] hydrogen,[37,38,50,92] and N_2O[93-95] have also been examined. The overall mechanism for potentiometric sensing has not yet been totally explained. Since Fleming's initial work in 1977, the deviation of potentiometric couples from the Nernst equation has been an extensively debated topic.

Initial ideas to explain the deviation from theory centered on the modification of the local O_2 atmosphere as a way of changing the potential at an electrode without complication of the phenomena associated with the O_2 reaction on the surface. It was noted that catalyst powders on resistive semiconductor electrodes had more rapid responses to carbon monoxide.[96] It was assumed that the catalyst was converting $CO \rightarrow CO_2$ by removing the oxygen above the electrode, and this behavior shifted the response.

2.4 Mixed Potential

In 1982, Williams[97] *et al.* applied a concept from aqueous corrosion theory, Mixed Potential, to the gas phase in order to model the potentiometric response. This theory supposed that multiple electrochemical reactions simultaneously occur over a conducting surface, and the potential of that surface is intermediate between the half-cell reactions of the electrochemistry occurring there. In sensors, the electrodes function independently, and the potential difference across the cell would be the additive sum of the potentials generated at each electrode.

In the case of the potentiometric sensor coupled around yttrium-stabilized zirconia (YSZ), the basic reactions with the environment occur as follows. YSZ, being an oxygen ion conductor, will equilibrate with the oxygen in the environment according to Equation 2-7.

$$\tfrac{1}{2} O_{2(g)} + V_O^{\bullet\bullet}(YSZ) \rightleftharpoons 2e'(exterior) + O_O^x(YSZ) \qquad [2\text{-}7]$$

Pollutant gases, such as CO or NO_x, will equilibrate according to the general expression in Equation 2-8.

$$\mathrm{Re}_{(g)} + O_O^x(YSZ) \rightleftharpoons Ox_{(g)} + V_O^{\bullet\bullet} + ne'(exterior) \qquad [2\text{-}8]$$

$\mathrm{Re}_{(g)}$ and $\mathrm{Ox}_{(g)}$ refer to the reduced and oxidized pollutant gases (NO/NO_2, CO/CO_2) in the mixture. Depending on the kinetics of each reaction at each electrode, a potential will evolve to drive the charges generated by the reactions around the exterior circuit. This simplified approach constitutes the Mixed Potential theory for sensors, and is more extensively explained in other articles.[31,45,81,98-100]

It is assumed by this mechanism that the gas concentrations at the interface of the electrodes and electrolytes reach a full equilibrium according to the reactions stated above. The potential between the electrodes comes about from the difference in electrochemical rate of reaction at the electrodes. At the time, this theory was widely adopted as the explanation for

almost all non-Nernstian sensors, though the conclusions of the mechanism had not been verified by gas analysis.

2.5 Differential Electrode Equilibria

In 2000, an alternate explanation, called Differential Electrode Equilibria,[63] was proposed. This approach postulated that the mixed potential theory adequately describes some of the behavior of sensors at high temperatures, where kinetics allows for fast equilibrium, but at lower temperatures the effect of the electrochemical reaction is only one of the factors affecting the surface.

In an environment where an electrochemical reaction can easily occur, such as methane and trace oxygen, the largest source of electrons will come from the establishment of steady state equilibrium by these electrochemical reactions.[101] By contrast, the thermodynamic equilibrium for NO gas at high temperature should result in decomposition to N_2 and O_2, but this outcome does not occur;[102] thus, the electrochemical conversion reaction cannot play a major role. If the reaction does not reach its thermodynamically defined equilibrium state, it is unlikely that the electrochemical reaction of the sensed gas is the sole factor in determining the voltage generated between the two electrodes of the sensor.

To accurately model the output of the sensor at lower temperatures, the Differential Electrode Equilibria theory suggested that the other contributions to the electrode potential must be combined with potentials from electrochemical reactions. Gas concentration at the electrode is affected due to non-electrochemical catalytic conversion, and this change must be accounted for in order to predict the change of voltage response to a change in concentration. In addition to this effect, adsorption contributes to the electrode potential by inducing changes in the Fermi level. These behaviors change with temperature and reactant concentration, which can affect the voltage response of the sensor.

For sensors utilizing a metal reference electrode in a relatively inert reference gas, it is possible for the electrochemical reactions over the sensing electrode to account for the majority of the potential across the electrolyte. Non-electrochemical catalysis at the sensing electrode will not affect the potential at the reference electrode directly, though it can modify the local concentration of the desired sensate gas over the electrode and so affect sensor response in that manner. If the sensing electrode catalyzes a reaction away from the three phase boundary (TPB), no electrons will be present in the exterior circuit as a result of the reaction, since no compensating ionic current can flow through the electrolyte from the TPB. Thus, no potential will be generated as a result of the reaction. Since the reference electrode will operate under constant atmosphere, any change in electrochemical reaction rate at the sensing electrode will be very important.[103]

By contrast, when both electrodes are exposed to the sensing environment, the presence of both electrochemical and non-electrochemical catalytic reactions at both electrodes magnifies the importance of adsorption. Reactions causing the shifts in the potential of the electrode now occur over both the sensing and counter electrodes, and so the contributions from these reactions cancel each other. This does not necessarily mean the contributions cancel out entirely. If a highly catalytic counter-electrode such as platinum is used, the sensed gas may react before reaching the three phase boundary of the counter-electrode. As a result, the partial pressure of both the sensing gas and oxygen will be different at the three phase boundary (TPB) for each electrode. Because of this, the potential generated becomes a function of both the concentration in the gas stream and the differing concentrations of gases at the electrode/electrolyte interface of each electrode.

In addition to the effects caused by catalysis, adsorption of gases onto the surface of the electrode may induce a shift in the electrode potential. Metals predispose to adsorb gases somewhat independently of the gas atmosphere and the charge concentration generated as a result of this adsorption tends to be small. Voltages created as a result of the adsorption behavior are assumed confined to the non-metal electrodes. If the sensing electrode is a semiconductor, adsorption can play a large role in potential generation. The Differential Electrode Equilibria model includes semiconductor sensing effects, and it is important to note them due to the effect of surface morphology on the experimental sensing behavior. The grain size of the electrode powder is closely related to the roughness, and hence, the surface area of the electrode. Small grains of powder contribute to the length of the three phase boundary by providing a more effective interface between the electrode and electrolyte. Since the powders used for these experiments often contain substantial amounts of sub-micron sized powders, the surface area of the sensing electrode can be quite large.[104]

2.6 The Semiconducting Response

The semiconducting response of a sensor is based on the change of the work function or surface charge by the influence of adsorbed radicals at the surface and interface regions. The work function of a compound is the sum of the energies required to remove an electron from the compound to a distance outside the surface. It includes the internal work function, known as the Fermi energy, the external work function, and the sum of adsorbate components corresponding to the surface charge.

The idea of semiconducting response has its basis in the resistive sensor, where the change in resistance indicates the sensor response. During adsorption, bonds form from the adsorbate to the surface, and as a result either reduce or enhance the concentration of electronic charge carriers at the surface of the semiconductor. The conductive process of the system is described

relative to the Debye length, expressed in Equation 2-10, where *k, T, q, ε*, and *n* are the Boltzmann constant, absolute temperature, electron charge, dielectric constant, and charge-carrier concentration.[105]

$$L_D = \left(\frac{kT\varepsilon}{q^2 n} \right)^{1/2} \qquad [2\text{-}10]$$

This characteristic length can span into the micrometer range, and become larger than the grains of the semiconductor, depending mostly on the temperature and charge-carrier concentration. This can range from 3-5 nm for SnO_2[106,107] to roughly 7 nm for TiO_2,[108] to 15 nm for WO_3[109] for an operating temperature of 400-500 ^oC.

The Debye length controls the depth of the Randschicht (space charge) layer,[110] which compensates for the charged species formed at the adsorbate/ substrate interface surface by the adsorption of gaseous species. (Figure 2-1) Material at the interface maintains equivalent charge density, which decreases with distance from the interface. The depth of this conduction pathway is highly dependent on the work function of the semiconductor compound.

For semiconductors with large charge carrier concentrations (*n*) the Debye length will be small and the Randschicht layer will have limited influence. As a result, adsorption will not greatly affect the resistivity of the material. In the case where the semiconductor has a very low charge carrier concentration (i.e. an insulator), the Randschicht layer will be very large in order to balance the charge, and the effect will be easily discernable through conductivity measurements.

For resistive sensors, the individual grains interconnect to provide an electronic pathway, and the size and connectivity can be influenced by ceramic processing. When L_D is small with respect to the grain size, only the outside of the grains are influenced by the space charge layer.

The conduction volume affected by gas interaction is limited to the actual interface between gas and grain, and at the grain/grain boundary. When grain size is small with respect to L_D, the entire grain is affected by the charge layer and the entire bulk conductivity is modified as a result. This effect has been seen on many semiconductors, for many different gases.[106-109,111]

This interconnection of the space charge layer due to grain size observed for resistive sensors also has implications on the potentiometric sensor. The change in bulk conductivity will naturally have an effect on establishing a charge balance, and small-grained electrodes also will have a greater surface area to establish the potential. This can shorten the response time to establish the potential, but may also impose an upper limit to detection capability if a sufficiently large Randschicht layer cannot form to compensate for the charge on the surface.

The semiconducting effect can influence the sensor behavior even without a gas environment. In the full sensor, the initial voltage between the electrodes may be a non-zero value. The Fermi level difference between a semiconducting sensing electrode and a metallic reference electrode generates a potential difference even in the absence of adsorbant gases. Surface adsorptions modify the surface with charge, changing the work function and altering the potential difference between the electrodes[112,113] as shown in Figure 2-2. The total work function (Φ) consists of the external work function (χ) combined with the Fermi energy (ε_v) and the contribution of the surface charge from adsorption (Φ_S).

2.7 Materials of Sensing

A key point in further deciphering the sensing mechanism for both potentiometric and conductivity sensors will be material selection. As mentioned previously, metals would be poor choices for a conductometric sensor, as the overall change in conductivity due to gas-phase variations is very small relative to the total conductivity of the metal. This problem becomes less important with respect to potentiometric sensors, as the metal can function as a known catalyst

and interface. Indeed, Pt[6,7,18,23-25,28-30,33,41,43,63-68,70,80,81,88,92,114-127] and Au[13,25,50,81-83,85,92,115,126-128] have found extensive use as counter electrodes in potentiometric sensors.

One type of material that has found a use in both potentiometric and conductometric sensors are metal oxides. Since the oxides of metals do not retain the full metallic bonding character of their parent, they have a far greater resistivity, and are thus classified as semiconductors. Additionally, metal oxides can extensively interact with gases due to modification of their oxygen chemistry. These changes allow catalytic conversion with charge transfer and cause significant changes in the concentration of charge carriers. Some examples and references of metal oxides used in conductometric and potentiometric sensors are given in Table 2-1. As different oxides demonstrate different catalytic properties with changes in composition, it is necessary to choose the correct oxide for the gas environment.

2.8 Gas Phase NO_x and CO Chemistry

NO_x composition in the gas phase can be complex, and the thermodynamically favored composition of the gas phase can be quite different than the actual composition. At low temperatures, a metastable equilibrium occurs. This equilibrium unbalances only in cases of extraordinary driving forces, such as large K_{eq} values seen at temperatures where sufficient thermal energy exists to overcome any barriers of activation energy. To calculate the equilibrium composition of a system, several components are required. First, possible occurring species must be identified, and the $\Delta G_{formation}$ values for each independent formation reaction must be found. The composition can then be optimized to minimize the free energy of the system at a given temperature. This process is best performed by a numerical solver software package coupled with a database of K_{eq} values.

Calculations were performed using TEST software[129,130] to determine the equilibrium composition of a simulated exhaust mixture (3% O_2, 15% CO_2, 3% H_2O, and 650 ppm NO) used

for potentiometric sensing experiments. The plot of the calculations can be seen in Figure 2-3. At all temperatures shown, thermodynamic equilibrium heavily favors the decomposition of NO to N_2 and O_2. NO_2 is more stable than NO at temperatures below 425 ^oC, but the overwhelming conversion is for NO_x species to decompose. Temperatures above 600 ^oC are more favorable to the formation of stable nitrogen compounds with oxygen, such as N_2O, NO and NO_2, with a significant majority of the balance resulting from N_2 and O_2 formed by decomposition, but these remain minor products until temperatures far above the values shown.

Low temperature thermodynamics support the decomposition of NO and NO_2 to the component molecules of N_2 and O_2. However, the large activation energy to achieve that result is difficult to muster at temperatures below 600 ^oC, so NO and NO_2 remain intact at those temperatures in the gas phase. At temperatures far above 600 ^oC, thermal energy is plentiful enough to provide for fast kinetics, so thermodynamic calculations provide a more accurate estimation of the true composition.

2.9 La_2CuO_4 Background

La_2CuO_4, the simplest member of the layered perovskites, is the parent compound of the $La_{2-x}(Sr,Ba)_xCuO_{4+y}$ family of high temperature (T_c< 40 K) superconducting oxides. A superconductor itself at temperatures below 30 K, La_2CuO_4 functions as an intrinsic semiconductor from 30 to 50 K, and above these ranges, as an extrinsic acceptor-doped (P-type) semiconductor.[131] The acceptor dopant in this case is O_2 gas, which induces interstitial O_i'' ions into the rock salt layer of the Ruddleson-Popper structure as the primary defect.[132-135] The concentration of interstitial oxygen is dependent on both the oxygen partial pressure and the extent to which the gas can equilibrate with the oxide. Equilibrium of La_2CuO_4 can be affected by the presence of ionically blocking adsorbates or very low temperatures.

Kanai proposed a valence change for copper from plus two to plus three to accommodate the excess oxygen, thus defect equilibrium condition can be expressed in Kröger-Vink notation in Equations 2-11 and 2-12.

$$\tfrac{1}{2}O_{2(g)} \rightleftharpoons O_i'' + 2h^{\bullet} \qquad [2\text{-}11]$$

$$K = {[O_i'']p^2}\Big/{P(O_2)^{1/2}} \qquad [2\text{-}12]$$

In this case, K represents the equilibrium constant with regards to oxygen. From these equations, the neutrality condition can be expressed by Equation 2-13.

$$2[O_i''] = p \qquad [2\text{-}13]$$

By substitution, the stoichiometric modifier can be defined as Equation 2-14.

$$\delta \propto [h^{\bullet}] \propto pO_2^{1/6} \qquad [2\text{-}14]$$

This is in agreement with the p-type behavior of $La_2CuO_{4+\delta}$.

La_2CuO_4 maintains a slight excess of oxygen with regard to stochiometry throughout the oxygen partial pressure range, but decomposes if exposed to a pO_2 of less than ~$10^{-6.8}$ atmospheres at 800 ^{o}C. At that partial pressure, the oxide is in stochiometric balance.[134] At higher temperatures, the oxide can become slightly hypostoichiometric before decomposition; however, for significant hypostoichiometry to manifest, the A site of the material must be doped. This doping greatly complicates the analysis of defects.

Due to its use in superconductivity research, the structure and electronic properties of the material have been studied extensively. The unit cell structure consists of a perovskite unit cell of CuO_2 sandwiched between layers of rock salt La_2O_2 lattice.[136,137] Below 200 ^{o}C, the unit cell organizes to an I4/mmm orthogonal structure; above that temperature, it retains tetragonal Fmmm structure.[138] The material can be constructed a number of ways, including solid-state

synthesis,[139,140] co-precipitation,[141] mixed-oxalate reaction,[132,142] sol-gel synthesis,[143] freeze-drying,[63,64] inverse microemulsions,[144] metal nitrate reaction in supercritical water,[145] and the Pechini method.[146] Most of these synthesis methods produce fine-grained, semi-crystalline powder that fully crystallizes during the calcination step.

The orthorhombic perovskite phase is formed by calcination at temperatures above 650 ^{o}C. Calcination temperatures below this threshold result in partially or completely amorphous solid oxides that can be crystallized by heating above the threshold.[141]

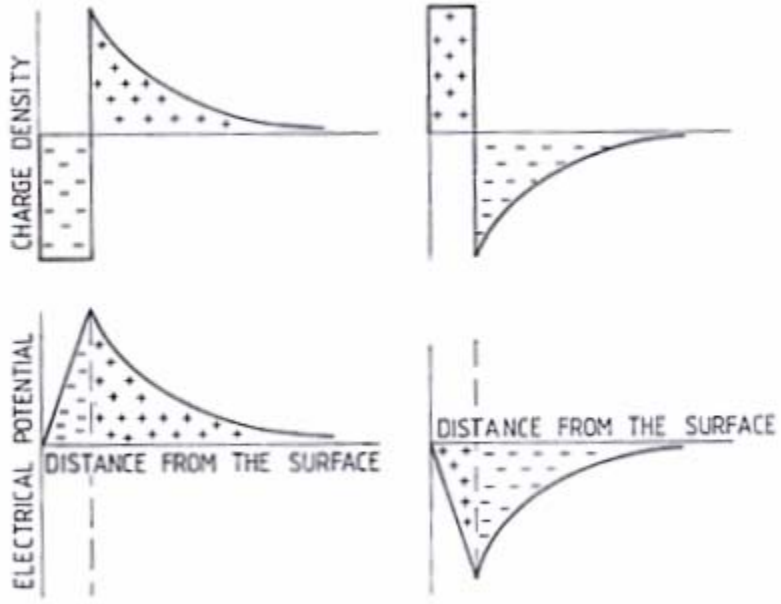

Figure 2-1. Diagram of the space charge layer at the surface of the electrode. Opposing charges build up inside the material to compensate for the charge established on the surface. The depth of this charged layer is dependant on the material (taken from Vayenas)[147]

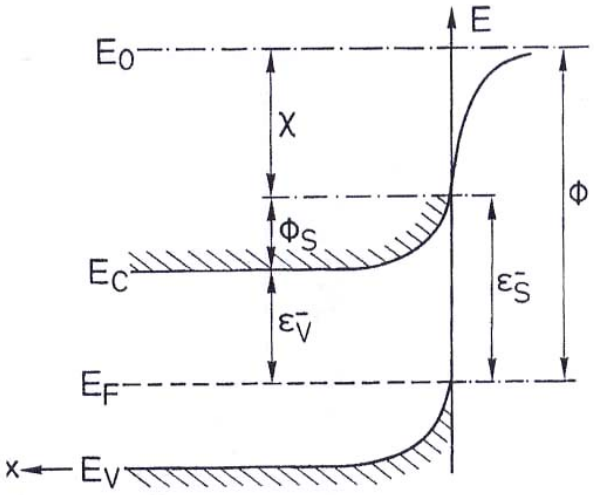

Figure 2-2: Surface band model of a p-type semiconductor involving positive surface charge. The total work function (Φ) consists of the external work function (χ) combined with the Fermi energy (ε_v) and the contribution of the surface charge from adsorption (Φ_S)(taken from Vayenas)[147]

Table 2-1. Metal oxides commonly used as resistance-type and potentiometric gas sensors and relevant publications.

Metal Oxide	Selected References for Resistance-type Sensors	Selected References for Potentiometric Sensors
WO_3	9[109,121,148-154]	9[19,21-23,25,33,34,68,155]
TiO_2	13[108,126,151,156-168]	2[14,57]
SnO_2	21[16,17,62,106,107,156,157,165,169-181]	3[67,70,182]
$LaFeO_3$	6[156,157,165,183-185]	6[18,19,23,32,34,71]
$SmFeO_3$	5[165,183,186-188]	1[18]
$LaCoO_3$	1[189]	1[18]
ZnO	9[37,180,190-196]	3[37,38,196]
In_2O_3	7[156,165,176,180,197-199]	4[24,86,200,201]
Nb_2O_5	1[202]	3[15,201,203]
La_2CuO_4	3[181,193,194]	6[7,64,66,125,204,205]

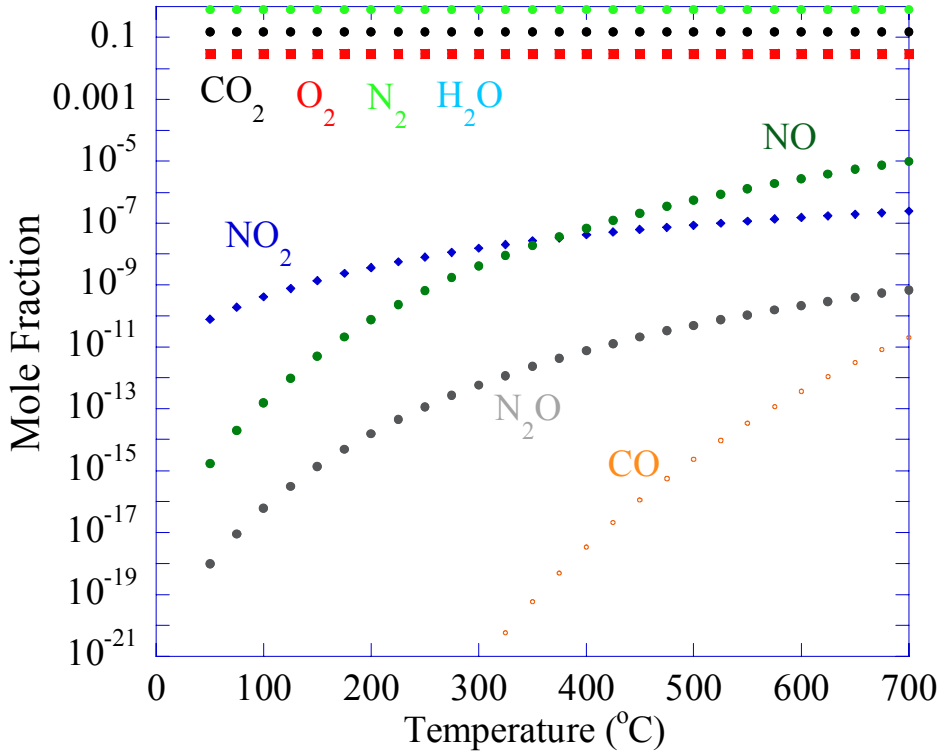

Figure 2-3. Plot of equilibrium mole fractions of exhaust gas consisting of 3% O_2, 15% CO_2, 3% H_2O, 650 ppm NO, and balance N_2 versus temperature in ^oC

CHAPTER 3
INITIAL TPD/TPR STUDIES OF LA2CUO4 AND PT

3.1 Introduction

A cornerstone tool for discerning the contributions of Mixed Potential versus contributions of the semiconducting effect in both potentiometric and conductometric sensors will be the evaluation of the effluent gas from the exposure of sensor electrode materials to gas mixtures commonly seen in combustion environments. The relative contribution of each mechanism will largely depend on the composition of the electrode and the temperature at which it operates.

For metal electrodes, electrochemical conversion is the most likely mechanism for changes in the potential, since adsorptive effects only contribute a small amount of charge relative to the large volume of charge carriers already present in the material. Adsorption on metals can cause changes in the local electronic environment through mixing of the adsorbate/metal orbitals[206,207] and can also form reaction barriers to electrochemical reaction[208] even without permanently affecting the surface. However, since pure metals cannot supply anything but electrons to form charge-generating complexes at the interface without passivation of the surface, the extent to which potential can generate at the interface is limited. Additionally, the intrinsic conductivity does not change much over the investigated temperature range, which, though not so important for the potentiometric sensor, lowers the possibility of error associated with conductivity. As a result, major changes in response are most likely due to the increased kinetic activity for reaction found at higher temperatures.

Conversely, a semiconducting compound involves different properties that complicate analysis, but also allow for more selective use. In semiconductors, adsorption causes a much larger relative change in the charge carrier concentration, and this change can be very important for determining the conductometric and potentiometric mechanisms. Thermal stimulation causes

a much greater, and positive, change in conductivity due to the excitation of electronic carriers within the material. This stimulation has the added effect of speeding up the electrochemical reaction kinetics and adsorption / desorption behavior at the surface, each of which can have substantial effects on the electrode potential. In general, the adsorption phenomena are the determining mechanisms at temperatures below 500 ^{o}C, and electrocatalytic reactions dominate above that temperature. This behavior has been examined previously on a TiO_2 sensor.[57]

La_2CuO_4 demonstrates promise as a sensing electrode material to explore the semiconducting mechanism due to its lack of catalytic activity for the $NO \rightarrow N_2$ reaction in the presence of oxygen.[102] Therefore, contributions from catalytic and electrochemical conversion reaction of this type are minimal during NO_x sensing. This allows the contribution from gas adsorption to be the primary influence of charge creation for a sensor under NO. Measurement of the adsorption behavior was compared to the sensor behavior, which better allowed for the separation of the various contributions to the electric potential generation and conductance. Platinum was selected as the counter electrode for the potentiometric couple due to its known catalytic ability and extensive documentation in the literature as an electrode in potentiometric sensors.[6,7,18,23-25,28-30,33,41,43,63-68,70,80,81,88,92,114-127]

Mass spectrometry (MS) was used to examine the heterogeneous catalytic activity and adsorption activity of the sensing and reference electrodes, specifically La_2CuO_4 and Pt, for NO_x and CO_x exposure. The use of MS to monitor reaction kinetics has some precedent.[209-220] By recording instantaneous changes in gas concentration with time and/or temperature, the desorption energy, quantity of NO_x gas desorption, and the decomposition products formed by reactions with NO_x at high temperatures were evaluated.

Profiling the heterogeneous catalytic activity of a sensing material was very important for determining the contribution of that catalytic reaction to the potential generated at that electrode for the complete device. NO and NO_2 mixtures are kinetically limited in the gas phase from reaching equilibrium, but in the presence of a catalyst can react in an attempt to establish equilibrium. By altering the reaction conditions and monitoring the result, the initiation point of catalytic activity can be observed. Additionally, since the gas composition can be recorded after the reaction has taken place, the extent of catalysis can be determined by comparison to the thermodynamic equilibrium.

3.2 Experimental

3.2.1 Synthesis of La_2CuO_4

La_2CuO_4 powder was synthesized by the autoignition technique.[221] A stoichiometric mixture of $La(NO_3)_3 \cdot 6H_2O$ (Kanto Chemical Company, 99.99%) and $Cu(NO_3)_2 \cdot 10H_2O$ (Alfa Aesar, 99.999%) was prepared in deionized water. After dissolving the metal nitrates, citric acid (Alfa Aesar, 99.5%) was added to the mixture until 0.25 mole percent was achieved, making this a fuel-lean solution. The solution was heated to ~70 ºC with constant stirring until a gel-like precipitate dropped from solution. The liquid was boiled down and the precipitate autoignited by further heating. The powder generated by the autoignition process was calcined at 600 ºC for 10 hours.

3.2.2 Powder Characterization

X-Ray diffraction (XRD) was performed on a Philips APD 3720 automated diffractometer (Cu Kα radiation, $\lambda = 1.54178$ Å) to verify the phase composition of La_2CuO_4 powder. Step scans were performed over a 2θ interval of 0.02 degrees and a retention time of 5 sec for each step in the $20^\circ \leq 2\theta \leq 60^\circ$ range. Surface area was recorded using a N_2-adsorption B.E.T.

measurement (NOVA, Quantachrome). Calcined powders were examined using an JEOL JSM6330F Field Emission SEM.

3.2.3 TPD/TPR Setup

Temperature Programmed Desorption and Reaction (TPD/TPR), as well as isothermal experiments, were performed in a quartz tube flow reactor. The reactor consisted of a 4 mm inner diameter quartz tube joined to a 1 mm inner diameter quartz tube by a glass frit. The tube ends linked to stainless steel tubing through Ultra-Torr fittings. A concentric glass tube containing a K type thermocouple was inserted through the upper fitting and suspended directly above the sample to monitor the temperature. Gas flow into the reactor was controlled using a bank of MKS mass flow controllers (MFC) through a stainless steel tube intake manifold into the top of the reactor. Effluent reactor gases flowed out the reactor exit into an Extrel Merlin 5220 quadrapole mass spectrometer. A full schematic of the gas setup can be seen in Figure 3-1.

3.2.4 TPD/TPR Procedure

The procedure of the temperature-programmed desorption (TPD) and reaction (TPR) experiments is described below.[66,68,69,205] Samples of La_2CuO_4 containing 43 milligrams of powder (total BET area 0.15 m^2) were initially purged of atmospheric adsorbed species by cycling the sample to 800 ^oC and back to room temperature under an atmosphere of 100 % oxygen, followed by heating under helium to show desorption spectra. The process was repeated until the spectra did not show any desorption peaks. Once clean, the sample was cooled under oxygen and then maintained under a helium atmosphere until further experiments were performed.

For standard TPD experiments, the sample was subjected to 30 cubic centimeters per minute (ccm) flow of a considered gas or gas combination at 300 ^oC for 30 minutes, followed by cooling to 30 ^oC at 5 ^oC / minute. At 50 ^oC, the sample was purged with 30 ccm helium until a

stable baseline for mass analysis was achieved. The sample was heated to 800 ^{o}C at 30 ^{o}C /minute under 30 ccm flowing helium atmosphere. During heating, the effluent gas was analyzed to determine the quantity and nature of desorbed products.

Parallel experiments utilizing adsorptions from 700 ^{o}C to room temperature yielded similar results to adsorptions cooled from 300 ^{o}C to room temperature. The lower adsorption temperature was standardized to prevent reaction of gases at high temperature and retain powder microstructure over time. Additional TPD experiments were performed with NO_x gases and CO at heating rates of 1, 5, 10, and 15 ^{o}C / minute in order to determine the activation energy of desorption of these gases on La_2CuO_4. TPD experiments are listed in Table 3-1.

For TPR experiments, the sample was exposed to 30 ccm of a reaction mixture at 30 ^{o}C, and held until gas flow and mass spectrometer signal remained steady. The sample was heated to 800 ^{o}C at 30 ^{o}C / minute, and the effluent spectra recorded to determine the extent of reaction and reaction products. These experiments were performed on La_2CuO_4 powder, a Pt electrode on YSZ, and in the blank reactor. TPR experiments were performed using Pt and the blank reactor to determine the temperature points of uncatalyzed gas-phase reaction, and the catalytic effect of Pt versus the gas phase reactions. Table 3-2 shows the list of experiments.

For all mass spectrometry experiments, specific mass to charge ratios were examined: m/z = 12 (C), m/z = 14 (N), m/z = 28 (CO and N_2), m/z = 30 (NO), m/z = 32 (O_2), m/z = 44 (CO_2 and N_2O), and m/z = 46 (NO_2).

The powder sample was evaluated by TPD and TPR for each combination of gas, and then cycled to 700 ^{o}C under helium before beginning the next gas combination. Raw data was collected in arbitrary intensity units for each ratio of mass to charge, which was converted to concentration in parts per million by comparison to previously collected calibration data.

Calibration of the system was achieved by measuring the intensity output of the mass spectrometer for m/z ratio of atomic weight for gas and characteristic fragment gases versus input concentration of sensed gas minus the background spectrum. Experiments were repeated from 6-10 times with variations of <10%. Spectrums shown in later figures are discrete, but representative of the average of all experiments.

3.3 Results and Discussion

3.3.1 Powder Characterization Results

X-ray diffraction of the calcined powder revealed formation of the La_2CuO_4 phase, showing good phase homogeneity with traces of copper oxide impurity. The La_2CuO_4 phase was able to form below the threshold calcination temperature due to the high-temperature powder formation inherent in the auto-ignition technique.[222] (Figure 3-2) Minor structural inhomogenaity left from processing was eliminated by cycling the sample to 700 ^oC during sample pretreatment. BET measurements using N_2 gas revealed a specific surface area of 3.48 m^2/g.

SEM images of the powder show fine-microstructured particles of irregular shape. The particles have average sizes of 100 to 300 nm and appear to contain networks of small pores in each particle.[223] (Figure 3-3)

3.3.2 TPD/TPR Results of NO Gas Exposure

Initial studies of the La_2CuO_4 powder focused on comparing the adsorption of NO gas in the absence of oxygen and contrasting that spectrum to NO adsorption in the presence of oxygen. Mass spectrometry spectra of the 1% NO in He adsorbed case showed clear desorption peaks at low temperature. (Figure 3-4) The low-temperature desorption begins just below 100 ^oC, peaking just above 150 ^oC. As heating continued, a larger desorption peak appeared, with its maximum coming around 275 ^oC. This higher temperature desorption continued as temperature increased, with a shoulder in the peak extending to 450 ^oC. Above 450 ^oC, the surface has been exhausted

of NO adsorbates, and shows no further NO desorption. NO_2 desorption was noticeably absent during the NO TPD experiment, so no conversion from NO→NO_2 takes place solely from interaction with the La_2CuO_4 powder.

When La_2CuO_4 adsorbed NO in the presence of oxygen, no change occurred in the desorption spectrum, seen in Figure 3-5. The quantity of NO desorbed from the surface for the 500 ppm NO / 0.95% O_2 adsorption was almost identical to the quantity desorbed from the 1% NO adsorption. No NO_2 desorbed during the experiment, though this was omitted from the plot for purposes of clarity. This means that O_2 has no effect on the adsorption of NO, nor does the presence of O_2 contribute to the NO→NO_2 reaction, even in 0.95% O_2. Further, it was demonstrated that the La_2CuO_4 powder can saturate to maximum surface coverage in 500 ppm NO. Thus, the NO adsorption was quite favorable on La_2CuO_4.

To examine the energies of adsorption, the NO adsorption and desorption cycle was repeated at multiple heating rates, as seen in the literature. First, following Redhead's flash-desorption work,[224] the rate of desorption was defined (Equation 3-1).

$$N(t) = -d\sigma/dt = \upsilon_n \sigma^n \exp(-E_a/RT) \qquad [3\text{-}1]$$

In this equation, n is the desorption reaction order, σ is the surface coverage (in molecules/cm^2), υ_n is the rate constant, and E_a is the activation energy of desorption in Joules/mole. By identifying the temperature for which gas emission from the surface peaks (T_p), the following relations can be expanded (Equations 3-2, 3-3, 3-4).

$$E_a/RT_p^2 = (\upsilon_1/\beta)\exp(-E_a/RT_p) \ : \text{if } n=1 \qquad [3\text{-}2]$$

$$E_a/RT_p^2 = (2\sigma_p\upsilon_2/\beta)\exp(-E_a/RT_p) \ : \text{if } n=2 \qquad [3\text{-}3]$$

$$E_a/RT_p^2 = (\frac{\sigma_0\upsilon_2}{\beta})\exp(-E_a/RT_p) \ : \text{if } n=2 \qquad [3\text{-}4]$$

In Equations 3-2, 3-3, and 3-4, β is the heating rate in ^{o}K / second, σ_0 is initial surface coverage, σ_p is the coverage at $T=T_p$ (^{o}K), υ_1 and υ_2 are reaction rate constants. υ_1 and υ_2 are assumed such that $10^{13}>\upsilon_n/\beta>10^{8}$ ($^{o}K^{-1}$).

For these equations, σ_p and σ_0 can be calculated from the individual TPD plots by measuring the total desorption from the surface. Using the known flow rate and time per scan, the mole value of gas desorbed can be calculated on a per second basis. Using *z* ccm flow of carrier gas as a basis, the amount of gas stored on the powder can be calculated (Equations 3-5 and 3-6).

$$\frac{(z)cm^3}{\min}\times\frac{1\min}{60\sec}\times\frac{1}{10^6\,ppm}\times\frac{1\sec}{scan}=1.67\times10^{-8}(z)\,cm^3/ppm\text{-}scan \qquad [3\text{-}5]$$

$$1.67\times10^{-8}(z)\,cm^3/ppm\text{-}scan\times\frac{1L}{1000cm^3}\times\frac{10^6\,\mu mol}{22.4L}=7.44\times10^{-7}(z)\,\mu mol/ppm\text{-}scan \qquad [3\text{-}6]$$

The total storage capacity of the powder for NO gas at each adsorption site type is represented by Equation 3-7.

$$\sigma_0=\sum_{scan=1}^{n}\frac{x_{scan}\,ppm\times7.44\times10^{-7}(z)\,\mu mol/ppm\text{-}scan}{(y)cm^2} \qquad [3\text{-}7]$$

The NO remaining on the surface is given by Equation 3-8.

$$\sigma_p=\sigma_0-\sum_{scan=1}^{p}\frac{x_{scan}\,ppm\times7.44\times10^{-7}(z)\,\mu mol/ppm\text{-}scan}{(y)cm^2} \qquad [3\text{-}8]$$

In Equations 3-7 and 3-8, *y* is given as an arbitrary basis for the surface area of the sample.

From these equations, the adsorption energy of NO for 1st and 2nd order desorption can be calculated. Second-order desorption can occur as a result of incomplete adsorption,[209] and while based on previous TPD that is unlikely, the equations needed to calculate that value have been included.

Using the assumed value for υ_1, the E_a value can be calculated at each ramp rate by substituting into the empirical equation developed by Redhead. (Equation 3-9)

$$E_a / RT_p = \ln\left[\frac{\upsilon_1}{\beta}\right] - 3.64 \qquad [3\text{-}9]$$

The value of E_a can also be found without assuming υ_1 by using a second empirical equation and plotting log β vs. log T_p. (Equation 3-10)

$$E_a / RT_p + 2 = d(\log\beta) \Big/ d(\log T_p) \qquad [3\text{-}10]$$

To be thorough, the activation energy calculations were repeated using a method previously applied to Temperature Programmed Reduction by Wimmers *et al.*[216,217] Adapting their conversion reaction to a gas-phase independent term transforms the expression into Equation 3-11.

$$\frac{d\alpha}{dT} = \frac{1}{\beta} k(T) f(\alpha) \qquad [3\text{-}11]$$

In this equation, α is the degree of desorption for that type and β is the heating rate. Further, the Arrhenius relationship can be substituted to remove *k* and produce Equation 3-12.

$$\frac{d\alpha}{dT} = \frac{A}{\beta} e^{-E_a/RT} f(\alpha) \qquad [3\text{-}12]$$

Following Kissinger's method for determining activation energies,[212] these equations can be related:

At the peak temperature T_p, Equation 3-13 holds.

$$\left[\frac{d}{dT}\left(\frac{d\alpha}{dT}\right)\right]_{T=T_p} = 0 \qquad [3\text{-}13]$$

Combining Equation 3-13 and 3-12 forms Equation 3-14.

$$\left[\frac{d}{dT}\left(\frac{A}{\beta}\exp(-E_a/RT)f(\alpha)\right)\right]_{T=T_p} = 0 \qquad [3\text{-}14]$$

This transforms to Equation 3-15.

$$\left(\frac{d\alpha}{dt}\right)_{T=T_p}\left[\frac{E_a}{RT_p^2}+\left(\frac{df(\alpha)}{d\alpha}\right)_{T=T_p}\left(\frac{A}{\beta}\exp(-E_a/RT_p)\right)\right] = 0 \qquad [3\text{-}15]$$

Since $\left(\frac{d\alpha}{dT}\right)_{T=T_p}$ does not equal zero, this expression reduces to Equation 3-16.

$$\frac{\beta E_a}{ART_p^2} = -\left(\frac{df(\alpha)}{d\alpha}\right)_{T=T_p}\left(\exp(-E_a/RT)\right) \qquad [3\text{-}16]$$

This expression further simplifies to Equation 3-17.

$$\ln\left(\frac{\beta}{T_p^2}\right)+\ln\left(\frac{E_a}{AR}\right) = \frac{-E_a}{RT_p}+\ln\left(-\frac{df(\alpha)}{d\alpha}\right)_{T=T_p} \qquad [3\text{-}17]$$

Making the assumption that f(α) and α at T_p are independent of β, and that $\left(\frac{df(\alpha)}{d\alpha}\right)_{T=T_p}$ does not equal zero, this equation further simplifies to Equation 3-18.

$$\ln\left(\frac{\beta}{T_p^2}\right) = \frac{-E_a}{RT_p}+\ln\left(\frac{AR}{E_a}\right)+C \qquad [3\text{-}18]$$

In Equation 3-18, C is assumed to be a constant. Thus, a plot of $\ln\left(\frac{\beta}{T_p^2}\right)$ vs. $\left(\frac{1}{T_p}\right)$ should give a straight line with slope $\frac{-E_a}{R}$. The results of these calculations can be seen in Table 3-3.

In the case of NO desorption, the difference between the three methods of calculation is readily apparent. While these activation energies are rather different in the first case versus the second and third case, it must be noted the Wimmers and Redhead 7 methods are particularly

susceptible to problems from a single outlier, as the desorptions take place at relatively low temperatures. Surveys of other metal oxides indicated the possibility of charged complexes on the surface of the powder due to adsorption.[225,226] This could cause lateral interactions, which might affect the peak position.[227] Each of the values obtained from Redhead's empirical equation relating only ramp rate and temperature for the desorption system were within 2 kJ/mol of one another for each ramp rate, and for that reason the calculations in the first column are assumed to be the correct ones within 5% and the other values provided as a consistency check.

Desorption peaks present in the TPD appear during the NO TPR, but no changes in concentration consistent with NO conversion occur with or without the presence of oxygen in the experiments. La_2CuO_4 was exposed to 500 ppm NO in He and no decomposition of NO to N_2 and O_2 was observed. (Figure 3-6a) Similarly, in the NO and O_2 TPR, when exposed to 500 ppm NO in 1000 ppm O_2 (Figure 3-6b), no NO_2 formation was observed. This experiment was repeated in a background of 21% O_2, and no NO_2 formation was observed. Therefore, La_2CuO_4 was catalytically inactive for NO decomposition or oxidation.

Thermodynamic calculations suggested a near-complete conversion to NO_2 at low temperatures. However, gas phase and Pt electrode measurement of the NO / O_2 system showed no activity towards NO conversion. (Figure 3-7) This deviation was unsurprising in the gas phase case, as per the discussion in Chapter 2. The experiments over Pt reinforced that oxidation from NO$\rightarrow$$NO_2$ was not occurring over either the La_2CuO_4 or Pt electrodes. From this, it can be stated that the response coming from the sensing electrode is not a result of electrochemical conversion reactions of NO. Further, the potential from the semiconducting effect was not influenced by changes in concentration as a result of reacting species.

3.3.3 TPD/TPR Results of NO_2 Gas Exposure

The desorption profiles obtained from the NO_2 on La_2CuO_4 powder show extensive surface adsorption. (Figure 3-8a) NO_2 exhibited strong chemisorption, but the desorption profile contained multiple unique adsorbed NO_x surface species. NO_2 begins desorption at 230 ºC with a peak maximum near 280 ºC. This NO_2 desorption peak coincided with a NO desorption peak near 300 ^oC, larger than the desorption peak from NO alone. A second NO desorption peak near 400 ºC superimposed itself over an O_2 desorption peak indicating decomposition of a surface NO_x species. From these patterns, it can be observed that a series of complex reaction steps occurred on the surface of La_2CuO_4 at the lower end of the temperature range. At temperatures above 600 ºC, lattice oxygen discharged from the sample. This oxygen emission resulted due to favorable energy conditions that allowed rearrangement of the degree of superstoichiometry of the La_2CuO_4.

Temperature programmed reaction of NO_2 showed that La_2CuO_4 was catalytically active for the decomposition of NO_2. (Figure 3-8b) The NO_2 began to decompose at 250 ^oC. The TPR for NO_2 was compared to previous experiments using a blank reactor. In the blank, which simulates gas phase reaction, NO_2 began to decompose at about 600 ^oC, and the reaction rate increased greatly above that temperature.

NO_2 reacted over the Pt/YSZ sample in the presence of O_2. (Figure 3-9a) The initial decomposition temperature was slightly higher than in the La_2CuO_4 case, beginning at 450 ^oC, and coming to steady-state equilibrium values by 500 ^oC. The surface area for reaction was much smaller in the Pt/YSZ case, explaining why the temperature must be higher for it to react, even though Pt is the more catalytic material. In the gas phase, the kinetics of reaction were so unfavorable that NO_2 did not begin to decompose until 600 ^oC, even in the absence of oxygen. (Figure 3-9b)

Calculations performed for the NO desorption were repeated for each peak in the NO_2 desorption spectrum, and the results can be seen in Table 3-4.

3.3.4 TPD/TPR Results of CO_x /NO_x Gas Mixture Exposure

While pure NO bonds weakly to the La_2CuO_4 powder during adsorption, the addition of CO causes a radical shift in the bonding behavior of NO, reflected in the spectra. In the presence of CO, the NO bonds much more strongly, and large desorption peaks appear at 500 and 600 ^oC in addition to the small peaks at 150 and 200 ^oC seen in the NO TPD. (Figure 3-10a). CO was observed to desorb slightly, increasing quasi-linearly from zero ppm at 50 ^oC to 8 ppm at 800 ^oC in the O_2 deficient case.

In the TPR of CO and NO, if oxygen is absent, the two gases will react with one another to form N_2O and CO_2 (Figure 3-10b). The boost in NO adsorption strength seen in the TPD is mirrored in the TPR experiment, visible in the slight rebound in NO gas-phase concentration near 600 ^oC. This occurred once the majority of gas-phase CO was consumed and the system heated past the NO desorption threshold. This phenomenon revealed some information about the cross-sensitivity of La_2CuO_4 to NO and CO, and revealed part of the problem of eliminating that cross-sensitivity. Since CO reacted with NO, then this means the concentration the sensor sees in an anaerobic environment is not the true concentration, regardless if the actual reaction is electrochemical. The further problem is that the cross-adsorption essentially poisoned the surface of La_2CuO_4 with NO. Since the desorption temperature (and thus, desorption energy) of NO rose dramatically, it will now respond much less quickly to downward changes in NO concentration at the sensor operation temperature.

The important consequence of the addition of O_2 to an environment containing NO and CO is the similar increased amount of NO adsorption seen without oxygen, and the increase in the strength of that adsorption versus the adsorption without CO. This effect was clearly seen in the

TPD. CO_2 and N_2O emission cannot be separated due to their identical mass (44). However, concurrent peaks of NO and mass 44 near 300 ^oC, as well as overlapping peaks of CO and 44 at 400 ^oC strongly suggested conversion of both NO and CO on the surface of the powder. In the presence of oxygen, the large peaks at 500 and 600 ^oC shrink to ~10-15 ppm, and the low T peaks become slightly larger, growing to ~20 ppm (Figure 3-11a).

In the presence of oxygen, CO will selectively react with O_2 to produce CO_2, leaving the NO to behave as if neither O_2 nor CO were present (Figure 3-11b). The dip in oxygen concentration near 450 ^oC likely corresponds to the consumption of carbon-containing species on the surface before settling to a steady-state value above 550 ^oC.

The combination of NO, CO, and O_2 over Pt and YSZ showed extensive conversion of CO beginning near 200 ^oC (Figure 3-12) The reaction with CO is entirely selective to O_2, and the speed of the reaction increased as higher temperatures made the reaction kinetics more favorable. The reaction rate did not scale upward as quickly as La_2CuO_4, on account of the smaller available surface area. In the gas phase, CO reacted with O_2 beginning near 300 ^oC, but without catalytic promotion, the overall extent of reaction was rather small.

The simultaneous adsorption of NO_2, CO and O_2 affected an interesting change on the desorption pattern. (Figure 3-13a) The spectrum resembles NO_2 desorption, except that peaks corresponding to NO desorption have been reduced in size. Additionally, the 44 m/z peak corresponding to N_2O and CO_2 increased, but remained in the same temperature range of desorption as in the NO_2 desorption experiment. CO clearly adsorbed, but did not desorb without first oxidizing to CO_2.

Heating the La_2CuO_4 system containing NO_2, O_2, and CO flow caused simultaneous reduction of NO_2 and oxidation of CO during the TPR (Figure 3-13b). Predictably, NO_2 began to

react near 200 ^{o}C, and completely reacted above 300 ^{o}C, in the presence of strongly reducing CO. The oxygen dip seen previously for CO-complex consumption again appeared near 450 ^{o}C.

Exposure of the Pt/YSZ system to CO, NO_2 and O_2 showed similar light-off temperatures to the La_2CuO_4 system for the $NO_2+CO \rightarrow NO+CO_2$ reaction, but the extent of conversion was limited by the surface area of the electrode versus an intended platinum catalyst (Figure 3-14). In the blank reactor, the reaction begins near 350 ^{o}C, but does not approach a near-complete conversion until nearly 800 ^{o}C, compared to 500 ^{o}C over Pt.

CO_2, by contrast, inhibited NO adsorption, and it adsorbs to a significant extent in the presence of NO (Figure 3-15a). CO_2 and NO do not react with each other upon heating.

While CO_2 on its own cannot be detected by the La_2CuO_4 sensing electrode, it appears that its presence may inhibit the adsorption of NO on the powder surface, which might explain the response reversal of the sensor in greater CO_2 concentration. These occurrences are all indicative of complex adsorptive behavior on the sensing electrode surface.

3.4 Summary

TPD and TPR experiments on La_2CuO_4 show quantifiable adsorption and reaction of NO_x and CO_x mixtures on the surface. Examination of the desorption peaks for Temperature Programmed Desorption allows for the calculation of desorption energy of gas species adsorbed on the powder, and gas phase conversion with respect to temperature could be tracked by examining concentration profiles during Temperature Programmed Reaction. NO was found to be mostly unreactive to other gas species while in the presence of oxygen, indicating that its response in the sensor is more strongly influenced by adsorption rather than mixed potential. NO_2 decomposed catalytically at sensor operating temperatures, and was found to fragment into several products at low temperature, indicating mixed potential may play a significant role for the sensing behavior of NO_2 on the potentiometric sensor.

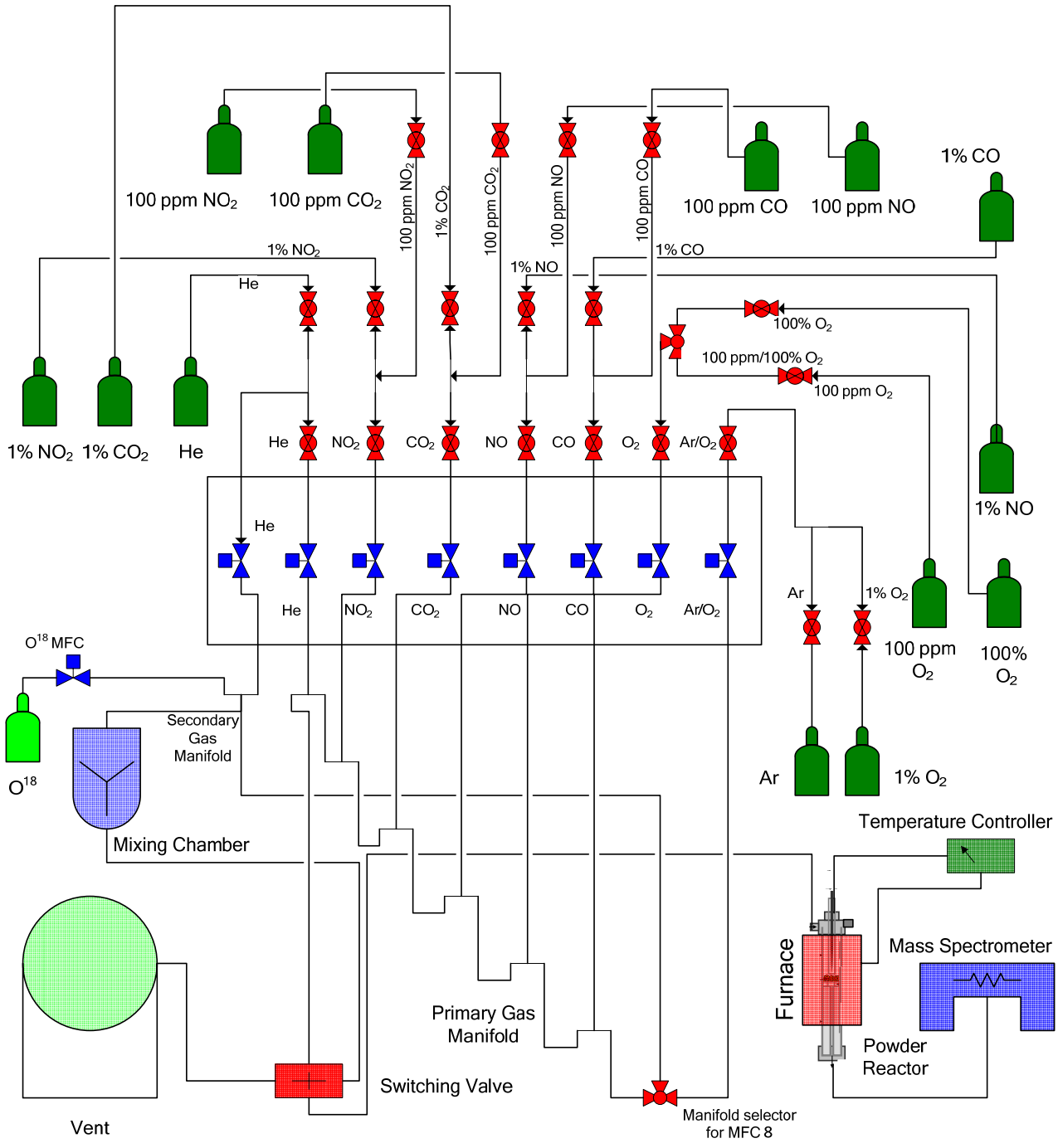

Figure 3-1. Pipeline diagram of the Mass Spectrometer gas system

Table 3-1. TPD experiments

Gas Mixture	Concentration (ppm)	Rate (^{o}C/minute)
NO	1% NO	30
$NO+O_2$	500 ppm NO /0.95% O_2	30, 15, 10, 5
NO_2	500 ppm NO_2	30, 15, 10, 5
NO+CO	0.67% NO/0.33% CO	30
$NO+CO+O_2$	500 ppm NO/500 ppm O_2/1% O_2	30
NO_2+CO+O_2	500 ppm NO_2 /250 ppm CO /1000 ppm O_2	30
$NO+CO_2$	500 ppm NO_2 /1000 ppm CO_2	30

Table 3-2. TPR experiments

Gas Mixture	Concentration (ppm)	Sample
NO	500 ppm NO	La_2CuO_4
$NO+O_2$	500 ppm NO / 1000 ppm O_2	La_2CuO_4, Blank, Pt on YSZ
	500 ppm NO / 21% O_2	La_2CuO_4, Blank, Pt on YSZ
NO_2	500 ppm NO_2	La_2CuO_4, Blank, Pt on YSZ
NO+CO	250 ppm CO / 1000 ppm NO	La_2CuO_4, Blank
$NO+CO+O_2$	500 ppm NO / 500 ppm CO /1000 ppm O_2	La_2CuO_4, Blank, Pt on YSZ
NO_2+CO+O_2	500 ppm NO_2 /500 ppm CO / 1000 ppm O_2	La_2CuO_4, Blank, Pt on YSZ
$NO+CO_2$	500 ppm NO /1000 ppm CO_2	La_2CuO_4

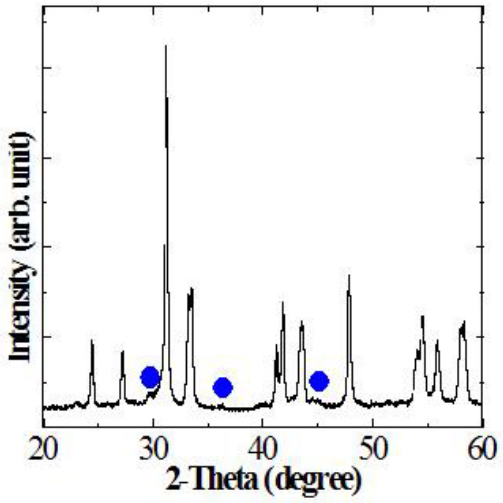

Figure 3-2. X-ray diffraction spectrum of La_2CuO_4 powder synthesized via the auto-ignition technique. Circles marked on the spectrum correspond to copper oxide impurities.

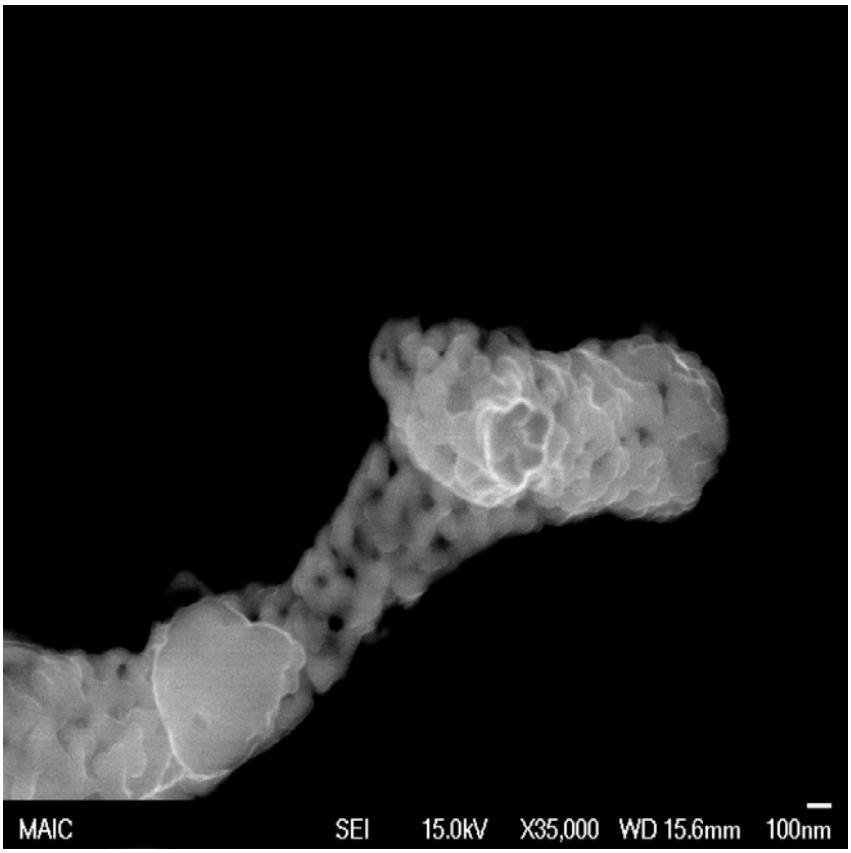

Figure 3-3. SEM image of the La_2CuO_4 powder generated via auto-ignition.

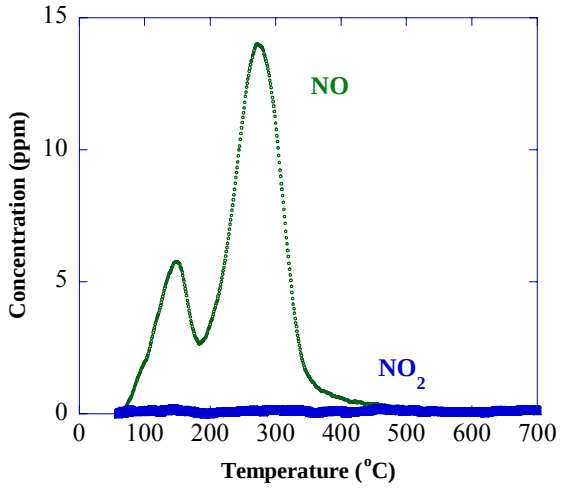

Figure 3-4. Temperature Programmed Desorption of 1% NO on La_2CuO_4.

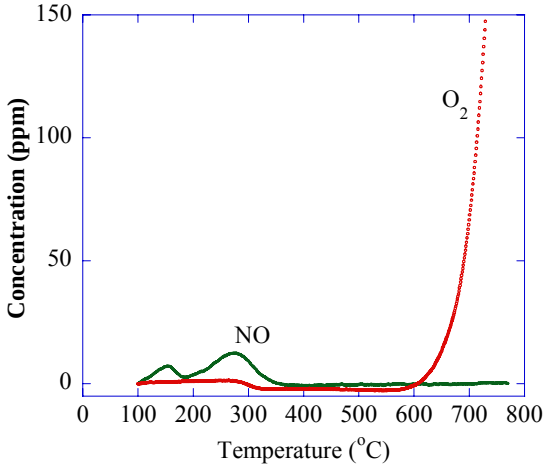

Figure 3-5. Temperature Programmed Desorption of 500 ppm NO + 0.95% O_2 on La_2CuO_4.

Table 3-3. Desorption energies of products resulting from NO adsorption on La_2CuO_4.

Peak Number	Assignment	Desorption Energy Equation 9 Average	Desorption Energy Equation 10	Desorption Energy Wimmers Derivation
0	Covalent/Ionic NO	73.78 kJ/mol	N/A	N/A
1	NO Nitrites	110.23 kJ/mol	82.3 kJ/mol	86.3 kJ/mol
2	NO Nitrates	127.56 kJ/mol	172.9 kJ/mol	168.85 kJ/mol

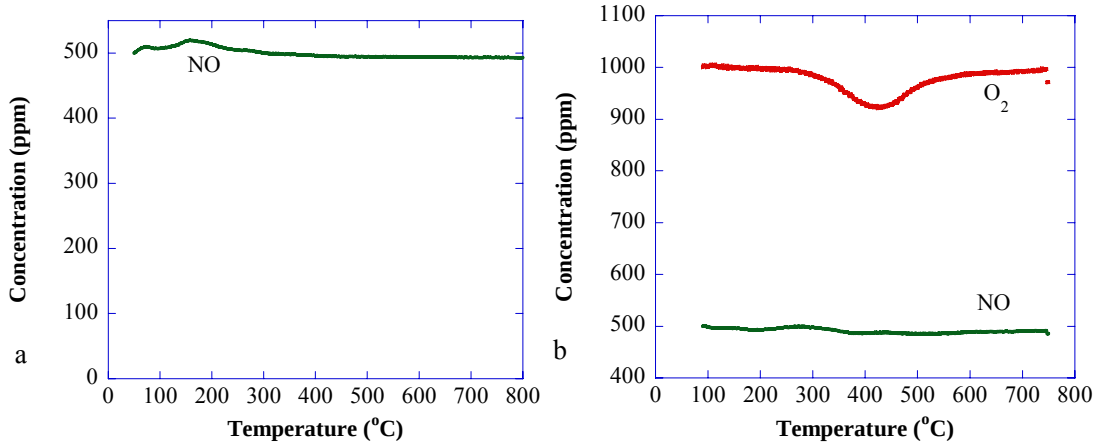

Figure 3-6. Temperature Programmed Reaction of 500 ppm NO (a.)/ Temperature Programmed Reaction of 500 ppm NO and 1000 ppm O_2 (b.) on La_2CuO_4.

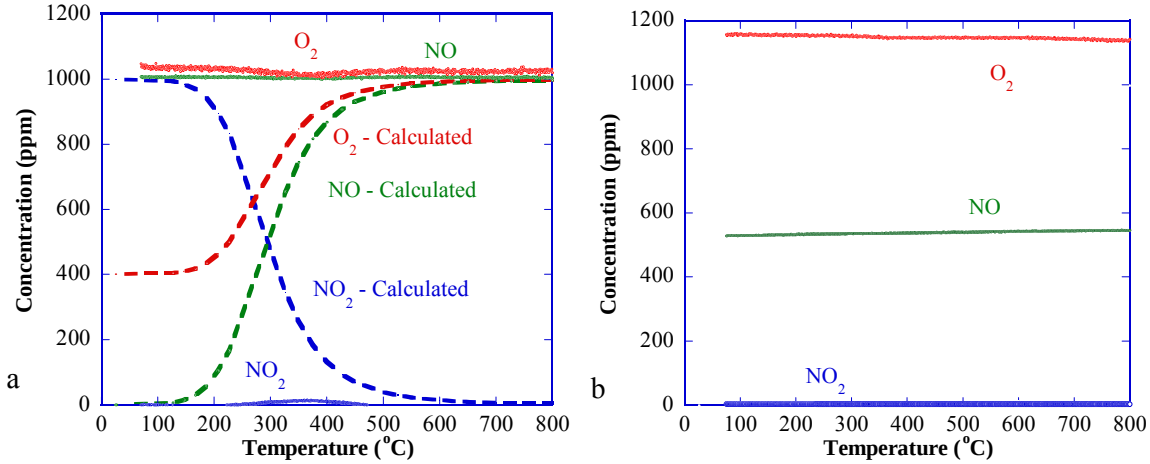

Figure 3-7. Temperature Programmed Reaction of 1000 ppm NO / 1000 ppm O_2 over (a.) Pt on YSZ and (b.) 500 ppm / 1000 ppm O_2 in the gas phase.

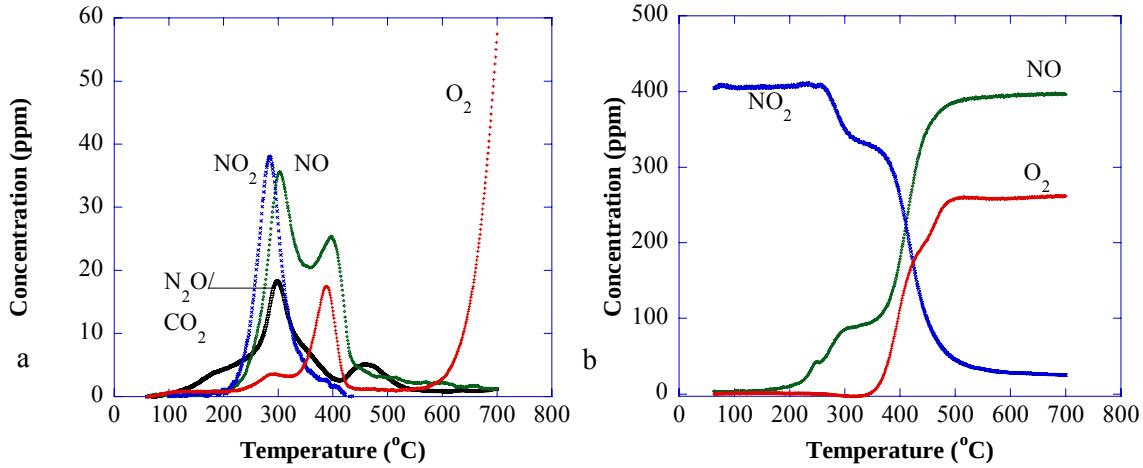

Figure 3-8. Temperature Programmed Desorption of 500 ppm NO_2 on La_2CuO_4. (a.)/ Temperature Programmed Reaction (b.) of 400 ppm NO_2 on La_2CuO_4.

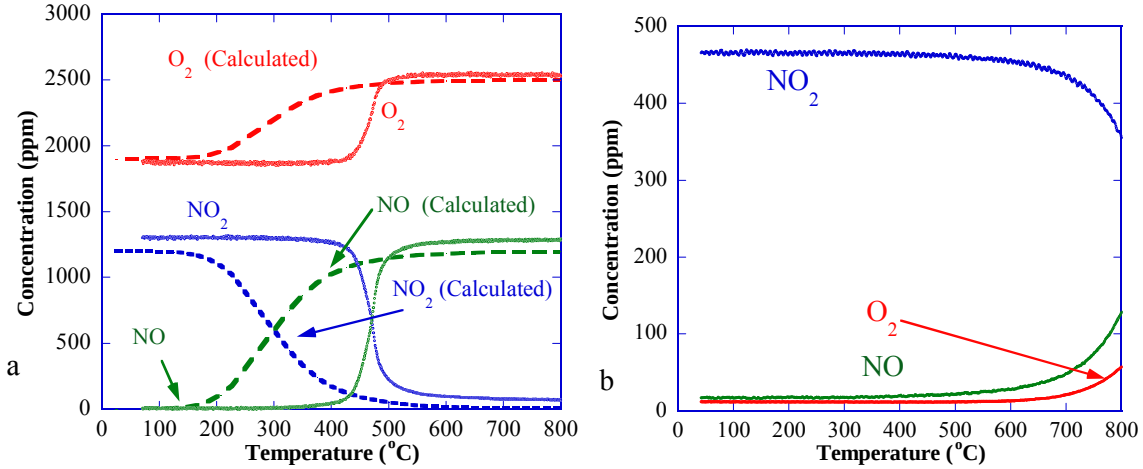

Figure 3-9. Temperature Programmed Reaction of (a) 1200 ppm NO_2+ 1800 ppm O_2 over Pt/YSZ plate (b) 500 ppm NO_2 Temperature Programmed Reaction in the gas phase.

Table 3-4. Desorption energies of products resulting from NO_2 adsorption on La_2CuO_4.

Peak Number	Assignment	Desorption Energy Equation 9 (Redhead A) Average	Desorption Energy Equation 10 (Redhead B)	Desorption Energy Wimmers Derivation
1	NO, NO_2, N_2O	115.2 kJ/mol	114.9 kJ/mol	118.8 kJ/mol
2	NO, O_2	131.575 kJ/mol	148.46 kJ/mol	153.72 kJ/mol
3	N_2O	152.79 kJ/mol	154.45 kJ/mol	158.5 kJ/mol

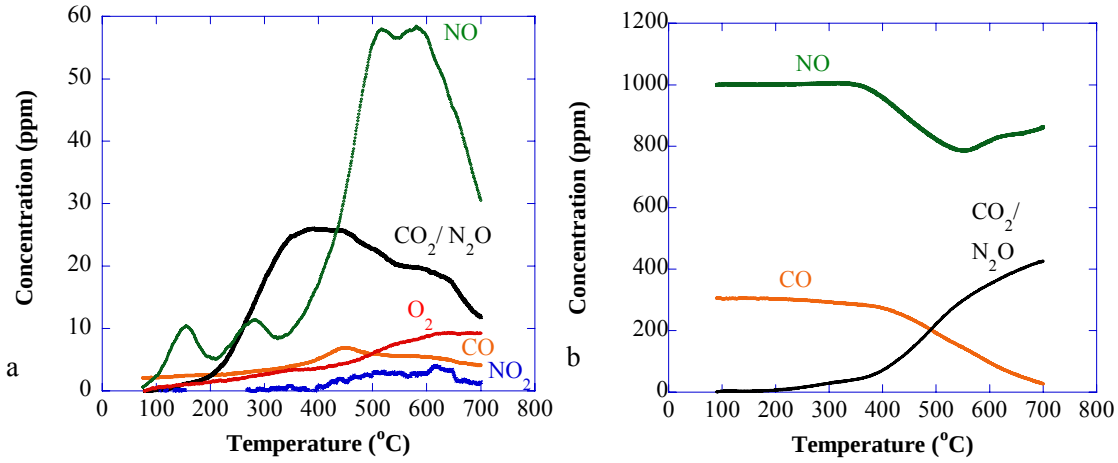

Figure 3-10. Temperature Programmed Desorption of 0.67% NO and 0.33% CO on La_2CuO_4. (a.)/ Temperature Programmed Reaction (b.) of 250 ppm NO and 1000 ppm CO on La_2CuO_4.

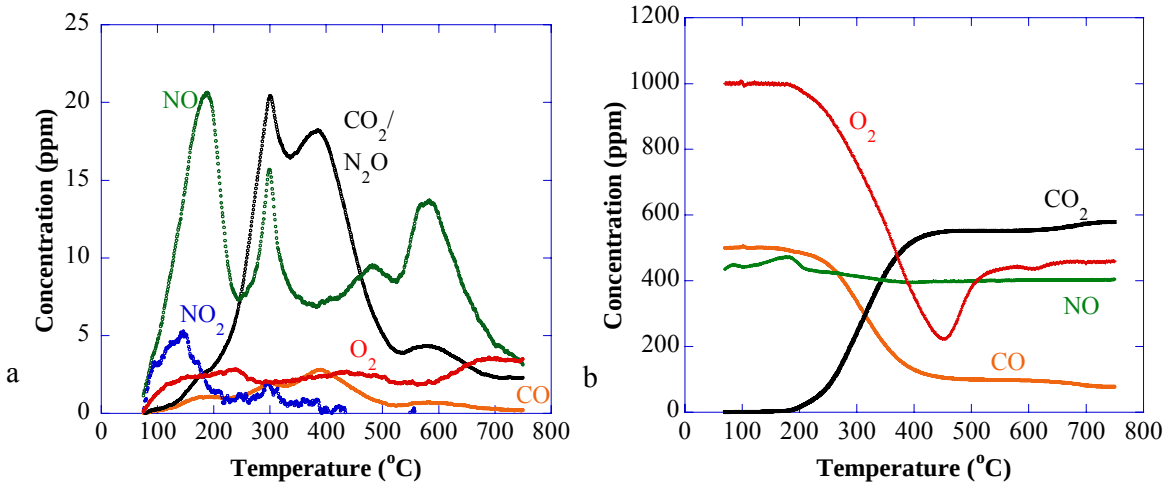

Figure 3-11. Temperature Programmed Desorption of 500 ppm NO, 500 ppm CO, and 1% O_2 on La_2CuO_4. (a.)/ Temperature Programmed Reaction (b.) of 500 ppm NO, 500 ppm CO, and 1000 ppm O_2 on La_2CuO_4.

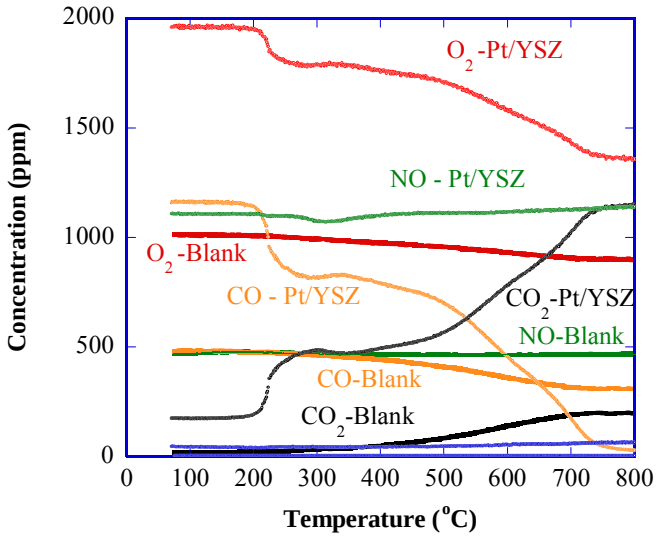

Figure 3-12. Temperature Programmed Reaction of 1000 ppm NO, 1000 ppm CO, and 2000 ppm O_2 on Pt/YSZ and 500 ppm NO, 500 ppm CO, and 1000 ppm O_2 in blank reactor

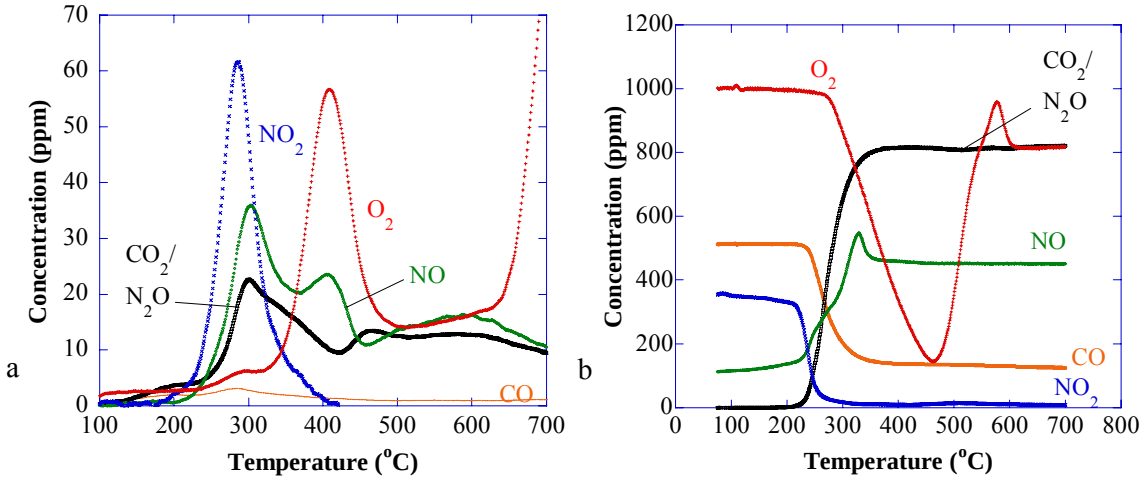

Figure 3-13. Temperature Programmed Desorption of 250 ppm CO, 500 ppm NO_2 and 1000 ppm O_2 on La_2CuO_4. (a.)/ Temperature Programmed Reaction (b.) of 500 ppm CO, 500 ppm NO_2 and 1000 ppm O_2 on La_2CuO_4.

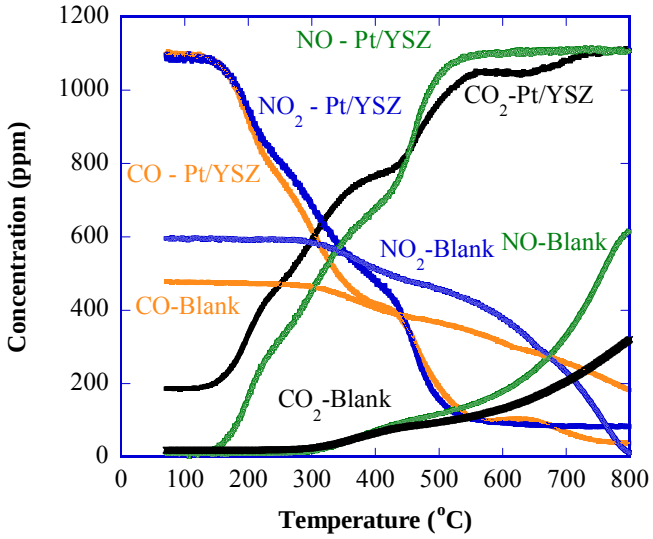

Figure 3-14. Temperature Programmed Reaction of 1000 ppm NO_2, 1000 ppm CO, and 2000 ppm O_2 on Pt/YSZ and 500 ppm NO_2, 500 ppm CO, and 1000 ppm O_2 in blank reactor.

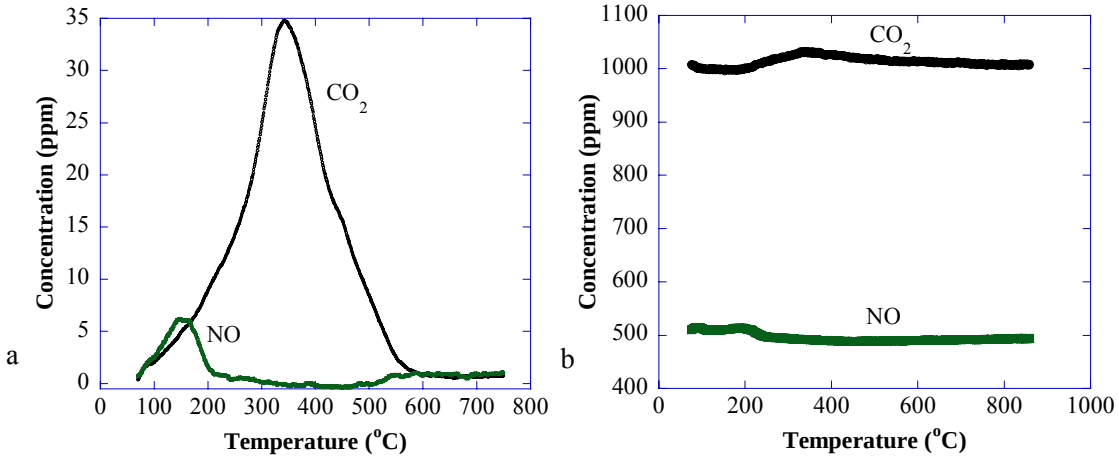

Figure 3-15. Temperature Programmed Desorption of 500 ppm NO and 1000 ppm CO_2 on La_2CuO_4. (a.)/Temperature Programmed Reaction (b.) of 500 ppm NO and 1000 ppm CO_2 on La_2CuO_4.

CHAPTER 4
ADSORBATE STUDIES ON LA2CUO4 USING INFRARED SPECTROSCOPY AND X-RAY PHOTOEMISSION SPECTROSCOPY

4.1 Introduction

The conventional explanation for non-Nernstian behavior for potentiometric sensors is the Mixed Potential theory. By this method, the voltage generated between the electrodes of the sensors arises purely as a result of the electrochemical reactions taking place at the electrodes. The difference between the non-equilibrium kinetics at the electrodes will cause a net voltage to arise.[189,228-231] However, this could account for the entirety of the deviation from Nernst potential only when the electrode pair is a working electrode coupled to a true reference electrode[232] and adsorption can be neglected. This mechanism operates on the premise that multiple electrochemical conversion processes simultaneously occur on the surface of the electrodes, and that only the kinetics of these reactions determine the potential generated between the electrodes. As a result, the mixed potential theory may adequately describe the response behavior of sensors to a gas mixture at high temperature (i.e. above 600 ^{o}C), where fast kinetics allow for equilibrium. However, at lower temperatures the effect of these electrochemical reactions are only one of the factors affecting the surface.

To address the shortcomings in Mixed Potential theory, a new approach known as Differential Electrode Equilibria was suggested.[63] This approach adds the contributions of adsorption/desorption, semiconducting behavior, and non-electrochemical catalytic reactions to the Mixed Potential contribution of electrochemical reactions, to explain the voltage response to a concentration change. The adsorption of gases forms charged species at the surface of the electrode, leading to an accumulation or depletion of electrons, which in turn can create an electric field across the electronically blocking electrolyte.[233,234]

La_2CuO_4 demonstrates promise as a material for a sensing electrode to explore this mechanism. The compound is catalytically unresponsive to the $NO \rightarrow N_2$ and $NO \rightarrow NO_2$ reactions in the presence of oxygen,[102] and so the contributions from these catalytic or electrochemical reactions during NO_x sensing are minimal. This allows the contribution from gas adsorption to be the primary potential generator for a sensor under NO. The material functions as a p-type semiconductor, and so the adsorption behavior will have an effect on the conductivity as well as the potential. The adsorption behavior can be measured and compared to conductometric and potentiometric sensor behavior, which better allows for the separation of contributions to the electric potential generation.

In this work, the techniques of diffuse reflectance infrared spectroscopy (DRIFT) and X-ray photoelectron spectroscopy (XPS) were used to investigate the adsorptive behaviors of La_2CuO_4 for NO_x gases.

4.2 Experimental

4.2.1 Sample Preparation

La_2CuO_4 powder was synthesized via an amorphous citrate autoignition route.[235] To prepare solid electrode samples, La_2CuO_4 powder was used to form a screen-printable slurry. This slurry was prepared by mixing La_2CuO_4 powder with polyvinyl butyral, alpha terpineol, and di-n-butyl phthalate dissolved in ethyl alcohol (8:47:6 ratios) until the desired viscosity was reached. The suspension was then screen printed onto 8% mole Y_2O_3- doped ZrO_2 substrates (Marketech International Inc., YSZ-8Y, 20 x 10 x 0.1 mm) in an identical configuration to sensors previously tested. Samples were dried at 400 ^oC for 1 hour to remove volatile organics before firing. The screen-printed sample was sintered in air at 800 ^oC for 10 hours, with a heating and cooling rate of 5 ^oC per minute. The La_2CuO_4 electrodes had a thickness of ~15 μm.

4.2.2 Infrared Characterization

The adsorbed sample was analyzed using diffuse reflective infrared (DRIFT) spectroscopy on a Nicolet MAGNA 760 IR. Spectra were obtained at room temperature under dry nitrogen. DRIFT was chosen to examine surface complexes after experiments with transmission infrared (IR) failed to generate sufficient signal for identification of surface complexes. Adsorbed samples were analyzed using identically mulled weight KBr/La_2CuO_4 mixture as a baseline in order to clearly observe changes on the surface as a result of adsorption. To use this subtraction technique, it was necessary to ensure the uniformity of the mulled mixture between the sample of La_2CuO_4 used as a background and the adsorbed sample, ruling out the possibility of mixing the pure powder with KBr following the adsorption procedure. This technique has some precedent in separating substrate signal from the signal due to material at interfaces[236-238] and was valid for these experiments due to the homogeneity of the La_2CuO_4/KBr mixture for both samples.

For infrared spectroscopy measurements, a 5% / 95% weight mixture of La_2CuO_4 / KBr powders was prepared using a Wig-L-Bug muller and dried in air at 120 ^oC for one hour. The mulled mixture was loaded into the reactor used for mass spectrometry measurements.[239] The mixture was heated under 20 cubic centimeters per minute (ccm) flowing He at 2 ^oC / min to 225 ^oC. At that temperature the sample was exposed to 30 ccm of 1% NO or NO_2 / balance He and cooled to room temperature at 2 ^oC/min. Once cooled to room temperature, the sample chamber remained under helium flow until transferred to an IR spectrometer. In the absence of water and acidic conditions, KBr remains stable under the conditions and temperatures listed above.[240] Use of dry gases assured that there would be no interaction between the KBr and gas phase during adsorption, and exposure temperatures remained well below the 730 ^oC melting point.

4.2.3 XPS Characterization

X-ray photoelectron spectroscopy (XPS) was performed on both the La_2CuO_4 electrode and on La_2CuO_4 powder. The solid sample was examined at the gas/electrode interface before and after exposure to a testing cycle in order to see the effect of aging on the electrode surface. Powder samples were tested in the unadsorbed condition, as well as after adsorptions of NO, NO_2, CO, NO+CO, and NO+NO_2.

Sensor treatment was conducted in a typical gas-flow reactor. Gas environments were controlled using MKS mass flow controllers. The sensors were exposed to step changes of the gas in 3% O_2 with N_2 balance. The total flow rate was set at a constant 300 ccm. NO steps were set at 0, 50, 100, 200, 400 and 650 ppm while NO_2 steps were set at 0, 50, 100, 200, 300 and 333 ppm. Each step was held for 200 seconds and was delivered in an upward and downward hysteresis loop.

After the aging treatment was completed, the sample was re-surveyed to examine the effects of gas exposure. Initial XPS measurements were obtained for the solid sample directly after firing. A XPS/ESCA Perkin-Elmer PHI 5100 ESCA System acquired spectra using an Mg anode at a 45 degree incidence angle. The sample was surveyed from 1-1000 eV in 0.5 eV steps over an area covered by the La_2CuO_4 electrode. Following the XPS measurement of the freshly sintered sample, it was placed in a sensor testing chamber and cycled over multiple testing conditions for a period of 3 weeks to examine the effects of thermal hysteresis and gas exposure on the composition of the electrode. The results of these studies were covered in more detail in Appendix B.

Powder samples of La_2CuO_4 were heated to 550 ^oC and held at temperature under flowing helium and oxygen for 1 hour to clear the surface of impurities. The adsorption sample chamber was identical to those used previously for mass spectrometry measurements.[239] The samples

cooled under various gas atmospheres to 50 ^{o}C. Adsorption samples of the following types were obtained: Helium, 1% NO, 1% NO_2, 0.5% CO+5% O_2, 0.5% NO/0.5% CO, and 0.5% NO/0.5% NO_2. All samples were heated and cooled under flow of 10 cubic centimeters gas mixture per minute, at a rate of 4 ^{o}C per minute.

The adsorbed powder samples were evaluated using a Kratos Analytical Surface Analyzer XSAM 800. Freshly adsorbed samples were dusted on double sided carbon tape and mounted on a revolving sample holder. The testing chamber was then evacuated to 10^{-7} Torr and held overnight. Each sample was scanned from 1 eV to 1000 eV in 0.5 eV steps to establish a survey spectrum. After obtaining a full range spectrum, the samples were scanned to measure the spectra of the C 1s, La 3p5, and O 1s electron orbitals.

These measurements were obtained over the ranges of 270-295 eV, 830-870 eV, and 500-550 eV binding energy, respectively, in 0.1 eV steps. NO and NO_2 adsorptions are examined here. Other experimental results are described briefly in Appendix C.

4.3 Results and Discussion

4.3.1 IR Results for NO_x Adsorption

IR spectra of the species adsorbed on the powders were obtained by subtracting the spectrum of the unadsorbed powder from the spectra of the adsorbed samples. By removing all the characteristic IR traces from the La_2CuO_4 powder as well as any unintentional carbonate traces from atmosphere exposure, the NO_x adsorbates can be more clearly seen on the surface of the powder.[241] Subtraction of the unadsorbed spectrum was necessary in order to accentuate the adsorption peaks, as La_2CuO_4 adsorbs the near-infrared spectrum quite strongly.[242] Peaks were fit using Fourier deconvolution of a Kubelka-Munk spectrum transformation in ThemoNicolet OMNIC 6.1a. On the NO adsorbed sample (Figure 4-1a, 4-2a), relevant peaks can be seen at 2400, 1766, 1510, 1468, 1435, 1385, 1355, 1338, 1310, 1046, and 833 cm^{-1}. In the NO_2 sample

(Figure 4-1b, 4-2b), the peaks are located at 2396, 1763, 1500, 1465, 1436, 1414, 1390, 1351, 1325, 1305, 1039, and 825 cm^{-1}. Peaks seen near 3000-3500 cm^{-1} correspond to vibration of the simple ionic complexes, and were superfluous for assignment of species. However, in the NO_2 adsorption case, the peak near 3400 is much larger than in the NO adsorption case, indicating a greater amount of ionic NO formation on the surface due to gas adsorption.

Numerations of the peak assignments are tabulated in Table 1. The NO sample showed greatest peaks corresponding to chelated nitrite and nitrito formation, but minor peaks supporting the presence of room-temperature unidentate nitrate were also observed. Species present on the surface were identified by isolating specific vibrational signatures and comparing these signatures to patterns found in the literature.

Unidentate nitrate can be seen in the asymmetrical NO_2 stretch at 1510 cm^{-1}, symmetrical NO_2 stretching vibration at 1310 cm^{-1}, and 1046 cm^{-1} NO vibrations.[243-246] Nitrito complexes were observed from stretching vibrations of (N=O) at 1466 cm^{-1}, NO vibrations at 1046 cm^{-1}, and 833 cm^{-1} ONO bending vibrations.[244,245,247,248] Chelated nitrite groups were evident from asymmetric NO_2 vibrations at 1355 cm^{-1}, symmetric NO_2 vibrations near 1338 cm^{-1}, and the 833 cm^{-1} ONO bending vibrations.[248-254] Additionally, ionic NO^+ was revealed by the NO vibrations at 2400 cm^{-1}, and covalent bonding of the NO to metal sites was shown by the peak at 1766 cm^{-1} wavenumbers.[255] Free ionic NO_3^- is seen at 1435 cm^{-1}, assigned for the general case.[256] This NO_3 variant represents the transition state between structures of nitrates.

Numerations of the peak assignments for NO_2 are also tabulated in Table 1. In the NO_2 adsorbed case, nitrito complexes were observed from stretching vibrations of (N=O) at 1463 cm^{-1}, NO vibrations at 1039 cm^{-1}, and ONO bending vibrations at 825 cm^{-1}. Chelated nitrite groups were evident from asymmetric NO_2 vibrations at 1351 cm^{-1}, symmetric NO_2 vibrations near 1325

cm^{-1}, and the ONO bending vibrations at 825 cm^{-1}. Nitro groups can be seen by asymmetric NO_2 vibration at 1436 cm^{-1}, symmetric NO_2 vibrations at 1351 cm^{-1}, ONO bending at 825 cm^{-1}, and evidence of conjugation with the surface at 1394 cm^{-1} was observed.[256] Ionic NO^+ was revealed by the NO vibrations at 2396 cm^{-1}, and covalent bonding of the NO to metal sites was shown by the peak at 1763 cm^{-1}. Unidentate nitrate can be seen in the asymmetrical NO_2 stretch at 1500 cm^{-1}, symmetrical NO_2 stretching vibration at 1305 cm^{-1}, and NO vibrations at 1039 cm^{-1}.

In discussing the composition of surface adsorbates, the limitations of IR must be stressed. The presence of nitrate (NO_3^-) and nitrite (NO_2^-) groups was well documented in the literature for metal oxides.[225,244-250,254,257] The composition of these adsorbate groups is somewhat malleable, depending on temperature. Isolating a specific nitrate or nitrite compound structure in the IR spectrum is mostly symbolic, as the different structures of the surface groups only represent the transient properties of the oxygen connection to the lattice involved in the formation of that group.[225] The individual structures within the nitrate and nitrite designations are not functionally different, and so in speaking of one structure in the group, similar characteristics can be assigned to other structures for that same compound. Further, the nitrate, nitrite, and bonded NO groups observed via IR likely possess the ability to shift from one configuration to another as part of a larger mechanism, suggested by the presence of the indefinable free NO_3^- on the surface after adsorption.

Previous results from TPD and TPR experiments show manifestly different desorption and reaction products resulting from the NO vs. NO_2 adsorptions, with total adsorbed NO_x a factor of two larger in the NO_2 case.[66] The IR signal in the spectrum following NO_2 adsorption was also observed to be twice as large as in the NO case, reinforcing the previous results for TPD/TPR studies. The IR results for NO adsorption versus NO_2 adsorption show very similar patterns, with

the exception of nitro groups visibly present on the NO_2 adsorbed sample spectrum. The formation of very similar complexes on the surfaces is important because it shows that while the mechanisms of their formation are distinct, the end products are related.

4.2.2 XPS Results for NO_x Adsorption

The solid La_2CuO_4 electrode on YSZ substrate was evaluated by XPS immediately after firing. XPS measurements were repeated after thermal cycling and gas cycling in order to determine the extent of change on the surface of the electrode. This comparison can be seen in Figure 4-3.

The peaks from the XPS measurement in the as received sample are consistent with those in the literature for La_2CuO_4.[258-261] The La_2CuO_4 was well visualized by the La 3d5 peak at 835 eV, O 1s peak at ~530 eV, and a weak Cu 2p3 line at 934 eV. Carbon impurities were observed for the C1s orbital at 282 eV for carbidic impurities[262] and 284.5 eV for graphitic carbon.[263] Graphitic carbon was present in the XPS spectra due to its use as the sample substrate and its peaks were utilized as anchors to identify peak shifting in the La 3d5 and O1s regions[264,265] through each NO_x adsorption spectrum.

Three weeks of thermal cycling changed the surface composition only slightly. Peaks corresponding to the La 3d5 orbital increased slightly in intensity, indicating relaxation of the La_2O_2 layer to the surface of the electrode grains. Thermal cycling causes the lanthanum layer to establish itself more strongly on the surface,[266,267] though the actual surface structure likely does not establish itself fully into this ideal structure. Correspondingly, peaks from the CuO_2 layer lost their intensity, and the signal from the Cu 2p3 orbital was reduced to a level just above noise. The Cu 2p3 peak is not especially large even when the sample is fresh, so its suppression was reasonable if the lanthanum layer became more prominent.

The XPS spectra of the electrode revealed that short term exposure to thermal cycling in sensor testing conditions did not fundamentally change the character of the electrode surface, reflected in the superposition of the spectra taken before and after aging. Local manipulation of oxygen partial pressure by the use of reducing gases causes no irreversible effects to the structure or composition of the electrode. Furthermore, obtaining XPS spectra in room temperature vacuum did not reduce La_2CuO_4 to its component oxides even at oxygen partial pressures far below the high temperature decomposition threshold in mechanically induced vacuum.[134] From these discoveries, it can be presumed that adsorption of gases on the surface will not cause permanent compositional changes that prevent examination of adsorbates via XPS.

The powder samples were examined after adsorption of gas mixtures on oxidized samples. The powder displayed a survey baseline spectrum essentially identical to that of the solid sample after thermal cycling. The spectrum reflected an O1s peak at 530 eV, La3p5 peak at 837 eV, and C1s peak at 281 eV, but showed no signs of Cu peaks throughout the survey. This is possibly in part due to the additional processing required to prepare the samples, where increased roughness of the powder may have obscured the copper signal,[268] but the reconstruction of the surface to favor lanthanum exposure may also have played a role.

NO adsorption induces splitting of the composite O 1s peak at 530 eV into a its component peaks representing oxygen unaffected by the adsorption of NO to the surface, and increases in the region near 534 eV (Figure 4-4). This shift was caused by the binding of surface lattice oxygen in the oxide by NO bonding.[269,270] The relative intensity of the two peaks indicates the extent to which NO affects the oxygen in the observable volume. The different chemical state of oxygen bonding is seen in the binding energy shift, which for the formation of the complexes on the surface, will result in a lower Fermi energy, and thus a higher binding energy of the core

oxygen electrons. The formation of complexes on the surface tied up the oxygen and accounted for the strengthening of the binding energy in the split peak. Since the powder sample is overall electrically isolated during NO adsorption, the amount of NO adsorbed cannot fully cover the surface of the powder, and so the XPS results show a combination of the La_2CuO_4 surface oxygen as well as the oxygen pulled into the surface complexes.

A stronger peak splitting was observed for the O1s orbital with the adsorption of NO_2 than in the NO adsorption case. (Figure 4-5) The large peak at 530 was observed to split into a peak at 527 and a larger peak at 534, with the total area underneath the peaks greater than in the unadsorbed or NO adsorbed case. This additional area can be explained by the stronger bonding behavior of NO_2 in relation to NO. The greater separation in this case corresponds to the greater perturbation of the observable volume by the adsorption of NO_2. The large shift of area to the 534 eV peak showed the oxygen chemistry of the observable volume shifts to the production of complexes on the surface. However, unlike the NO adsorption case, the oxygen rearrangement was compensated by the formation of charge carrying species (electron holes) evidenced by the peak shift to 527 eV.

We reported that La_2CuO_4 powder TPR experiments for NO and $NO+O_2$ showed no compositional changes due to homogeneous gas-phase or heterogeneous gas-solid reactions over the 50-800 ^oC range of the experiment.[66,239,271] TPD results also show no dissociation of NO to N_2 and O_2, or oxidation from NO to NO_2, only a very small conversion of NO to N_2O, due to direct bonding to Cu^+ sites during adsorption.[225] Since desorption of NO almost exclusively produces species chemically identical to the adsorbed NO, the catalytic production of electrochemical products for generation of voltages was unlikely. Instead, it seems that the formation of the surface complexes facilitated the formation of a charged layer at the surface.

Thus, instead of full and irreversible electrochemical production, a reversible but stable equilibrium occurs at the interface. Since NO lacks the oxygen to form the nitrate and nitrito surface complexes on its own, it draws oxygen from the surface to complete the compound.

The proposed complexing mechanism for NO adsorption can be seen in Figure 4-6. Upon encountering the La_2CuO_4 surface, the molecule had the possibility of attaching to either a metal or oxygen site. For the sake of simplicity, the NO molecule is assumed to orient in the N-up or N-down configuration for bonding with the surface. In the case where NO bonds to a metal site, bonding N-down creates covalent or ionic NO which can interact with other NO complexes, but are otherwise stable. In the N-up configuration, the nitrosyl complex can form as an intermediate before re-orienting to a chelated nitrite group. This group is functionally equivalent to the nitrito clearly seen in the IR spectra, and with sufficient thermal perturbation, can likely relax to the nitrito configuration.

In the case of NO bonding to an oxygen site, N-down bonding produces a nitrito group after the lattice oxygen retains one bond to a metal site, then relaxes away from the surface. The N-up bonding configuration would force an oxygen-oxygen bond, which does not form any complexes seen in the IR spectra.

Unidentate nitrate forms from NO complexing to two oxygen sites. The mechanism for nitrate formation is not entirely clear; however, the bridged nitrate complex forms on La_2O_3, which realigns to form the unidentate nitrate.[257] Although the bridged nitrate cannot be reliably observed at room temperature on the surface of La_2CuO_4 after NO adsorption, its presence as an intermediate can be dependably postulated, since the nitrito group would be a precursor to bridged nitrate formation.

As the complexes tie up a greater amount of oxygen, the surface layers of La_2CuO_4 became oxygen deficient:

$$O_O^x + NO_{(g)} \leftrightarrow NO'_{2(ad)} + V_O^{\bullet\bullet} + e' \quad [4\text{-}1]$$

$$O_O^x + NO'_{2(ad)} + V_O^{\bullet\bullet} + e' \leftrightarrow NO'_{3(ad)} + 2V_O^{\bullet\bullet} + 3e' \quad [4\text{-}2]$$

Due to the net addition of electrons to the bulk, there is a shift in the Fermi level at the surface, raising the potential to push electrons to the counter-electrode. This Fermi change for the full sensor cannot be measured directly via XPS, due to the need for vacuum, but a Kelvin probe capable of atmospheric pressure operation could quantify the shift by measuring the work function while the sensor is operating.[177,182] By monitoring the ionisorbed layer, the extent of charge conversion could be determined over an area.[173] At the time of writing, the ability to make this measurement was unavailable.

The oxygen deficiency lowers the availability of electron holes, due to the p-type semiconductive nature of La_2CuO_4, leading to a drop in electronic conductivity, consistant with observed resistive changes.[125] The electron binding was seen in the XPS spectra of the O1s orbital following NO adsorption. When compared directly to the fully oxidized La_2CuO_4 sample, a significant shift upwards in the binding energy is clear. This increased energy results from the integration of the oxygen electron into the unpaired orbital of the nitrogen in NO.[272] This shift in potential due to surface complexing is reversible, as the potential across a full sensor will disappear with removal of NO.

Upon heating, there is no evidence of low temperature oxygen emission, only NO desorption. The lack of oxygen emission meant the complexes that formed by oxygen removal from the surface replace the oxygen before disassociating. As a result, the surface retains its original state after low temperature NO complex breakdown and desorption. One possible

explanation for this behavior is the rearrangement of the complexes on the surface to favorable compositions for O_2 retention and NO desorption (i.e. nitrito). In these configurations, oxygen bonds to the surface are sufficiently strong to allow separation from a nitrogen atom without removal from the surface. Reversibility is unique to the NO adsorption due to its weak association with surface oxygen, seen in temperature programmed desorption experiments in earlier chapters. It does not retain surface oxygen when it desorbs, as opposed to CO, which retains the composition of CO_2 while desorbing.

The adsorption behavior of NO_2, by contrast, was much more complicated. The adsorption of NO_2 caused a stronger effect of peak splitting than in the NO adsorption case. The large peak at 530 eV was observed to split into a small peak at 527 eV and a relatively larger peak at 534 eV, with a greater total area than in either the unadsorbed or NO adsorbed case. This can be explained by the stronger bonding behavior of NO_2 in relation to NO. Desorption products of NO_2 from the surface were much more complex than those of NO desorption, and the quantities evolved from the surface were much greater.[66]

The possible mechanism of NO_2 adsorption can be explained similarly to NO adsorption (Figure 4-7). Upon encountering the La_2CuO_4 surface, the NO_2 molecule had the possibility of attaching to either a metal or oxygen site. Again, the NO_2 molecule is assumed to orient in the N-up or N-down configuration for bonding with the surface. In the case where NO_2 bonds whole to a metal site, bonding N-down forms nitro groups. These groups can either remain in the nitro configuration, which desorbs as NO_2, or realign to form ionic or covalent NO, and releases the second oxygen atom to the oxide surface. In the N-up configuration, oxygen bonds to metal and directly forms the nitrito group, which can reconstruct into a chelated nitrite or interact with the surface oxygen to form a bridged nitrate intermediate. For oxygen sites, the N-up bonding

configuration would force an oxygen-oxygen bond, which does not form any complexes seen in the IR spectra. N-down bonding to the oxygen directly forms the unidentate nitrate once the oxygen relaxes away from the surface. At that point, the nitrate groups can shift from one construction to another.

NO_2, in contrast to NO, does not draw oxygen from the surface to complete all the complexes- for nitrite formation, it enriches the local lattice oxygen concentration by removing an electron to form ion complexes without removing oxygen, causing valence changes in the subsurface copper atoms, while increasing the conductivity due to electron hole formation.

$$M_M^x + NO_{2(g)} \leftrightarrow NO_{2(ad)}^{'} + h^{\bullet} + M_M^x \qquad [4\text{-}3]$$

This behavior is analogous to electron hole creation caused by doping on the A-site of La_2CuO_4, such as Sr.[273-275] Electron hole formation was shown by the lessening of the O1s electron binding energy peak from 530 eV to 527 eV.

NO_2 has more available oxygen than NO, so when forming an NO_3^- negative complex, it does not need to bond to two oxygen sites, requiring only one. This oxygen can be obtained in a number of ways. The adsorbed nitro complex may dissociate to an NO molecule and adsorbed oxygen, which provides for the formation of the nitrate complex without oxygen removal from the lattice by a second adsorption of NO_2. If this occurs, the nitrate forms in a similar manner to the nitrite group.

$$M_M^x + NO_{2(g)} + O_{(ad)} \leftrightarrow NO_{3(ad)}^{'} + h^{\bullet} + M_M^x \qquad [4\text{-}4]$$

If adsorbed oxygen is unavailable, the nitrate can be formed by NO_2 bonding to an oxygen site, where the complex can relax into one of several configurations.

$$O_O^x + NO_{2(g)} \leftrightarrow NO_{3(ad)}^{'} + V_O^{\bullet\bullet} + e^{'} \qquad [4\text{-}5]$$

This complex desorbed identically to the analogue formed by NO. The oxygen bonded to the metal site at the surface remains attached, and the NO desorbs, whereupon the oxygen proceeds to bond with another metal-bonded oxygen or surface oxygen, and desorb as an oxygen molecule to maintain charge balance. This process occurs both when the third oxygen was removed from the surface and when the third oxygen results from nitro group decomposition. It accounts for the dissociation of NO_2 into NO and O_2 seen in the mass spectrometry desorption profiles and the raised binding energy seen in the XPS results.

4.4 Conclusions

It can be noted that while the intermediates on the surface due to adsorption are for all intents similar, the method in which they form greatly affects the charge the surface layer generates, and leads to the differences in potential across the electrolyte. By examining the working electrode material independently of the sensor, the adsorptive component can be examined without compensation for possible charging effects on the sensor electrodes. NO adsorption generates charge depletion layers by the formation of NO_2^- and NO_3^- at the gas/solid interface, where electrons are taken from the bulk and held.

These depleted layers form a potential gradient that (in a full sensor) draws electrons from the counter-electrode, for a positive voltage. This phenomenon was observed in the absence of catalytic conversion of NO to N_2 or NO_2, thus advancing the theory that NO sensing via the LCO electrode is entirely adsorptive. NO_2 forms similar complexes, but due to the extra oxygen present for some of these complexes, electron holes are generated, which produced a negative potential gradient across the sensor couple in a full device.

Table 4-1. IR Peak assignments of the NO/NO_2 adsorbed samples of La_2CuO_4

NO_x species	Structure	Vibration	Inorganic compound or metal oxide[225,243-257]	NO Wavenumber (cm^{-1})	NO_2 Wavenumber (cm^{-1})
Ionic NO	NO^+ / NO^-	$\upsilon\upsilon_{(NO)}$	2100-2400	2400	2396
Ionic NO_3^-	Transitional	$\upsilon\upsilon_{(NO2,as)}$	1350-1450	1435	1414
Covalent NO	M-NO		1600-1800	1766	1763
Chelated Nitrite	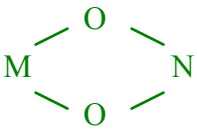	$\upsilon\upsilon_{(NO2,as)}$ $\upsilon\upsilon_{(NO2,s)}$ $\delta\delta_{ONO}$	1270-1390 1360-1260 840-860	1355 1338 833	1351 1325 825
Unidentate Nitrate	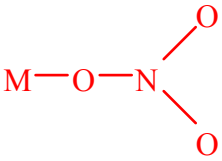	$\upsilon\upsilon_{(NO2,as)}$ $\upsilon\upsilon_{(NO2,s)}$ $\upsilon\upsilon_{(NO)}$	1450-1570 1250-1330 970-1035	1510 1310 1046	1500 1305 1039
Nitrito		$\upsilon\upsilon_{(N=O)}$ $\upsilon\upsilon_{(NO)}$ $\delta\delta_{ONO}$	1400-1485 1050-1100 820-840	1466 1046 833	1463 1039 825
Nitro	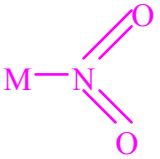	$\upsilon\upsilon_{(NO2,as)}$ $\upsilon\upsilon_{(NO2,s)}$ $\delta\delta_{ONO}$ $\upsilon\upsilon_{(NO2,as)}$ Conjugated Nitro	1370-1470 1320-1340 820-850 1350-1400		1436 1351 825 1390

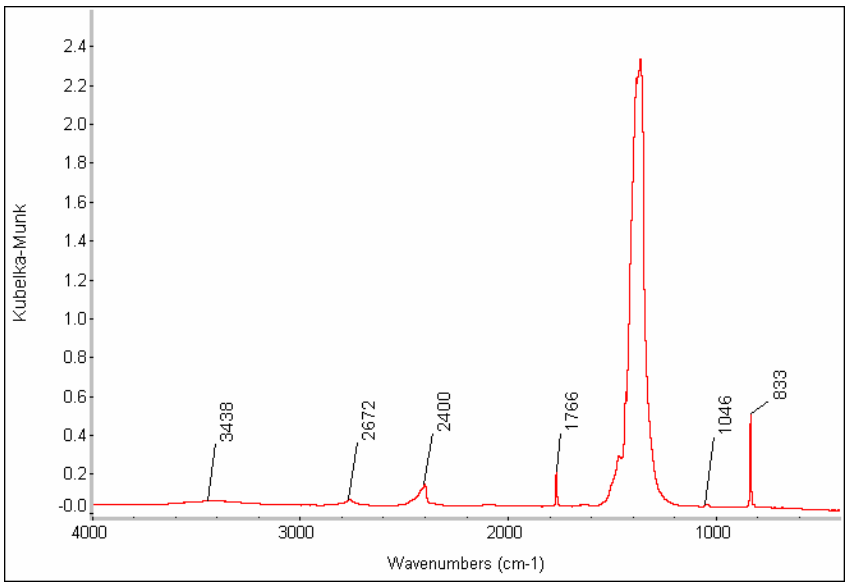

Figure 4-1a. IR spectra of La_2CuO_4/KBr mulled mixture after NO adsorption.

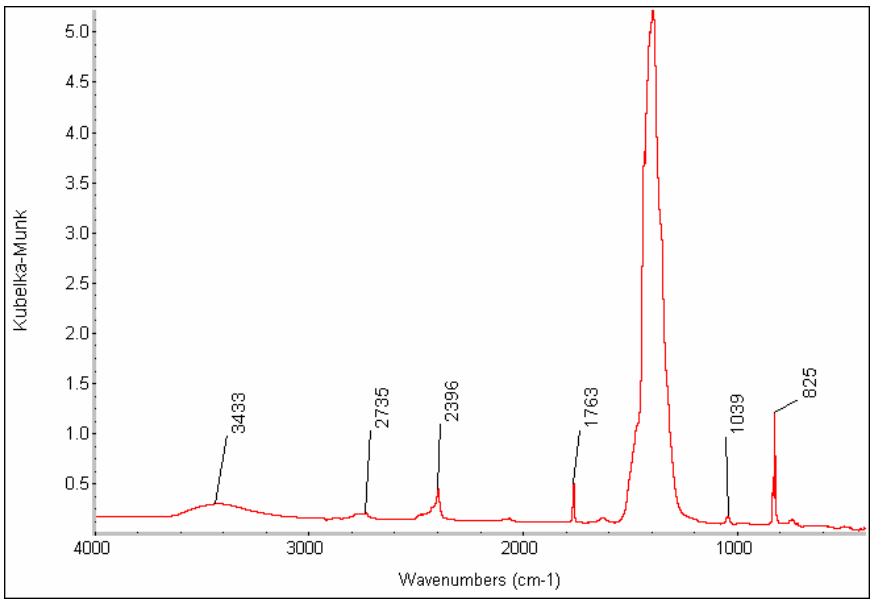

Figure 4-1b. IR spectra of La_2CuO_4/KBr mulled mixture after NO_2 adsorption

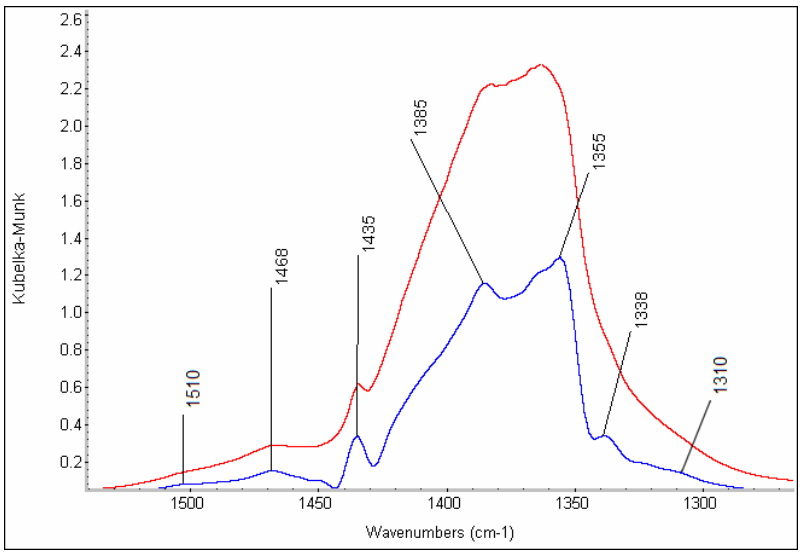

Figure 4-2a. Fourier Deconvolution of 1550-1200 cm^{-1} spectrum of NO-adsorbed La_2CuO_4 (Labeled line corresponds to the Fourier deconvolution)

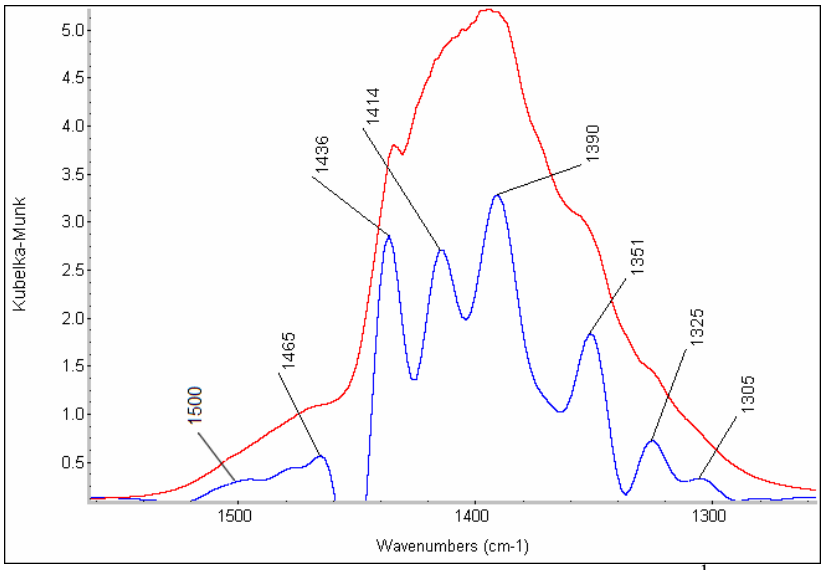

Figure 4-2b. Fourier Deconvolution of 1550-1200 cm^{-1} spectrum of NO_2 – adsorbed La_2CuO_4 (Labeled line corresponds to the Fourier deconvolution)

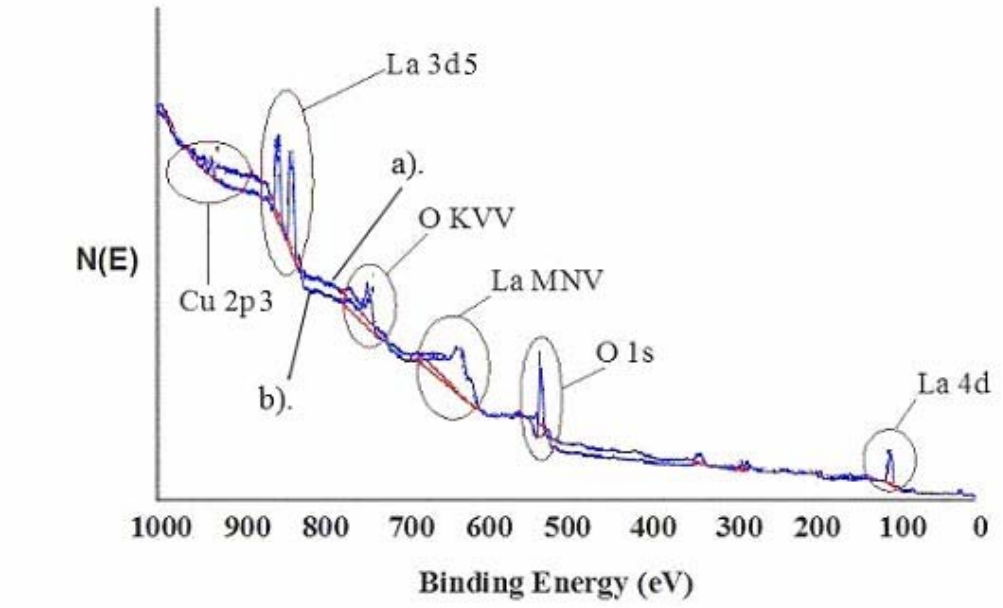

Figure 4-3. Full range XPS spectra of solid La_2CuO_4 samples in the (a) freshly sintered case and (b) after 3 weeks of exposure to sensor testing conditions.

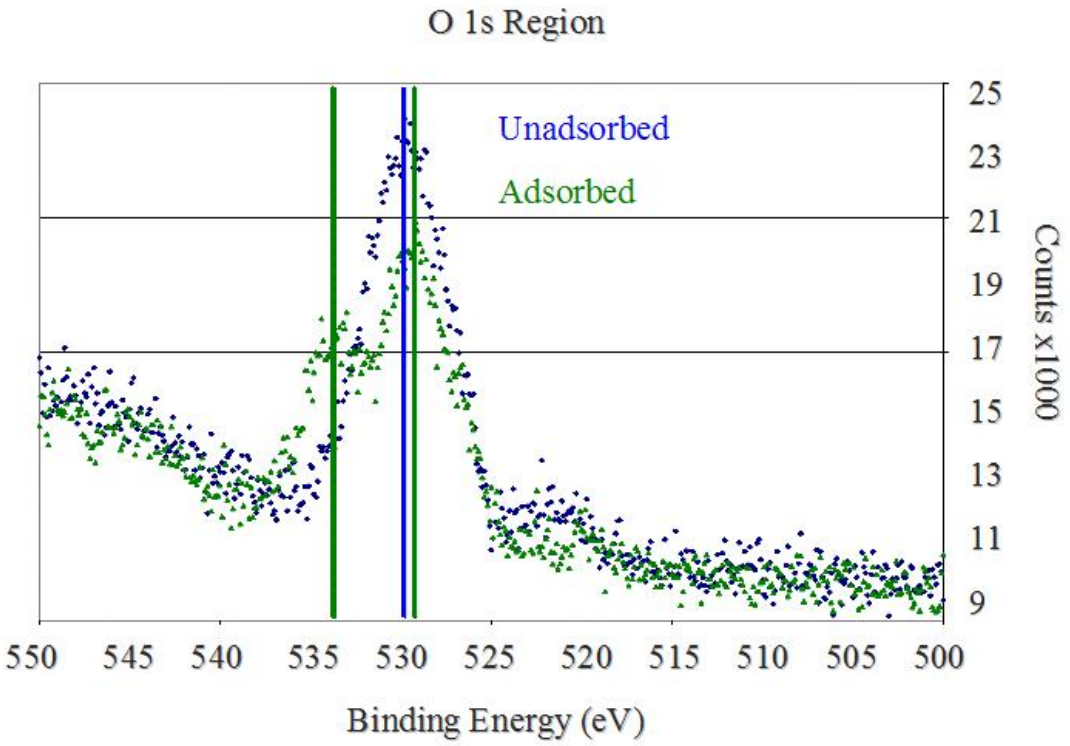

Figure 4-4. O1s XPS spectra of NO adsorbed La_2CuO_4 versus the unadsorbed case.

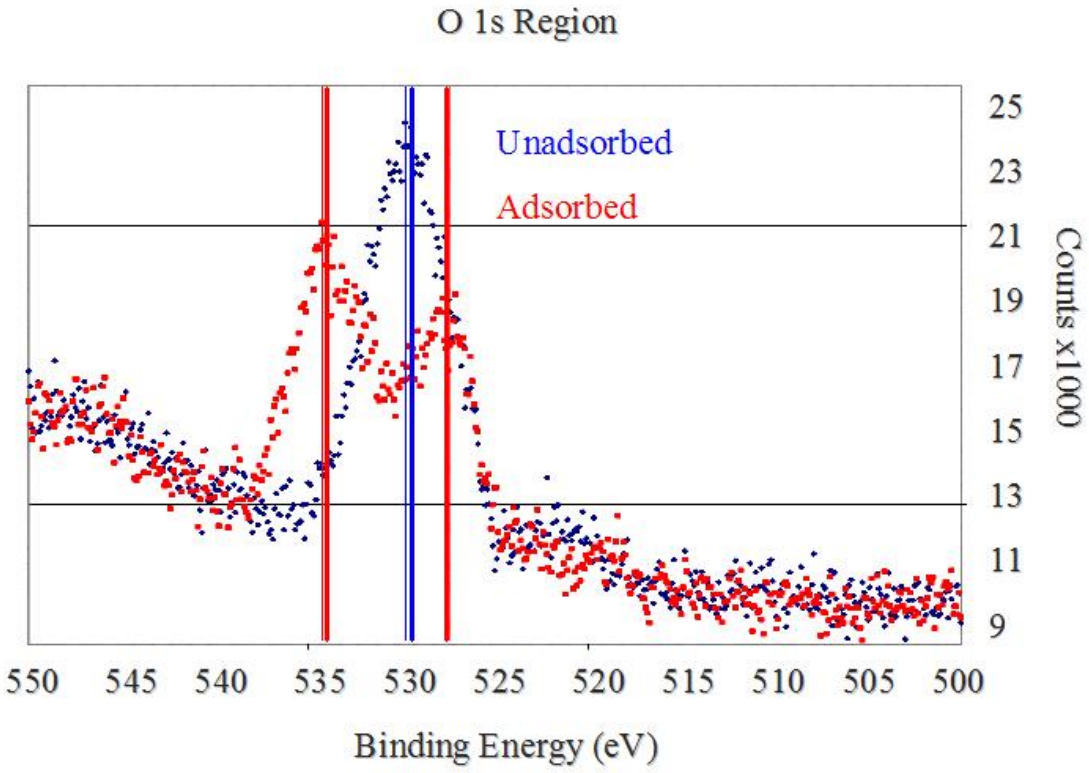

Figure 4-5 - O1s XPS spectra of NO_2 adsorbed La_2CuO_4 versus the unadsorbed case.

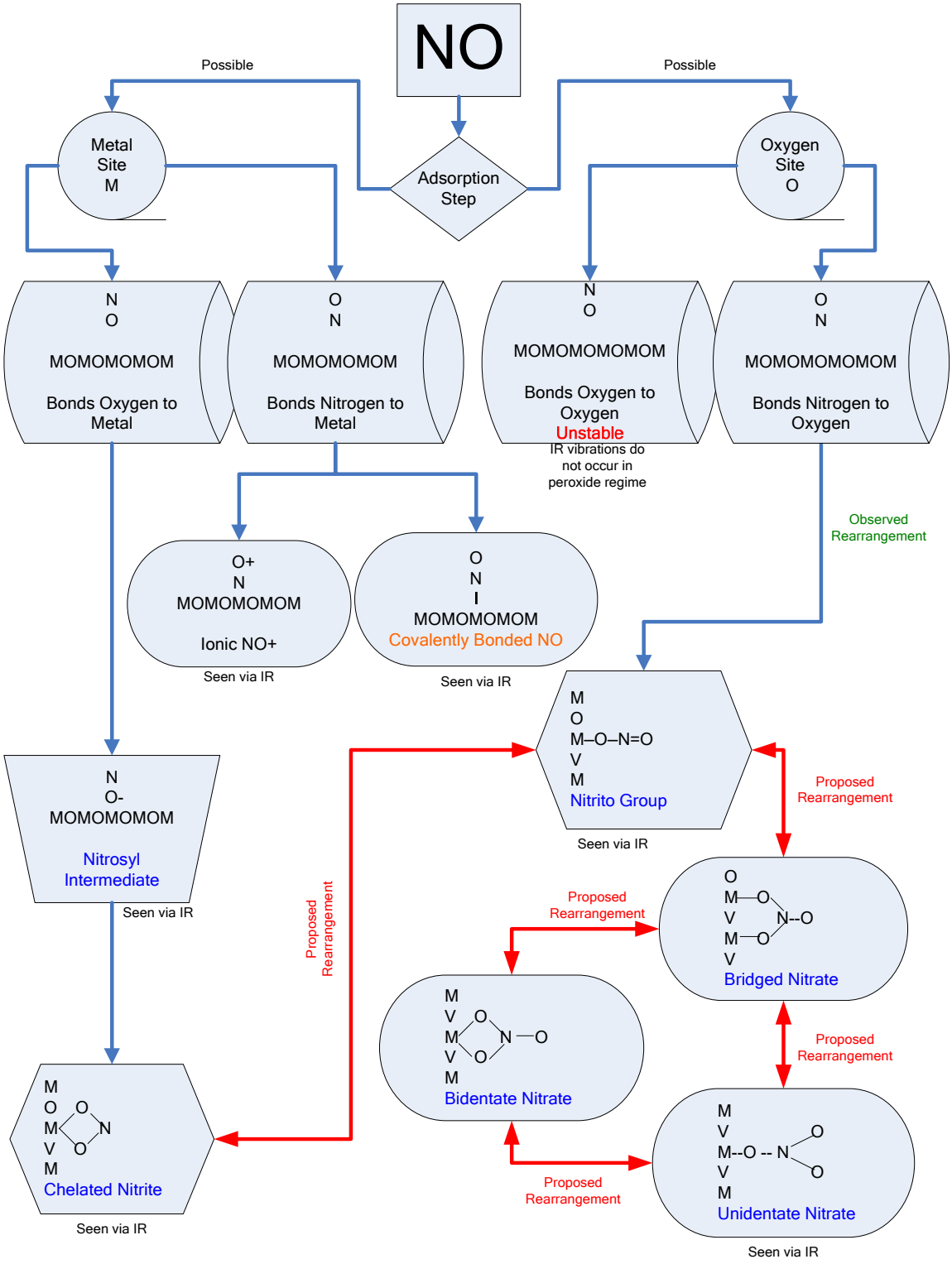

Figure 4-6. Flowchart of proposed NO adsorption mechanism

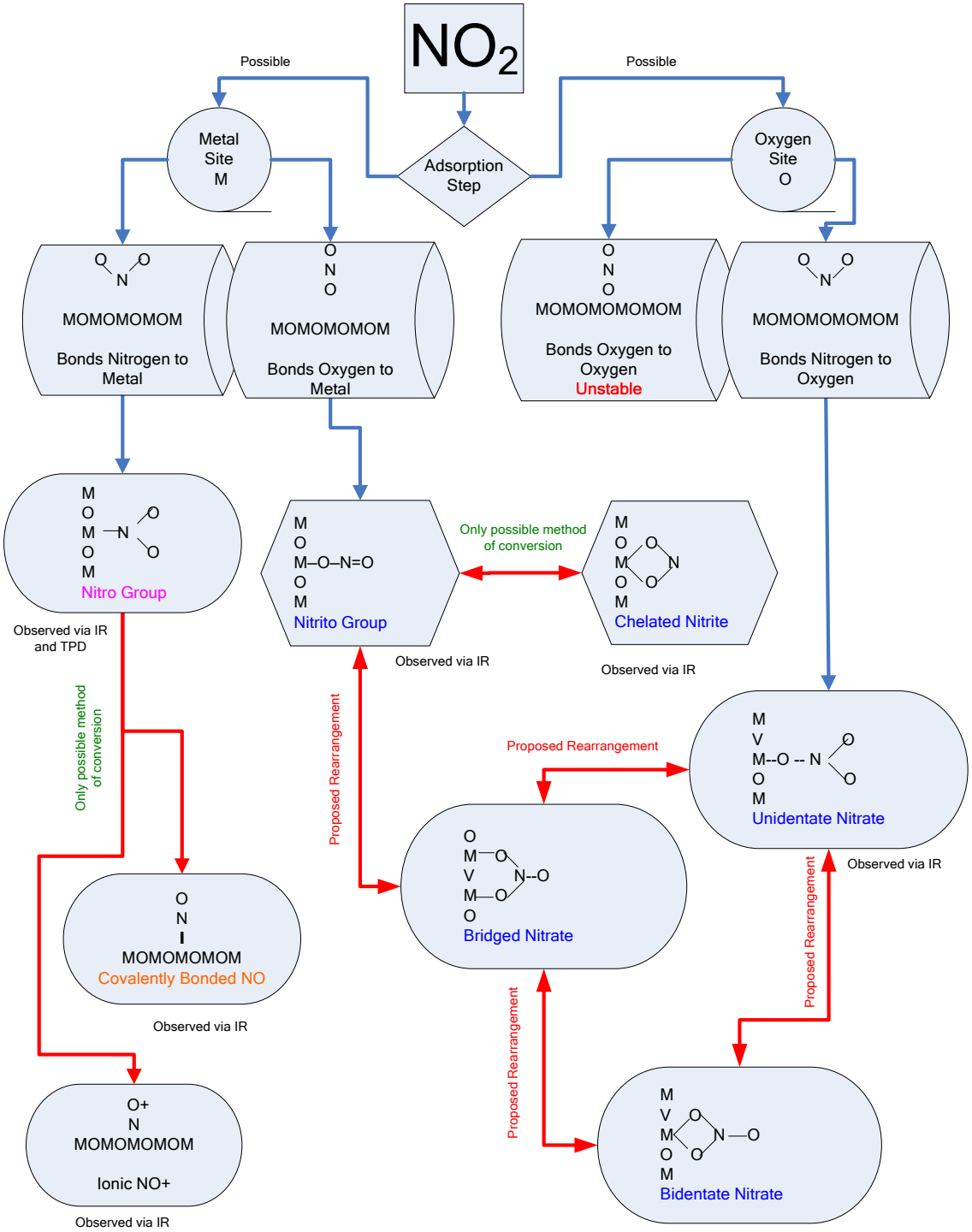

Figure 4-7. Flowchart of proposed NO_2 adsorption mechanism.

CHAPTER 5
ISOTOPICALLY LABELED OXYGEN STUDIES OF THE EXCHANGE BEHAVIOR OF NOX OVER LA2CUO4

5.1 Introduction

Isotope exchange studies utilizing heavy oxygen ($^{18}O_2$) have proven useful in the study of catalysis, and by use on sensor materials, permit further exploration of the adsorption and reaction mechanism of NO_x involved in solid-state gas sensor response. Previous research in this topic focused on diffusion, using secondary ion mass spectrometry (SIMS)[276-279] and gas-phase mass spectrometry to track exchange with surface oxygen.[219,280,281] Gas phase mass spectrometry (MS) using heavy oxygen has also been used to examine reactions at the gas/solid interface through temperature programmed experiments.[218,282-285] Standard temperature programmed reaction (TPR) and temperature programmed desorption (TPD) experiments provide important information about the composition of reaction/desorption products, but can only inform of the presence of compounds, not necessarily their method of formation.

We demonstrated in past chapters, using infrared spectroscopy and X-ray photoelectron spectroscopy experiments, that a substantial amount of nitrate and nitrite complexes form on the surface of La_2CuO_4 powder as a result of NO_x adsorption.[286] Through MS analysis of the TPR/TPD effluent we determined that NO remained unconverted to either NO_2 or N_2, but NO_2 will decompose to NO over La_2CuO_4.[66,102] NO adsorption resulted in a mix of adsorbate complexes that utilize adsorbed gas-phase or lattice oxygen. These complexes decomposed on the surface to re-form the NO molecule, and desorbed NO while desorbing the sequestered oxygen in both the purely adsorptive and in the reactive case. While these experiments confirmed the uncatalytic nature of La_2CuO_4 to the NO→NO_2 and NO→N_2 reactions, the mechanism by which the NO reformed as it desorbed was still unknown.

Similarly, NO_2 formed nitrate, nitrite, and nitro complexes on the powder surface that decomposed to NO, NO_2, and O_2. The products of desorption and reaction were easily characterized, but there again remained only a suggestion of the process by which these gases formed during separation from the powder surface.

By using heavy ^{18}O in place of the naturally occurring ^{16}O, the origin of molecules desorbing from the surface could be determined. Mass spectra of the effluent gas from the reactor can separate N or C containing molecules desorbed with their original atoms from those produced from scrambling $^{16}O/^{18}O$ compounds on the surface.[110]

By utilizing the reaction mechanism constructed in Chapter 4 for NO_x adsorption, a sequence of all possible pathways from adsorption to desorption was obtained. Using $^{18}O_2$ as the gas-phase oxygen, the possible reaction pathways can be probed experimentally. By examining the results of TPD, TPR, and isothermal reaction, the most likely methods of complex formation can be obtained. If the compounds desorbing from the surface show a large amount of ^{18}O-containing products, the gas-phase adsorbates of oxygen will play a much larger role than previously considered. If the mass of the products is the same as the naturally occurring type, then the oxygen in NO_x/CO_x compounds results from a complete reversal to the same atoms during desorption or the oxygen in the compounds is a result of exchange with the lattice. This mechanism allowed the separation of the relative contribution of electrochemical (i.e. Mixed Potential) reactions to the sensor response to NO_x gas.

To determine the mechanism, it proved necessary to anneal the sample in order to exchange ^{18}O into the lattice, and then repeat experiments in order to see whether the powder exchanges lattice oxygen by measuring for desorption products of increased mass. The possible sequence for NO adsorption can be seen in Figure 5-1.

The simplest possible path for NO is to bond in the nitrogen-down configuration to a metal site, and desorb identically by simply breaking the metal-nitrogen bond. These bonds can be expressed as either ionic or covalent in character, and the adsorption/desorption reactions are shown in Equations 5-1 and 5-2.

$$N^{16}O_{(g)} \leftrightarrow (NO)^{+} + e^{-} \quad [5\text{-}1]$$

$$N^{16}O_{(g)} \leftrightarrow (NO) \quad [5\text{-}2]$$

A possible branch of this adsorption is for the upward extended oxygen to exchange with oxygen on the surface, shown in Equation 5-3 and 5-4.

$$(NO)^{+} + \tfrac{1}{2}{}^{18}O_{2(surface)} \leftrightarrow (N^{18}O)^{+} + \tfrac{1}{2}{}^{16}O_{2(surface)} \quad [5\text{-}3]$$

$$(NO) + \tfrac{1}{2}{}^{18}O_{2(surface)} \leftrightarrow (N^{18}O) + \tfrac{1}{2}{}^{16}O_{2(surface)} \quad [5\text{-}4]$$

The covalent and ionic NO complexes are the least strongly bonded to the surface of La_2CuO_4, so if this exchange occurs during the adsorption process, low temperature desorption peaks corresponding to $N^{18}O$ will be visible during heating. However, the nature of the ionic bond generated by NO occurs due to its resonance in the N-O pseudo-triple bond.[287] As a result, oxygen exchange cannot occur without destroying the bond to the surface, and the mechanism proceeds according to Equations 5-1 and 5-2.

Adsorption of NO as a nitrite (NO_2^-) or nitrate (NO_3^-) species requires extra oxygen atoms, and these can be drawn from the adsorbed surface or the bulk. The key step was to determine the source of the exchange, if any occurred. If NO exchanged its oxygen, the MS profile would change to reflect the scrambled oxygen product at m/z 34, as well as an increase in m/z 32 that would almost exclusively correspond to $N^{18}O$. These mechanisms are represented by Equation 5-5 for nitrite species, and Equations 5-6 to 5-10 for nitrates.

Nitrite species form by bonding in the nitrogen-down configuration to a lattice oxygen, pulling an electron from the bulk to complete the complex, seen in Equation 5-5.

$$N^{18}O + \tfrac{1}{2}\,{}^{16}O_{lattice} + e^- \leftrightarrow (N^{16}O_2)^- \quad [5\text{-}5]$$

Following nitrite formation, the complex can desorb by reversing the adsorption mechanism, or can further alter its structure. By combining with surface oxygen, the nitrite can become a nitrate, as seen in Equation 5-6 and 5-7.

$$(N^{16}O_2)^- + \tfrac{1}{2}\,{}^{16}O_{2(surface)} \leftrightarrow (N^{16}O_3)^- \quad [5\text{-}6]$$

$$(N^{16}O_2)^- + \tfrac{1}{2}\,{}^{18}O_{2(surface)} \leftrightarrow (N^{16}O_2\,{}^{18}O)^- \quad [5\text{-}7]$$

This nitrate can remain on the surface, or reverse the formation to revert to the nitrite configuration. By retaining the ^{18}O atom added in Equation 5-7, the nitrite can effectively exchange the extended oxygen, and this change would be reflected upon desorption. These steps can be seen in Equation 5-8 and 5-9.

$$(N^{16}O_2\,{}^{18}O)^- \leftrightarrow (N^{16}O^{18}O)^- + \tfrac{1}{2}\,{}^{16}O_{2(surface)} \quad [5\text{-}8]$$

$$(N^{18}O^{18}O)^- \rightarrow N^{18}O + {}^{16}O_{lattice} + e^- \quad [5\text{-}9]$$

The exchanged nitrite can again complex with an adsorbed ^{18}O to reform the nitrate, seen in Equation 5-10.

$$(N^{16}O^{18}O)^- + {}^{18}O_{(surface)} \rightarrow (N^{18}O_2\,{}^{16}O)^- \quad [5\text{-}10]$$

Once the nitrates have formed, they decompose upon heating to form the highest temperature desorption peak via Equations 5-11 to 5-14 below.

$$(N^{16}O_3)^- \rightarrow N^{16}O + {}^{16}O_{(gas)} + {}^{16}O_{surface} + e^- \quad [5\text{-}11]$$

$$(N^{16}O_2\ ^{18}O)^- \rightarrow N^{16}O + {}^{18}O_{(gas)} + {}^{16}O_{surface} + e^- \quad [5\text{-}12]$$

$$(N^{16}O_2\ ^{18}O)^- \rightarrow N^{18}O + {}^{16}O_{(gas)} + {}^{16}O_{surface} + e^- \quad [5\text{-}13]$$

$$(N^{18}O_2\ ^{16}O)^- \rightarrow N^{18}O + {}^{18}O_{(gas)} + {}^{16}O_{surface} + e^- \quad [5\text{-}14]$$

From previous studies, it has been demonstrated that the reaction and desorption profiles are identical in the case of NO exposure. As a result, the TPD and TPR using ^{18}O should look quite similar. However, while the chemical composition of the effluent gas is the same as the adsorbate, the question remains if the desorbing species are identical to those that adsorb. Since the desorption spectra was fairly simple, the steps in the adsorption mechanism can be determined readily.

As observed in Chapter 3, the NO desorption spectra has three distinct peaks, corresponding roughly to the decomposition and desorption of ionic/covalent NO, nitrite, and nitrate species. The weakly bonded ionic/covalent NO species desorb with the lowest amount of activation energy, and can be identified at ~150 ^oC during 30 ^oC per minute heating. Thus, if exchange occurs between the adsorbed NO complexes, there should be an increase in 32 m/z intensity during the TPD or TPR in that temperature range.

Above the desorption threshold for the ionic and covalent species, there are peaks corresponding to the decomposition of other NO_x complexes. Nitrate and nitrite species are more stable on the surface than the ionic and covalent complex, and so they desorb at a higher temperature. Thus, changes due to ^{18}O acquisition can be resolved by monitoring the level of m/z 32 relative to m/z 30. If the only method of acquiring ^{18}O is by integrating adsorbed surface oxygen, then the higher 32 peak corresponding to nitrate decomposition should be a larger fraction of the total NO desorption at that temperature range relative to the fraction of 32/ 30 due

to nitrite decomposition. If the ^{18}O can substitute for the ^{16}O already in the nitrite and nitrate complexes by oxygen exchange with the surface, the signal for m/z 32 should be much larger than the signal for m/z 30. If the complexes still desorb identically as $N^{16}O$, then one of two paths occurs. Either the adsorption favors the N-^{16}O bond to the point that it always remains (which rules out $^{18}O/^{16}O$ exchange), or the complex forms by bonding exclusively to lattice oxygen. This can be further resolved by repeating the experiments with a LCO powder that was annealed in ^{18}O to promote lattice oxygen exchange, then adsorbed under NO and $^{16}O_2$. If $N^{18}O$ desorption can be stimulated by this method, then the lattice oxygen plays a major role.

NO_2 has a much more complicated desorption profile due to the extra oxygen present during adsorption, and as such, the possible mechanisms for adsorption and exchange are more extensive, as can be seen in Figure 5.2. Ionic and covalent complexes were observed to form on the surface, which necessitates a dissociative adsorption of NO_2 in order to form the (NO) complexes. The formation of these groups is described by Equations 5-15 and 5-16.

$$N^{16}O_2 \rightarrow (N^{16}O)^+ + \tfrac{1}{2}{}^{16}O_{2(surface)} + e^- \qquad [5\text{-}15]$$

$$N^{16}O_2 \rightarrow (N^{16}O) + \tfrac{1}{2}{}^{16}O_{2(surface)} \qquad [5\text{-}16]$$

Similarly to NO adsorption, the ionic and covalent groups are likely incapable of exchanging their extended oxygen with one from the surface. These steps are identical to Equation 5-3 and 5-4. NO_2 can also adsorb non-dissociatively on a metal site in order to form the nitro group, shown in Equation 5-17.

$$N^{16}O_2 \rightarrow (N^{16}O_2) \qquad [5\text{-}17]$$

The possible methods of exchange for nitro oxygen with surface oxygen are similar to that of the ionic and covalent NO groups, and can be seen in Equations 5-18 and 5-19.

$$(N^{16}O_2) + \tfrac{1}{2}\,{}^{18}O_{2(surface)} \rightarrow (N^{16}O^{18}O) + \tfrac{1}{2}\,{}^{16}O_{2(surface)} \quad [5\text{-}18]$$

$$(N^{16}O^{18}O) + \tfrac{1}{2}\,{}^{18}O_{2(surface)} \rightarrow (N^{18}O_2) + \tfrac{1}{2}\,{}^{16}O_{2(surface)} \quad [5\text{-}19]$$

Nitro group desorption accounts for part of the NO_2 effluent in the gas phase during desorption, and the mechanism can be seen in Equations 5-20 to 5-22.

$$(N^{16}O_2) \rightarrow N^{16}O_{2(g)} \quad [5\text{-}20]$$

$$(N^{16}O^{18}O^{18}) \rightarrow N^{16}O^{18}O_{(g)} \quad [5\text{-}21]$$

$$(N^{18}O_2) \rightarrow N^{18}O_{2(g)} \quad [5\text{-}22]$$

Nitrite formation for NO_2 adsorption does not require oxygen from the surface or lattice to form. By bonding one oxygen atom to a metal site NO_2 directly forms a nitrite ion, shown by Equation 5-23.

$$N^{16}O_2 + e^- \rightarrow (N^{16}O_2)^- \quad [5\text{-}23]$$

The nitrite ion can decompose to desorb NO, as shown in Equation 24, desorb in combination with another nitrite ion, shown in Equation 5-25, or simply reverse the formation reaction seen in Equation 5-23.

$$(N^{16}O_2)^- \rightarrow N^{16}O \; + \tfrac{1}{2}\,{}^{16}O_{2(surface)} + e^- \quad [5\text{-}24]$$

$$2(N^{16}O_2)^- \rightarrow N_2\,{}^{16}O + {}^{16}O_2 + 2e^- \quad [5\text{-}25]$$

The nitrite may also use an oxygen atom at the surface in order to form the nitrate ion, shown in Equations 5-26 and 5-27.

$$(N^{16}O_2)^- + \tfrac{1}{2}\,{}^{16}O_{2(surface)} \leftrightarrow (N^{16}O_3)^- \quad [5\text{-}26]$$

$$(N^{16}O^{18}O)^- + \tfrac{1}{2}\,{}^{16}O_{2(surface)} \leftrightarrow (N^{16}O_2\,{}^{18}O)^- \quad [5\text{-}27]$$

By reconfiguring according to Equation 5-27, then returning to the nitrite ion via Equation 5-28, the complex could then return to the nitrate configuration and pick up a second isotopically labeled oxygen, shown in Equation 5-29.

$$(N^{16}O_2\,{}^{18}O)^- \leftrightarrow (N^{16}O^{18}O)^- + \tfrac{1}{2}\,{}^{16}O_{2(surface)} \quad [5\text{-}28]$$

$$(N^{16}O^{18}O)^- + \tfrac{1}{2}\,{}^{18}O_{2(surface)} \leftrightarrow (N^{16}O^{18}O_2)^- \quad [5\text{-}29]$$

From this point, the nitrates can either revert to nitrite ions or decompose as seen in Equations 5-11 to 5-14. Since the nitrate-nitrite conversion can result in oxygen substitution, this may result in desorption of a $N^{16}O^{18}O$ molecule.

$$(N^{16}O_3)^- \rightarrow N^{16}O + {}^{16}O_{(gas)} + {}^{16}O_{lattice} + e^- \quad [5\text{-}11]$$

$$(N^{16}O_2\,{}^{18}O)^- \rightarrow N^{16}O + {}^{18}O_{(gas)} + {}^{16}O_{lattice} + e^- \quad [5\text{-}12]$$

$$(N^{16}O_2\,{}^{18}O)^- \rightarrow N^{18}O + {}^{16}O_{(gas)} + {}^{16}O_{lattice} + e^- \quad [5\text{-}13]$$

$$(N^{18}O_2\,{}^{16}O)^- \rightarrow N^{18}O + {}^{18}O_{(gas)} + {}^{16}O_{lattice} + e^- \quad [5\text{-}14]$$

NO_2 adsorption is somewhat more complex due to the extra oxygen that must be accounted for, but fortunately the desorption spectrum breaks down into three regions. The NO desorption from ionic and covalent complexes is noticeably absent in the spectrum. In that temperature range there is a small increase in m/z 44 signal, which corresponds to a desorption of N_2O. This is likely a low-temperature precursor to the larger peak later, with the N_2O formed by combination of weakly bonded ionic NO^+ on Cu sites. Since NO_2 must dissociate in order to form the NO ionic/covalent complexes, they are especially weakly bound, due to the excess oxygen.

5.2 Experimental

5.2.1 Powder Preparation

A new batch of La_2CuO_4 powder was prepared by the autoignition technique[221] similarly to the method detailed in Chapter 3. A stoichiometric mixture of $La(NO_3)_3 \cdot 6H_2O$ (Kanto Chemical Company, 99.99%) and $Cu(NO_3)_2 \cdot xH_2O$ (Alfa Aesar, 99.999%) was prepared in deionized water. After dissolving the metal nitrates, citric acid (Alfa Aesar, 99.5%) was added to the mixture until 0.25 mole percent was achieved, making this a fuel-lean solution. The solution was heated to ~60 ºC with constant stirring until the solution thickened. The gel was held near 70 ^oC for 7 hours, until the gel hardened from water loss. Following the drying step, the crusty gel was heated ~3 ^oC/minute until the precipitate autoignited due to heating. The powder generated by the autoignition process was calcined at 600 ºC for 10 hours.

Samples weighing nominally 12 milligrams were placed in the TPR/TPD reactor and cycled to 700 ^oC under 21% O_2 to clean the sample of atmospheric adsorbates and fully oxidize the sample. After cooling the sample, it was stored in a flowing helium atmosphere at room temperature.

5.2.2 Isotopically Labeled TPR/ TPD

The procedure of the temperature-programmed desorption (TPD) and reaction (TPR) experiments was described previously.[66,68,69,205] Samples of La_2CuO_4 containing nominally 12 mg of powder (BET area 10 m^2/g) were initially purged of atmospheric adsorbed species by cycling the sample to 700 ^oC and back to room temperature under an atmosphere of 1 % $^{16}O_2$.The process was repeated until spectra did not show any desorption peaks. Once clean, the sample was cooled under 1 % $^{16}O_2$ and then maintained under the helium atmosphere until further experiments were performed. Concentrations for the reactor were maintained by MKS

mass flow controllers (MFC) for all standard gases, and $^{18}O_2$ was controlled by a custom-built Alicat MFC.

For all mass spectrometry experiments, specific mass to charge ratios were examined: m/z = 14 (nitrogen species), m/z = 16 (oxygen species), m/z = 28 ($C^{16}O$ and N_2), m/z = 30 ($N^{16}O$ and $C^{18}O$), m/z = 32 ($N^{18}O$ and $^{16}O_2$), m/z = 34 ($^{16}O^{18}O$), m/z = 36 ($^{18}O_2$), m/z = 44 ($C^{16}O_2$ and $N_2{}^{16}O$), m/z = 46 ($N_2{}^{18}O$, $C^{18}O_2$ and $NO_2{}^{16}$) and m/z=48 ($N^{16}O^{18}O$). The ratios of m/z 14 and m/z 16 were monitored to distinguish between gases with the same m/z ratio, in particular m/z =32, corresponding to $N^{18}O$ and $^{16}O_2$. To distinguish between the two gases, a matrix approach was used. The characteristic signal strength ratio of m/z 14 and 16 was isolated and compared to the identifying m/z of a nitrogen or oxygen containing species, for each gas present in the gas stream. Using these ratios, the contribution of every identifiable species was subtracted from signal intensity at m/z 14 and 16, and so the remainder of m/z 14 and 16 after subtraction served as the contribution to the undetermined species. This process allowed the determination of each gas concentration, but had the undesired effect of injecting some noise into the measurement for $N^{18}O$, as that concentration was typically low.

For TPR experiments, the sample was exposed to 30 cubic centimeters per minute (ccm) of a reaction mixture at 30 ^{o}C, and held until gas flow and mass spectrometer signal remained steady. The sample was heated to 700 ^{o}C at 30 ^{o}C / minute, and the effluent spectra recorded to determine the extent of reaction and reaction products.

Experimental procedure for TPD was modified slightly to conserve isotopic oxygen. The sample was cooled to 30 ^{o}C from 300 ^{o}C at 10 ^{o}C / minute without a dwelling period at elevated temperature. At 30 ^{o}C, the sample was purged with 30 ccm helium until a stable baseline for mass analysis was achieved. The sample was heated to 700 ^{o}C at 30 ^{o}C /minute beneath 30 ccm

flowing helium atmosphere. During heating, the effluent gas was analyzed to determine the quantity and nature of desorbed products. Measurements were normalized to the initial surface area of the powder sample measured following calcination step. This surface area was assumed to change during heating cycles, but samples used for the experiments were too small to accurately determine the change through BET analysis. Table 5-1 shows the list of experiments.

TPR and TPD experiments were carried out on separate powder samples in order to preserve the sequence and maximize similarity between experiments. Primary experiments maintained an atmosphere of $N^{16}O_x$ and $^{16}O_2$. After the initial run, the sample pretreatment consisted of annealing in $^{16}O_2$ at 500 ^oC followed by cooling to room temperature. After this pretreatment, runs were performed in $N^{16}O_x$ and $^{18}O_2$. Subsequent pretreatments of the sample were performed in 1% $^{18}O_2$ in order to exchange lattice oxygen for isotopic oxygen to produce $La_2Cu^{18}O_4$ in lightly and heavily ^{18}O-enriched forms. The "lightly enriched" sample was prepared by annealing $La_2Cu^{16}O_4$ in 1% $^{18}O_2$ for 1 hour at 500 ^oC, and the "heavily enriched" sample by a further 2 hours under 1% $^{18}O_2$ for at 500 ^oC. The final runs in the sequence contained $N^{16}O_x$ and $^{18}O_2$ and $N^{16}O_x$ and $^{16}O_2$ in the gas phase, respectively. Additionally, a TPR of 1000 ppm $^{18}O_2$ was performed on a freshly prepared sample in order to examine the oxygen exchange behavior of pure $La_2Cu^{16}O_4$.

5.3 Results and Discussion

5.3.1 $^{18}O_2$ Temperature Programmed Reaction

A 12 milligram La_2CuO_4 sample was exposed to 1000 ppm of $^{18}O_2$ at room temperature and heated to examine the exchange behavior of oxygen on La_2CuO_4. The mass spectrum for this experiment can be seen in Figure 5-3. Near 400 ^oC, $^{18}O_2$ begins to exchange with $^{16}O_2$ from the La_2CuO_4 lattice. The concentration of $^{18}O_2$ in the gas phase begins to decrease and the concentration of $^{16}O_2$ increases correspondingly so that the overall oxygen concentration in the

gas phase remains essentially unchanged. Interestingly, the exchange is mostly between whole molecules. The consumed oxygen is $^{18}O_2$, and the emitted oxygen remains mostly as $^{16}O_2$ or $^{18}O_2$, with only ~40 ppm of $^{16}O^{18}O$ formed at 700 ^{o}C. This is a small amount compared to the 500 ppm of $^{16}O_2$ emitted at that temperature.

Since the potentiometric sensors operate at temperatures above 400 ^{o}C,[66,271] the experiment revealed that the La_2CuO_4 was capable of oxygen exchange for all temperature regions currently tested for the sensors. Further, due to the large exchange even in dilute oxygen, it can be assumed that at temperatures above 400 ^{o}C, gas-phase oxygen can be considered to integrate into the La_2CuO_4 lattice.

5.3.2 Determination of NO_x Adsorption via TPD/TPR

Since lattice oxygen begins to exchange at temperatures approaching 400 ^{o}C, TPD was performed by first adsorbing 1% NO and 1% $^{18}O_2$ from 300 ^{o}C down to room temperature over $La_2Cu^{16}O_4$. The subsequent desorption profiles of this experiment can be seen in Figure 5-4.

The desorption profile reveals no evidence of $N^{18}O$ throughout the temperature range, and only a very small amount of $^{16}O^{18}O$ on the high edge of the $^{16}O_2$ desorption peak from 400 to 500 ^{o}C, seen in Figure 5-4b. This range falls above the oxygen exchange threshold of the powder, and so it can be concluded that it is the reaction product of residual gas-phase $^{18}O_2$ exchanging with the $La_2Cu^{16}O_4$ lattice during the experiment, or simply a result of naturally occurring ^{18}O (~0.4%) during La_2CuO_4 synthesis. As such, it was shown that no ^{18}O was present in the surface complexes, and so no gas phase O_2 reacted with the adsorbed NO.

The desorption peaks observed in the first TPD (Figure 5-4a and 5-4b) are very large compared to subsequent runs. Some aging effects were expected in later tests, as observed below, however, the high capacity of the fresh sample provided the best opportunity to produce $N^{18}O$, and so this mass spectrum was displayed. An additional TPD run on a more aged sample

is shown in Figure 5-4c. The magnitude of gas adsorption and desorption decreases with age, most likely due to the coarsening of the grains. In addition, the aging resulted in an increase in O_2/NO desorption as well as a continued evolution of O_2 at high temperatures above 500 ^oC in Figure 2c, is most likely bulk evolution of O_2 from the lattice and contributed to greater O_2/NO ratios in subsequent TPD experiments.

When the oxygen sources are reversed (i.e. $^{16}O_2$ in the gas phase and highly enriched $La_2Cu^{18}O_4$ lattice), a much different situation emerges. For the TPD of 1% $N^{16}O$ / 1% $^{16}O_2$ over $La_2Cu^{18}O_4$, (Figure 5-5a) scrambled oxygen products were observed even below the bulk oxygen exchange temperature. Above the oxygen exchange threshold, $N^{18}O$ tracked a similar desorption to $N^{16}O$ until all NO was exhausted on the surface. It was previously shown that the bulk supplies oxygen for surface complexes, so ^{18}O was present in the complexes. To determine the effect of ^{18}O enrichment on the system, TPD of $N^{16}O$ and $^{18}O_2$ were performed on a partially substituted $La_2Cu^{18}O_4$ lattice. The TPD (Figure 5-5b) showed oxygen scrambling behavior intermediate to the previous two experiments. Concentrations of $^{16}O_2$ remained the highest, followed by scrambled $^{16}O^{18}O$ at concentrations near $N^{16}O$, and $^{18}O_2$ levels were the lowest. In this partially enriched lattice, $N^{18}O$ production occurred above 400 ^oC, similarly to the highly enriched $La_2Cu^{18}O_4$ case, but at a much lower level. Thus, ^{18}O in the bulk is a necessary but not sufficient factor for $N^{18}O$ production. In addition, energy must be provided to decompose surface complexes in a way to produce $N^{18}O$.

Deconvolution of NO TPD results

We subsequently used MATLAB code adapted from O'Haver[288] to perform Gaussian analysis and deconvolute the TPD spectra into individual desorption peaks. The deconvolutions can be seen in Figure 5-6. The identified peaks of $N^{18}O$ (Figure 5-6b) served as the initial

guesses for the peak positions, which line up well with the middle peaks in the NO desorption spectra. The $N^{18}O$ peaks are noisy due to the effects of matrix subtraction of mass spec signal. This effect is lessened when $N^{18}O$ levels are large, and does not impact peak placement since the program accounts for this during analysis.

Previous evaluation studies of desorption energies for NO_x without labeled oxygen could only generate approximate results due to the lack of anchor peaks in the TPD. Substituted NO_x products provided basis peak values for nonlinear Gaussian curve fitting, and these results allow quantitative analysis of the scrambling process as well as better peak separation for desorption regions. The products of $^{16}O_2$ (Figure 5-6c), $^{16}O^{18}O$ (Figure 5-6d), and $^{18}O_2$ (Figure 5-6e) were analyzed to determine first guesses for the larger desorption peaks. Using these first guesses, the program evaluated larger convoluted peaks and output curve data and peak temperature. Peaks were evaluated to minimize overall error. The program removed the high temperature scrambled oxygen data in the TPD spectrum since it levels off at high temperatures, and corresponds to lattice oxygen emission. As such, it was not included in the area calculations in the deconvolution tables.

The peak values and desorption energies for these regions can be seen in Table 5-2. Integration of the peaks compiles the total quantity of desorption product due to a particular complex environment formed on the powder surface, and these values can also be seen in Table 5-2.

The separated NO signal breaks into four separate peak groupings, identifiable as species found on the powder surface at room temperature.[286] These complexes were identified, in terms of increasing stability as: ionic and covalent NO, nitrite, and nitrate groups.[225,243,250,255,257,289,290] The peak at 315 ^{o}C corresponded to simple ionic and covalent complexes, as desorption of these

complexes was not accompanied by oxygen desorption of any type. As expected, there is not concurrent desorption of $N^{18}O$, since this region is far below the oxygen exchange threshold in the surface complexes. The $^{16}O_2$ peak at 383 ^{o}C also likely corresponds to loosely bound adsorbed oxygen from the gas phase, and its contribution is not included in the analysis of the desorption data.

The next, largest, NO desorption peak at 420 ^{o}C should correspond to the formation of nitrite groups, identified by the fairly large amount of NO release. The ratio of total O_2 to total NO is approximately 1:1. This region is accompanied by desorption of a large amount of all three oxygen species, with labeled oxygen species representing about 60% of total oxygen in the effluent stream, indicating that much of the oxygen is resulting from the bulk and the complexes in this region. When NO desorption is compared to isotopically labeled oxygen emission (which will almost exclusively result from complex desorption and bulk emission), the ratio of O_2 to NO rose to 1.5:1. This ratio of total O_2 to total NO is still too large for even nitrate formation, let alone nitrite, thus the data suggested that bulk oxygen emission was obscuring the representative ratio. Additionally, $N^{18}O$ desorption occurs following rearrangement of oxygen in the surface complexes, representing approximately 1/7 of total NO.

Eighty degrees higher at ~496 ^{o}C, the third NO desorption peak occurred. This desorption represents the mixed nitrates formed from conversion of nitrite groups, which ideally would show an O_2 to NO ratio of ~1:1. However, the labeled O_2 to NO ratio remains 2:1, which indicated a much larger amount of oxygen coming from the complexes, suggesting nitrate group decomposition due to the shift of the oxygen to favor labeled groups, as well as a substantial emission of bulk oxygen as gas. The groups interconvert from nitrite to nitrate at these temperatures, and this behavior can be observed by the substantial overlap between the two

peaks of $N^{16}O$ and $N^{18}O$, with $N^{18}O$ representing about 1/5 of total NO in this region. Again, desorption of oxygen species of each type is centered in this region, and is much larger than NO desorption, emphasizing the breakdown of nitrate complexes and bulk emission.

The highest temperature region for NO desorption at 582 ^{o}C represents the unidentate nitrate complex, and is almost exclusively $N^{16}O$. In this region, very little NO remains on the surface and lattice oxygen emissions are very low, evidenced by the extremely low ratio of O_2 to NO emission.

NO_2 TPD

Adsorption of $N^{16}O_2$ and $^{18}O_2$ over $La_2Cu^{16}O_4$ resulted in the desorption pattern seen in Figure 5-7a. The spectrum exhibits no evidence of $N^{18}O$ or $N^{16}O^{18}O$ throughout the entire temperature range. The spectrum exhibits matching peak placement to the $N^{16}O_2$ and $^{16}O_2$ TPD repeated for this study previously (Figure 5-7b). Previous studies showed NO_2 formed nitro, nitrite, and nitrate complexes on the powder surface.[286]

Deconvolution of NO_2 TPD results

Analysis of the NO_2 peaks in Figure 5b in comparison with XPS and IR results[286] separates the spectrum into nitro desorption, nitrite desorption, nitrite decomposition, and nitrate decomposition in order of ascending temperature. The peak corresponding to nitro desorption shows minor oxygen substitution in the corresponding temperature range centered at 339 ^{o}C. Above this range, in the region where nitrite desorption may produce $N^{16}O_2$ (Figure 6a), the scrambled product $N^{16}O^{18}O$ (Figure 6b) and its decomposition product $N^{18}O$ (Figure 6c) were observed to occur from 325-450 ^{o}C. This is reasonable due to the slightly greater thermal stability of the nitrite complex.

At higher temperatures than the peak assumed for nitrite desorption, the mechanism for NO_2 formation was assumed to be decomposition during the nitrite-nitrate conversion. $N^{16}O^{18}O$ emission decreased simultaneously with $N^{16}O_2$, replaced by increasing concentration of oxygen products $^{16}O_2$ (Figure 5-8d), $^{18}O_2$ (Figure 5-8e), and $^{16}O^{18}O$ (Figure 5-8f) with $N^{16}O$ (Figure 5-8g) and $N^{18}O$ resulting from nitrate decomposition. Total amounts of desorption from each species can be seen in Table 5-3.

The spectrum following $N^{16}O_2$ and $^{16}O_2$ adsorption over $La_2Cu^{18}O_4$ revealed a complicated desorption, seen in Figure 5-7c. The four zones described above are expressed as a series of five regions, described below.

The peak at 340-350 likely corresponding to nitro desorption shows no substitution in the corresponding temperature range of 275-375 ^oC, only a small amount of apparent NO desorption from ionic and covalent NO, with no oxygen emission occurring in this range. $N^{16}O_2$ and $N^{18}O^{16}$ desorbed in a 10:1 ratio, demonstrating oxygen exchange even at temperatures below the La_2CuO_4 oxygen exchange threshold. This region results from the dissolution of the relatively weak bond between a metal site on the powder surface to the nitrogen of NO_2.

Just above this region, peaks appeared at 362 and 382 ^oC, corresponding to $N^{16}O_2$ and $N^{18}O^{16}O$, respectively. These peaks result from nitrite desorption, where the adsorption of NO_2 as a nitrite complex reverses itself. Desorption in this region was 50% greater than for the nitro region (4.078 vs. 2.74 μmol), but the ratio of $N^{16}O_2$ to $N^{18}O^{16}O$ remained steady at 10:1. These complexes were more stable on the surface than the nitro complex, and this was reflected in the higher temperature emissions range from 325-450 ^oC.

The next region starts with a $N^{16}O_2$ desorption peak at 404 ^oC, accompanied by desorption of $^{16}O_2$ starting at 392 ^oC. This threshold likely corresponds to the beginning of

nitrate/nitrite transitioning, and oxygen from the original $N^{16}O_2$ loosed as a result. At 434 ^oC, $N^{16}O$ peaks, accounting for the oxygen released during the final $N^{16}O_2$ desorption, with the total NO and O_2 ratio established at about 4:1. This region also contains $^{16}O^{18}O$ and $^{18}O_2$ emission overlapped with the NO desorption section, which accounts for approximately 20% of total oxygen.

Above this temperature range, nitrate decomposition began to dominate, and this region was where the majority of $N^{18}O$ was seen. Just above 450 ^oC, $N^{18}O$ reaches its final peak, accompanied by oxygen products $^{16}O_2$, $^{18}O_2$ and $^{16}O^{18}O$ in larger quantities than in lower regions. $^{16}O_2$ dominated the release, representing ~7/10 of total oxygen in this region corresponding to complex decomposition, with the NO to O_2 ratio shifting to 1:2. This indicated that the majority of oxygen in the gas phase at this temperature comes as a result of complex decomposition, as $^{16}O_2$ can only result from the original oxygen adsorbed as $N^{16}O_2$.

$N^{16}O$ levels resulting from nitrate decomposition remained large, finally trailing off to zero ppm just below 650 ^oC. Oxygen levels from the decomposition of the complexes remain very small, though some constant lattice oxygen emission occurs as $^{16}O^{18}O$ and $^{18}O_2$. This contribution was removed in the deconvolution process, since it corresponds to oxygen enrichment from previous NO_2 decomposition on the surface of the powder.

Another partially substituted lattice of $La_2Cu^{18}O_4$ was supplied for $N^{16}O_2$ experiments. The TPD (Figure 5-7d) revealed identical peaks to the TPD over the highly enriched lattice, but as expected, substituted products due to exchange on the nitrogen complexes were significantly lessened by the relative unavailability of ^{18}O from the lattice. Additionally, scrambled oxygen complexes were reduced in gas-phase concentration.

NO TPR

The TPR of 700 ppm $N^{16}O$ and 600 ppm $^{16}O_2$ over heavily enriched $La_2Cu^{18}O_4$ displayed nearly immediate conversion of $N^{16}O$ to $N^{18}O$ even at temperatures lower than the oxygen exchange threshold of the lattice (Figure 5-9a). Above the threshold, $N^{18}O$ conversion continues to increase until ~50% conversion, stabilized near 550 ^oC. Oxygen exchange occurs freely, and scrambled $^{16}O^{18}O$ is the major oxygen product above 400 ^oC. $N^{18}O$ concentrations were determined by a total nitrogen balance ($N^{16}O/N^{18}O$) throughout the system referenced to a matrix of characteristic signal ratios from m/z 14, 16, 30, and 32 to determine levels of $^{16}O_2$ and $N^{18}O$. This balance accounted for each species in the spectrum, but generates noise in the data as a result.

TPR under 700 ppm $N^{16}O$ / 300 ppm $^{16}O_2$ over lightly enriched $La_2Cu^{18}O_4$, shown in Figure 5-9b, reveals a similar pattern of reaction as the $N^{16}O$ / $^{16}O_2$ TPR over highly enriched $La_2Cu^{18}O_4$, though $N^{18}O$ levels and conversion are significantly lower across the entire temperature range. The lesser degree of ^{18}O enrichment was shown by $^{16}O_2$ concentration dominating the total oxygen level at temperatures above the exchange threshold.

NO_2 TPR

The TPR for 700 ppm $N^{16}O_2$ and 250 ppm $^{18}O_2$ over $La_2Cu^{16}O_4$ showed no signs of oxygen exchange at temperatures below 400 ^oC, shown in Figure 5-10a. Decomposition of $N^{16}O_2$ was observed beginning near 300 ^oC, with corresponding rise of $^{16}O_2$ from the lattice and as a decomposition product. At higher temperatures, $N^{18}O$ was seen due to gas phase $^{18}O_2$ promotion into the lattice, in similar fashion to the $N^{16}O$ and $^{18}O_2$ TPR.

TPR of 700 ppm $N^{16}O_2$ and 700 ppm $^{16}O_2$ over heavily substituted $La_2Cu^{18}O_4$ produces a similar spectrum to the TPD, shown in Figure 5-10b. $N^{16}O^{18}O$ forms from 275-450 ^oC, tracking

desorption and decomposition of $N^{16}O_2$ as it disappears from the spectrum. $N^{18}O$ rose as $N^{16}O^{18}O$ began to decompose, and stabilized near 200 ppm above the oxygen exchange threshold of 400 ^{o}C. Scrambled $^{16}O^{18}O$ was observed to be a major oxygen product of the nitrate decomposition above the exchange threshold.

The TPR of 700 ppm $N^{16}O_2$ and 250 ppm $^{18}O_2$ (Figure 5-10c) was almost exactly the same as the highly enriched $La_2Cu^{18}O_4$ TPR of the same $N^{16}O_2$ concentration, in both peak placement and peak intensity. Only oxygen concentrations differ between the two TPR, which was most likely due to aging effects from the sequential testing of the fresh sample.

NO_x Adsorption Mechanism

From these experiments, the sequence of adsorption and exchange for NO on La_2CuO_4 can be determined. The framework established in a previous study provides an adequate starting point to explain the mechanism.[286] NO formed an initial bond with the La_2CuO_4 surface. If oriented on a metal site, ionic or covalently bonded NO results. If the ionic bond forms on a Cu site, the ionic complex may serve as a reaction intermediate for N_2O formation, but this mechanism is minor, only occurring during low temperature adsorption and so does not play a role in the sensing mechanism.

On the La site, the covalent/ionic complex reversibly desorbs at low temperatures and should not be observed at the operating temperature of the sensor (>400 ^{o}C). The covalent and ionic NO complexes are the least strongly bonded to the surface of La_2CuO_4, and the nature of the ionic bond generated by NO occurs due to its resonance in the N-O pseudo-triple bond.[287] As a result, oxygen exchange cannot occur without destroying the bond to the surface, and the mechanism proceeds according to Equations 1 and 2 at temperatures near 250 ^{o}C. The formation of these complexes is the likely reason for saturation of the sensor at low temperatures, and the

decomposition point for ionic and covalent species is likely the lowest possible operation temperature for the sensor itself.

$$N^{16}O_{(g)} \leftrightarrow (NO)^{+} + e^{-} \quad [1]$$

$$N^{16}O_{(g)} \leftrightarrow (NO) \quad [2]$$

For oxygen-down bonding to the metal site, the nitrosyl ionic complex forms. This complex has the possibility of desorption at low temperatures, due to the dominant bonding between N and O, but if sufficient tilt was induced to allow bonding to a lattice O, the chelated nitrite complex may form, and may relax to form the nitrite complex, seen in Figure 5-11.

From the spectra of NO_x adsorption on La_2CuO_4 powder, it was determined that the amount of heavy NO_x species was dependant on the level of oxygen substitution in the lattice. Even in the presence of $^{18}O_2$, $La_2Cu^{16}O_4$ lattice with only partial substitution of $^{18}O_2$ produced less $N^{18}O_x$ species than the fully substituted $La_2Cu^{18}O_4$ in the presence of gas phase $^{16}O_2$. This supports the conclusion that the reaction during adsorption occurs solely with bulk oxygen. This was important since the reaction due to nitrate/nitrite group decomposition is not mixed potential, since it is not a true electrocatalytic reaction. Thus, by proving the interaction of NO_x with oxygen is only with the bulk, it has been proven that the adsorption of gas onto the sensor, and the formation of complexes is the dominant potential generator for voltage establishment across the La_2CuO_4/Pt couple. Since oxygen integration to the lattice at high temperature is important to the mechanism, it is possible that the over-step of voltage generated by gas steps (when it occurs) is caused by the removal or addition of oxygen, and those contributions relax out as equilibrium is reestablished with oxygen in the gas phase. The ability of complexes to interconvert means that the adsorption signal will also be a function of the ratio of complexes formed on the surface at a given temperature.

In the TPDs, the bond between N and the original O dominates all complexes, and so in the nitrite configuration, it will relax to a configuration where the original oxygen extends away from the surface as the sample cools, according to Figure 5-12.

If NO bonds nitrogen down to an oxygen lattice site, the distinction becomes irrelevant, as the original O atom is already oriented upwards. In formation of the nitrate complex, the third oxygen in the complex was taken from the bulk, so all complexes forming on the pure $La_2Cu^{18}O_4$ surface contain at least one ^{18}O atom, and usually two. Since NO reacts with lattice oxygen during adsorption and desorption and not gas-phase O_2, this means that the complexes withdraw oxygen from the bulk to form positively charged oxygen vacancies, creating a voltage expressed across the sensor as a whole. However, even in the heavily enriched surface, the $N^{16}O$ still dominates the effluent stream, indicating that the original oxygen was retained when the nitrate or nitrite complex decomposed. In the TPD of $N^{16}O$ / $^{18}O_2$ over partially substituted $La_2Cu^{18}O_4$ and $N^{16}O$ / $^{16}O_2$ over $La_2Cu^{18}O_4$ a very small amount of $N^{18}O$ was seen in the nitrate decomposition region, which supports that conclusion.

Oxygen in the original NO molecule is bound via double bonds and this bond retains its character in the adsorption process during nitrite formation. Further, it retains enough of that character that during nitrate formation, it remains the retained oxygen when the complex decomposes. The only way to get around the character of the bond is to provide sufficient thermal energy to undergo the nitrite-nitrite conversion repeatedly to increase the probability for exchange of the primary oxygen. The stability of surface complexes is at most as stable as bulk oxygen, so even heating during adsorption (as in the TPR case) supplies sufficient thermal excitement to destabilize the bonding between the nitrogen and primary oxygen.

In the TPR, adsorption and nitrite complex formation were combined with additional energy since the sample was heated during NO adsorption. This destabilized the complex, allowing realignment of bulk oxygen into the primary position. This behavior was seen during TPR of the ^{18}O enriched lattices. In those experiments, peaks near 300 ^{o}C corresponding to nitrite complex decomposition were observed to produce $N^{18}O$, though this was not a product seen in the TPD. To form the nitrate, the nitrite complex must procure one more oxygen atom, and with energy from heating in addition to oxygen exchange into the bulk, allows destabilization and substitution.

This required destabilization was likely also why NO_2 does not result from NO adsorption- the amount of energy required to make the transition from NO to nitrate and nitrite destabilizes the complex too much for the NO_2 molecule to form, on this material. Additionally, the nitrate and nitrite are stable enough to retain at least one oxygen atom and prevent N_2 from being the product. From these results, a simplification of the possible NO adsorption mechanism shown earlier can be established. This simplification is shown in Figure 5-13.

For each of the six NO_2 TPR and TPD, there is no concurrent desorption of scrambled NO_2 or $N^{18}O$ in the nitro desorption range, so it can reasonably be concluded the exchange of oxygen in that complex does not occur. The second peak corresponding to NO_2 resulted in the high end of the nitrite desorption region, which indicated that the complex dissociated as it rearranged through the unstable bridged nitrate configuration, seen in Figure 5-14.

In the case of NO_2 adsorption, the majority of complexes formed result in the injection of negative charge into the electrode, since bonds to the surface occurs for this adsorption without simultaneous oxygen removal from the bulk to produce charge from oxygen vacancies. The remainders of the complexes (nitrate) require oxygen from the bulk to form, as in the NO case.

These nitrates cancel the voltage contribution of the nitrite formation, and so the total charge movement is determined by the relative amount of each complex. This accounts for the voltage generated across the sensor during NO_2 exposure.

This also occurs in TPD of $N^{16}O_2$ and $^{18}O_2$ over $La_2Cu^{18}O_4$ and $N^{16}O_2$ and $^{18}O_2$ over $La_2Cu^{18}O_4$ so it suggests the rearrangement is necessarily less energetic than in the NO case for nitrite/nitrate rearrangement, but operates similarly in all other respects. The analysis of the qualitative data allows for the simplification of the earlier reaction mechanism, and this can be seen in Figure 5-15.

5.4 Summary

Labeled oxygen studies were performed on La_2CuO_4 powder samples. The main techniques utilized were Temperature Programmed Reaction and Temperature Programmed Desorption experiments. The material was examined under multiple gas conditions of NO_x and $^{16}O_2/^{18}O_2$ atmospheres, as well as varied levels of ^{18}O enrichment in the lattice itself. Through these studies, it was determined that the formation of charged surface complexes occurs solely through the use of lattice oxygen. Gas-phase oxygen exchange with the La_2CuO_4 bulk occurs at temperatures above 400 ^oC. This substitution of the lattice allows gas phase oxygen to indirectly integrate into surface complexes, shown in TPR experiments. In TPD experiments, the concentration of scrambled O_2 and NO_x products was noted to increase with greater $^{18}O_2$ pretreatment. Substitution of ^{18}O for ^{16}O in surface NO_x complexes was postulated to occur due to the repeated transformation between the nitrite and nitrate complexes, as well as resonance between multiple nitrate configurations. Oxygen-18 retention from the gas phase occurred due to substitution in the surface complex combined with thermally induced vibration leading to the destabilization of the bond between nitrogen and the primary (original) oxygen in the complex. Since the surface complexes formed solely due to lattice oxygen, the Mixed Potential

electrochemical reaction does not occur as such on La_2CuO_4, and so that theory of sensor response does not adequately explain the mechanism of gas sensing. A more comprehensive model that includes the shift in Fermi level due to adsorption and charged complex formation can be found in Differential Electrode Equilibria.

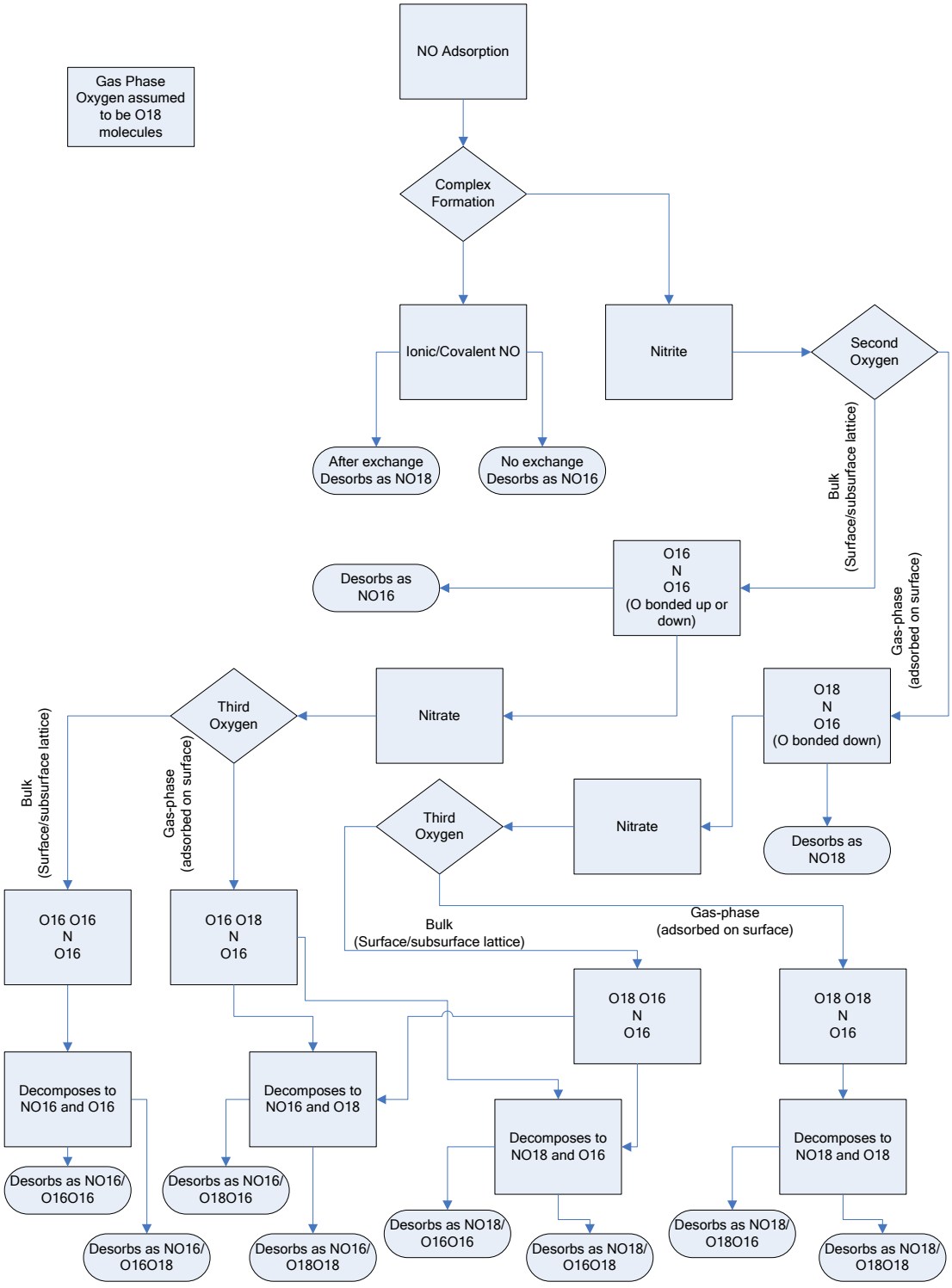

Figure 5.1 Flowchart of possible isotopic oxygen exchange mechanisms during NO adsorption on La_2CuO_4.

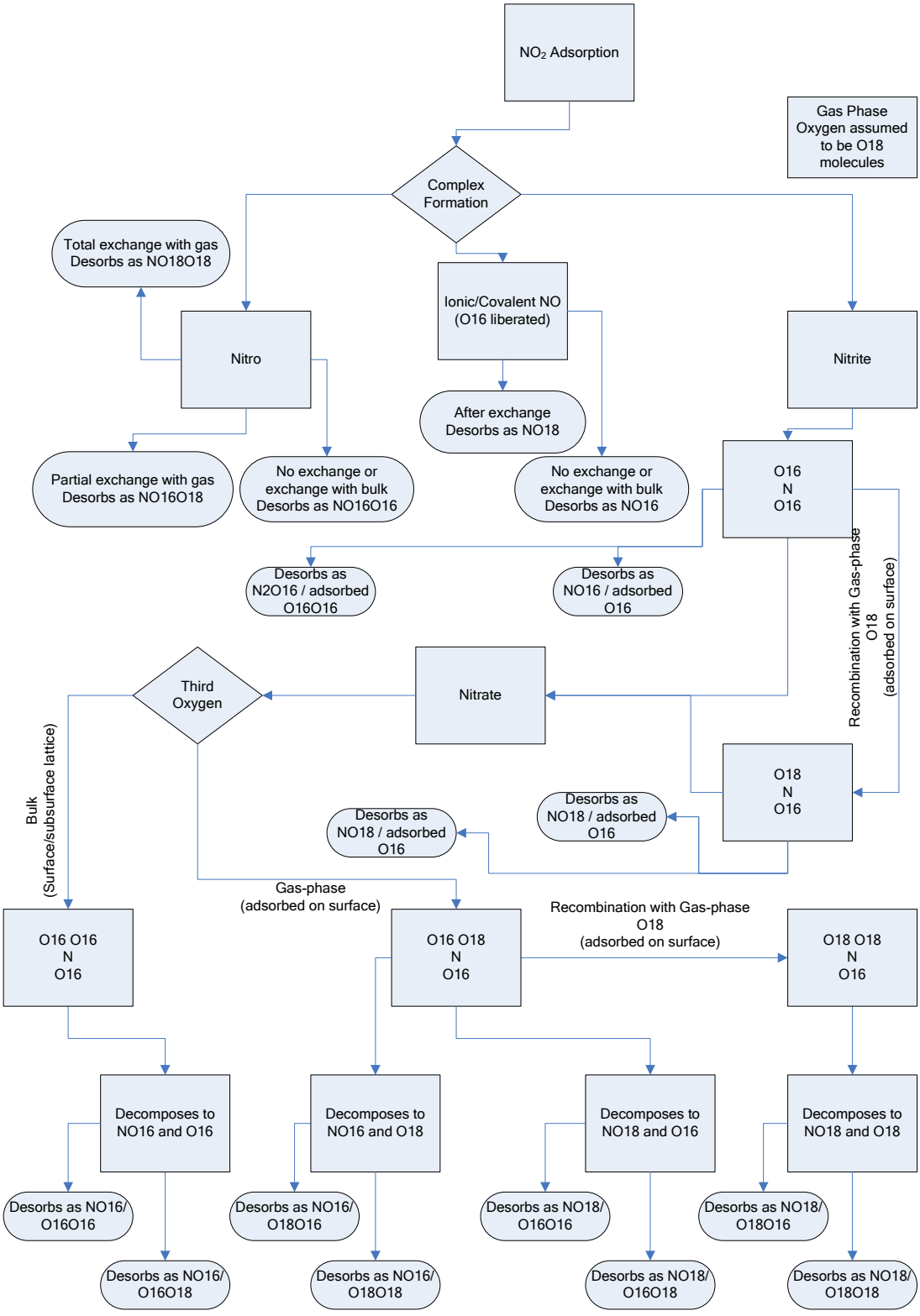

Figure 5.2 Flowchart of possible oxygen exchange mechanisms during NO_2 adsorption on La_2CuO_4.

Table 5-1. List of Experiments Performed

Gas Mixture (ppm)	Type	Initial Lattice Oxygen	Gas Mixture (ppm)
$^{18}O_2$ (1000)	TPR	$La_2Cu^{16}O_4$	$^{18}O_2$ (1000)
NO (10000) + $^{16}O_2$ (10000), NO_2 (10000) +$^{16}O_2$ (10000)	TPD	$La_2Cu^{16}O_4$ ^{18}O partially enriched ^{18}O fully enriched	NO (10000) + $^{16}O_2$ (10000), NO_2 (10000) +$^{16}O_2$ (10000)
NO(10000) +$^{18}O_2$ (10000), NO(10000) $_2$+$^{18}O_2$ (10000)	TPD	$La_2Cu^{16}O_4$ ^{18}O partially enriched ^{18}O fully enriched	NO(10000) +$^{18}O_2$ (10000), NO(10000) $_2$+$^{18}O_2$ (10000)
NO(700) +$^{16}O_2$(600), NO_2(700) +$^{16}O_2$(600)	TPR	$La_2Cu^{16}O_4$ ^{18}O partially enriched ^{18}O fully enriched	NO(700) +$^{16}O_2$(600), NO_2(700) +$^{16}O_2$(600)
NO(700) +$^{18}O_2$(600), NO_2(700) +$^{18}O_2$(600)	TPR	$La_2Cu^{16}O_4$ ^{18}O partially enriched ^{18}O fully enriched	NO(700) +$^{18}O_2$(600), NO_2(700) +$^{18}O_2$(600)

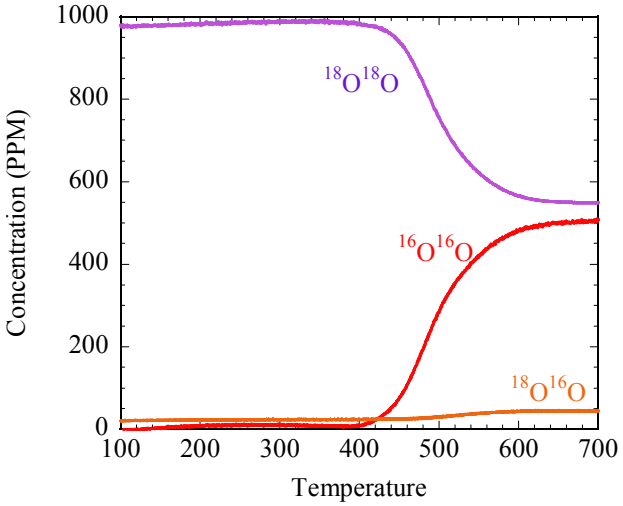

Figure 5-3. Temperature programmed reaction of 1000 ppm $^{18}O_2$ over $La_2Cu^{16}O_4$

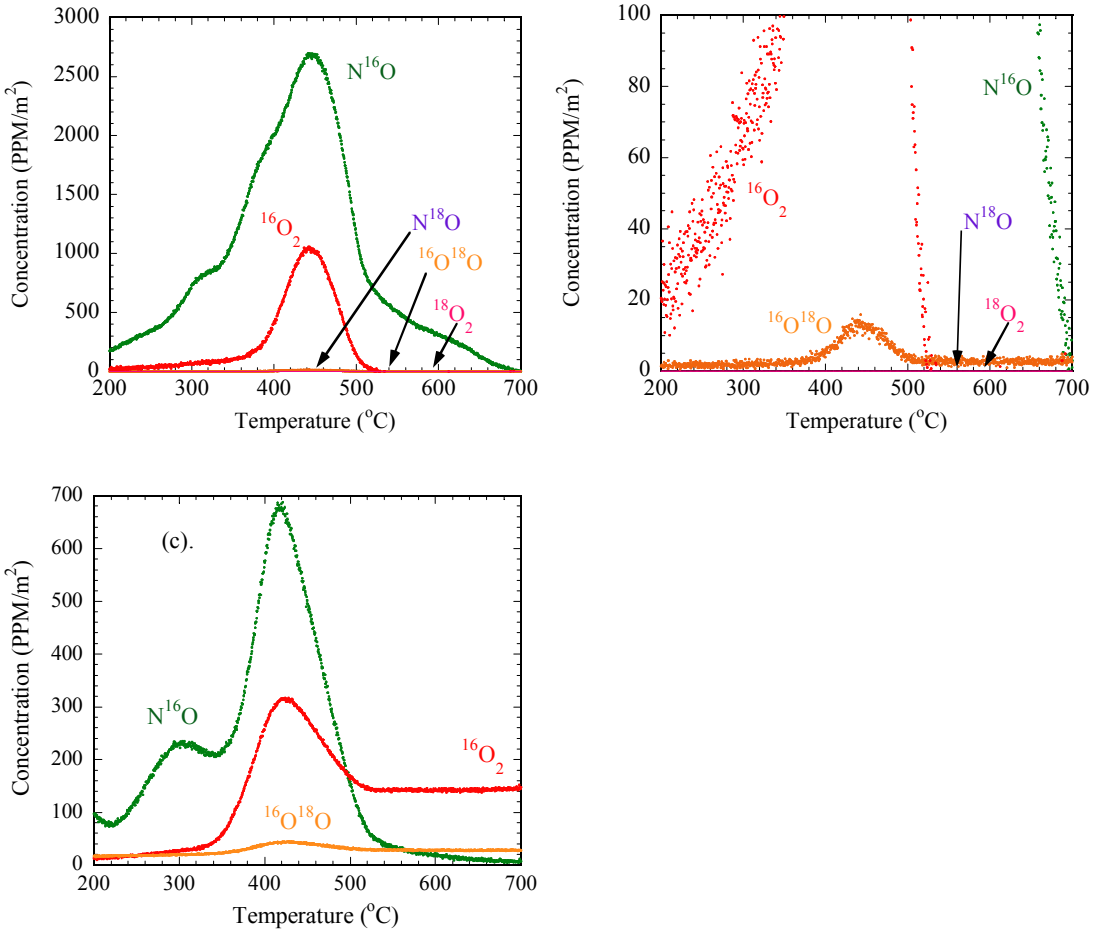

Figure 5-4 (a). 1% NO+ 1% $^{18}O_2$ TPD over $La_2Cu^{16}O_4$ Lattice, (b) Low Concentration Detail, (c).TPD of aged La_2CuO_4 sample

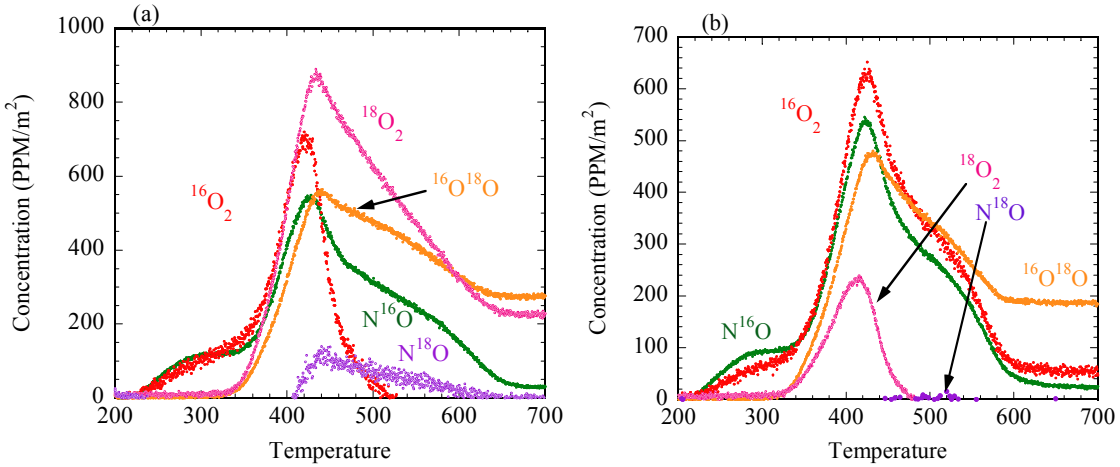

Figure 5-5. (a) 1% NO+ 1% $^{16}O_2$ TPD over heavily enriched $La_2Cu^{18}O_4$ Lattice; (b) 1% NO+ 1% $^{18}O_2$ TPD over lightly enriched $La_2Cu^{18}O_4$ Lattice

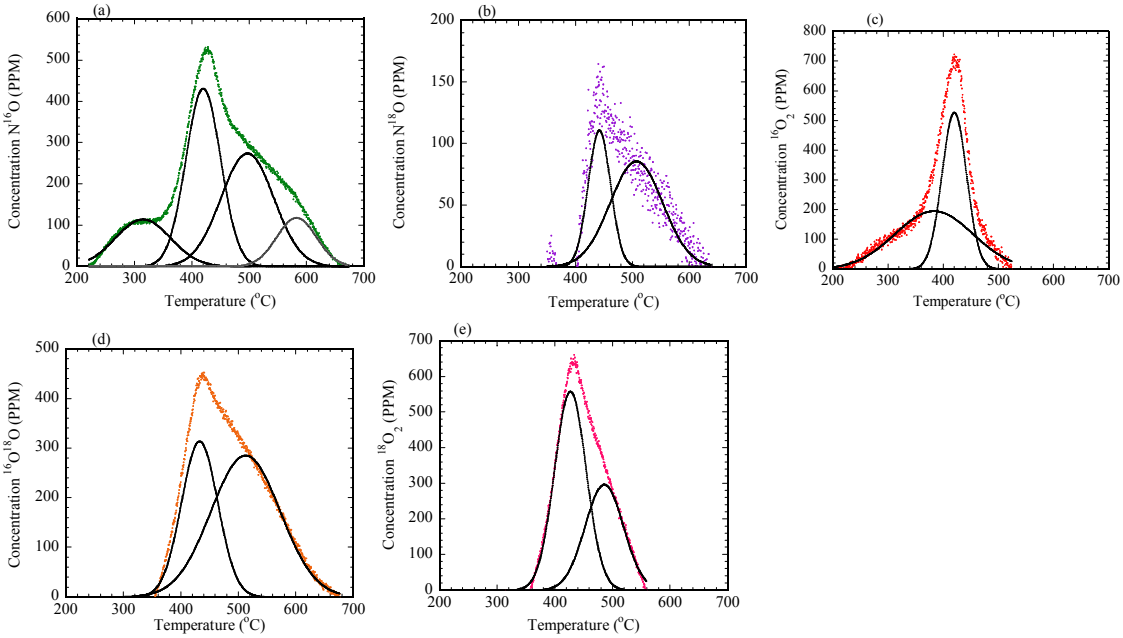

Figure 5-6. Gaussian Analysis of (a) Desorption Peak of $N^{16}O$; (b) Desorption Peak of $N^{18}O$; (c) Desorption Peak of $^{16}O_2$; (d) Desorption Peak of $^{16}O^{18}O$; (e) Desorption Peak of $^{18}O_2$

Table 5-2: Desorption Peaks for 1% NO/1% $^{16}O_2$ Adsorption on $La_2Cu^{18}O_4$

Species	Temperature (^oC)	Desorption Energy (kJ/mol)	Peak μmol/m^2 Adsorbed	Total μmol/m^2 Adsorbed	Peak Fit % Error
$N^{16}O$	315	543	0.626	4.12	1.15
	420	644	1.54		
	497	718	1.48		
	582	802	0.475		
$N^{18}O$	442	665	0.255	0.717	9.86
	507	728	0.462		
$^{16}O_2$	383	608	1.57	2.95	2.31
	420	644	1.38		
$^{16}O^{18}O$	433	656	1.17	3.18	2.87
	513	734	2.01		
$^{18}O_2$	427	651	1.14	2.94	2.31
	486	708	1.80		

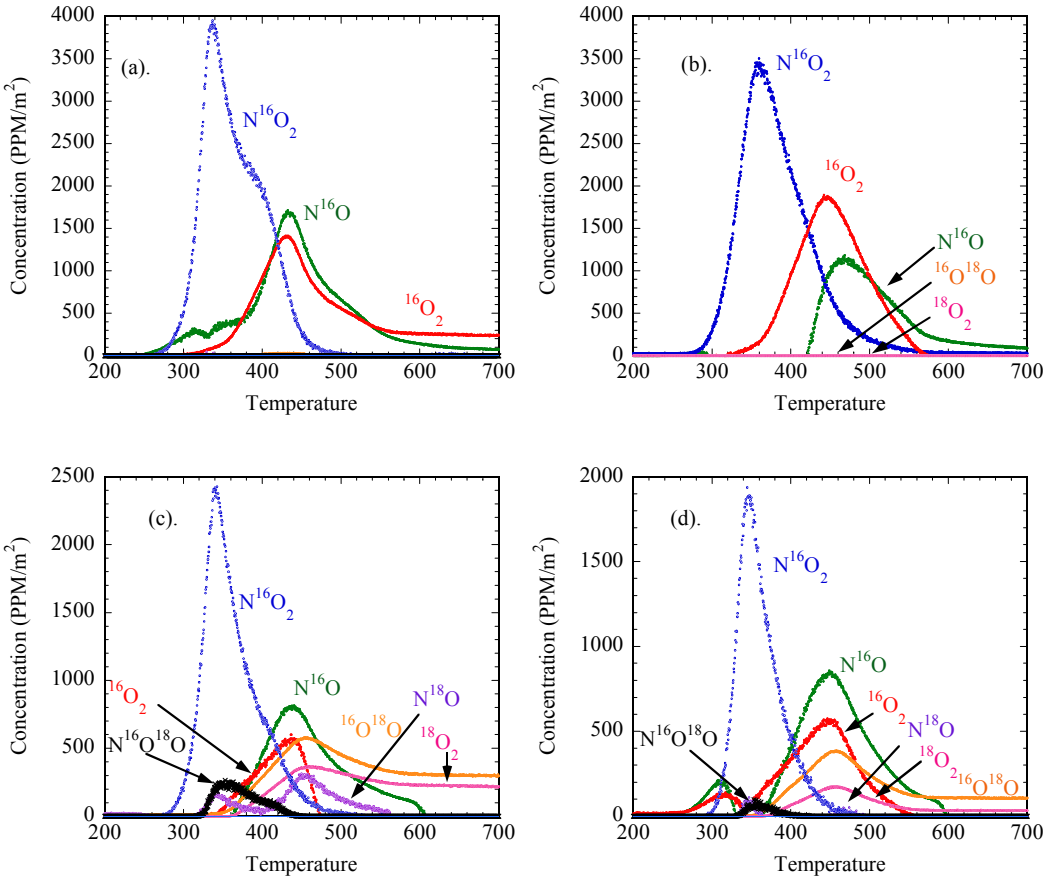

Figure 5-7. (a) 1% NO_2 + 1% $^{18}O_2$ TPD over $La_2Cu^{16}O_4$ Lattice; (b) 1% NO_2 + 1% $^{16}O_2$ TPD over $La_2Cu^{16}O_4$ Lattice; (c) 1% NO_2 + 1% $^{16}O_2$ TPD over heavily enriched $La_2Cu^{18}O_4$ Lattice; (d) 1% NO_2 + 1% TPD over lightly enriched $La_2Cu^{18}O_4$ Lattice.

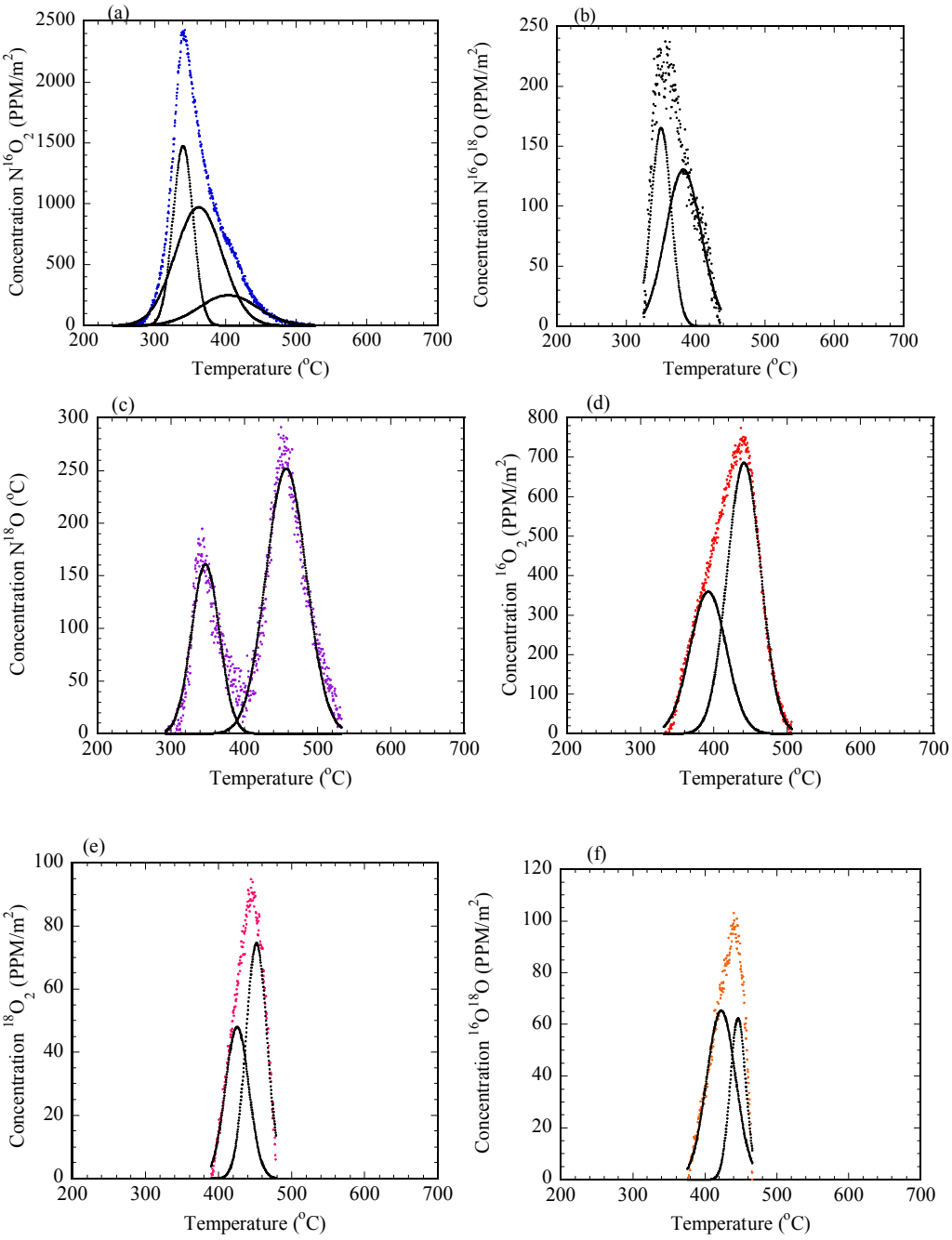
(a)
Concentration $N^{16}O_2$ (PPM/m^2)
Temperature (^{o}C)
(b)
Concentration $N^{16}O^{18}O$ (PPM/m^2)
Temperature (^{o}C)
(c)
Concentration $N^{18}O$ (^{o}C)
Temperature (^{o}C)
(d)
Concentration $^{16}O_2$ (PPM/m^2)
Temperature (^{o}C)
(e)
Concentration $^{18}O_2$ (PPM/m^2)
Temperature (^{o}C)
(f)
Concentration $^{16}O^{18}O$ (PPM/m^2)
Temperature (^{o}C)

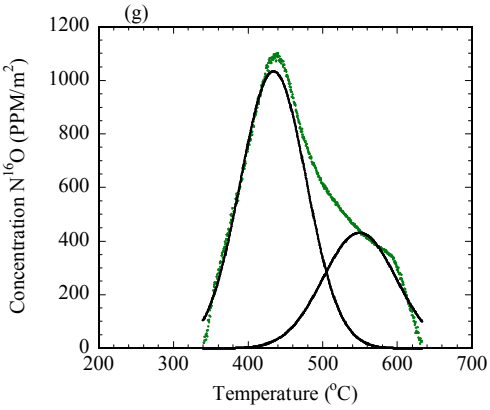

Figure 5-8. Gaussian Analysis of: (a) Desorption Peak of $N^{16}O_2$; (b) Desorption Peak of $N^{16}O^{18}O$; (c) Desorption Peak of $N^{18}O$; (d) Desorption Peak of $^{16}O_2$; (e) Desorption Peak of $^{18}O_2$; (f) Desorption Peak of $^{16}O^{18}O$; (g) Desorption Peak of $N^{16}O$

Table 5-3: Desorption Peaks for 1% $N^{16}O_2$ and 1% $^{16}O_2$ Adsorption on $La_2Cu^{18}O_4$

Species	Temperature (^oC)	Desorption Energy (kJ/mol)	Peak μmol/m^2 Adsorbed	Total μmol/m^2 Adsorbed	Peak Fit % Error
$N^{16}O$	434	658	5.28	7.66	2.77
	549	769	2.39		
$N^{18}O$	347	574	0.357	1.17	6.51
	457	680	0.812		
$N^{16}O_2$	340	567	2.47	7.48	1.27
	362	589	3.81		
	404	629	1.20		
$N^{16}O^{18}O$	350	577	0.268	0.650	6.81
	382	608	0.381		
$^{16}O_2$	392	617	1.04	2.88	2.18
	441	664	1.84		
$^{16}O^{18}O$	422	647	0.150	0.227	4.24
	446	669	0.0770		
$^{18}O_2$	425	649	0.0897	0.212	3.09
	452	675	0.122		

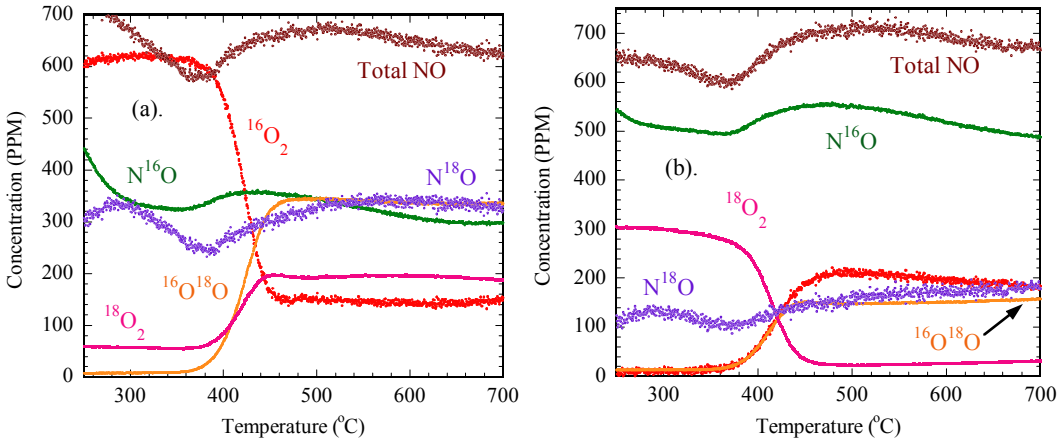

Figure 5-9. (a) 700 ppm $N^{16}O$+600 ppm $^{16}O_2$ TPR over heavily enriched $La_2Cu^{18}O_4$ Lattice; (b) 700 ppm NO+ 300 ppm $^{18}O_2$ TPR over lightly enriched $La_2Cu^{18}O_4$ Lattice.

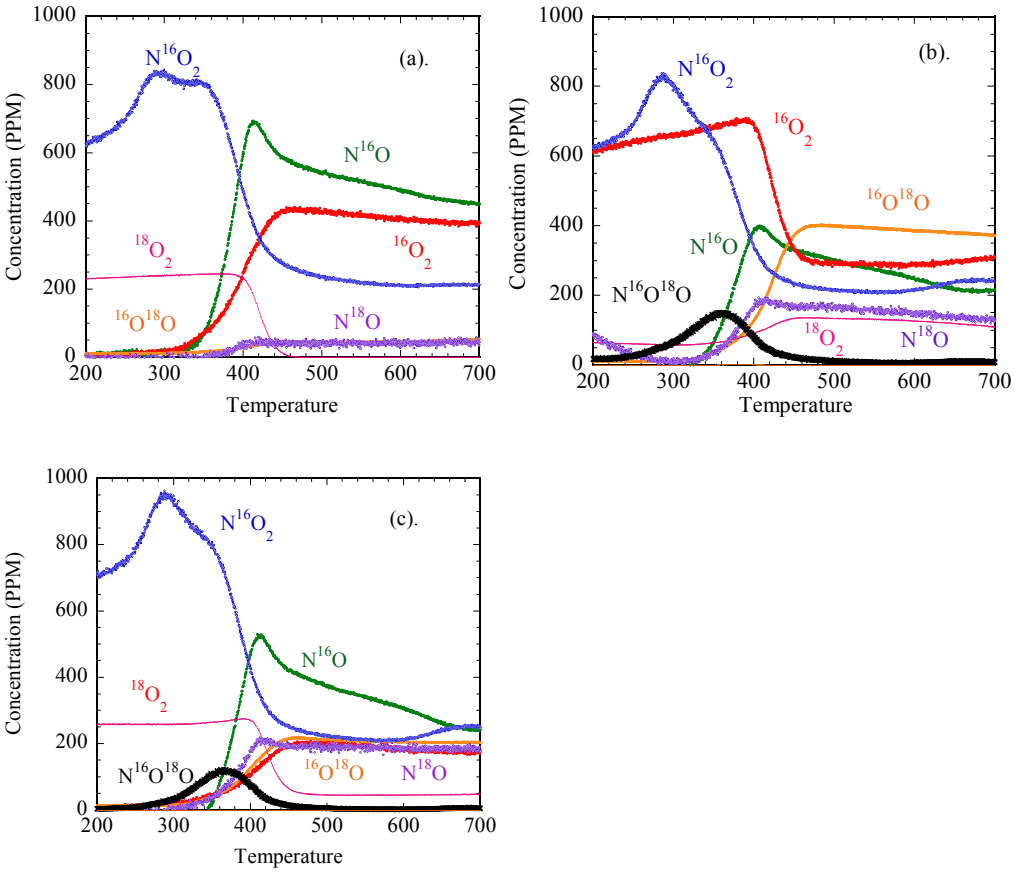

Figure 5-10. (a) 600 ppm NO_2 + 250 ppm $^{18}O_2$ TPR over $La_2Cu^{16}O_4$ Lattice; (b) 700 ppm NO_2+ 700 ppm $^{16}O_2$ TPR over $La_2Cu^{18}O_4$ Lattice; (c) 700 ppm NO_2 + 250 ppm $^{18}O_2$ TPR over heavily enriched $La_2Cu^{18}O_4$ Lattice

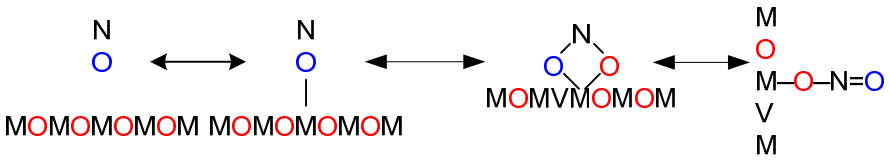

Figure 5-11. Formation of nitrito via nitrosyl ion/ chelated nitrite intermediate

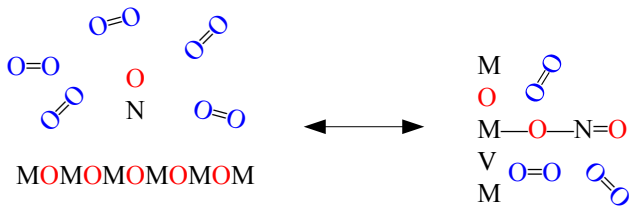

Figure 5-12. Nitrogen-down bonding to ^{16}O surface to form one-step nitrito charged complex.

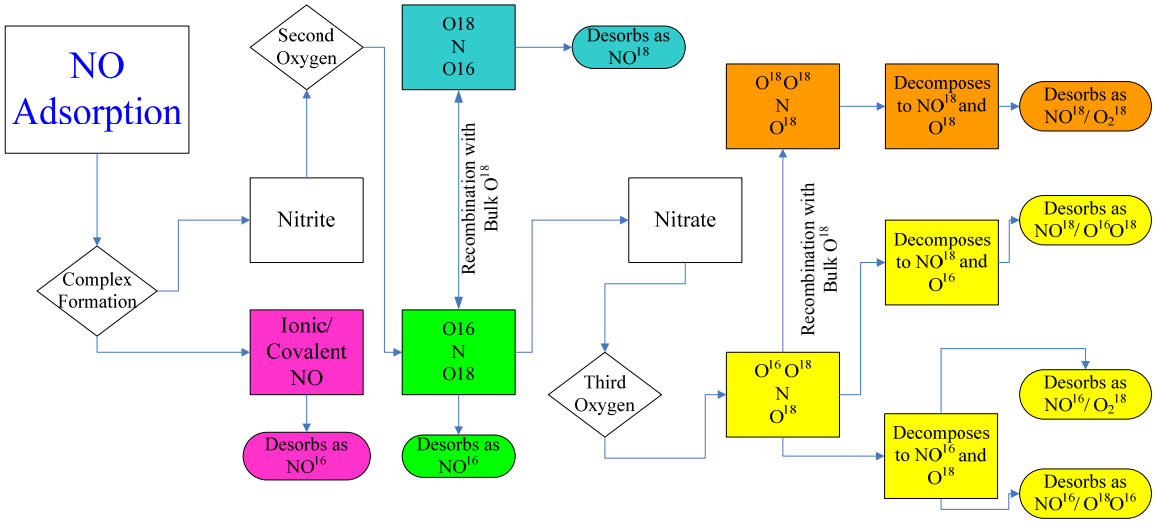

Figure 5-13. Simplified Mechanism for NO Adsorption on La_2CuO_4.

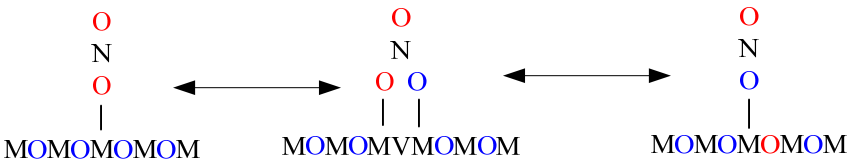

Figure 5-14. Reversible rearrangement of the nitrite to nitrate formed by NO_x adsorption.

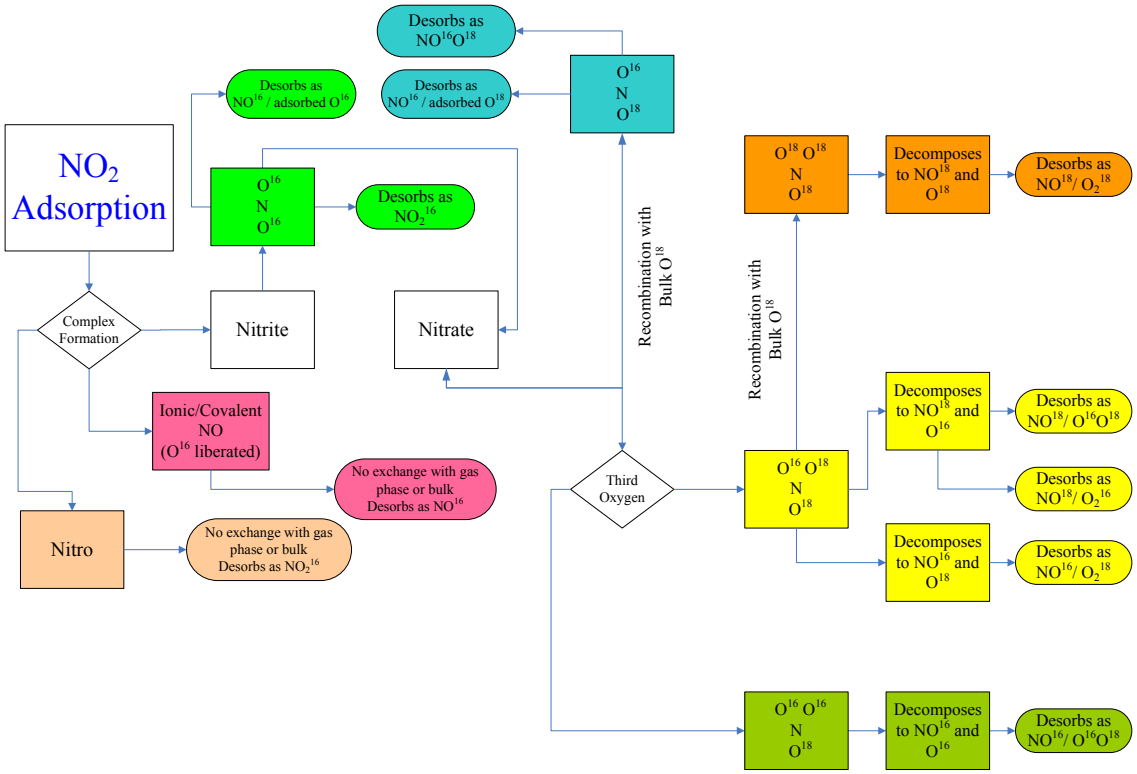

Figure 5-15.Simplified Mechanism for NO_2 Adsorption on La_2CuO_4.

CHAPTER 6
MASS SPECTROMETRY AND ELECTRICAL ANALYSIS OF A LA2CUO4/YSZ/PT FIELD MODIFIED DESORPTION SENSOR

6.1 Introduction

Temperature Programmed Desorption and Reaction (TPD/TPR) has been an effective method for examining the storage and reaction behavior of gases on the surface of a material.[72,215,234,291-295] The techniques are very useful in determining the processes and parameters of reaction for catalysis and sensing mechanisms of gas sensors. However, the requirements of heating to provide energy for desorption or reaction makes the technique inapplicable to *in situ* observation of potentiometric sensors at a constant temperature. One method of navigating this obstacle is to provide the energy for desorption in a different manner.

A separate method used for desorption of molecules from a substrate is termed Pulse Programmed Desorption (PPD), as this technique uses voltage pulses to provide the necessary energy for removing molecules from the surface. The PPD technique has its basis in high vacuum studies, where high voltage was used to ionize organic samples off of an emitter tip surface.[296] Its utility was extended to metal microelectrodes for the purpose of constructing functionalized proteins,[297] and also on gold electrodes to reverse the adsorption of thiols.[298] These techniques examined fundamental patterns of adsorption using direct mass spectrometry at low temperatures.

In sensor experiments utilizing a potentiometric gas sensor with heating elements, another member of the research group noticed large sensor responses to small applied heater voltages after a small crack formed in one of the heaters.[299] This crack formed an effective capacitor which produced an electric field that penetrated the sensing electrodes and caused a change in the response. This researcher then made a sensor with capacitors purposefully constructed on the opposite side of the YSZ from the sensing electrodes. The capacitors consisted of an alumina

layer with gold contacts, all deposited on top of the YSZ. Experiments from this sample verified that an electric field from the capacitors has an effect on the EMF formed at the sensing electrodes, and hence on the sensor response. Using these results and the field desorption concept as a basis, it was expected that the application of direct or externally generated electronic fields could be used to analyze and influence a potentiometric sensor during operation at elevated temperatures.

There exist important differences between these techniques applied to the vacuum condition versus ambient pressure. The energy supplied by the voltage pulse will be insufficient in the macro-scale to desorb gas complexes in the absence of another driving force. In the microscale, pure desorption requires electric fields of tenths of a volt per angstrom to supply the desorption energy,[300-302] which would be difficult to supply for sensors previously used. Fortunately, the application of an external field on the sensor couple for gas desorption has the effect of shifting the equilibrium of the sensor complexing reaction, which does not require as strong an electric field.[303] In the macroscale case, desorption energy will be provided by thermal energy, while the field only modifies the conditions for formation and decomposition of the charged complexes. This effect has been observed and modeled for the simpler case of charged colloid particles in liquid.[304,305] The formation of charged complexes on the surface of the sensing electrode of the La_2CuO_4/YSZ/Pt has previously been demonstrated to provide most of the asymmetric potential between the sensing and counter electrodes.[223] Therefore, polarization of the electrode field in a direction that assists the reversal of the formation reaction should allow a substantial fraction of the adsorbed gases to desorb, and change the sensor signal. Additionally, the effect of the voltage pulse on the response time of the sensor can be observed, possibly opening new methods of sensor operation at low temperatures. Conversely, the adsorption can be

assisted by maintaining an electric field that favors complex formation,[306] which can lead to greater sensitivity at low ppm concentrations and higher temperatures. In both cases, the field should lead to shifts in the bonding orbitals, changing the bonding behavior.[307] By modifying the system in this manner, the sensitivity of the sensor can be altered for multiple concentration ranges and temperatures. Modification of the sensor response and sensitivity using a perpendicularly applied magnetic field by this method has been previously observed in a resistive, MOSFET-type SnO_2 sensor.[308] We have also observed changes in the potentiometric sensor response due to both perpendicular and parallel electric fields.

Previous desorption studies in this La_2CuO_4 work utilized powder samples, where the surface area of the sample allows significant quantities of gases to adsorb. By desorbing these species, it was possible to begin constructing a mechanism in order to explain the individual contributions to the potential of a La_2CuO_4/YSZ/Pt potentiometric couple. One significant limitation of the mass spectrometry technique used thus far was the inability to observe the quantities adsorbed on the surface of the La_2CuO_4 electrode corresponding to the potential generated by NO_x gases. By examining the electrode while in operation, the amount of catalytic reaction due to the electrode can be quantified, and this provides useful data when examining the relative contribution of electrochemical reaction to the overall potential.

6.2 Reactor Construction

In order to conduct mass spectrometry experiments for field modified devices, it proved necessary to construct two additional reactor setups. The reactors were designed individually to provide maximum flexibility in experimental technique. To perform TPD device analysis, a variant of the original powder reactor tube was constructed using a longer section of 2 mm inner diameter tubing welded to a short section of 1 mm inner diameter tube. This configuration allowed for the insertion of a full device into the tube center for rapid heating, while maintaining

minimal dead volume downstream of the sample into the mass spectrometer. Samples loaded into the wide end, and were then connected to gold leads supported in a small alumina tube which remains in the upstream volume. The alumina tube cuts down the dead volume and serves to isolate the leads from each other. This array of leads extends to a pass-through at the Ultra-Torr seal to allow connection to a voltage source outside the reactor.

The reactor used for device testing at constant temperature was fabricated according to the following procedure. Two concentric alumina tubes were obtained from Ortech Ceramics. The outer tube was wound with resistive nichrome heating element and placed within a section of insulating pipe. The area between the ceramic and pipe was coated with a ceramic cement to stabilize the ceramic wool insulation. The inner pipe was machined to provide a gas channel through the length of the pipe, and a small window was ground from the tube side in order to provide a mounting point for sensor samples. A schematic of the reactor can be seen in Figure 6.1.[309]

6.3 Experimental

6.3.1 Sample Preparation

Two configurations of electrochemical cells were fabricated to test changes in desorptive properties and changes in potentiometric sensor behavior during exposure to varying strengths and directions of externally applied electric fields. To construct La_2CuO_4 electrodes for devices used in this chapter, a portion of the powder prepared for Chapter 5 experiments was pressed into a solid porous bar for the purpose of increasing surface area. Two grams of La_2CuO_4 powder was combined with graphite to produce a 97/3 La_2CuO_4/C ratio, mixed with a 5 milliliters of 10% polyvinyl buytral (PVB, Alfa Aesar, Ward Hill, MA) in ethanol and then uniaxially pressed at 2000 psi for 2 minutes. The bar was sintered for 10 hours at 800 ^oC for 10 hours. Electrode slices for each device were cut from the bar and ground to size using fine grit silicon carbide on a

polishing wheel. Alumina slices were prepared by combining 5 grams alumina powder (Alcoa) with 5 milliliters 10% PVB in ethanol, pressing isotatically to 2000 psi for 1 minute, and then sintering the resulting bar at 1250 ^{o}C for a half-hour. The bar was cut using a diamond wheel, and thin slices were polished down using a polishing wheel.

To study the electric-field effect on desorption, a La_2CuO_4- capacitor type sample was constructed with a 1.26 mm La_2CuO_4 section attached between two thin alumina slices using an alumina paste (ESL 450) as cement, followed by drying for 4 hours at 115^{o}C. After drying, Au paste (Engelhard, Newark, NJ) was applied to the outer areas of the alumina slices to form electrodes. The device was again dried for 1 hour. Following this drying step, Au wire leads were attached to the electrodes on the alumina and the entire device was sintered at 800^{o}C for 10 hours. A schematic of the device can be seen in Figure 6-2.

The external electric-field sensor was constructed in a similar configuration to sensors built by other members of the research group.[66,67,69,118,204,205,235] In this basic configuration, a sensing electrode and a pseudo-reference are aligned on opposite sides of a yttrium-stabilized zirconia (YSZ) substrate. The modified sensor device consisted of a rectangular ring of alumina paste applied to a 100 μm YSZ (Marketech) substrate dried at 115 ^{o}C for one hour, and then sintered at 1000 ^{o}C for 3 hours. Next, a gold contact layer was deposited onto the alumina and a gold lead was attached. After drying, a second alumina layer was applied over the gold layer, the sample was dried, and the device was sintered for 10 hours at 800 ^{o}C. A platinum air-reference electrode was applied to the YSZ inside the alumina ring using the paste described above, then dried. A La_2CuO_4 section was attached to the opposite side of the YSZ substrate by means of a La_2CuO_4 / poly-ethylene glycol (PEG 800) solution of ~15% solid load. A thin Pt wire was attached to the top of the electrode with the PEG based paste. Both the top face of the porous La_2CuO_4 electrode

and the Pt wire were capped with a thin alumina section. A gold contact was painted on the top of the alumina section, and dried for an additional hour. A gold lead was attached to the gold contact. The entire device was dried for one hour, and then sintered at 800 ^{o}C for 10 hours.

6.3.2 Testing Setup

For all experiments in the tubular alumina reactor, gas environment was provided by a bank of mass flow controllers (M100B, MKS, Wilmington, MA) used for sensor measurements. This system utilized a manifold of four gas cylinders: 1000 ppm NO (N_2 balance), 1000 ppm NO_2 (N_2 balance), 100% O_2. and 100% N_2, controlled by a LabVIEW program[310] to provide a total flow rate of 50 cubic centimeters per minute. Differences in electronic potential were measured with a Keithley 2000 digital multimeter outfitted with a scanning card in order to monitor sensor signal and applied field bias. Voltage for field testing was provided by a Hewlett-Packard 6681A DC power supply, interfaced with a separate LabVIEW program[311] or manually set to deliver a constant potential.

6.3.3 Electric-field Effect on Desorption

The La_2CuO_4 capacitor-type sample was exposed to 1% NO_x/1% O_2 gas mixtures at 300 ^{o}C, subsequently cooled at 5 ^{o}C/minute to 25 ^{o}C under gas atmosphere from the mass flow controller setup used for mass spectrometry measurements. The sample was then outgassed under pure helium for 8 hours to remove all residual NO_x species from the reactor chamber. Following outgassing, the helium flow rate was increased to 30 cubic centimeters per minute, and the sample was heated at 10 ^{o}C/minute to 600 ^{o}C. During heating, the effluent from the reactor was analyzed via mass spectrometry to determine the desorption points of the NO_x from the La_2CuO_4 surface. This experiment was performed at 0 V, 2 V, 5 V, and 8 V across the gold electrodes attached to the alumina sections.

6.3.4 Electric-Field Effect on Sensing Behavior

During testing of the external electric-field sensor, the potentiometric voltage signal between the La_2CuO_4 and platinum electrodes was measured for NO_x concentrations of 0, 50, 100, 200, 400, and 650 parts per million. These conditions were repeated for electric-field biases of 0 V, ±2 V, ±5 V, and ±8 V between the gold/alumina ring surrounding the platinum air-reference and the gold electrode atop the La_2CuO_4 sensing electrode. Flow rates were held at 50 ccm total flow. The effluent gases from the reactor during testing were analyzed by mass spectrometry.

6.4 Results and Discussion

6.4.1 Testing of La_2CuO_4 Capacitor-Type Sample

The effect of the electric field on the desorption profile of La_2CuO_4 was measured in a small dead-volume reactor tube. The initial desorption series performed on this La_2CuO_4 capacitor-type sample was 1% NO/1% $^{16}O_2$ for conditions of zero, 2, 5, and 8 V applied to the electrically isolated electrodes. The first desorption profile under zero volt bias shows an NO spectra similar to the powder samples in the previous chapters, but at lower temperatures. The sample exhibits easy desorption of NO from the surface, with 3 peaks in the region below 400 ^{o}C. The NO spectrum slowly tapers downward above these temperatures, as the pores begin to exhaust NO_x species from the pellet interior. Subsequent experiments increase the voltage across the sample, and the result of this change can be seen in Figure 6-3. As the electric-field voltage setpoint increased (polarity being irrelevant due to the device configuration), the desorption peaks for NO shifted to higher temperatures, while maintaining similar initial peak shape. The solid sample was also compared to earlier data on powder samples under similar experimental conditions (Figure 6-4). The peaks from desorption under the effect of an electric field more closely resemble the spectrum of slightly aged La_2CuO_4 powder than the virgin solid sample,

though the solid sample exhibited a more prominent nitrate decomposition peak. The peak temperatures in the solid sample were slightly higher than in the powder sample. In addition to the upward temperature shift of the peaks, the lingering desorption of NO at high temperatures was expressed as more defined peaks. These peaks sharply reduce to zero concentration as the system approaches 600 ^{o}C. This shift was accompanied by the appearance of substantial NO_2 desorption peaks at the same temperatures as NO desorption, shown in Figure 6.5.

The area underneath both the NO and NO_2 peaks increased due to the voltage step from 0 V to 2 V during desorption. The subsequent application of 5 V during the desorption cycle following NO adsorption resulted in a minor increase in peak temperatures, but was accompanied by a small decrease in the intensity of the low temperature NO peak at ~300 ^{o}C, a doubling of the peak sizes for NO_2 desorption and a decrease in the high-temperature NO peak roughly equivalent to the increase in NO_2 emission. The 8 V desorption field left peak placement for NO unchanged, but the high temperature NO peak returned to a larger area, and the NO_2 desorption peaks returned to the 2 V level, albeit with slightly higher peak temperatures. The desorption experiment was immediately repeated at 0 V to determine the residual effect of the field on the sample. The sample was observed to gain a small amount of area in the low temperature NO desorption region, and lose a substantial amount in the high temperature region. Peak placement for NO remained similar to the 8 V case, but NO_2 desorption levels rose to the rough midpoint between the 5 V and 8 V case. The quantity of gases desorbed from the sample can be found in Table 6.1. The behavior of the sample can most likely be explained as a result of two factors: polarization of the lattice and the electrostatic interaction of the complexes, and orientation of the NO molecules for adsorption.

Since La_2CuO_4 is paramagnetic at temperatures of interest[312,313] it shows some degree of susceptibility to polarization by electromagnetic fields[314], owing to the general polarizability of its perovskite layers.[315] As a result, during the desorption step, the orientation of electron orbitals interacting with the charged surface complexes may, in zones, allow the release of an oxygen from the surface to the nitrite complexes during decomposition. This mechanism was discussed in Chapters 4 and 5. The modification of bonding in these zones due to the orientation changes might allow for the separation of an NO_2 molecule during the nitrate/nitrite transition, which in the non-modified case decomposes without oxygen release. A second factor to consider is the simple electrostatic forces exerted on the ionic complexes as they sit on the surface.[316] Complexes remaining on the electrode surface at moderate to high temperatures in the non-modified case all possessed negative charge, and while the adsorbate layer was not entirely independent of the surface, a preferential orientation of electrons towards the surface of a complex would, by simple repulsion, tend to force the charged complex further from the surface, and make it more likely to desorb intact. The possibility of gas-phase orientation of NO_x may also play a role, as the adsorption bonding direction can play a role in the statistical complex formation due to the different formation mechanisms. As polar molecules, both NO and NO_2 would show some degree of rotational shift in the field generated from the electrodes on the insulating alumina layer.

Identical experiments were subsequently performed on the sample, substituting 1% NO_2 for 1% NO in the adsorption step. These spectra can be seen in Figures 6-6 and 6-7. The desorption spectra obtained from 0 V approximates the results from powder samples, though the amount of NO desorbed at the higher temperature peak is larger compared to the NO_2 desorption peak for the solid sample experiment. Increase in field voltage from 0 to 2 V caused a 300 ppm

drop in NO_2 peak desorption at 325 ^oC, but the peak at 425 ^oC was roughly equivalent to the 0 V desorption. NO concentration at the low temperature peak was slightly reduced from the 0 V sample, but again remains roughly constant over the higher temperature region. Desorption amounts can be seen in Table 6-2.

Stepping the voltage to 5 V results in an increase of NO and NO_2 at the low temperature peak, and a decrease for both gases at the high temperature peak against the 2 V case. This experiment produced the least amount of NO desorption of all the NO_2 adsorption experiments. At 8 volts, the NO_2 signal dips below the concentration at 2 V for the lower peak, and the 5 V level for the high peak. Overall, this experiment generated the lowest level of NO_2 emission. NO emission at the low temperature peak is slightly above the 2 V case, and slightly above the 5 V case at the high temperature peak.

In both the NO and NO_2 adsorption cases, the desorption at a 5 V electric bias setpoint produced a higher relative amount of NO_2 versus the other bias conditions. In the NO adsorptive case, the difference is substantial, exhibiting a much lower NO desorption than any of the other experiments, and emitting the most NO_2 of any experiment under those adsorption conditions. This same effect of higher NO_2/lower NO emission was observed in the NO_2 adsorption case. This suggests that the bias region corresponding to this field strength must be examined in more detail during future testing. Unfortunately, space constraints on these initial samples forced the construction of a field generating device that does not lend itself to a simple modeling of the field strength. Though the area of the gold electrodes was sufficiently large to allow for coverage of the La_2CuO_4 layer, the ratio between the areas of the gold electrodes to the square of the distance between the electrodes was only ~2. This situation does not well resemble the archetypal case of two infinite parallel plates,[317] and as a result, Laplace's equation

$$\frac{d^2V}{dx^2}+\frac{d^2V}{dy^2}+\frac{d^2V}{dz^2}=0$$

cannot reduce to the simplification of change only in the z direction (i.e. fringing of the electric field occurs near the edges). However, the concentrations of gas desorbed during the experiment were sufficient to allow for a ten-fold reduction in volume of the La_2CuO_4 pellet, in future designs. This change would allow for a different configuration of the device and result in a much better (solvable) approximation of an ideal multiple dielectric condenser.[318] Fringing and non-ideal fields have advantages in certain applications, but by reduction to a better approximation of ideality allows for easier modeling when the device voltage is stepped.

6.4.2 Testing of External Electric-Field Sensor

The sensor was evaluated for multiple NO_x concentrations in 3% O_2 under a bias of 0, 2, 5, and 8 V in the positive (high potential on La_2CuO_4 side) and backward (high potential on Pt side) directions. These experiments were performed at temperatures of 450, 500, and 550 ^oC and repeated twice. The sensors under bias voltage were compared to the unbiased sample for each temperature. The unbiased case was evaluated first to avoid the effects of polarization seen in the La_2CuO_4 capacitor-type sample described above. In similar fashion to previous studies,[223] the unbiased La_2CuO_4 electrode behaves with positive response to NO_2 gas and negative response to NO when compared to Pt maintained under a reference atmosphere at 550 ^oC, but exhibits reversed response at 500 and 450 ^oC. The field-assisted desorption studies shown above demonstrated that an indirectly applied electric field can affect the behavior of NO_x on the surface of La_2CuO_4 even at relatively small field strengths. As such, this indicates that the response of a sensor under field bias has at least three components. The first component is the EMF generated from the Nernstian response, as the counter-electrode in this case is a true air-reference electrode (Equation 6-1).

$$\Delta V = \frac{RT}{4F} \ln \frac{[P_{O_2}(Unknown)]}{[P_{O_2}(Reference)]} \quad [6\text{-}1]$$

Since this contribution comes out to be a result of the constant difference between the test chamber and the outside atmosphere, it will remain constant at a given temperature and electric-field bias voltage setpoint. The second effect acting on the system is the voltage induced via polarization due to the presence of the field. This will vary depending on the voltage applied to the outer electrodes, but will be constant for each condition, and the deviation from 0V baseline for each case was observed by comparison of the baselines at 0ppm NO_x. The third effect comes from the influence of the field on the bonding of NO_x to the surface of La_2CuO_4 and its influence on the formation of the nitrite and nitrate complexes that produce the potential seen by the voltmeter. The effects of these changes were expressed by the differences as the slope of the signal/concentration curves.

The comparison of the sensitivity of the device to NO atmospheres can be seen in Figure 6-8, and r^2 values for logarithmic curve fitting are shown in Figure 6-9.[299] At 550 ^oC the signal showed sensitivity of ~0.25 mV/decade for 0 V bias, but even this limited sensitivity was reduced further by the application of field in both directions. Field application appeared to induce instability in the sensor signal, evidenced by the large drop in r^2. Recorded data from the voltage source indicated that the actual voltage across the outer electrodes did not remain constant, which could be responsible for noise in the inner electrode couple.[299] At 550 ^oC, the signal even in the unbiased case was small, and further decreases in the sensitivity due to the electric field made the signal to noise ratio sufficiently small to cause a poor logarithmic fit to data. Data fitting was too poor to draw any significant conclusions from the trends shown by the sample at this temperature, other than that the response to increasing NO concentration was a small negative voltage.

Previous sensor series showed an increased sensitivity as temperature was decreased, and this effect was also observed on this sample. At 500 ^{o}C, the sensor was observed to respond positively to increasing NO concentration. This response was found to increase in sensitivity under applied-field conditions, increasing with bias voltage. Bias in the backwards direction displayed greater NO sensitivity than in the forward bias. At 8 volt backwards bias, the sample jumped from a positive sensitivity of 1 mV/decade ppm to 24 mV/decade ppm.

At 450 ^{o}C, sensitivity also increased with increasing electric-field strength. The effect of the field was more pronounced, displaying an increase from 3.2 mV/decade at 0 V to 5.2 mV/decade at 2 V forward bias. This sensitivity increased slightly when biased in the backwards direction. Forward bias from 5 V showed very little difference from the 2 V backwards case, but when bias was reversed in the 5 V case, sensitivity stepped from ~5.6 mV/decade to 40 mV/decade. Increasing bias to 8 V forward decreased sensitivity to 4.8 mV/ decade, and reversing polarity at 8 V rebounded the signal to 28 mV/decade.

The sensor response of La_2CuO_4 was shown previously to exhibit greater sensitivity to NO_2 relative to NO, even at 550 ^{o}C. This had the effect of improving the signal to noise ratio of sensing behavior, allowing for meaningful analysis of the data.[299] Sensitivity plots for NO_2 can be seen in Figure 6-10 and plots of r^2 in Figure 6-11.[299] The non-modified case for La_2CuO_4 against platinum reference produced 0.55 mV/decade ppm at 550 ^{o}C, and this was increased slightly to 0.65 mV/decade at 2V forward bias. Reversing bias at 2V resulted in sensitivity of 0.9 mV/decade for NO_2. A maximum sensitivity was reached at 5V forward bias of ~1 mV/decade, and this was only slightly reduced in the case of 8V forward bias. Reverse bias at both 5 and 8 V caused marked decreases of sensitivity, to 0.65 and 0.8 mV/decade, respectively. The data displayed good logarithmic fit, with r^2 values of ~0.9 for every testing condition.

At 500 ^{o}C, sensitivity of the sample in the unbiased case was ~0.9 mV/decade. Forward bias at 2, 5, and 8 V increased this value to 1.2 mV/decade with logarithmic fitting, comparable to the unbiased case. Reverse bias at 2 V lowered sensitivity to 0.8 mV/decade, raised to ~1.2 mV/decade for 5 V, and to 1.4 mV/decade at 8 V. As the electric-field strength increased, the r^2 value of the fit decreased, but remained comparable to the cases at 550 ^{o}C (~0.9) except for the case with 8 V backward.

The most promising results of the study came for the NO_2 case at 450 ^{o}C. Initial sensitivity of 2 mV/decade for the unbiased case was found to increase to about 3 mV/decade for both the forward and reverse case for 2 V bias. At 5 V forward bias, that increased to 4 mV/decade, but upon testing at 5 V backwards bias, the sensitivity was found to reverse direction and increase in magnitude to -24 mV/decade. At 8 V forward bias, the maximum sensitivity of -29 mV/decade was achieved. Reverse bias of 8 V reduced this value to -18 mV/decade. All data fitting of the bias conditions at 450 ^{o}C were as good as or better than the unbiased case with r^2 of 0.8.

The effluent gases from the reactor were sampled for analysis by an Extrel 5220 Mass Spectrometer. The effluent profiles for the 450 ^{o}C case are displayed in Figures 6-12 to 6-15, staggered slightly in order to separate the spectra. To mimic the sensor testing setup as closely as possible, the sensor test gas manifold was used to provide atmosphere for the reactor chamber. Since those gases contain nitrogen as a balance gas, the identifier m/z ratios of 14 and 28 were unavailable to determine conversion of NO_2 to NO or the reverse. As a result, the only definitive conclusions can be drawn using the major m/z ratio for the gas being tested. For forward bias conditions, a weak field generated by the 2 V bias showed no conversion of NO$\rightarrow$$NO_2$ in the NO test case, but did decrease the conversion of $NO_2\rightarrow$NO in the NO_2 testing case. Higher forward biases decrease the concentration of NO below 0 V baseline levels during NO testing, indicating

some conversion is taking place. For NO_2 testing, the levels of NO_2 decrease further below baseline with increasing bias strength. In the reverse bias case, NO testing shows a trend of decreasing NO concentration with increasing field strength, with the 5 V case showing an outlier of baseline NO concentration. This outlier result was also seen in the field desorption study at 5 V, suggesting that the electric-field strength at that voltage may be near a critical point. In the NO_2 test case, increasing field strength lowers the concentration of NO_2 in the gas phase, indicating greater conversion of $NO_2 \rightarrow NO$.

6.5 Summary

Temperature programmed desorption experiments were performed on a La_2CuO_4 pellet. Initial bias and aging effects of the sample were shown to increase the desorption temperature of NO from the virgin case to subsequent runs. Increases in field strength were shown to change the desorption profile of NO and NO_2 gases from the surface of the La_2CuO_4 pellet. A sensor utilizing a La_2CuO_4 pellet with similar field generating structures was also constructed. The sensor displayed changes in sensitivity to NO_x gases with changes in field voltage and bias. This effect was the most pronounced at the lowest temperature in the study, 450 ^oC.

Analysis of the data in this study provided a few factors to guide further experiments in the work. Firstly, the improvement on the sensitivity comes mainly at low temperatures for the low field strengths. To more fully evaluate the effect of fields at high temperatures, a voltage source capable of producing voltages up to kV levels will be needed. The second improvement for further experiments is in the design of the device itself. As noted above, neither the field desorption device, nor the sensor device, approximated the ideal case of a parallel plate capacitor. Desorption experiments demonstrated that the electrode pellets used for both studies were large enough to be significantly reduced in volume while maintaining sufficient surface area for further desorption experiments. As a result, a better fabrication process that produces a

larger area/ electrode distance ration will produce a satisfactory sample. In this way, a field can be established to apply equally throughout the La_2CuO_4 electrode.

Figure 6.1 Tubular reactor for sensor reference studies

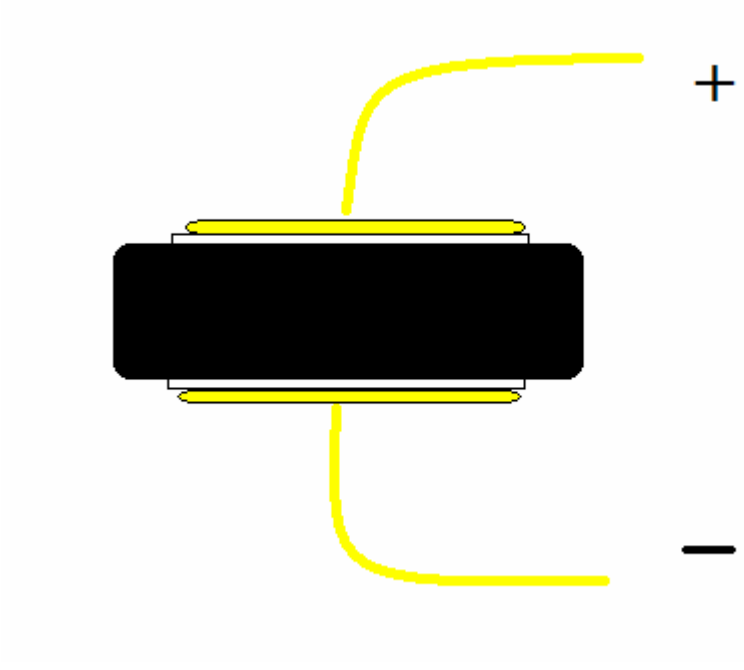

Figure 6.2 La_2CuO_4 capacitor device for determining E-field effects on desorption

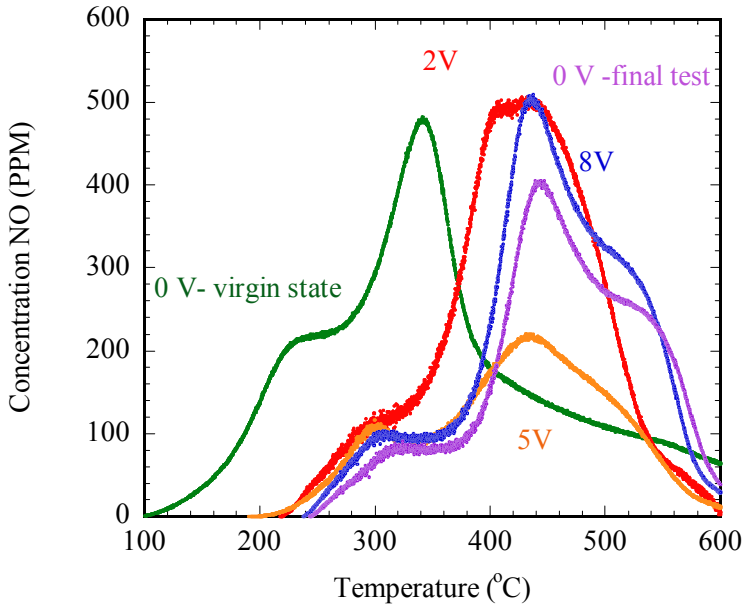

Figure 6.3 NO desorption from the La_2CuO_4 capacitor following NO adsorption

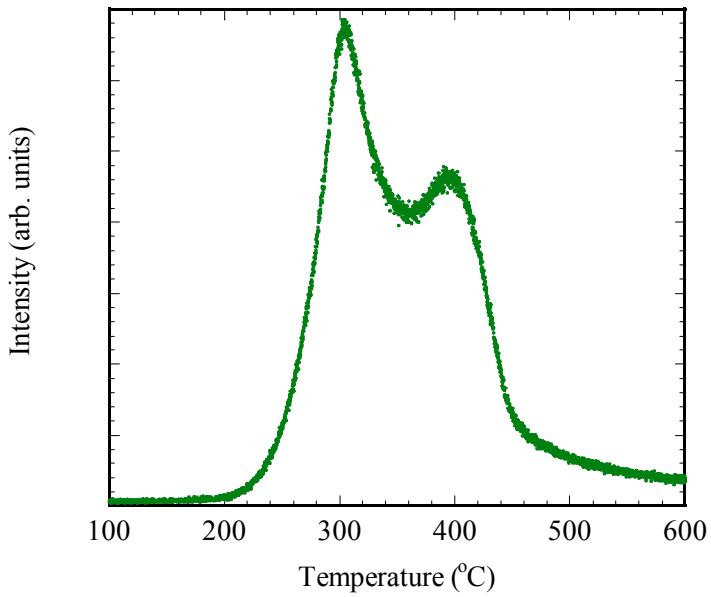

Figure 6.4 NO desorption from La_2CuO_4 powder following NO adsorption

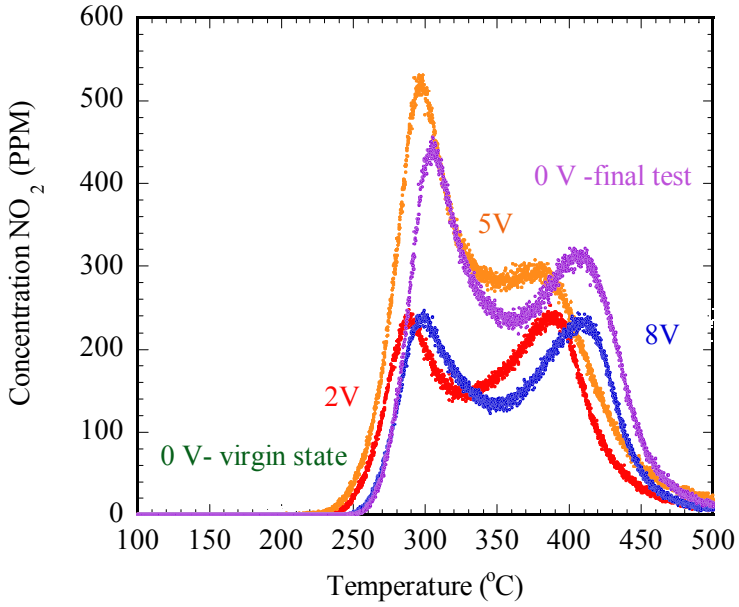

Figure 6.5 NO_2 desorption from the La_2CuO_4 capacitor following NO adsorption

Table 6.1 NO adsorption TPD of device

Species	Voltage	Total µmol Adsorbed
NO	0 V-initial	13.08
	2 V	13.45
	5V	6.706
	8 V	11.04
	0 V-repeat	10.11
NO_2	0 V-initial	-
	2 V	5.165
	5V	8.591
	8 V	4.994
	0 V-repeat	7.848

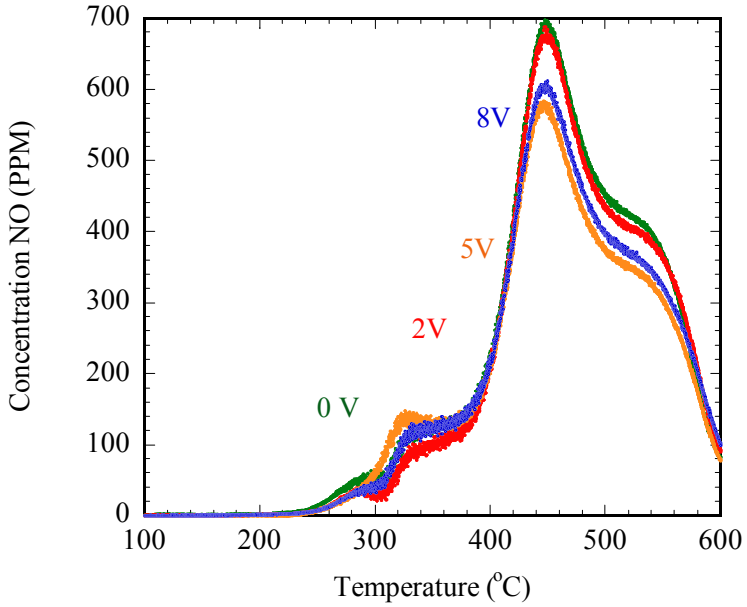

Figure 6.6. NO desorption from the La_2CuO_4 capacitor following NO_2 adsorption

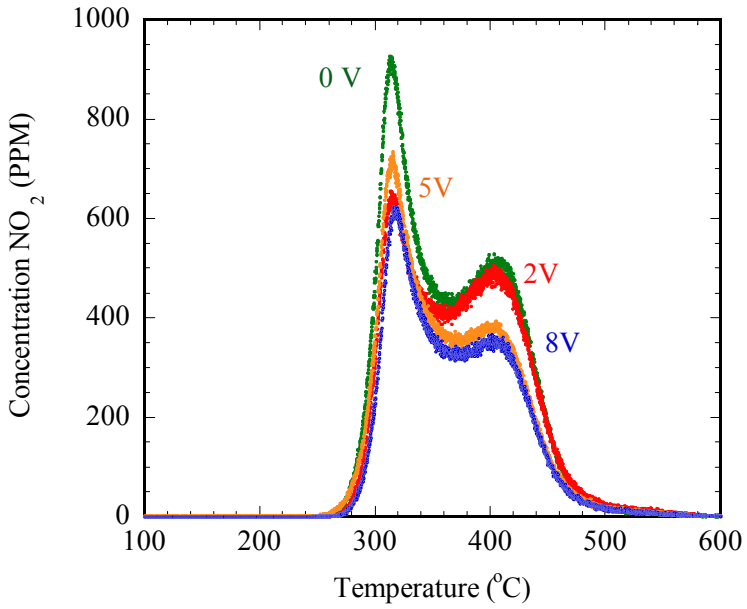

Figure 6.7. NO_2 desorption from the La_2CuO_4 capacitor following NO_2 adsorption.

Table 6.2. NO_2 adsorption TPD of device

Species	Voltage	Total µmol Adsorbed
NO	0 V	15.22
	2 V	14.55
	5V	13.29
	8 V	14.00
NO_2	0 V	13.24
	2 V	11.47
	5V	10.38
	8 V	9.105

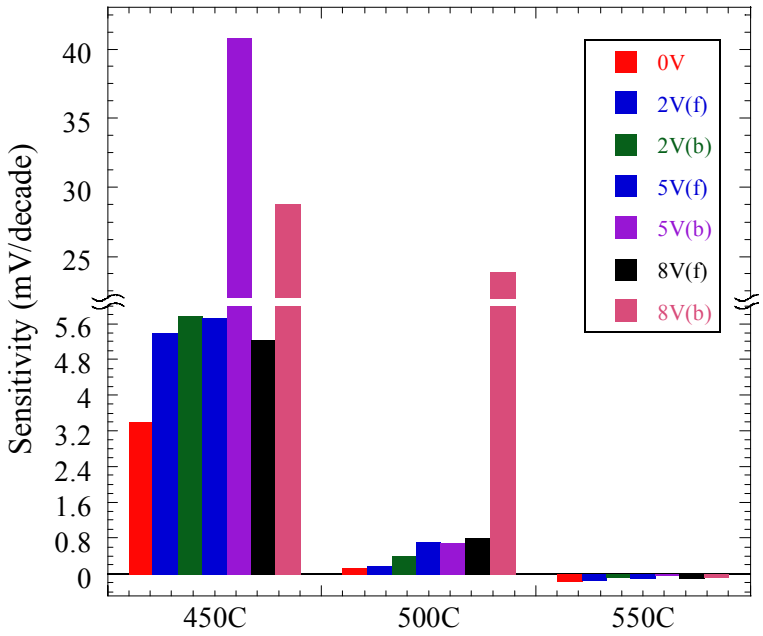

Figure 6-8. Sensitivity plot of NO for the sensor

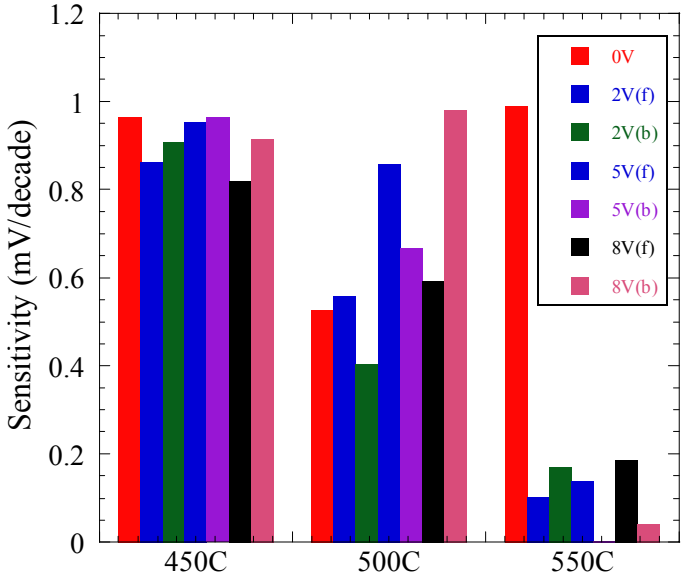

Figure 6-9. R^2 values of data fitting to linear plots for NO

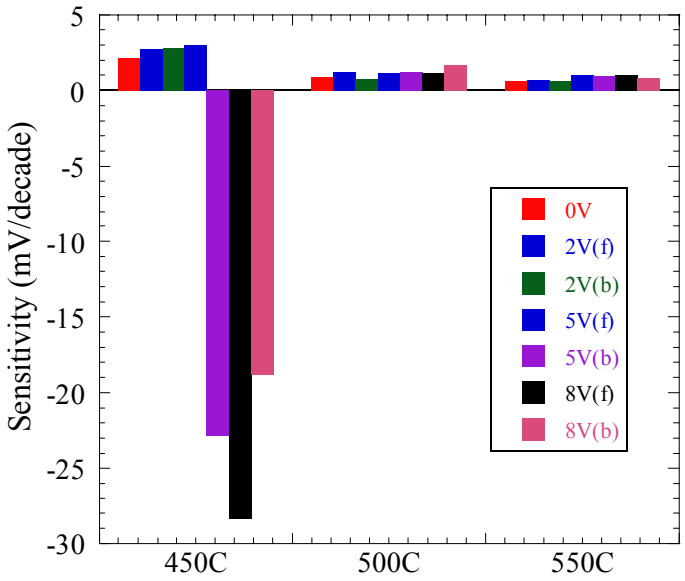

Figure 6-10. Sensitivity plot of NO_2 for the sensor

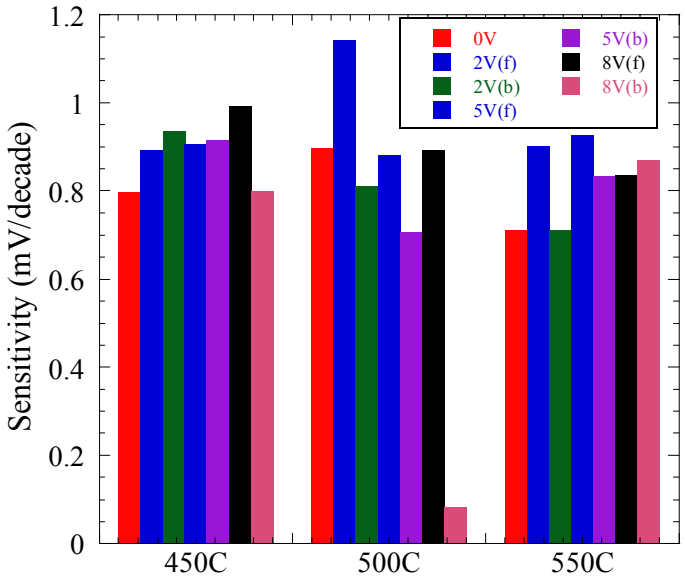

Figure 6-11. R^2 values of data fitting to linear plots for NO_2

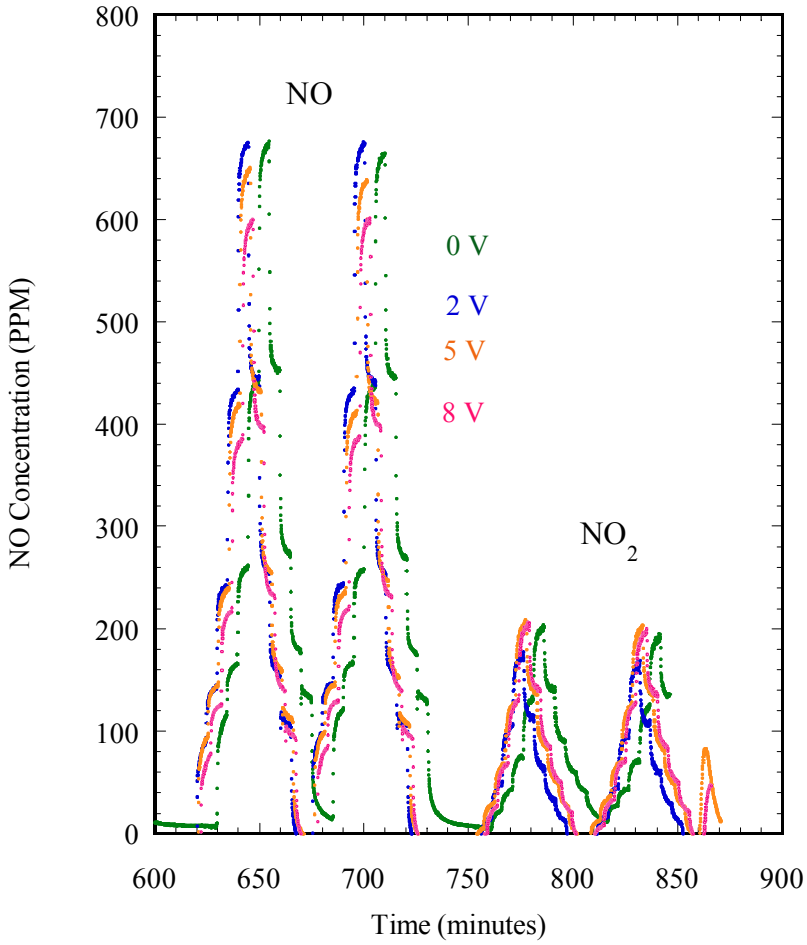

Figure 6-12. Mass spectrometry comparison of NO in reactor effluent from forward biased sensor testing

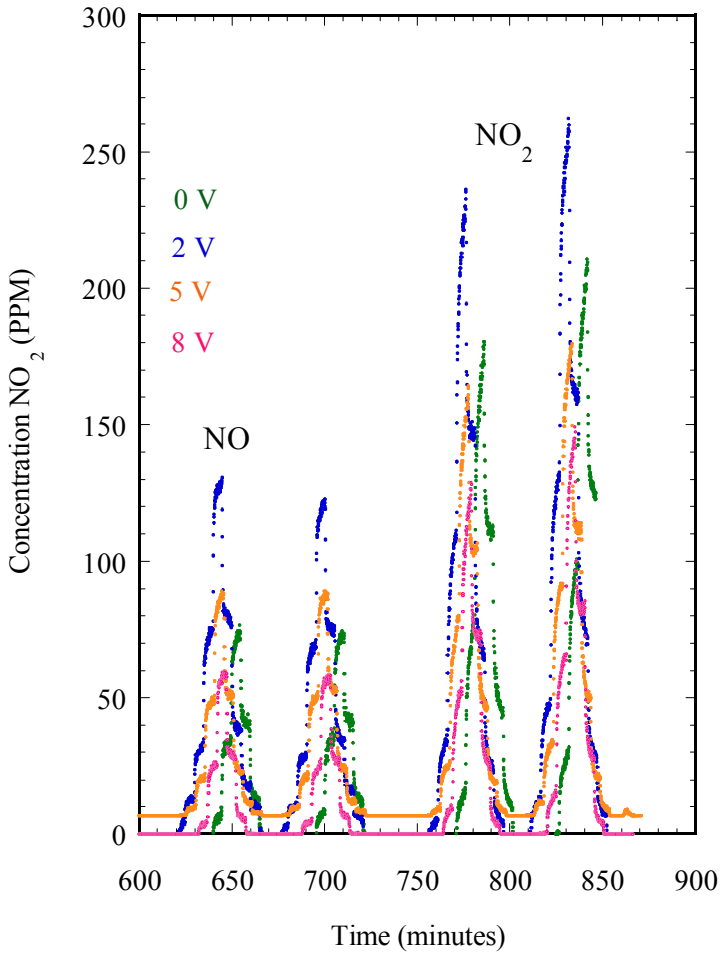

Figure 6-13. Mass spectrometry comparison of NO_2 in reactor effluent from forward biased sensor testing

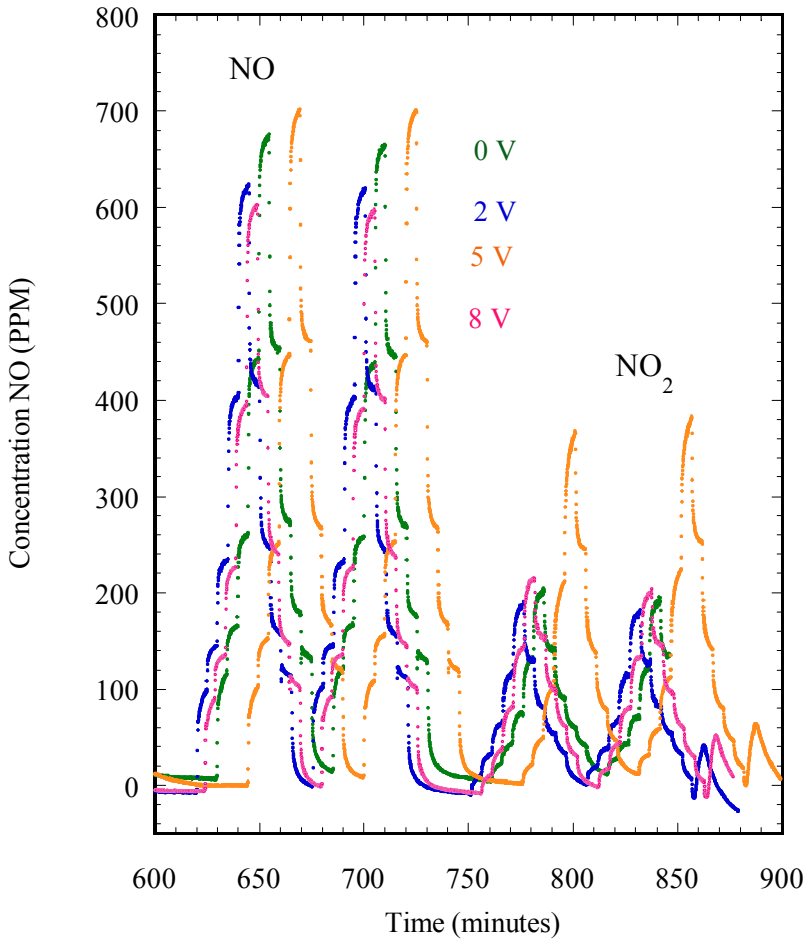

Figure 6-14. Mass spectrometry comparison of NO in reactor effluent from reverse biased sensor testing

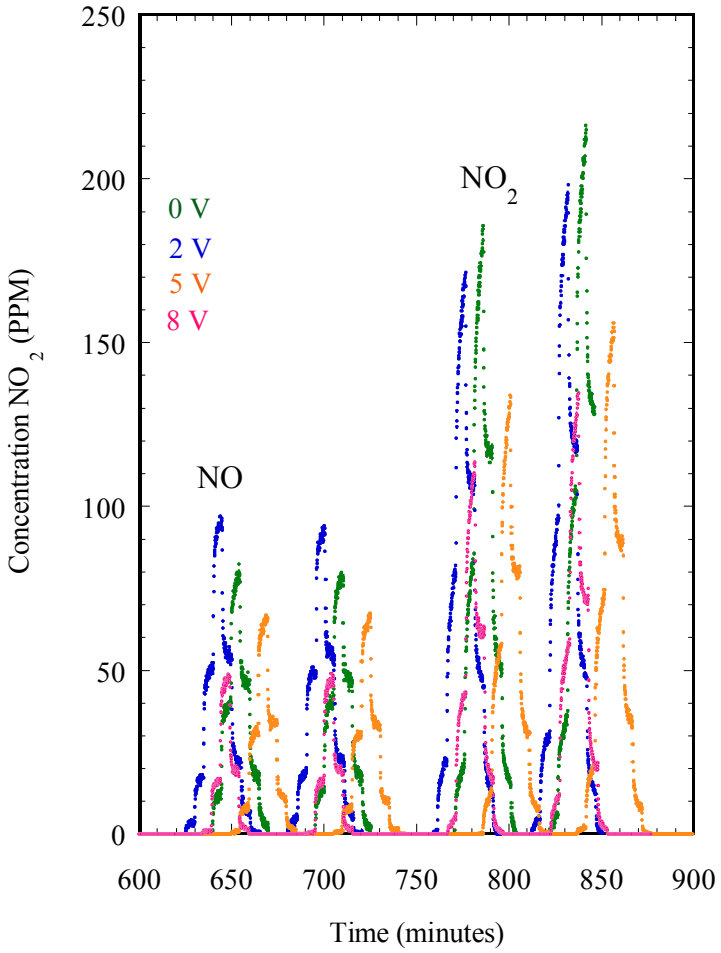

Figure 6-15. Mass spectrometry comparison of NO_2 in reactor effluent from reverse biased sensor testing

CHAPTER 7
CONCLUSIONS

Temperature Programmed Desorption and Temperature Programmed Reactions (TPD/TPR) were performed on La_2CuO_4. Experiments on La_2CuO_4 show quantifiable adsorption and reaction of NO_x and CO_x mixtures on the surface. Examination of the desorption peaks for Temperature Programmed Desorption allowed for the calculation of desorption energy of gas species adsorbed on the powder, and gas phase conversion with respect to temperature could be tracked by examining concentration profiles during Temperature Programmed Reaction. NO was found to be unreactive for conversion to other NO_x gas species even in the presence of oxygen, indicating that its response in the sensor is more strongly influenced by adsorption rather than mixed potential. NO_2 decomposed catalytically at sensor operating temperatures, and was found to fragment into several products at low temperature, indicating mixed potential may play a significant role for the sensing behavior of NO_2 on the potentiometric sensor.

To determine the composition of surface species, the techniques of diffuse reflectance infrared spectroscopy (DRIFT) and X-ray photoelectron spectroscopy (XPS) were used to investigate the adsorptive behaviors of La_2CuO_4 for NO_x gases. In both the NO and NO_2 case, the presence of ionically charged nitrite and nitrate species was detected by IR. While these complexes appear under both gas adsorptions, the response of a full sensor was different for NO than for NO_2. Thus, while the complexes on the surface due to adsorption are for all intents similar, the method in which they form greatly affects the charge the surface layer generates, and leads to the differences in potential across the electrolyte.

By examining the working electrode material by XPS independently of the sensor, the adsorptive component can be examined without compensation for possible charging effects on the sensor electrodes. Peak splitting to higher ejection energies from surface oxygen

demonstrated NO adsorption generates charge depletion layers by the formation of NO_2^- and NO_3^- at the gas/solid interface, where electrons are taken from the bulk and held. These depleted layers form a potential gradient that (in a full sensor) attempted to draw electrons from the counter-electrode, for a positive voltage. This phenomenon was observed in the absence of catalytic conversion of NO to N_2 or NO_2, thus advancing the theory that NO sensing via the La_2CuO_4 electrode is entirely adsorptive. NO_2 forms similar complexes, but due to the extra oxygen present for use in these complexes, electron holes are generated, which produced a negative potential gradient across the sensor couple in a full device. This phenomena was demonstrated by peak splitting towards the lessening of electron ejection energy from oxygen in XPS studies.

Labeled oxygen studies were performed on La_2CuO_4 powder samples. The main techniques utilized were Temperature Programmed Reaction and Temperature Programmed Desorption experiments. The material was examined under multiple gas conditions of NO_x and $^{16}O_2/^{18}O_2$ atmospheres, as well as varied levels of ^{18}O enrichment in the lattice itself. Through these studies, it was determined that the formation of charged surface complexes occurs solely through the use of lattice oxygen. Gas-phase oxygen exchange with the La_2CuO_4 bulk occurs at temperatures above 400 ^oC. This substitution of the lattice allows gas phase oxygen to indirectly integrate into surface complexes, shown in TPR experiments. In TPD experiments, the concentration of scrambled O_2 and NO_x products was noted to increase with greater $^{18}O_2$ pretreatment. Substitution of ^{18}O for ^{16}O in surface NO_x complexes was postulated to occur due to the repeated transformation between the nitrite and nitrate complexes, as well as resonance between multiple nitrate configurations. Oxygen-18 retention from the gas phase occurred due to substitution in the surface complex combined with thermally induced vibration leading to the

destabilization of the bond between nitrogen and the primary (original) oxygen in the complex. Since the surface complexes formed solely due to lattice oxygen, the Mixed Potential electrochemical reaction does not occur as such on La_2CuO_4, and so that theory of sensor response does not adequately explain the mechanism of gas sensing for this material. A more comprehensive model that includes the shift in Fermi level due to adsorption and charged complex formation can be found in Differential Electrode Equilibria.

In an attempt to modify the adsorption equilibrium to modify sensor response, Temperature Programmed Desorption experiments under electric field bias were performed on a La_2CuO_4 pellet. Initial bias and aging effects of the sample were shown to increase the desorption temperature of NO from the virgin case to subsequent runs. Increases in field strength were shown to change the desorption profile of NO and NO_2 gases from the surface of the La_2CuO_4 pellet. A sensor utilizing a La_2CuO_4 pellet with similar field generating structures was also constructed. The sensor displayed changes in sensitivity to NO_x gases with changes in field voltage and bias. This effect was the most pronounced at the lowest temperature in the study, 450 ^oC.

Analysis of the data in this study provided a few factors to guide further experiments in the work. Firstly, the improvement on the sensitivity comes mainly at low temperatures for the low field strengths. To more fully evaluate the effect of fields at high temperatures, a voltage source capable of producing voltages up to kV levels will be needed. The second improvement for further experiments is in the design of the device itself. As noted above, neither did the field desorption device, nor the sensor device, approximate the ideal case of a capacitor dielectric. Desorption experiments demonstrated that the electrode pellets used for both studies were large enough to be significantly reduced in volume while maintaining sufficient surface area for

further desorption experiments. As a result, a better fabrication process that produces a larger area/electrode distance ratio will produce a satisfactory sample. In this way, a field can be established to apply equally throughout the La_2CuO_4 electrode, and facilitate the optimization of the electric field.

APPENDIX A
CALIBRATION AND CORRECTION OF MASS SPECTROMETRY DATA

Calibration of the mass spectrometer takes two main factors into account while obtaining a calibration profile. These factors consist of the primary m/z ratio, or the largest peak unique to that species of gas, and the fragmentary peaks caused by the decomposition of gas under ionization as the analyte passes into the mass spectrometer. Ideally, each gas species would have an identifier m/z independent of all other gas species, but since this outcome is not possible, the contributions of each gas must be removed to obtain the true concentration.

Experiments in Chapter 3 have a common set of searched m/z ratios, and these were analyzed differently than results in later work. The initial TPD/TPR experiments monitor m/z ratios of 12, 14, 28, 30, 32, 44, and 46. The list of primary and secondary items is listed in Table A-1.

Table A-1. Primary and secondary ions found in Chapter 3 experiments

Gas Species	Primary m/z	Secondary m/z
NO	30	14
NO_2	46	14, 30, 32
N_2O	44	14, 30
CO	28	12, 14
CO_2	44	12, 14, 28, 32
O_2	32	16

Instances where the secondary ions overlap with primary ions can be resolved by a concentration balance. This can be achieved with careful experimental control to allow a known concentration of gas to enter the reaction chamber. For most experiments, the task of separating the individual gases is simply to work from the m/z calibration profile and set up a series of equations to relate the primary m/z intensity to a concentration profile. Once the concentration

profile has been established for the primary m/z of each gas, it is a simple matter to relate concentration of the gas species to its fragments. Thus, the concentration of all components of a mixture can be found by starting with a unique non-overlapping primary m/z ratio and constructing a series of equations to subtract signal intensity prior to fitting the gas calibration profile. In cases where the primary m/z ratio is identical (CO_2/N_2O), a second series of equations must be instituted to assure balance of nitrogen and carbon. Fortunately, since the fragmentation of these gases is small due to their stability, a useful approximation can be obtained even without additional analysis during a TPR.

The most important overlap results from the fragmentation of the NO_2 molecule to NO during the ionization process. The primary m/z ratio of 46 was used to determine the actual concentration of NO_2 in the gas phase, and the attendant m/z of 30 was plotted in order to provide a second set of equations to compensate for the falsely inflated intensity of m/z 30 during TPD and TPR experiments.

$$C_{NO_2} \propto I_{46}$$

$$I_{30\,from\,46} = A_{30/46} I_{46}$$

$$C_{NO} \propto P_{NO}(I_{30} - A_{30/46} I_{46}) + B_{NO}$$

In later work, the ^{18}O isotope of oxygen was introduced into TPR and TPD of NO and NO_2 gases. As a result of oxygen exchange of the gas with the bulk, and interface reactions between the ^{16}O lattice and NO_x gas, $N^{16}O$ (m/z=30), $N^{18}O$ (m/z=32), $N^{16}O_2$ (m/z=46), $N^{16}O^{18}O$ (m/z=48), and $N^{18}O_2$ (m/z=50) are present in the effluent stream. At temperatures above 400 ^oC, the gas phase $^{18}O_2$ (m/z=36) interacts with the bulk to exchange $^{16}O_2$ (m/z=32), and $^{16}O^{18}O$ (m/z=34), into the gas phase. $^{18}O_2$ and $^{16}O^{18}O$ each have a unique m/z ratio, and so the concentrations of

these species are easily monitored without resorting to a series of matrices. The m/z ratio of 32, however, is common to the atmospherically prevalent $^{16}O_2$ as well as the isotopically exchanged $N^{18}O$. To separate these two gases, it is necessary to employ a series of equations, shown below.

$$I_{14\,fromNO_2} = A_{14/46} I_{46}$$

$$I_{14\,from N^{18}O} = A_{14/30} I_{30}$$

$$I_{14\,from N^{18}O} = I_{total\,14} - I_{14\,from N^{16}O} - I_{14\,from NO_2}$$

$$C_{N^{18}O} \propto P_{NO} I_{14\,from N^{18}O}$$

$$C_{^{16}O_2} = P_{O_2} (I_{total\,32} - A_{32/14} I_{14\,from N^{18}O})$$

C = concentration

I = intensity

P = proportionality constant

B= background constant

A= fragmentation ratio

APPENDIX B
TEMPERATURE PROGRAMMED DESORPTION DATA FOR RELEVANT GAS COMBINATIONS

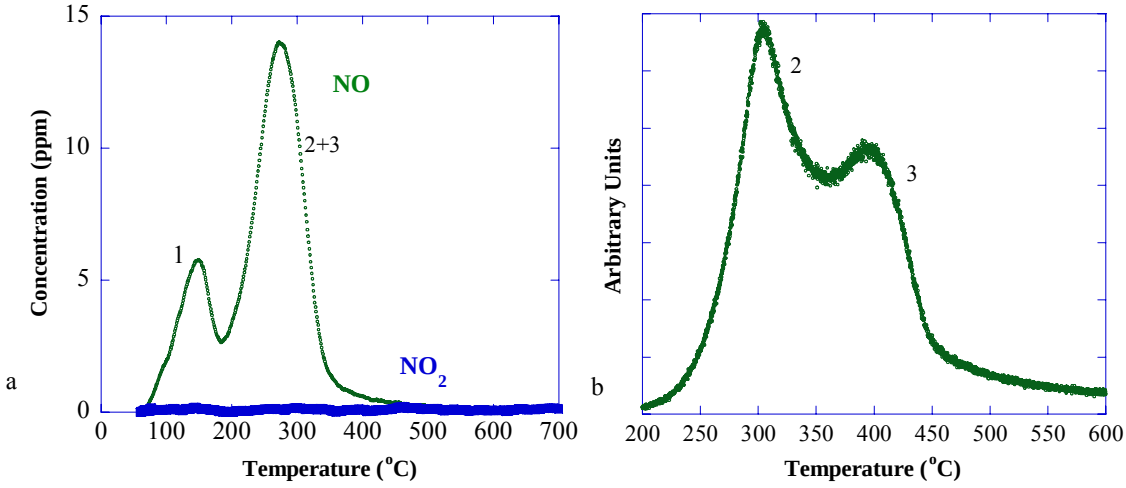

Figure B-1. Temperature Programmed Desorption of 1% NO on La_2CuO_4 at 30 °C per minute (a.) and 5 °C per minute (b.).

Table B-1. Temperature Programmed Desorption Characteristics of 1% NO on La_2CuO_4 for the 30 °C per minute desorption

Species	Peak	Temperature (°K)	Desorption Energy (kJ/mol)	µ-moles Desorbed	µ-moles Desorbed Per m^2	µ-moles Desorbed Per g
NO	1	423	73.78	1.87 E-02	0.125	0.434
	2	559	110.23	6.22 E-02	0.415	1.45
	3	650	127.56			
	Total			8.22 E-02	0.548	1.91

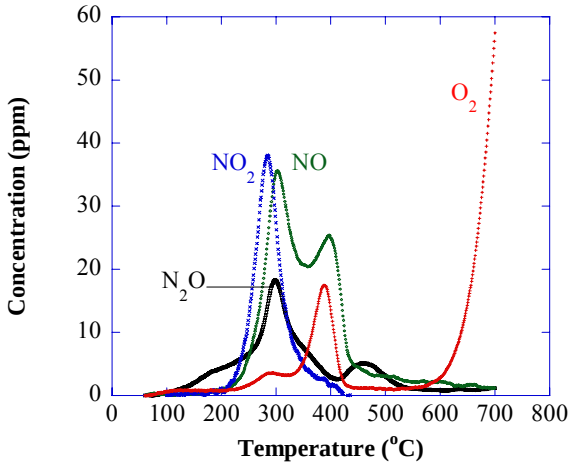

Figure B-2. Temperature Programmed Desorption of 500 ppm NO_2 on La_2CuO_4.

Table B-2. Temperature Programmed Desorption Characteristics of 1% NO_2 on La_2CuO_4

Species	Peak	Temperature (°K)	Desorption Energy (kJ/mol)	µ-moles Desorbed	µ-moles Desorbed Per m^2	µ-moles Desorbed Per g
NO	1	586	115.2	1.12 E-01	0.747	2.60
	2	672	131.575	8.79 E-02	0.586	2.04
	Total			2.21 E-01	1.47	5.14
NO_2	1/Total	586	115.2	1.10 E-01	0.733	2.56
N_2O	1	586	115.2	N/A	N/A	N/A
	2	741	152.79			
O_2	1	586	115.2	1.71 E-02	0.114	0.397
	2	672	131.575	4.53 E-02	0.302	1.05
	Total			6.90 E-02	0.460	1.60

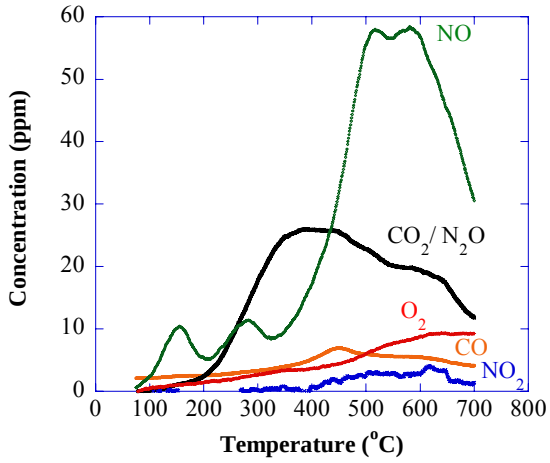

Figure B-3. Temperature Programmed Desorption of 0.67% NO and 0.33% CO on La_2CuO_4.

Table B-3. Temperature Programmed Desorption Characteristics of 0.67% NO and 0.33% CO on La_2CuO_4

Species	Peak	Temperature (°K)	Desorption Energy (kJ/mol)	µ-moles Desorbed	µ-moles Desorbed Per m^2	µ-moles Desorbed Per g
NO	1	436	104.74	3.48 E-02	0.232	0.809
	2	560	135.7	6.06 E-02	0.404	1.41
	3	795	146.8	6.60 E-01	4.40	15.3
	4	859	159.2			
	Total			7.56 E-01	5.04	17.6
CO	1	731	134.5	2.94 E-02	0.196	0.684
	Total			1.23 E-01	0.820	2.86
CO_2 / N_2O	1 / Total		----	4.41 E-01	2.94	10.3

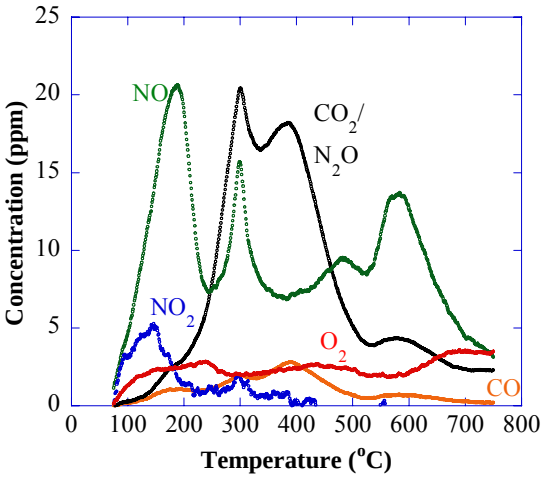

Figure B-4. Temperature Programmed Desorption of 500 ppm NO, 500 ppm CO, and 1% on La_2CuO_4.

Table B-4. Temperature Programmed Desorption Characteristics of 500 ppm NO, 500 ppm CO, and 1% O_2 on La_2CuO_4.

Species	Peak	Temperature (^oK)	Desorption Energy (kJ/mol)	μ-moles Desorbed	μ-moles Desorbed Per m^2	μ-moles Desorbed Per g
NO	1	466	84.0	9.48 E-02	0.632	2.20
	2	575	104.6	6.33 E-02 4.91 E-02	0.422	1.47
	3	763	140.6	8.70 E-02 2.94 E-01	0.327	1.14
	4	859	159.2		0.580	2.02
	Total				1.96	6.84
CO_2	1	450	81.0	7.27 E-03	0.048	0.169
	2	576	104.8	7.94 E-02	0.529	1.85
	3	664	121.7	1.02 E-01 3.43 E-02	0.680	2.37
	4	858	159.0	2.23 E-01	0.229	0.798
	Total				1.49	5.19
CO	1	452	81.4	5.72 E-03	0.0381	0.133
	2	578	105.2	5.32 E-03 1.65 E-02	0.0354	0.124
	3	669	122.6	3.23 E-02	0.110	0.384
	Total				0.215	0.751

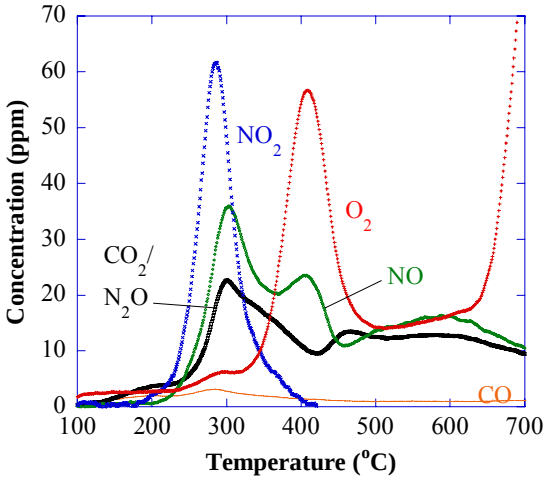

Figure B-5. Temperature Programmed Desorption of 500 ppm NO_2, 250 ppm CO and 1000 ppm O_2 on La_2CuO_4.

Table B-5. Temperature Programmed Desorption Characteristics of 500 ppm NO_2, 250 ppm CO and 1000 ppm O_2 on La_2CuO_4.

Species	Peak	Temperature (^oK)	Desorption Energy (kJ/mol)	μ-moles Desorbed	μ-moles Desorbed Per m^2	μ-moles Desorbed Per g
NO	1	580	105.6	1.25 E-01	0.833	2.91
	2	685	125.7	9.17 E-02 1.61 E-01	0.611	2.13
	3	871	161.5	3.77 E-01	1.07	3.74
	Total				2.51	8.77
NO_2	1	564	102.6	1.84 E-01	1.23	4.28
CO	1	474	85.5	6.88 E-03	0.0458	0.160
	2	562	102.2	2.02 E-02 4.13 E-02	0.135	0.469
	Total				0.275	0.960
CO_2	1	481	86.8	1.50 E-02	0.100	0.349
	2	578	105.2	1.29 E-01 5.18 E-02	0.860	3.00
	3	743	136.8	1.03 E-01 2.92 E-01	0.345	1.20
	4	877	162.7		0.687	2.40
	Total				1.95	6.79
O_2	1	567	103.1	2.81 E-02	0.187	0.653
	2	685	125.7	2.29 E-01 5.00 E-01	1.53	5.33
	Total				3.33	11.6

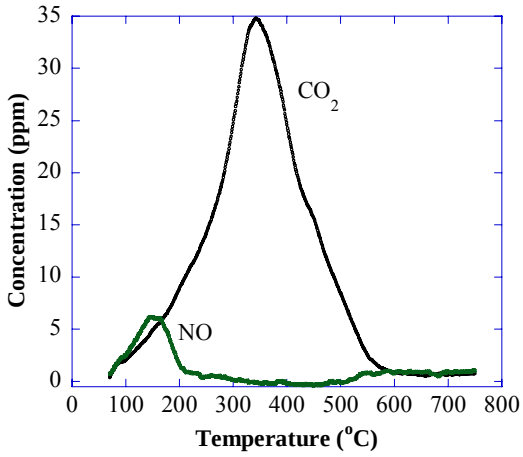

Figure B-6. Temperature Programmed Desorption of 500 ppm NO and 1000 ppm CO_2 on La_2CuO_4.

Table B-6. Temperature Programmed Desorption Characteristics of 500 ppm NO and 1000 ppm CO_2 on La_2CuO_4.

Species	Peak	Temperature (^oK)	Desorption Energy (kJ/mol)	µ-moles Desorbed	µ-moles Desorbed Per m^2	µ-moles Desorbed Per g
NO	1/Total	428	76.9	2.35 E-02	0.157	0.547
CO_2	1/Total	621	113.4	3.25 E-01	2.17	7.56

APPENDIX C
SILICA CONTAMINATION OF THE SENSOR ELECTRODE INTERFACE

The development of a long term model for behavior of a potentiometric sensor requires an understanding of the modification of the electrode and electrolyte surfaces, as well as accounting for changes at the interface between electrode and electrolyte.

Many factors contribute to changes over time in the output of a potentiometric sensor.[319] Most of these factors can be mitigated by altering processing conditions[320] and operating environment.[321] One variable that proves very difficult to remove is the presence of silicon oxide in Yttrium Stabilized Zirconia (YSZ).

This oxide rests in the grain boundaries and diffuses to the surface of the YSZ, forming an oxygen diffusion barrier of its own accord and by reaction with material from the electrode may form silicates.[322-324] Additionally, siloxane decomposition may occur due to heating of the vacuum grease used to seal the reactor, as seen in the literature.[325] The aim of this study is to examine the structure of the contamination of silica on the electrode, electrolyte, and interfaces of a screen-printed La_2CuO_4/YSZ/Pt potentiometric sensor that occurs over time.

X-ray photoelectron spectroscopy (XPS-Perkin-Elmer PHI 5100 ESCA System) was used to examine the composition of the electrode, bare electrolyte, and exposed electrolyte surfaces. Scanning electron microscopy (SEM-JEOL JSM-6335F) was utilized to examine the surface and interface regions to detect the presence and structure of any amorphous silicon-based contaminants. A quartz tube reaction chamber was used to cycle the sample thermally and environmentally.

The paste for screen-printing sensor electrodes was prepared by ball-milling the La_2CuO_4 powders with poly ethylene glycol (Avocado, PEG 400) and excess ethyl alcohol for 2 hours. After evaporating the ethyl alcohol, the paste was screen-printed onto commercial dense YSZ

substrates (Marketech) of dimension (20 mm × 0.1 mm × 100 mm). The device was sintered at 800°C for 10 hours.

The sensor was then loaded into a glass testing chamber for exposure testing. Gas mixing was carried out using MKS mass flow controllers. The total flow was kept constant at 300 standard cubic centimeters with background gas containing 3% O_2 and a balance of N_2. The concentration of either NO or NO_2 was stepped up and down using a cycle of 0 ppm, 50 ppm, 100 ppm, 200 ppm, 400 ppm and 650 ppm steps, at temperatures of 450, 500, 550, and 600 ^oC.

SEM and XPS of the sensing electrode showed no deposition of silica on the La_2CuO_4 surface. Silicon compounds appeared on the YSZ surface, however but their presence was lessened by the electrode layer above. The presence of these compounds was expected, and so it was concluded that the aging of the sample does not produce silicon compounds that interfere with sensor operation over the useful testing lifetime of sensors used in the research group.

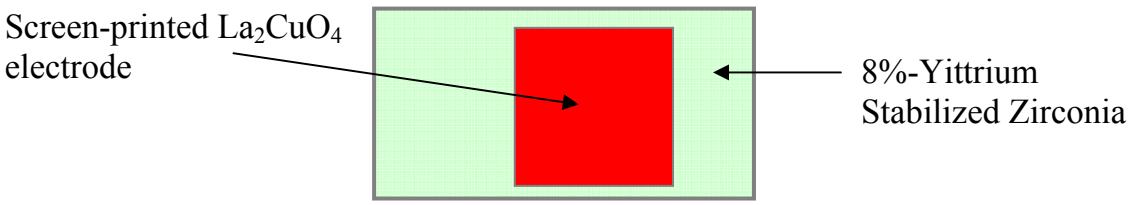

Figure C-1. La_2CuO_4 electrode on 8% YSZ substrate used for heat and gas cycling tests.

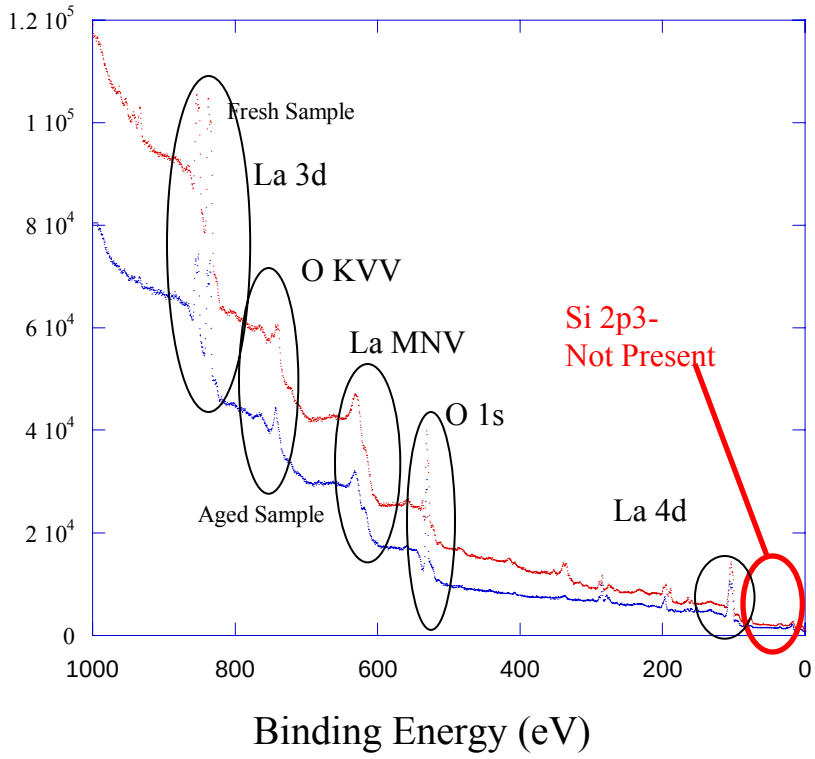

Figure C-2. XPS of La_2CuO_4 electrode surface following 3 weeks of cycling under sensor testing conditions. After 3 weeks in a thermally cycled environment and exposure to NO, NO_2, CO, and CO_2 gas mixtures, the structure and composition of the La_2CuO_4 electrode remains constant according to XPS, indicating no silica deposition from siloxane occurs in the short term.

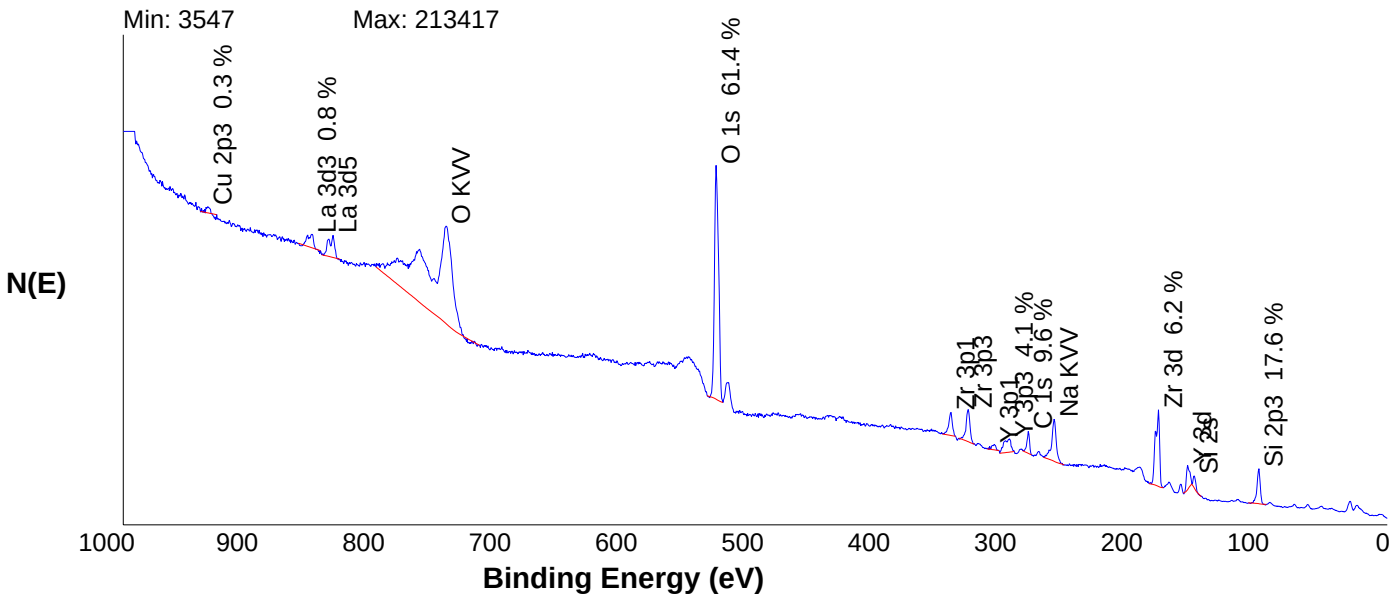

Figure C-3. XPS spectra of YSZ electrolyte on the just-sintered sample. Some trace peaks of the La_2CuO_4 electrode can be seen due to slurry wetting during the screen printing process.

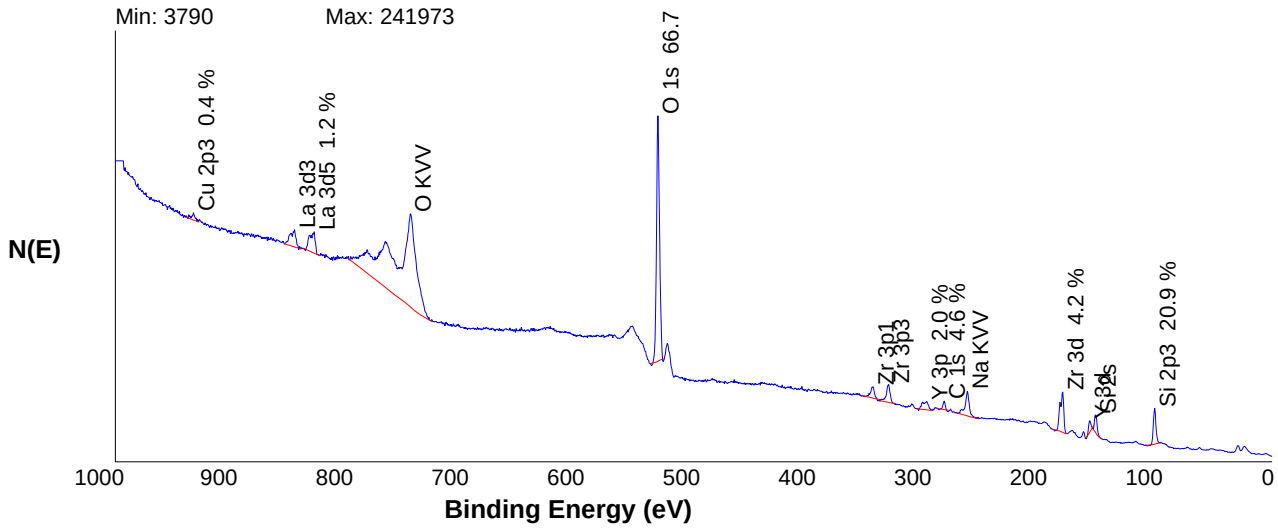

Figure C-4. XPS spectra of the YSZ electrolyte after thermal cycling in sensor testing conditions. The peak for the Si 2p3 orbital was seen to increase due to diffusion of Si to the grain boundaries of the YSZ.

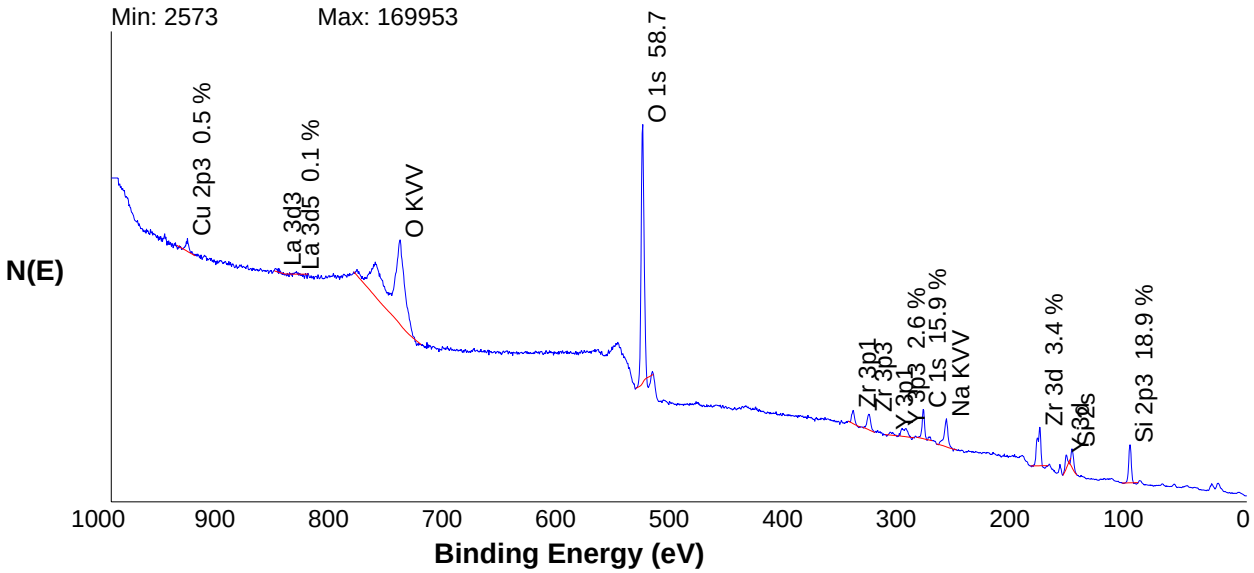

Figure C-5. XPS spectra of the YSZ electrolyte below the La_2CuO_4 electrode after thermal cycling. The Si 2p3 peak was observed to increase over the uncycled sample, but remained lower than the uncovered and cycled YSZ sample.

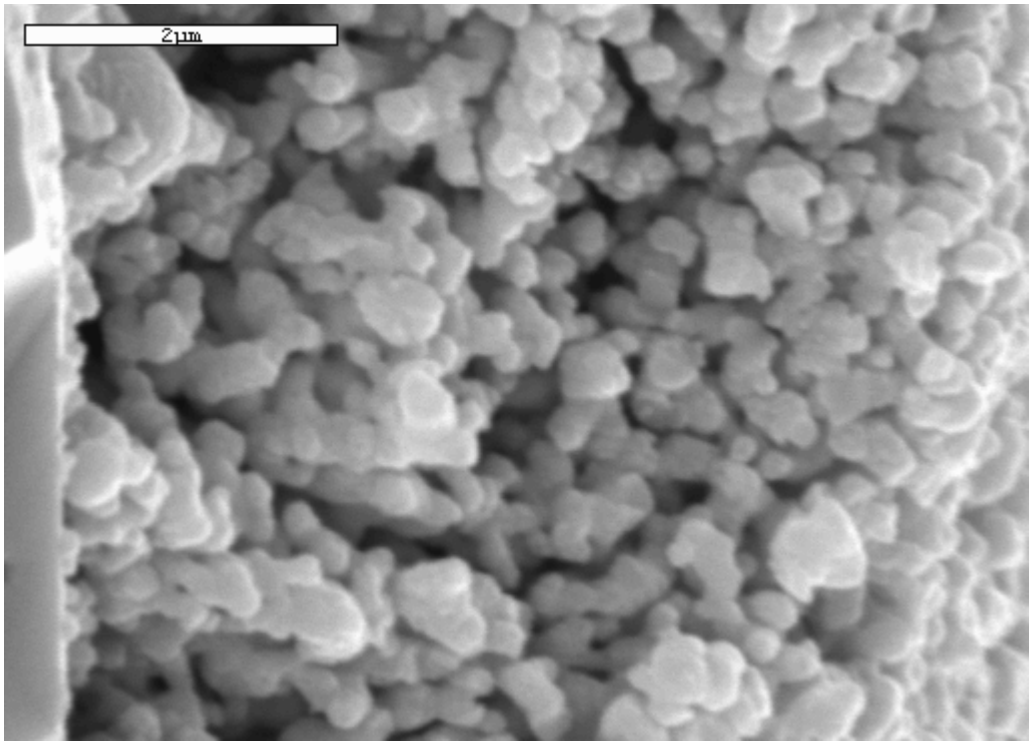

Figure C-6. SEM photograph of the electrode/electrolyte interface after sintering at 800 ^{o}C for 10 hours. The La_2CuO_4/YSZ interface was well-adhered, and showed no sign of auxiliary phases.

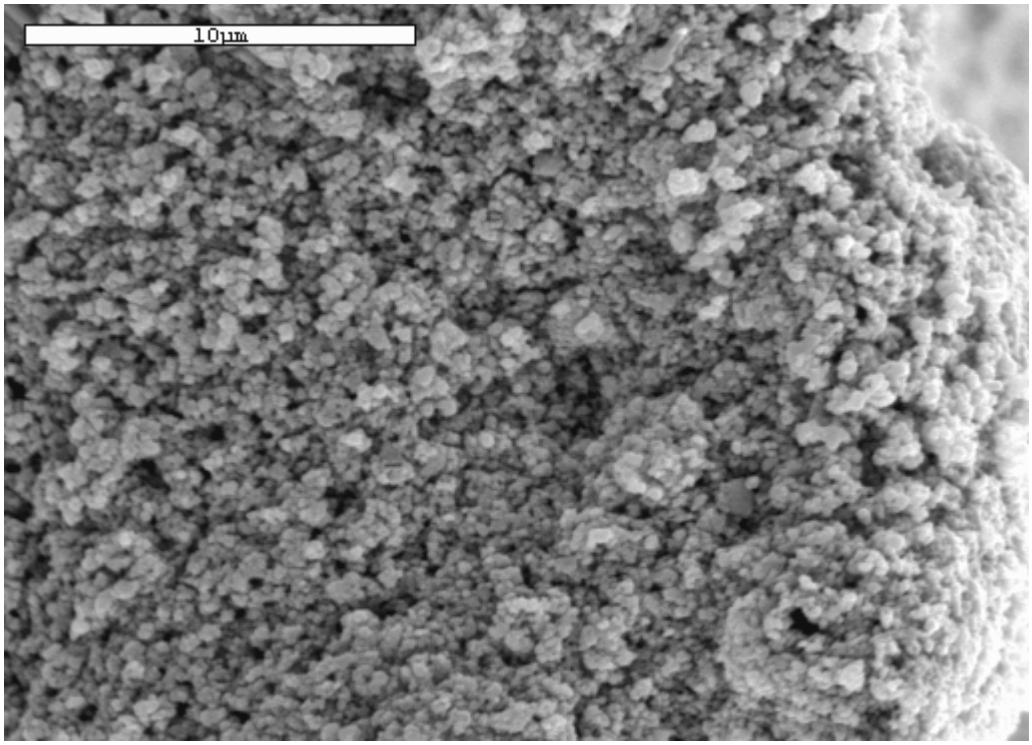

Figure C-7. The surface of the La_2CuO_4 electrode shows no visible deposits of silica products after 3 weeks of thermal cycling under sensor testing conditions.

APPENDIX D
ADSORPTION XPS OF NO/NO2/CO ON LA2CUO4 POWDER

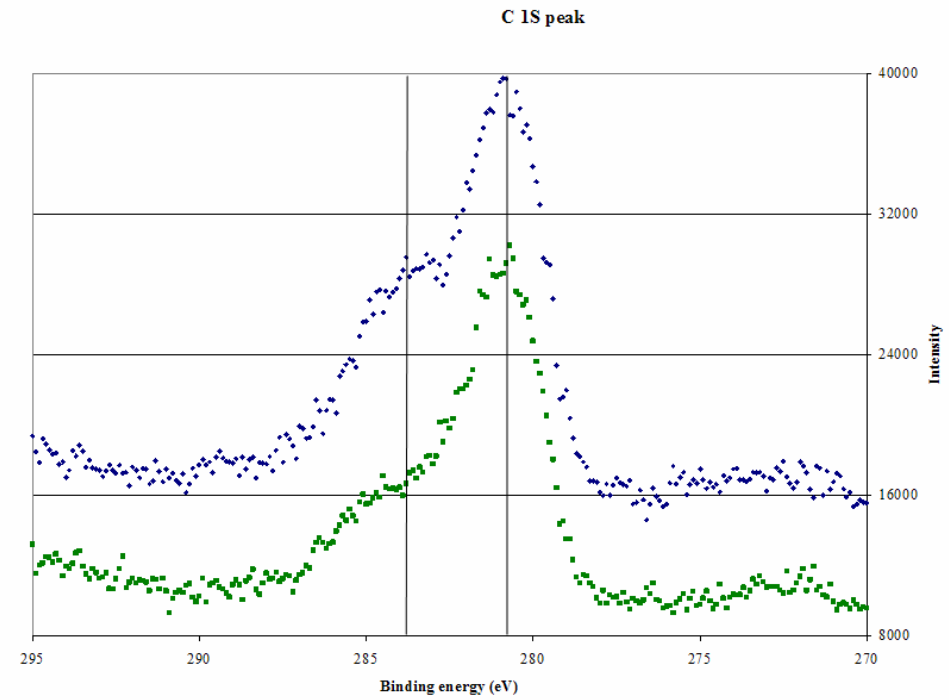

Figure D-1. C1s XPS spectra for unadsorbed (blue) and NO adsorbed (green) La_2CuO_4 powder.

The counts from the carbon peak are somewhat reduced by the presence of NO, with the peak near 285 flattening out, and near 280 keeping the similar shape but lesser intensity. This effect is likely due to the prevailing adsorption of NO to the surfaces in the absence of gas phase CO.

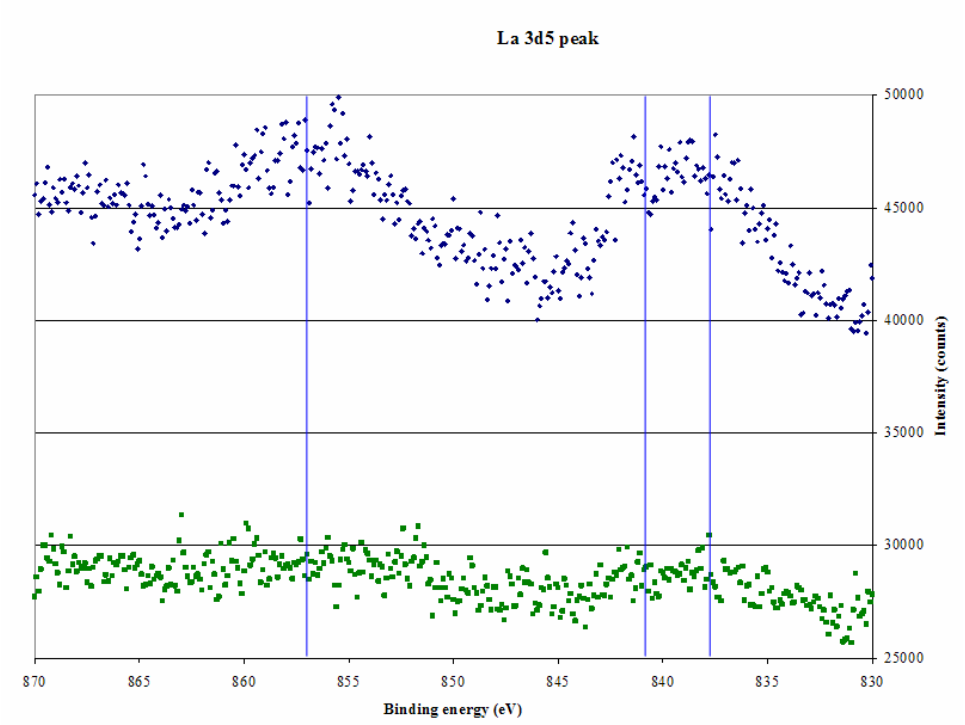

Figure D-2. La3d5 XPS spectra of unadsorbed (blue) and NO adsorbed (green) La_2CuO_4 powder. NO heavily damps the peaks at 857, 842, and 837.

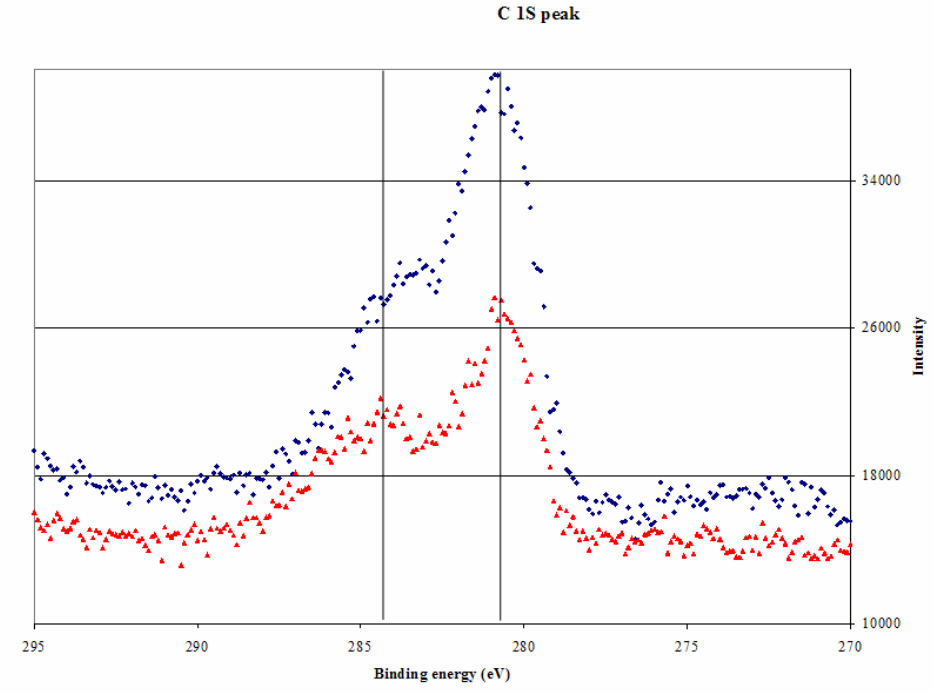

Figure D-3. C1s XPS spectra of unadsorbed (blue) and NO_2 adsorbed (red) La_2CuO_4 powder.

For the case of NO_2 adsorption, the C 1s spectrum does not vary too much from the unadsorbed spectrum. The intensity is damped down, but there appears to be no shifting of peaks, and no appreciable splitting.

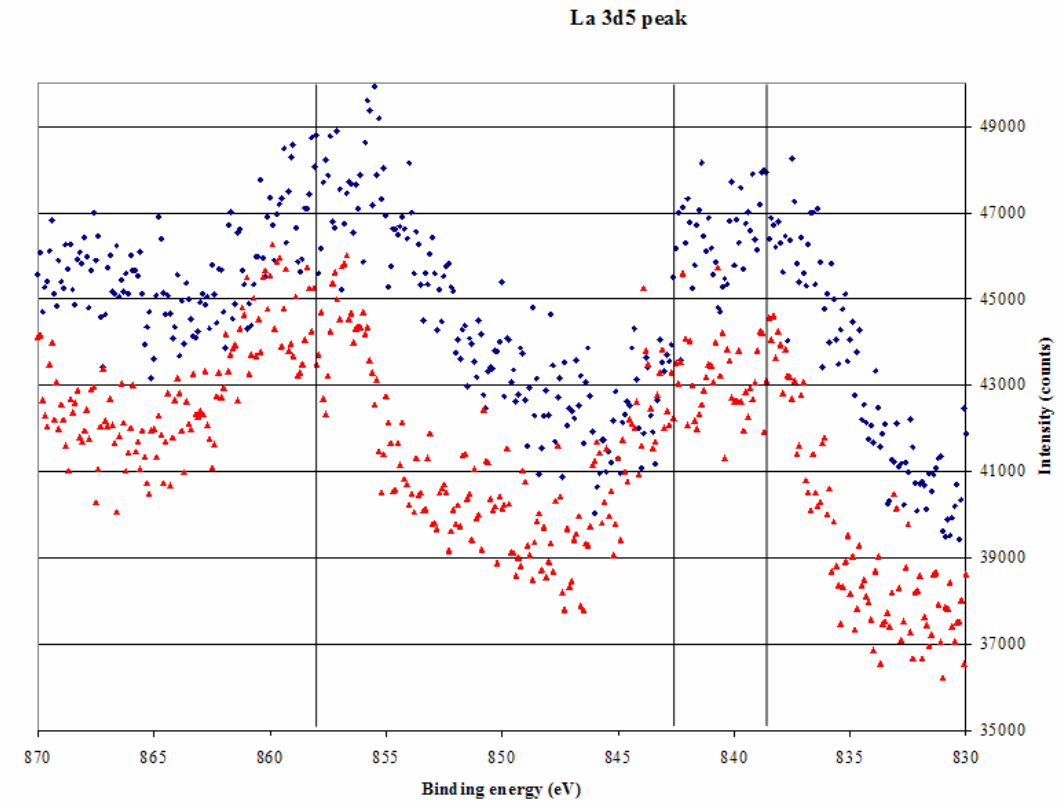

Figure D-4. La3d5 XPS spectra of unadsorbed (blue) and NO_2 adsorbed (red) La_2CuO_4 powder.

The qualities of the La peaks seem to be almost identical for the unadsorbed and NO_2 adsorbed cases, but there seems to be a very minor lessening of intensity in the adsorbed case.

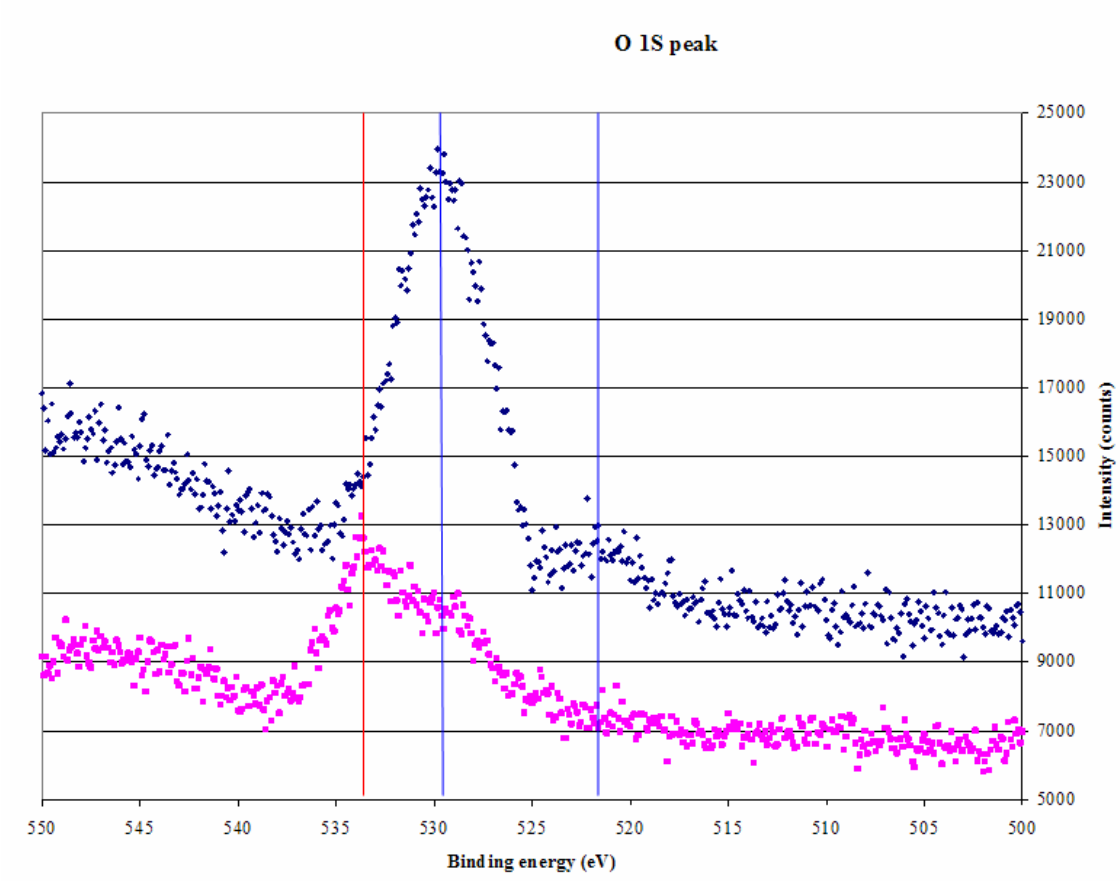

Figure D-5. O1s XPS spectra of unadsorbed (blue) and NO+CO adsorbed (purple) La_2CuO_4 powder.

For NO+CO, we see a very similar pattern to NO; the peak at ~330 remains unshifted, and there is a stronger binding energy peak sitting at 535 eV. Notable difference comes as a result of the CO interference on the surface. The more strongly bound peak is larger than the original peak, since CO causes NO to bond more thoroughly to the surface. The secondary weak peak near 522 drops in intensity also- whether this is a consequence of CO stealing the oxygen to form a CO_2 molecule or CO_3^- ion is not certain.

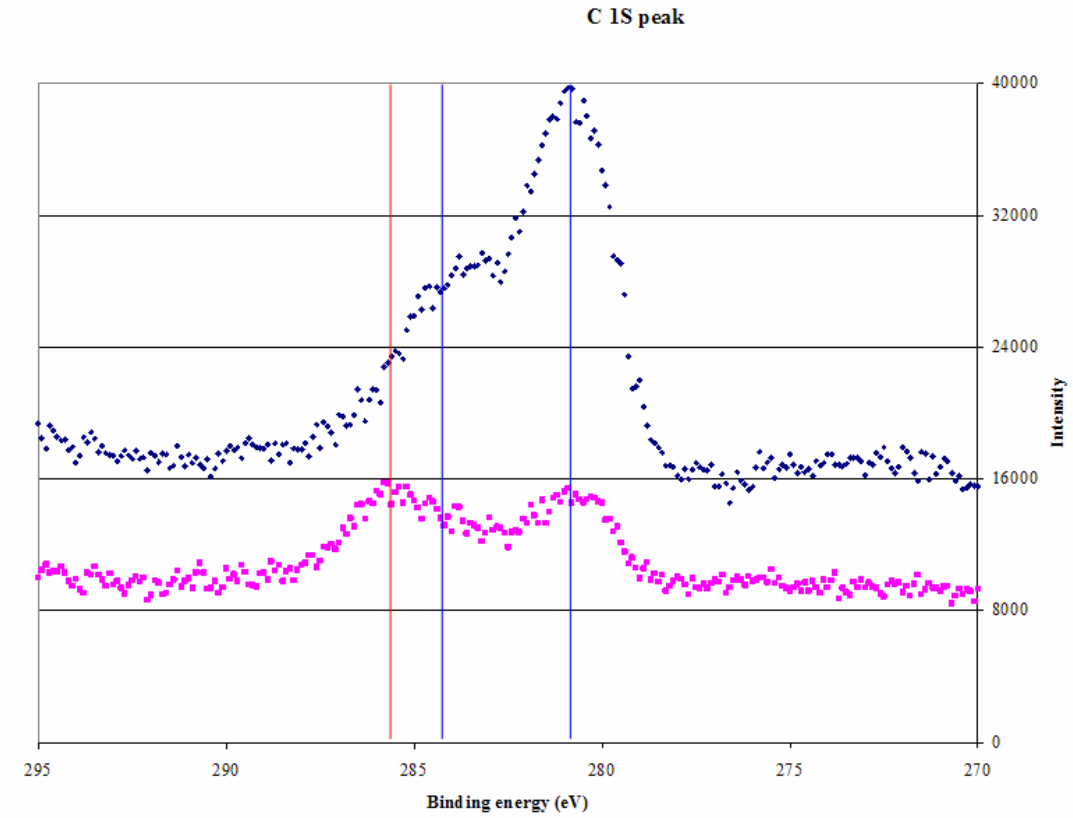

Figure D-6. C1s XPS spectra of unadsorbed (blue) and NO+CO adsorbed (purple) La_2CuO_4 powder.

Here, the two peaks assigned to carbon are lesser in intensity, but are now equally intense, likely as a result of the CO interference.

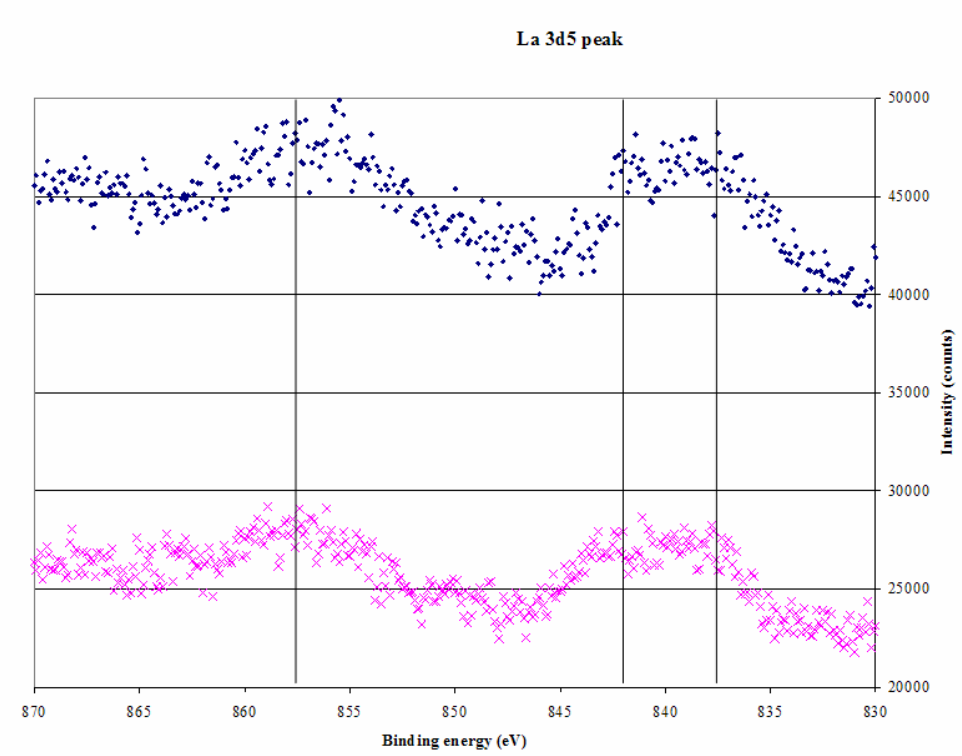

Figure D-7. La3d5 XPS spectra of unadsorbed (blue) and NO+CO adsorbed (purple) La_2CuO_4 powder.

In the La spectra, the peaks and intensities match up- though the adsorbed sample has much lower counts.

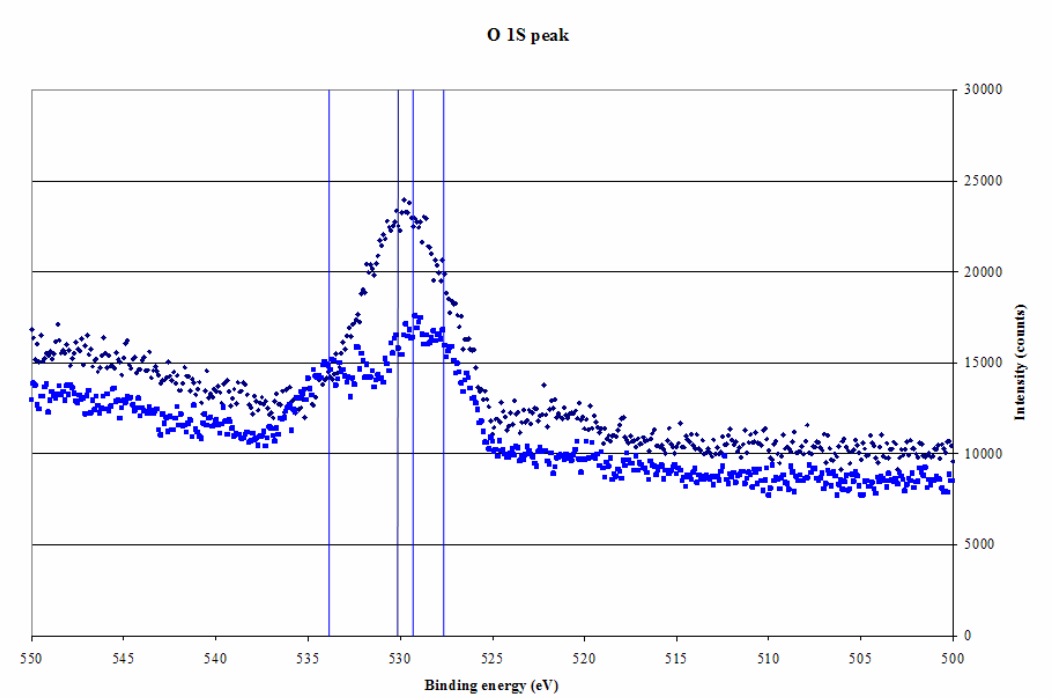

Figure D-8. O1s XPS spectra of unadsorbed (blue) and NO_2+NO adsorbed (dark blue) La_2CuO_4 powder.

Here peak spitting was present for both NO and NO_2. The peak shape was much more characteristic of NO than for NO_2. The larger peak appears to be another doublet, split between the NO peak at 529 eV, and the NO_2 shifted peak at 527. The intensity of the peak at 529 has been mostly preserved, indicating that the adsorbed species on the surface are mostly composed of NO, implying that the presence of NO on the surface assists the dissociation of NO_2, or at least the NO is more prone to bond. The former seems more likely, since TPD experiments show the NO_2 has more gas adsorbed on the surface. The more strongly bound peak is slightly less intense than in pure NO adsorption, likely owing to the hybrid adsorption of NO vs. NO_2. The reduction and oxidation oppose each other, which might account for this reduction in intensity.

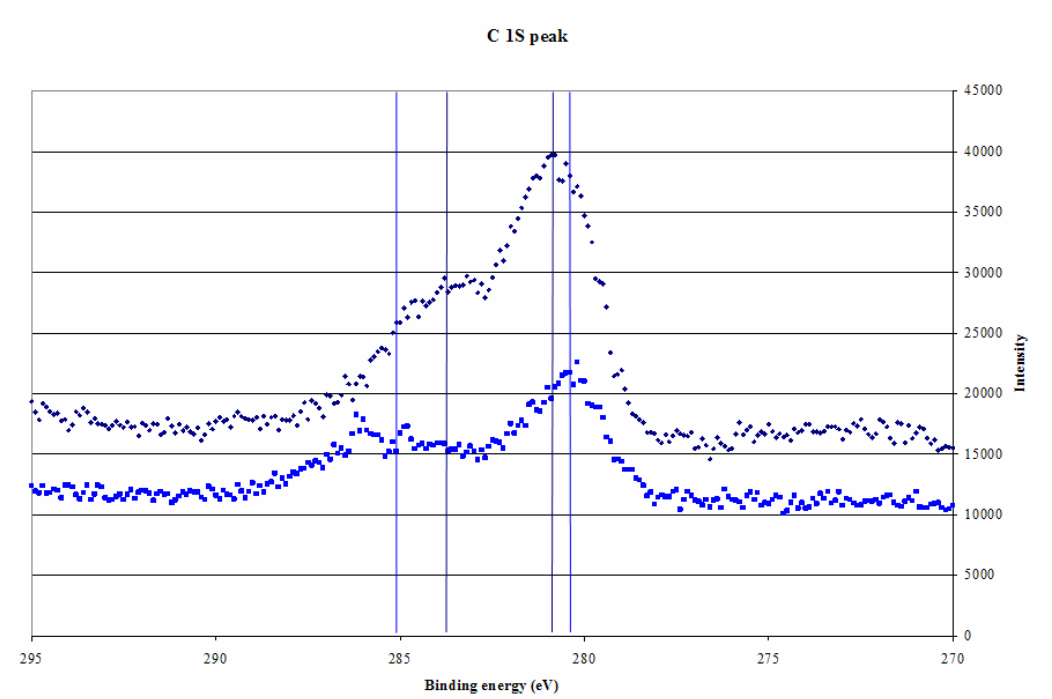

Figure D-9. C1s XPS spectra of unadsorbed (blue) and NO_2+NO adsorbed (dark blue) La_2CuO_4 powder.

The structures of these peaks were very similar to that of the NO_2 adsorption case, but were slightly less intense overall. Keep in mind, however, that the NO-adsorbed peaks looked very similar to that of the unadsorbed sample (with lesser intensity over the whole area), so NO_2 will be the only adsorbate seen in this spectra. The more weakly bound peak near 280 eV is slightly shifted to lower binding energy from the unadsorbed case, which differentiates it from the individual adsorptions of NO and NO_2.

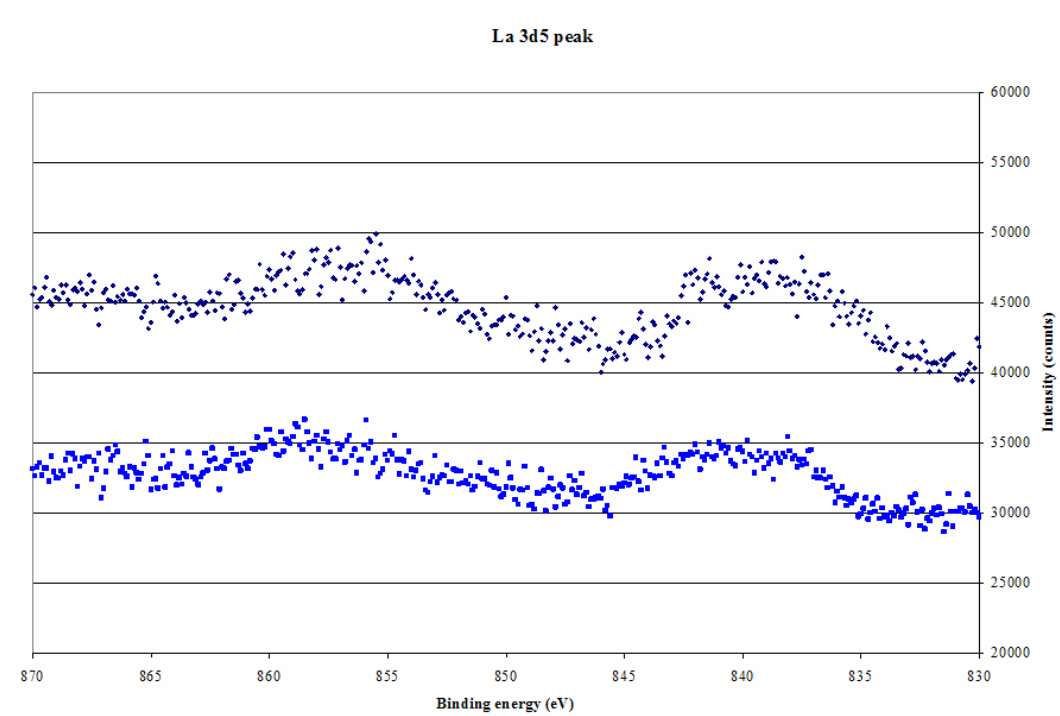

Figure D-10. La3d5 XPS spectra of unadsorbed (blue) and NO_2+NO adsorbed (dark blue) La_2CuO_4 powder.

The peaks from the mixed adsorption resembled the unadsorbed and NO_2 cases, but the NO adsorption is shown by the damping down of intensity across the whole peak range.

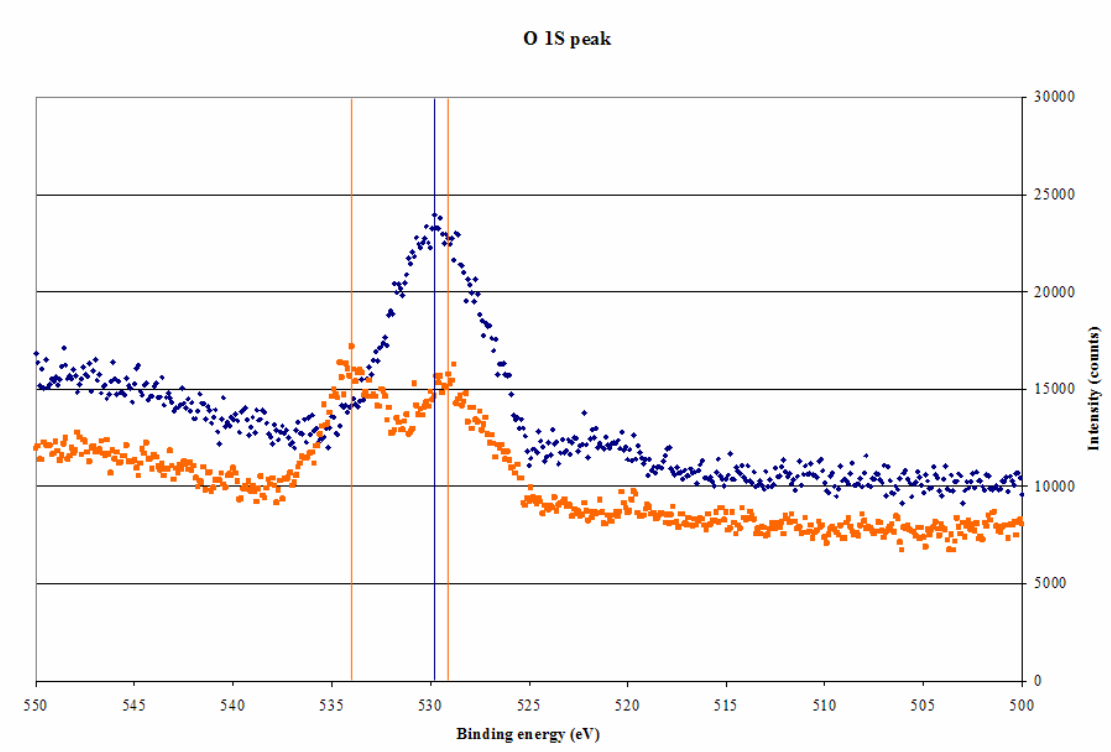

Figure D-11. O1s XPS spectra of unadsorbed (blue) and CO adsorbed (orange) La_2CuO_4 powder.

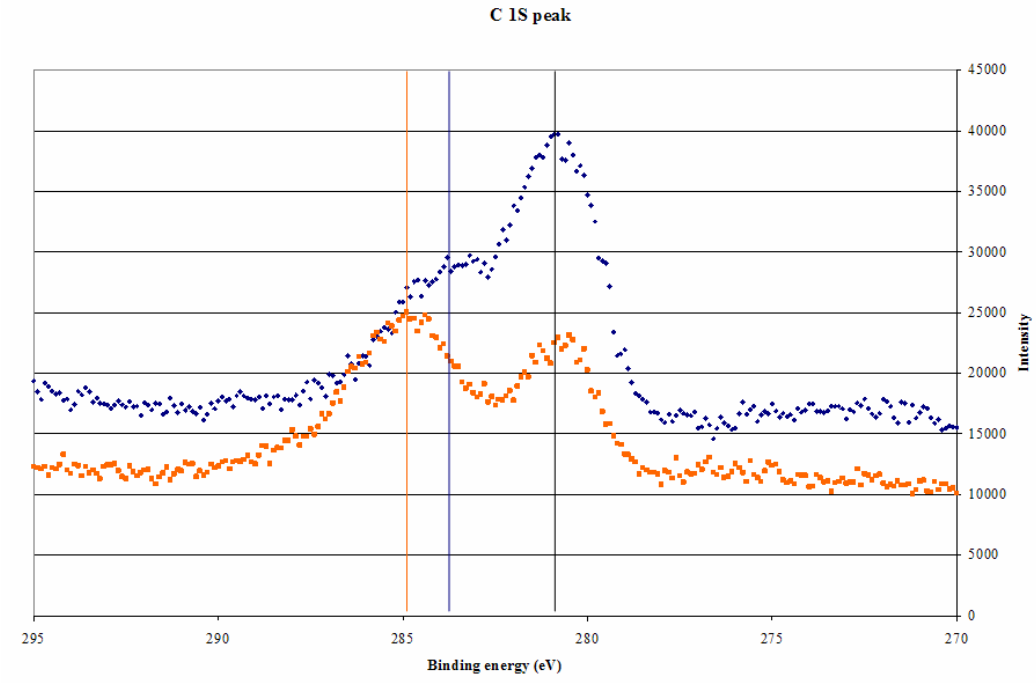

Figure D-12. C1s XPS spectra of unadsorbed (blue) and CO adsorbed (orange) La_2CuO_4 powder.

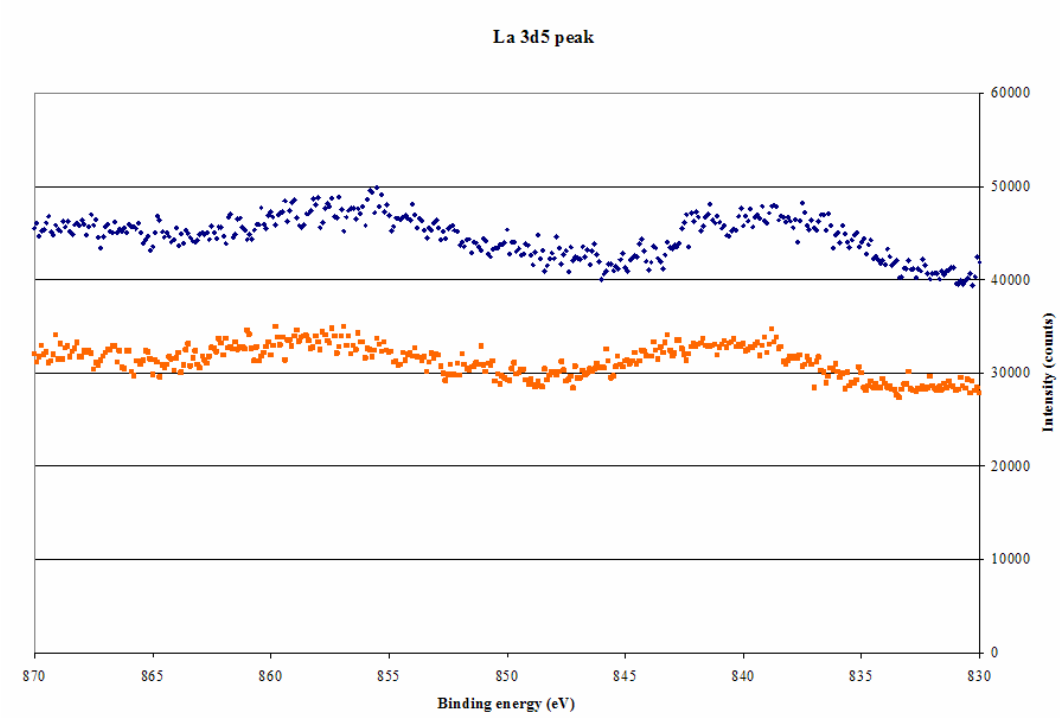

Figure D-13. La3d5 XPS spectra of unadsorbed (blue) and CO adsorbed (orange) La_2CuO_4 powder.

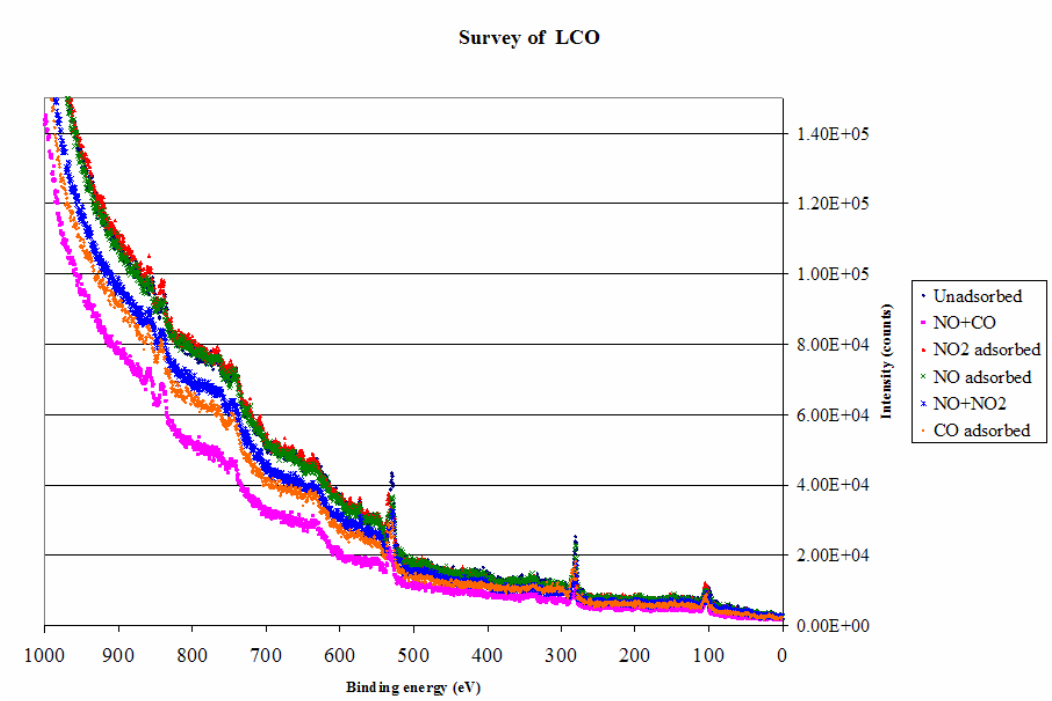

Figure D-14. Full range XPS comparison spectra of unadsorbed and adsorbed La_2CuO_4 powder samples.

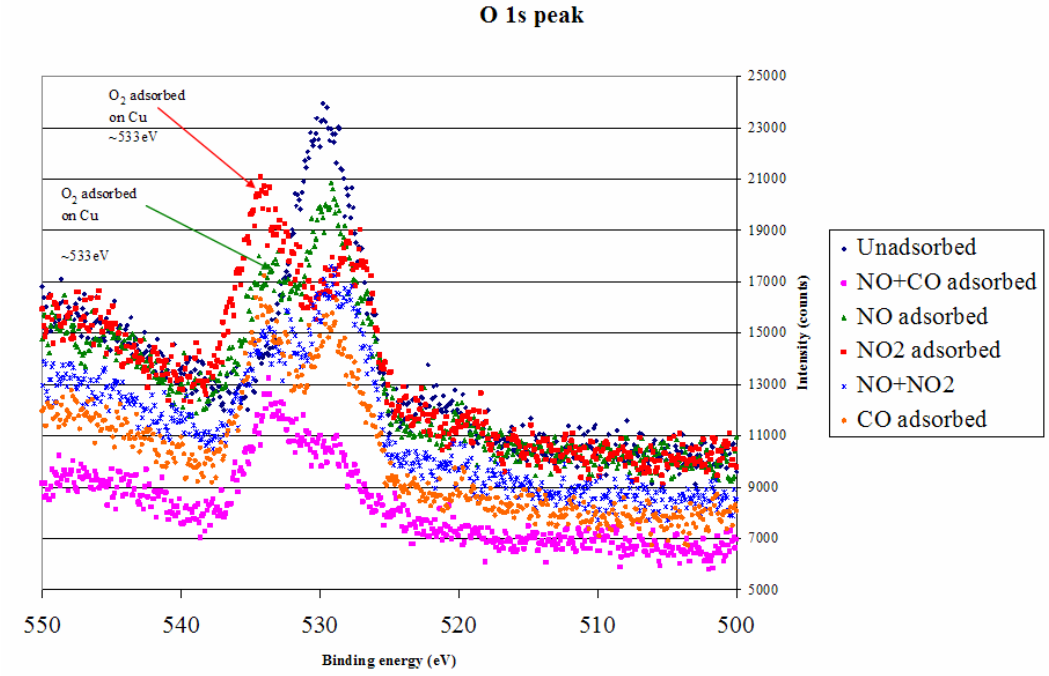

Figure D-15. O1s XPS comparison spectra of unadsorbed and adsorbed La_2CuO_4 powder samples.

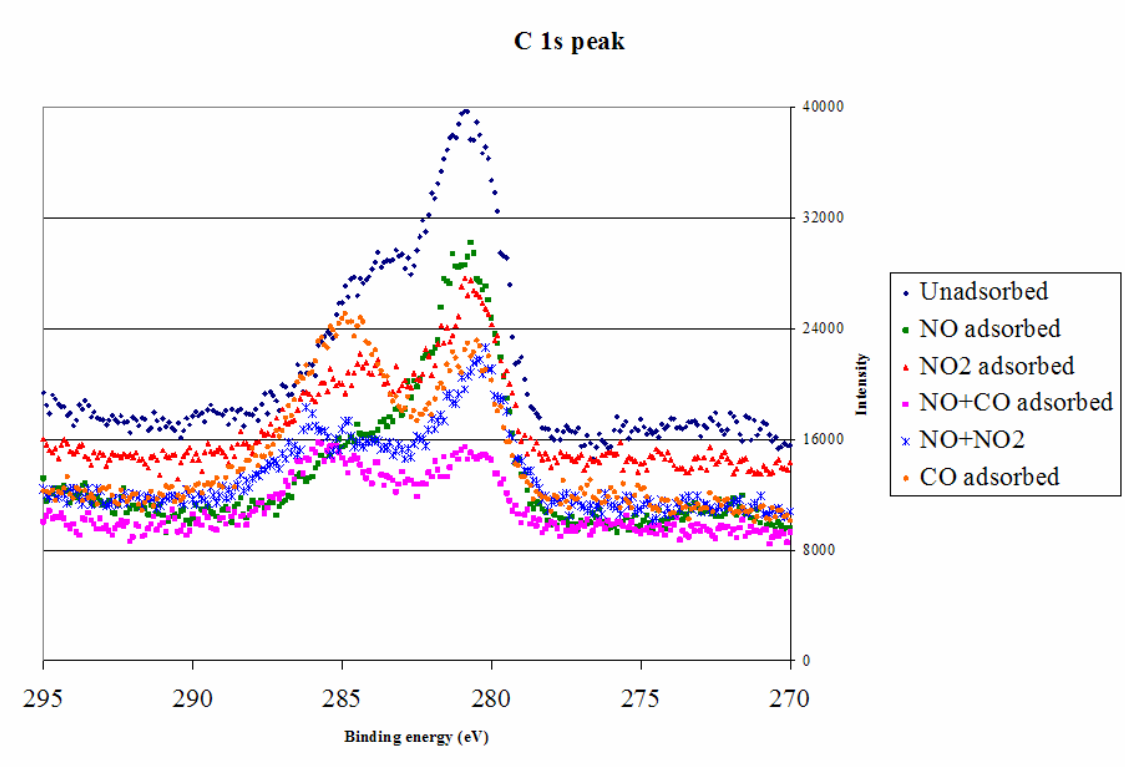

Figure D-16. C1s XPS comparison spectra of unadsorbed and adsorbed La_2CuO_4 powder samples.

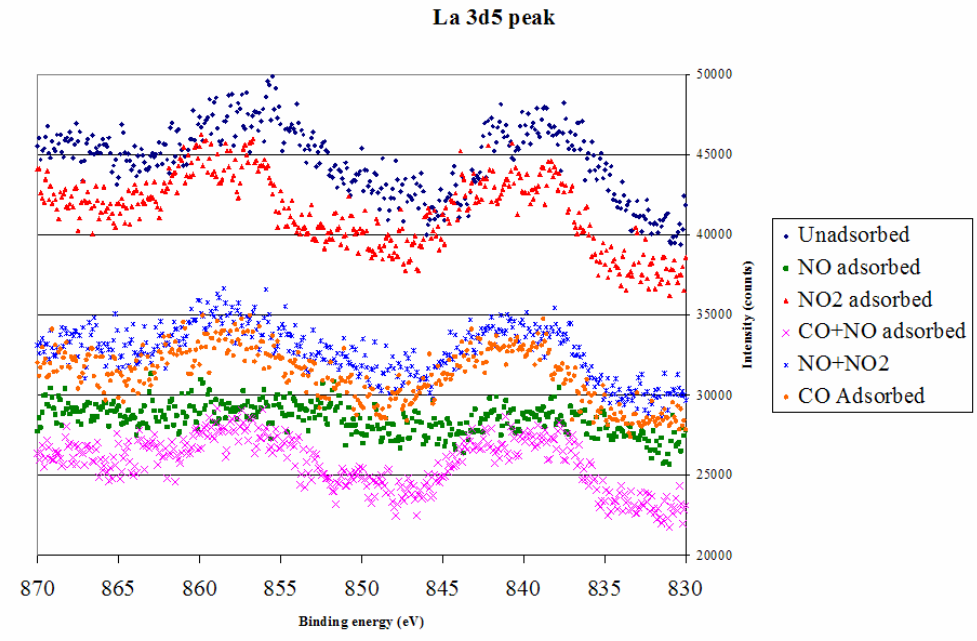

Figure D-17. La3d5 XPS comparison spectra of unadsorbed and adsorbed La_2CuO_4 powder samples.

APPENDIX E
DECONVOLUTED MASS SPECTRA OF ISOTOPICALLY LABELED NOX/LA2CUO4 TPD EXPERIMENTS

Table E-1: Desorption Energy of Peaks for 1% NO and 1% $^{16}O_2$ Adsorption on $La_2Cu^{16}O_4$

Species	Temperature (^oC)	Desorption Energy (kJ/mol)	Peak µmol/m^2 Adsorbed	Total µmol/m^2 Adsorbed	Peak Fit % Error
NO	313	129.62	1.81	16.4	0.9385
	386	146.10	4.40		
	453	161.51	9.15		
	550	183.90	1.03		
$^{16}O_2$	367	141.65	0.629	4.18	1.165
	445	159.69	3.55		
$^{16}O^{18}O$	444	159.31	0.037	0.037	5.567

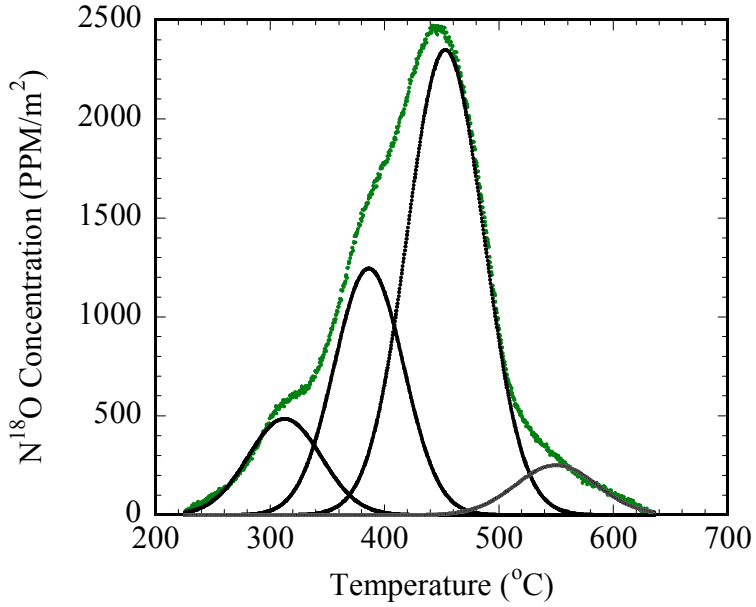

Figure E-1. Desorption Peak of $N^{16}O$ after NO adsorption on $La_2CuO_4{}^{16}$ with Gaussian Analysis

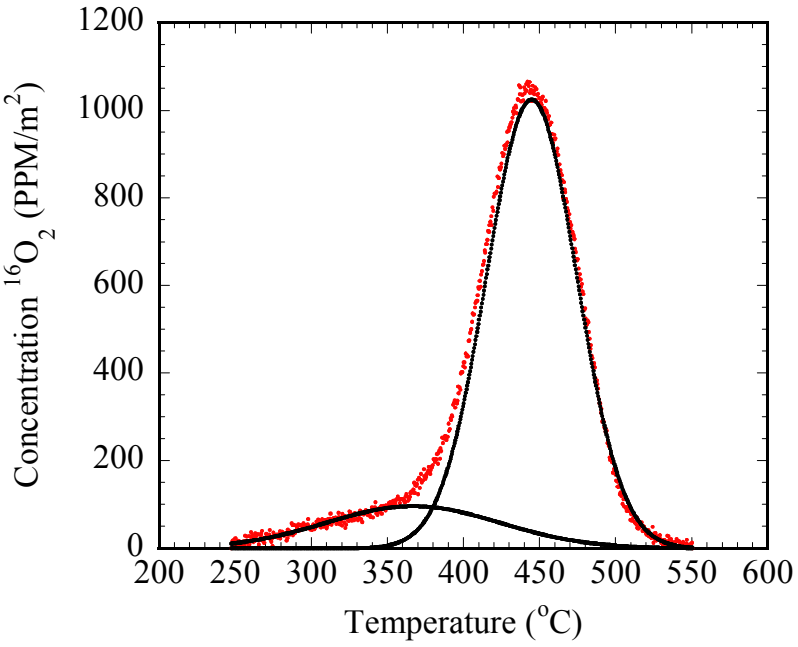

Figure E-2. Desorption Peak of $^{16}O_2$ after NO adsorption on $La_2Cu^{16}O_4$ with Gaussian Analysis

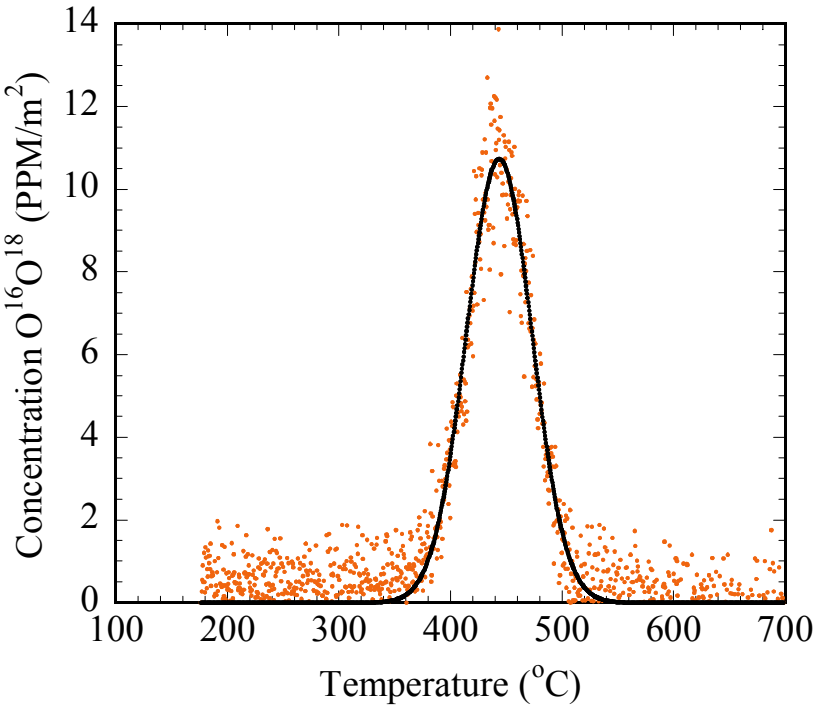

Figure E-3. Desorption Peak of $^{18}O^{16}O$ after NO adsorption on $La_2Cu^{16}O_4$ with Gaussian Analysis

Table E-2: Desorption Energy and Adsorption Capacity for 1% NO and 1% $^{18}O_2$ Adsorption on $La_2Cu^{16}O_4$ Partially Substituted with ^{18}O

Species	Temperature (^oC)	Desorption Energy (kJ/mol)	Peak μmol/m^2 Adsorbed	Total μmol/m^2 Adsorbed	Peak Fit % Error
NO	309	128.45	0.496	3.49	1.334
	419	153.57	1.74		
	505	173.51	1.25		
$^{16}O_2$	423	154.60	2.39	3.43	3.178
	516	176.09	1.04		
$^{16}O^{18}O$	422	154.28	1.20	2.49	1.375
	496	171.36	1.29		
$^{18}O_2$	411	151.77	1.16	1.41	1.411
	510	174.63	0.247		

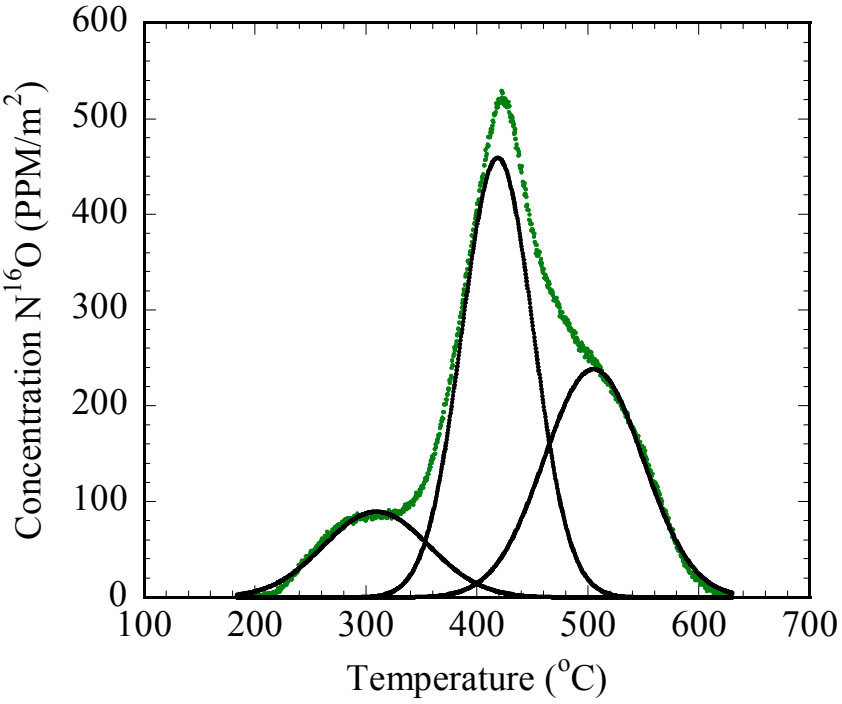

Figure E-4. Desorption Peak of $N^{16}O$ after NO adsorption on partially substituted $La_2Cu^{18}O_4$ with Gaussian Analysis

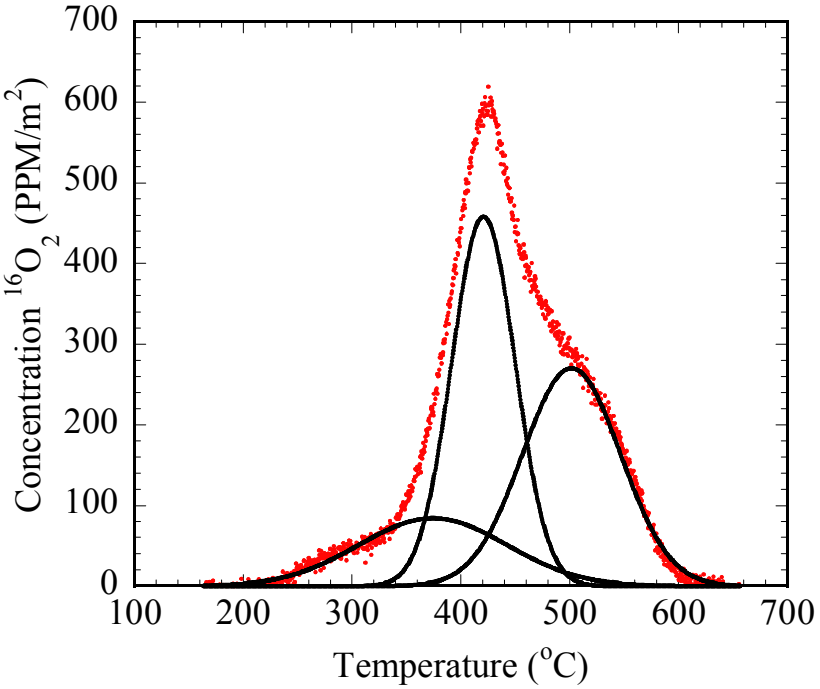

Figure E-5. Desorption Peak of $^{16}O_2$ after NO adsorption on partially substituted $La_2Cu^{18}O_4$ with Gaussian Analysis

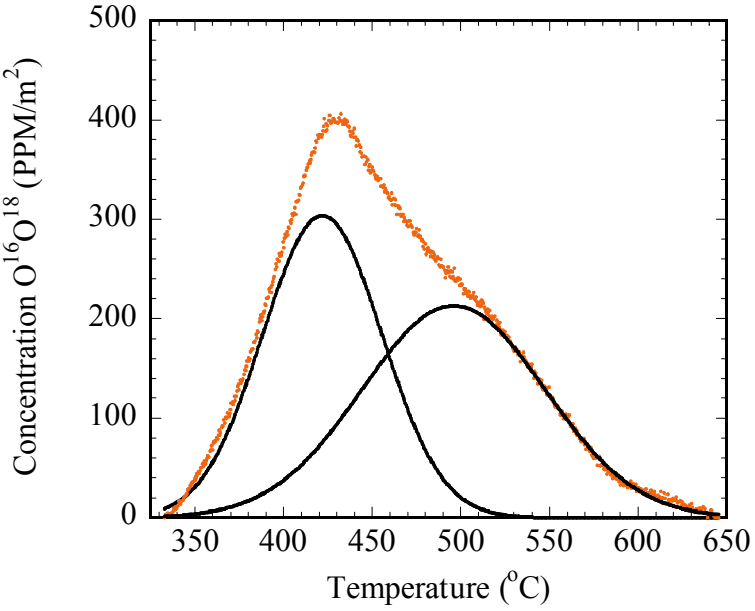

Figure E-6. Desorption Peak of ^{16}O ^{18}O after NO adsorption on partially substituted $La_2Cu^{18}O_4$ with Gaussian Analysis

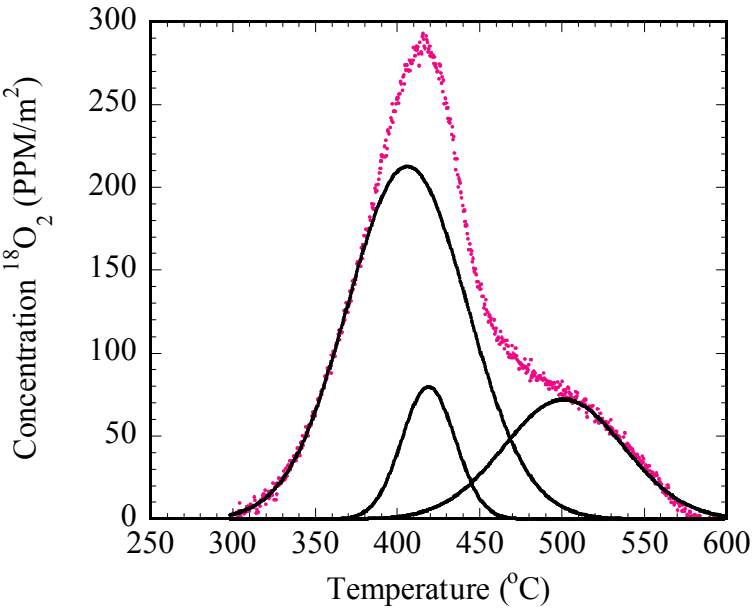

Figure E-7. Desorption Peak of $^{18}O_2$ after NO adsorption on partially substituted $La_2Cu^{18}O_4$ with Gaussian Analysis

Table E-3: Desorption Energy and Adsorption Capacity of $La_2Cu^{18}O_4$ for Adsorption of 1% NO and 1% $^{16}O_2$

Species	Temperature (^{o}C)	Desorption Energy (kJ/mol)	Peak µmol/m^2 Adsorbed	Total µmol/m^2 Adsorbed	Peak Fit % Error
$N^{16}O$	315	543	0.626	4.12	1.15
	420	644	1.54		
	497	718	1.48		
	582	802	0.475		
$^{16}O_2$	383	608	1.57	2.95	2.31
	420	644	1.38		
$^{16}O^{18}O$	433	656	1.17	3.18	2.87
	513	734	2.01		
$^{18}O_2$	427	651	1.14	2.94	2.31
	486	708	1.80		
$N^{18}O$	442	665	0.255	0.717	9.86
	507	728	0.462		

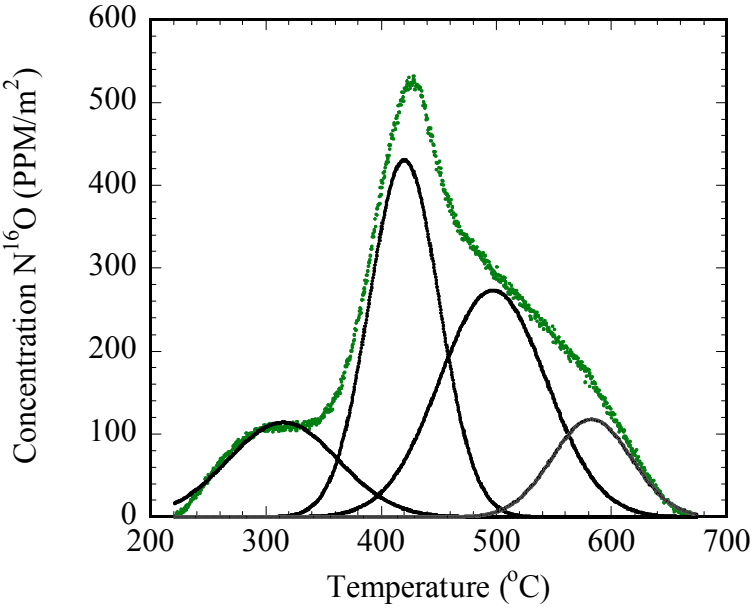

Figure E-8. Desorption Peak of $N^{16}O$ after NO adsorption on $La_2Cu^{18}O_4$ with Gaussian Analysis

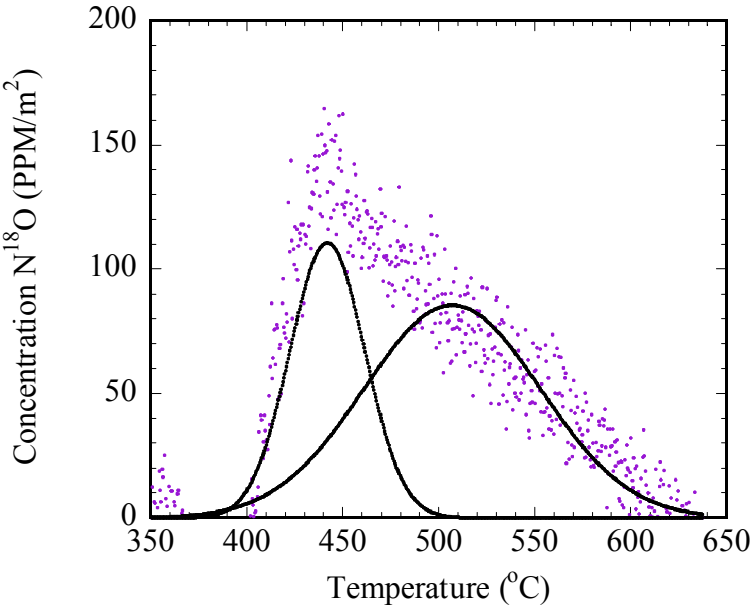

Figure E-9. Desorption Peak of $N^{18}O$ after NO adsorption on $La_2Cu^{18}O_4$ with Gaussian Analysis

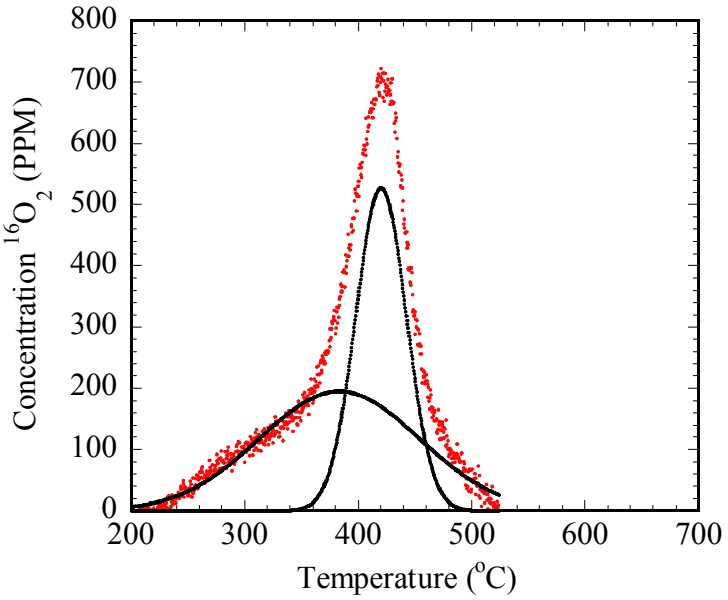

Figure E-10. Desorption Peak of $^{16}O_2$ after NO adsorption on $La_2Cu^{18}O_4$ with Gaussian Analysis

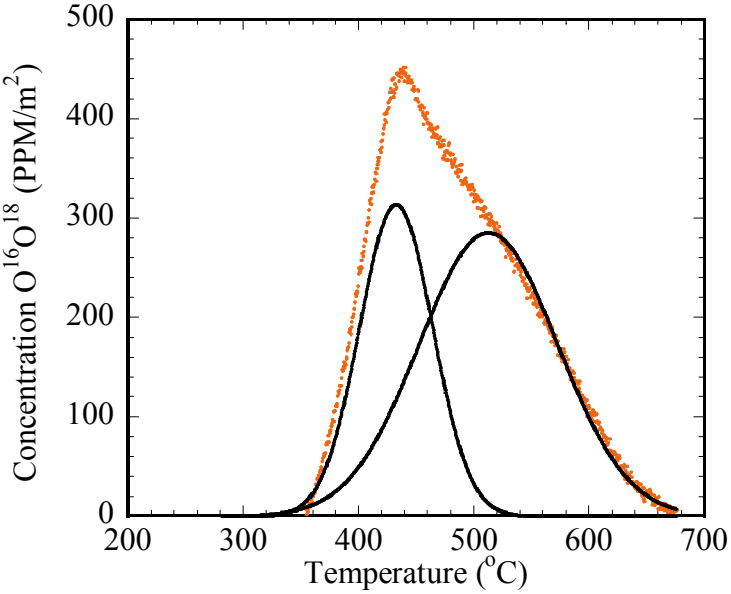

Figure E-11. Desorption Peak of ^{16}O ^{18}O after NO adsorption on $La_2Cu^{18}O_4$ with Gaussian Analysis

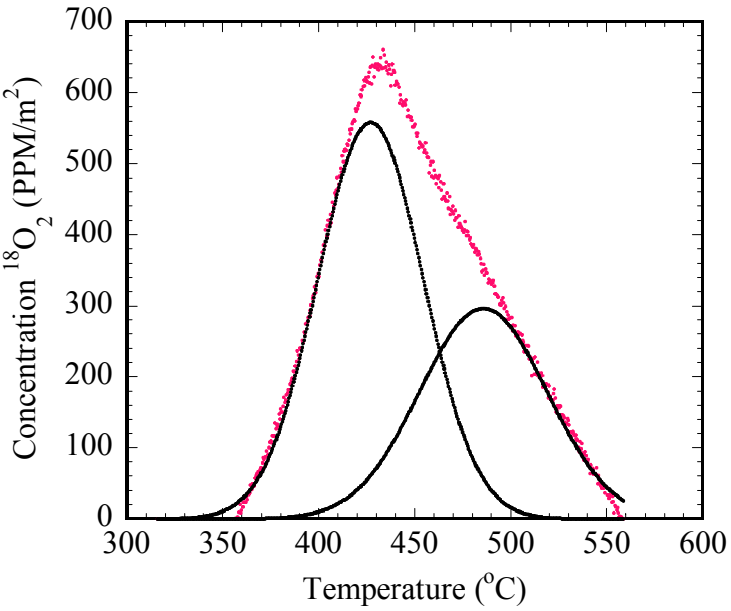

Figure E-12. Desorption Peak of $^{18}O_2$ after NO adsorption on $La_2Cu^{18}O_4$ with Gaussian Analysis

Table E-4: Desorption Energy and Adsorption Capacity for 1% NO_2 and 1% $^{18}O_2$ Adsorption on $La_2Cu^{16}O_4$

Species	Temperature (^{o}C)	Desorption Energy (kJ/mol)	Peak µmol/m^2 Adsorbed	Total µmol/m^2 Adsorbed	Peak Fit % Error
$N^{16}O$	370.9	142.59	0.217	5.03	1.530
	431.7	156.58	3.45		
	485.4	168.98	1.36		
$^{16}O_2$	426.1	155.29	4.16	4.89	0.6498
	433.5	156.99	0.214		
	497.6	171.79	0.516		
$^{16}O^{18}O$	427.0	155.51	0.102	0.114	3.928
	512.8	175.32	0.0118		
$^{18}O_2$	416.9	153.18	0.065	0.065	8.580
$N^{16}O_2$	333.9	134.10	1.46	14.54	0.8011
	343.3	136.25	7.56		
	398.2	148.87	5.52		

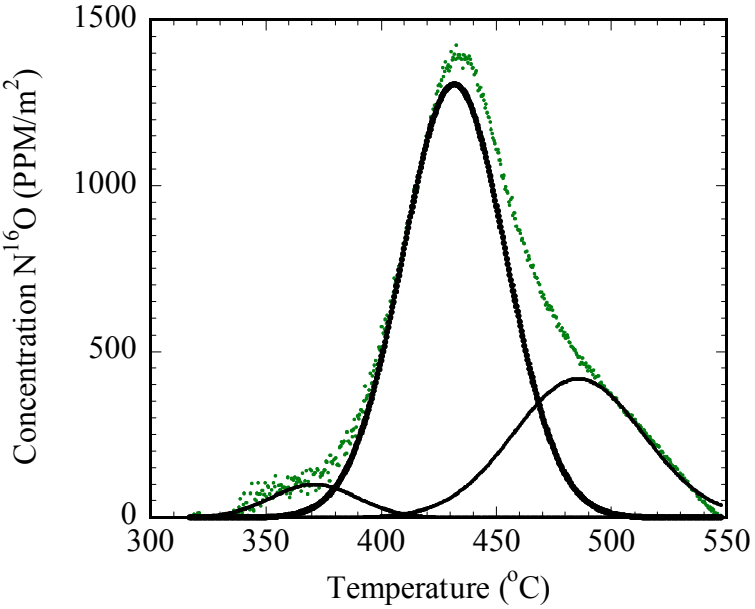

Figure E-13. Desorption Peak of $N^{16}O$ after NO_2 adsorption on $La_2Cu^{16}O_4$ with Gaussian Analysis

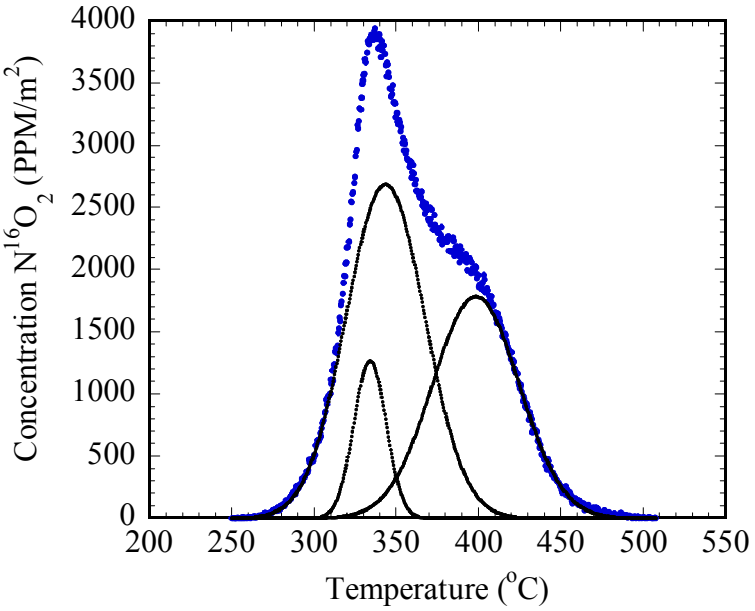

Figure E-14. Desorption Peak of $N^{16}O_2$ after NO_2 adsorption on $La_2Cu^{16}O_4$ with Gaussian Analysis

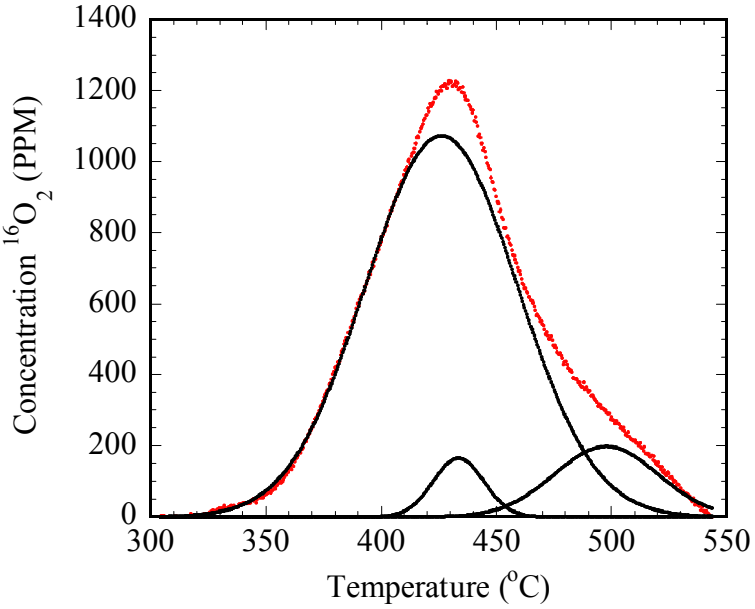

Figure E-15. Desorption Peak of $^{16}O_2$ after NO_2 adsorption on $La_2Cu^{16}O_4$ with Gaussian Analysis

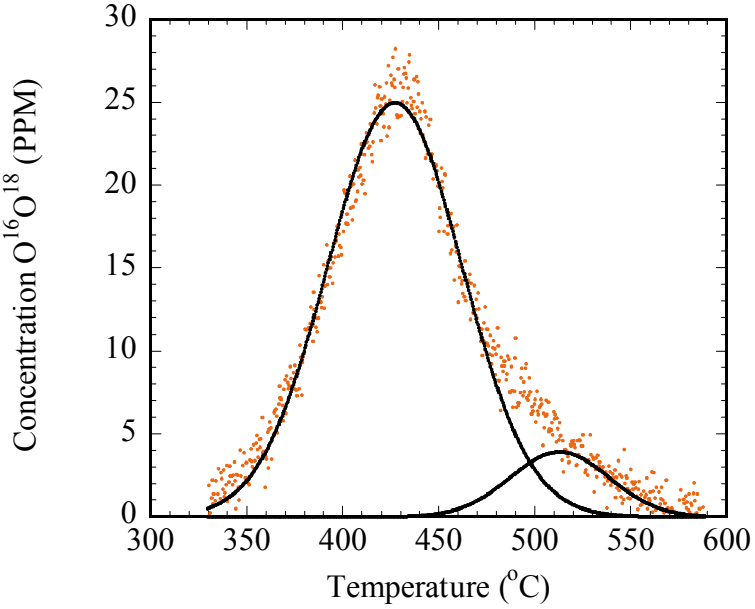

Figure E-16. Desorption Peak of ^{16}O ^{18}O after NO_2 adsorption on $La_2Cu^{16}O_4$ with Gaussian Analysis

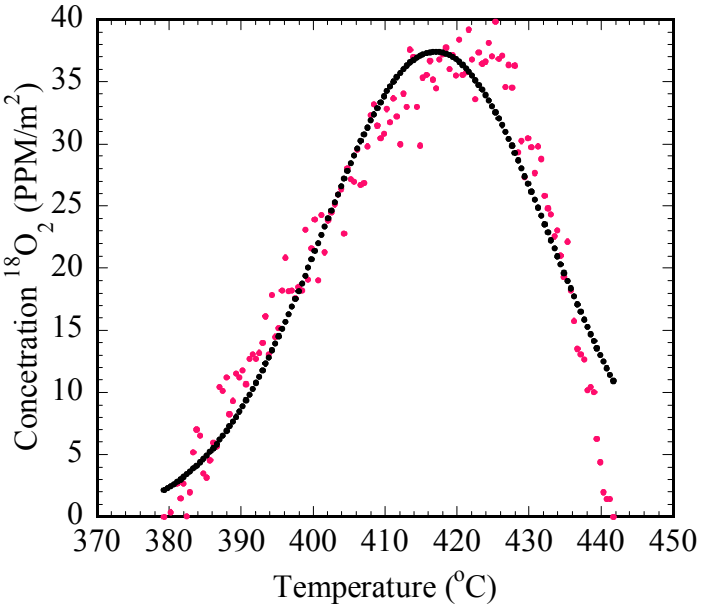

Figure E-17. Desorption Peak of $^{18}O_2$ after NO_2 adsorption on $La_2Cu^{16}O_4$ with Gaussian Analysis

Table E-5: Desorption Energy of Peaks for 1% NO_2 and 1% $^{18}O_2$ Adsorption on $La_2Cu^{16}O_4$ Partially Substituted with ^{18}O

Species	Temperature (^{o}C)	Desorption Energy (kJ/mol)	Peak µmol/m^2 Adsorbed	Total µmol/m^2 Adsorbed	Peak Fit % Error
$N^{16}O$	443.9	159.40	5.18	5.85	2.531
	542.5	182.20	0.665		
$^{16}O^{16}O$	311.8	129.03	0.279	3.72	1.719
	381.9	145.13	0.473		
	445.3	159.73	2.28		
	526.0	178.38	0.686		
$^{16}O^{18}O$	452.2	161.32	1.41	1.80	1.930
	529.6	179.21	0.390		
$^{18}O^{18}O$	453.3	161.57	0.598	0.764	1.956
	510.4	174.76	0.166		
$N^{18}O$	349.3	137.63	0.357	0.679	9.500
	466.2	164.55	0.322		9.861
$N^{16}O^{16}O$	344.1	136.45	1.94	4.66	1.636
	367.6	141.84	2.72		
$N^{16}O^{18}O$	360.8	140.28	0.122	0.122	6.731

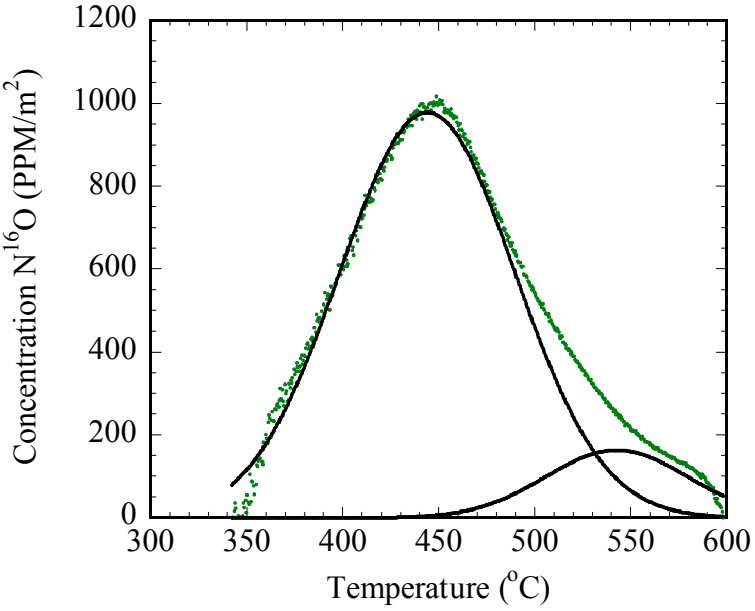

Figure E-18. Desorption Peak of $N^{16}O$ after NO_2 adsorption on partially substituted $La_2Cu^{18}O_4$ with Gaussian Analysis

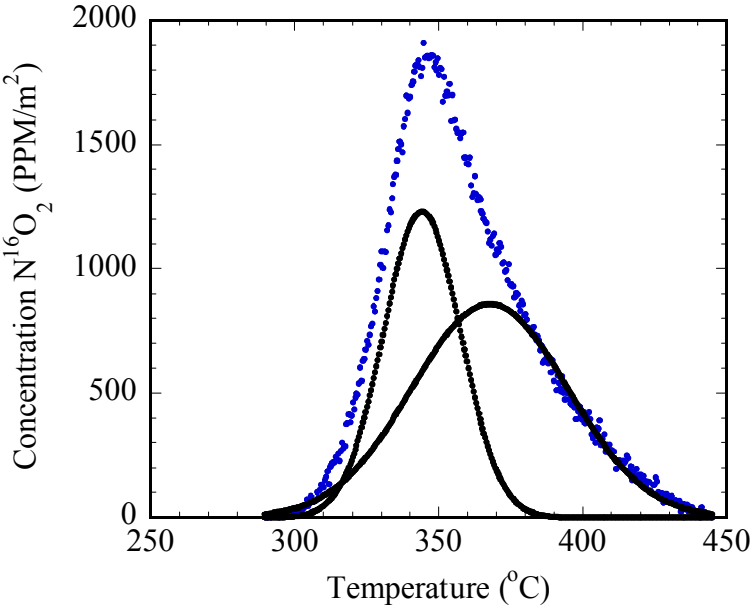

Figure E-19. Desorption Peak of $N^{16}O_2$ after NO_2 adsorption on partially substituted $La_2Cu^{18}O_4$ with Gaussian Analysis

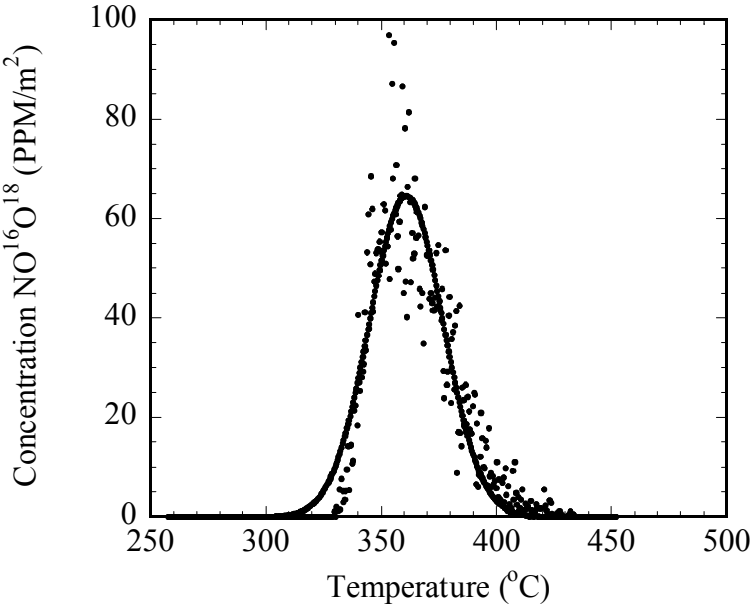

Figure E-20. Desorption Peak of $N^{16}O^{18}O$ after NO_2 adsorption on partially substituted $La_2Cu^{18}O_4$ with Gaussian Analysis

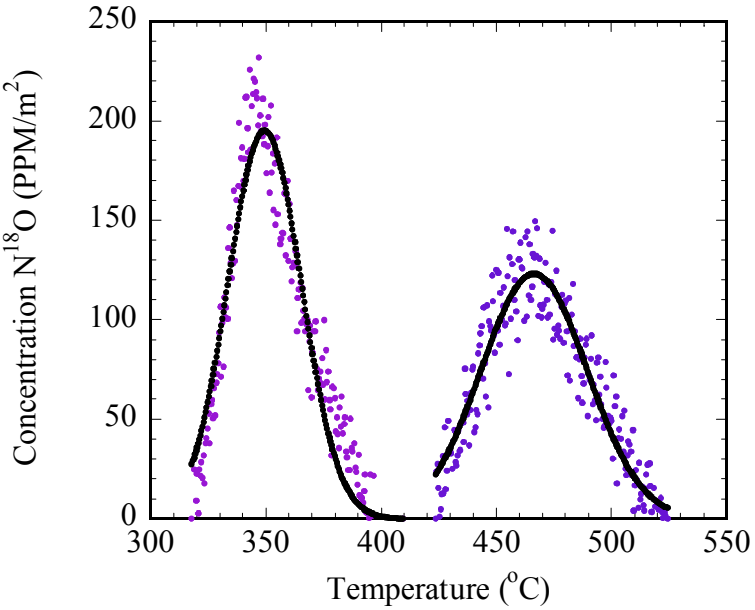

Figure E-21. Desorption Peak of $N^{18}O$ after NO_2 adsorption on partially substituted $La_2Cu^{18}O_4$ with Gaussian Analysis

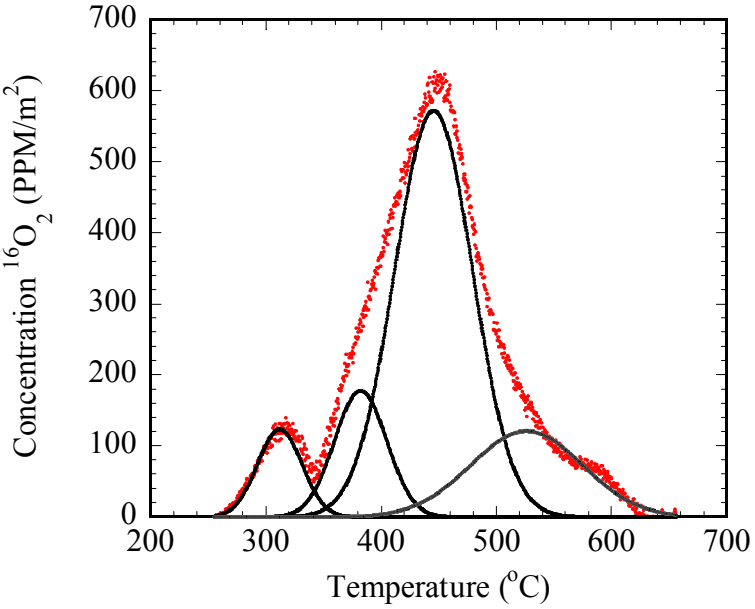

Figure E-22. Desorption Peak of $^{16}O_2$ after NO_2 adsorption on partially substituted $La_2Cu^{18}O_4$ with Gaussian Analysis

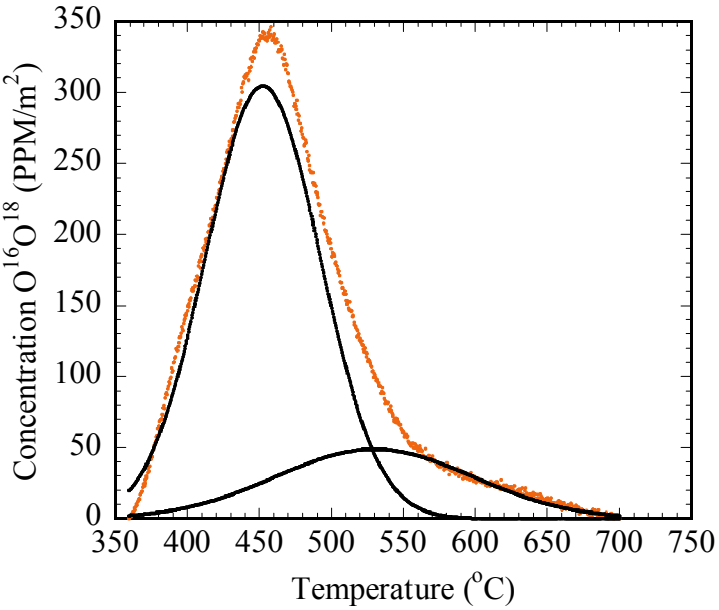

Figure E-23. Desorption Peak of $^{16}O^{18}O$ after NO_2 adsorption on partially substituted $La_2Cu^{18}O_4$ with Gaussian Analysis

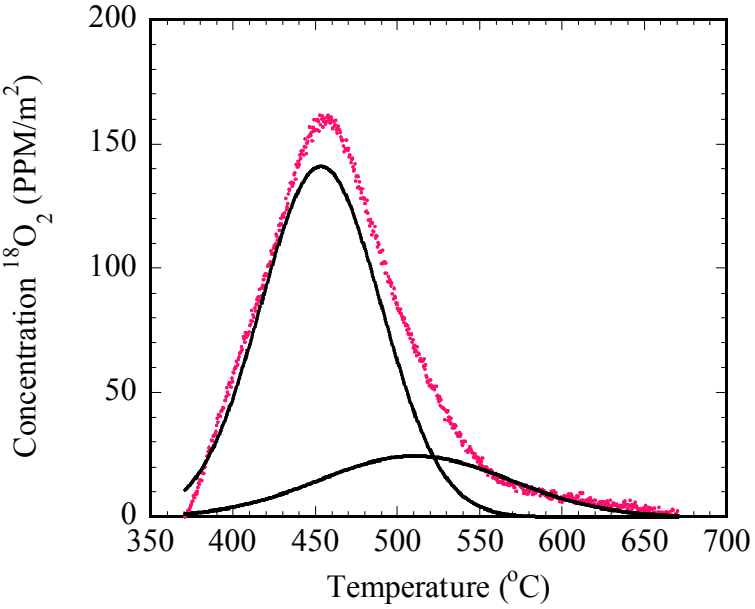

Figure E-24. Desorption Peak of $^{18}O_2$ after NO_2 adsorption on partially substituted $La_2Cu^{18}O_4$ with Gaussian Analysis

Table E-11: Desorption Energy and Adsorption Capacity for 1% NO_2 and 1% $^{16}O_2$ Adsorption on $La_2Cu^{18}O_4$

Species	Temperature (^oC)	Desorption Energy (kJ/mol)	Peak μmol/m^2 Adsorbed	Total μmol/m^2 Adsorbed	Peak Fit % Error
$N^{16}O$	434	658	5.28	7.66	2.77
	549	769	2.39		
$^{16}O_2$	392	617	1.04	2.88	2.18
	441	664	1.84		
$^{16}O^{18}O$	422	647	0.150	0.227	4.24
	446	669	0.0770		
$^{18}O_2$	425	649	0.0897	0.212	3.09
	452	675	0.122		
$N^{18}O$	347	574	0.357	1.17	6.51
	457	680	0.812		
$N^{16}O_2$	340	567	2.47	7.48	1.27
	362	589	3.81		
	404	629	1.20		
$N^{16}O^{18}O$	350	577	0.268	0.650	6.81
	382	608	0.381		

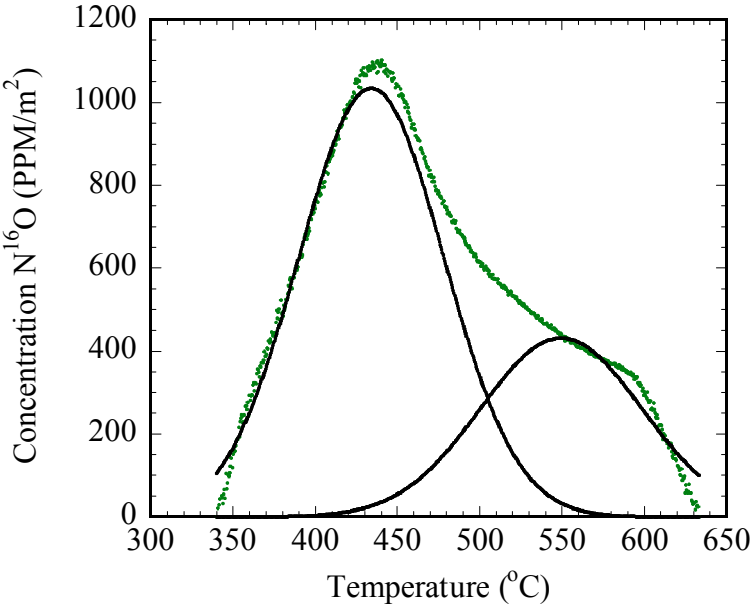

Figure E-25. Desorption Peak of $N^{16}O$ after NO_2 adsorption on $La_2Cu^{18}O_4$ with Gaussian Analysis

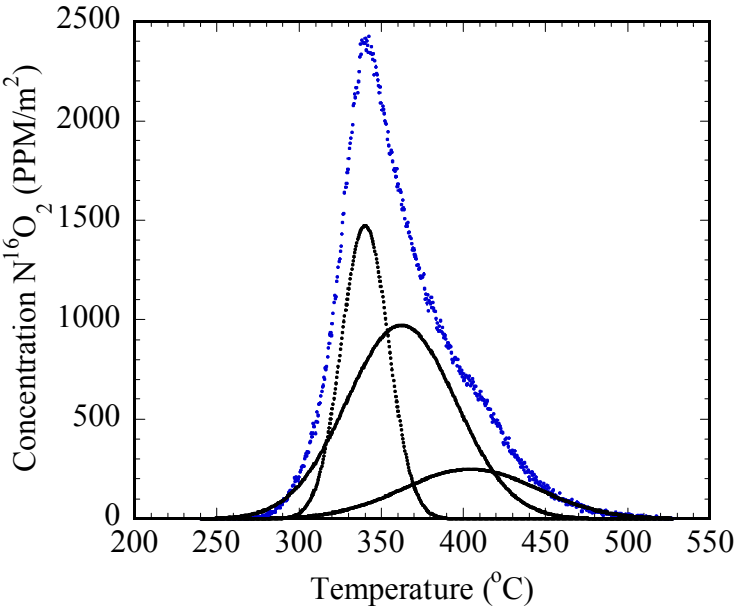

Figure E-26. Desorption Peak of $N^{16}O_2$ after NO_2 adsorption on $La_2Cu^{18}O_4$ with Gaussian Analysis

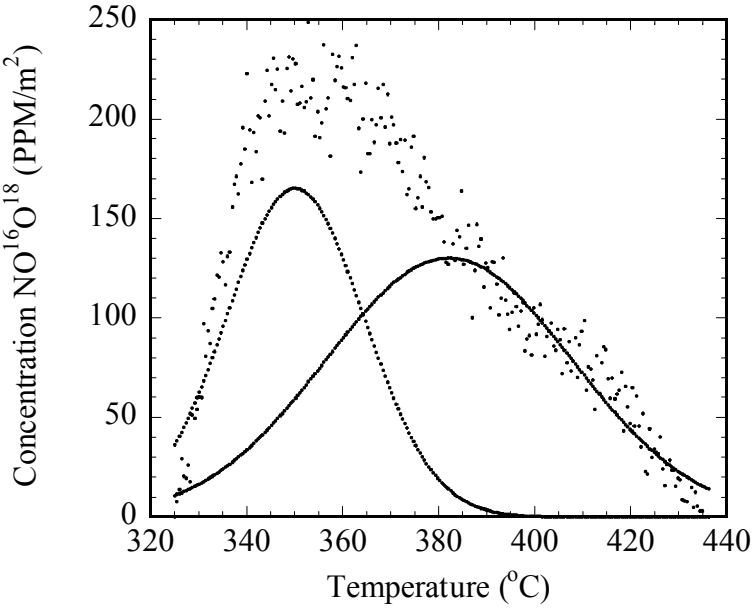

Figure E-27. Desorption Peak of $N^{16}O^{18}O$ after NO_2 adsorption on $La_2Cu^{18}O_4$ with Gaussian Analysis

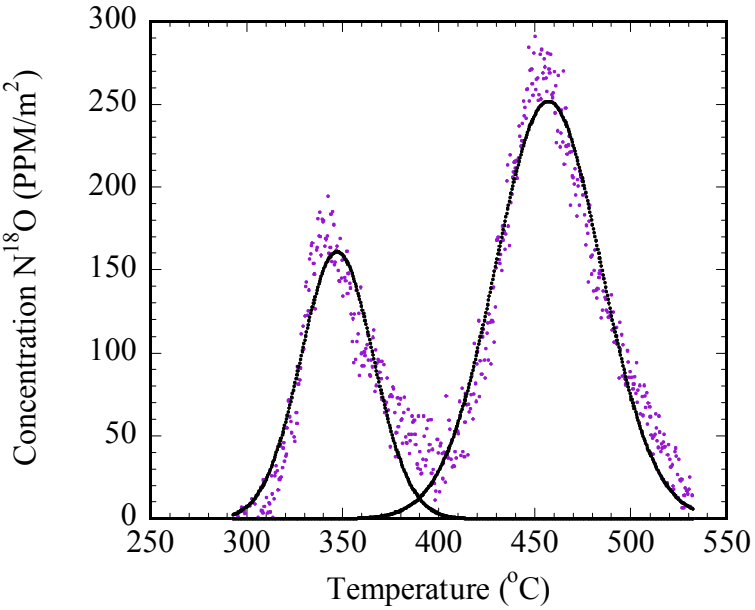

Figure E-28. Desorption Peak of $N^{18}O$ after NO_2 adsorption on $La_2Cu^{18}O_4$ with Gaussian Analysis

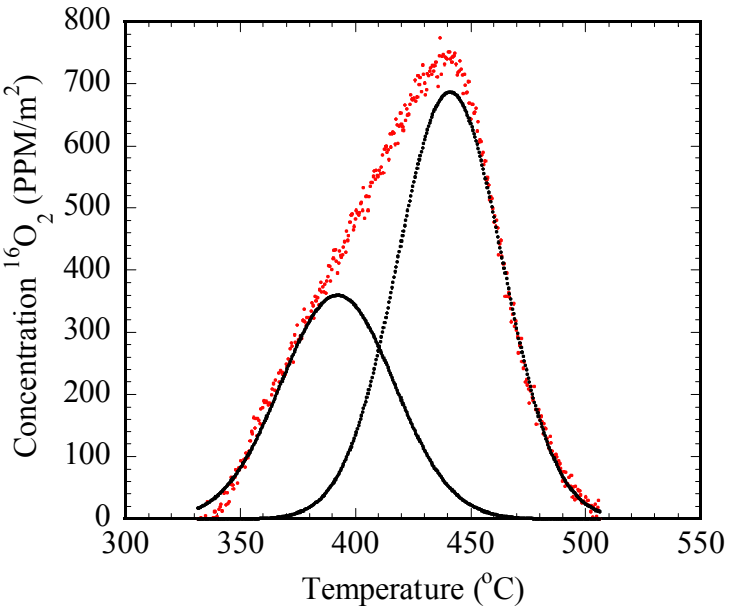

Figure E-29. Desorption Peak of $^{16}O_2$ after NO_2 adsorption on $La_2Cu^{18}O_4$ with Gaussian Analysis

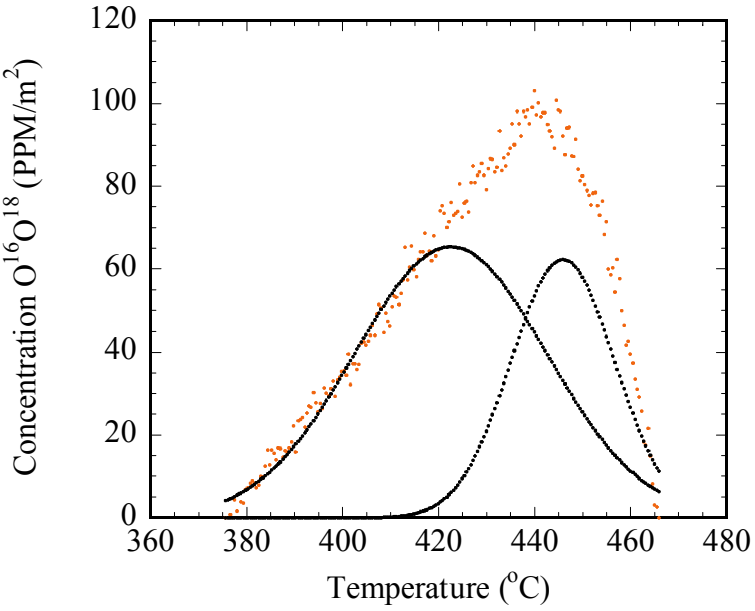

Figure E-30. Desorption Peak of $^{16}O^{18}O$ after NO_2 adsorption on $La_2Cu^{18}O_4$ with Gaussian Analysis

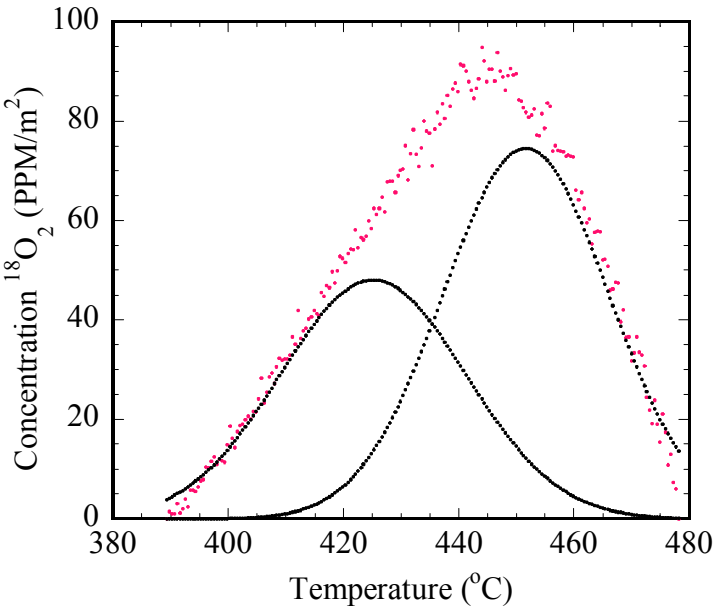

Figure E-31. Desorption Peak of $^{18}O_2$ after NO_2 adsorption on $La_2Cu^{18}O_4$ with Gaussian Analysis

LIST OF REFERENCES

1. de Sa, R. A. B.; da Silva, R. M. C. F.; Dauzacker, E. R. Mathematical Model to Predict the Otto Cycle Vehicles Exhaust Emissions From Automotive Gasoline Consumption. In *Emissions Measurement and Testing, Advanced Catalysts and Substrates, and Diesel Gaseous Emissions*, Society of Automotive Engineers, Inc.: Warrendale, PA, 2004; pp 27-54.

2. H.Oshima, M.Tatemichi, and T.Sawa, "Chemical Basis of Inflammation Induced Carcinogenesis," *Archives of Biochemistry and Biophysics,* [417] 3-11 (2003).

3. J. N. Seinfeld, and S. N. Pandis, *Atmospheric Chemistry and Physics From Air Pollution to Climate Change* John Wiley and Sons, New York, 1997.

4. E. Gutt, V. Patton, and N. Spencer. Building on 30 Years of Clean Air Act Success: The Case for Reducing NO_X Air Pollution. *Retrieved January 5, 2007, from www.environmentaldefense.org.*

5. W. J. Fleming, "Physical Principles Governing Nonideal Behavior of Zirconia Oxygen Sensor," *Journal of the Electrochemical Society,* 123 [8] C237 (1976).

6. W. J. Fleming, "Physical Principles Governing Nonideal Behavior of Zirconia Oxygen Sensor," *Journal of the Electrochemical Society,* 124 [1] 21-28 (1977).

7. B. M. White, E. Macam, F. M. Van Assche, E. Traversa, and E. D. Wachsman, "A Theoretical Framework for Predicting Solid-State Potentiometric Gas Sensor Behavior" pp 179. in Proceedings of the 210th Meeting of The Electrochemical Society, Vol. 3, *Chemical Sensors 7 - and MEMS/NEMS 7, ECS Transactions.* Edited by G. Hunder, S. Akbar, S. Bhansali, O. Brand, C. Bruckner-Lea, M. Carter, J. Davidson, E. Enikov, P. Hesketh, R. Hillman, C. Kranz, J. Li, R. Maboudian, R. Mukundan, C. Roper, S. Shoji, A. Simonian, and M. Tabib-Azar. The Electrochemical Society, Pennington, NJ, 2006.

8. S. Akbar, P. Dutta, and C. H. Lee, "High-Temperature Ceramic Gas Sensors: A Review," *International Journal of Applied Ceramic Technology,* 3 [4] 302-311 (2006).

9. A. D. Brailsford, M. Yussouff, and E. M. Logothetis, "Theory of Gas Sensors," *Sensors and Actuators B-Chemical,* 13 [1-3] 135-138 (1993).

10. A. D. Brailsford, M. Yussouff, and E. M. Logothetis, "Steady State Model of Electrochemical Gas Sensors With Multiple Reactions," *Sensors and Actuators B-Chemical,* 36 [1-3] 392-397 (1996).

11. A. D. Brailsford, M. Yussouff, and E. M. Logothetis, "Theory of Gas Sensors: Response of an Electrochemical Sensor to Multi-Component Gas Mixtures," *Sensors and Actuators B-Chemical,* 34 [1-3] 407-411 (1996).

12. A. D. Brailsford, M. Yussouff, E. M. Logothetis, T. Wang, and R. E. Soltis, "Experimental and Theoretical Study of the Response of ZrO_2 Oxygen Sensors to Simple One-Reducing-Gas Mixtures," *Sensors and Actuators B-Chemical,* 42 [1] 15-26 (1997).

13. E. L. Brosha, R. Mukundan, R. Lujan, and F. H. Garzon, "Mixed Potential NO_X Sensors Using Thin Film Electrodes and Electrolytes for Stationary Reciprocating Engine Type Applications," *Sensors and Actuators B-Chemical,* 119 [2] 398-408 (2006).

14. L. Chevallier, M. L. Grilli, E. Di Bartolomeo, and E. Traversa, "Non-Nernstian Planar Sensors Based on YSZ With Ta (10 at.%)-Doped Nanosized Titania As a Sensing Electrode for High-Temperature Applications," *International Journal of Applied Ceramic Technology,* 3 [5] 393-400 (2006).

15. L. Chevallier, E. Di Bartolomeo, M. L. Grilli, M. Mainas, B. M. White, E. D. Wachsman, and E. Traversa, "Non-Nerstian Planar Sensors Based on YSZ With an Nb_2O_5 Electrode: Discussion on Sensing Mechanism" pp 163. in Proceedings of the 208th Meeting of The Electrochemical Society, Vol. 1, *Solid State Ionic Devices IV, ECS Transactions.* Edited by E. D. Wachsman, V. Birss, F. H. Garzon, R. Mukundan, and E. Traversa. The Electrochemical Society, Pennington, NJ, 2006.

16. E. Comini, G. Faglia, and G. Sberveglieri, "UV Light Activation of Tin Oxide Thin Films for NO_2 Sensing at Low Temperatures," *Sensors and Actuators B-Chemical,* 78 [1-3] 73-77 (2001).

17. E. Comini, G. Faglia, G. Sberveglieri, D. Calestani, L. Zanotti, and M. Zha, "Tin Oxide Nanobelts Electrical and Sensing Properties," *Sensors and Actuators B-Chemical,* 111 2-6 (2005).

18. E. Di Bartolomeo, E. Traversa, M. Baroncini, V. Kotzeva, and R. V. Kumar, "Solid State Ceramic Gas Sensors Based on Interfacing Ionic Conductors With Semiconducting Oxides," *Journal of the European Ceramic Society,* 20 [16] 2691-2699 (2000).

19. E. Di Bartolomeo, M. L. Grilli, and E. Traversa, "Sensing Mechanism of Potentiometric Gas Sensors Based on Stabilized Zirconia With Oxide Electrodes: Is It Always Mixed Potential?" pp 222. in Proceedings of the 202nd Meeting of The Electrochemical Society, Vol. 2002-26, *Solid State Ionic Devices III.* Edited by E. D. Wachsman, K. Swider-Lyons, M. F. Carolan, F. H. Garzon, M. Liu, and J. R. Stetter. The Electrochemical Society, Pennington, NJ, 2003.

20. E. Di Bartolomeo, M. L. Grilli, J. W. Yoon, and E. Traversa, "Zirconia-Based Electrochemical NO_X Sensors With Semiconducting Oxide Electrodes," *Journal of the American Ceramic Society,* 87 [10] 1883-1889 (2004).

21. E. Di Bartolomeo, M. L. Grilli, and E. Traversa, "Sensing Mechanism of Potentiometric Gas Sensors Based on Stabilized Zirconia With Oxide Electrodes - Is It Always

Mixed Potential?," *Journal of the Electrochemical Society,* 151 [5] H133-H139 (2004).

22. E. Di Bartolomeo, N. Kaabbuathong, M. L. Grilli, and E. Traversa, "Planar Electrochemical Sensors Based on Tape-Cast YSZ Layers and Oxide Electrodes," *Solid State Ionics,* 171 [3-4] 173-181 (2004).

23. E. Di Bartolomeo, N. Kaabbuathong, A. D'Epifanio, M. L. Grilli, E. Traversa, H. Aono, and Y. Sadaoka, "Nano-Structured Perovskite Oxide Electrodes for Planar Electrochemical Sensors Using Tape Casted YSZ Layers," *Journal of the European Ceramic Society,* 24 [6] 1187-1190 (2004).

24. E. Di Bartolomeo, M. L. Grilli, N. Antonias, S. Cordiner, and E. Traversa, "Testing Planar Gas Sensors Based on Yttria-Stabilized Zirconia With Oxide Electrodes in the Exhaust Gases of a Spark Ignition Engine," *Sensor Letters,* 3 [1] 22-26 (2005).

25. A. Dutta, N. Kaabbuathong, M. L. Grilli, E. Di Bartolomeo, and E. Traversa, "Study of YSZ-Based Electrochemical Sensors With WO_3 Electrodes in NO_2 and CO Environments," *Journal of the Electrochemical Society,* 150 [2] H33-H37 (2003).

26. A. Dutta, D. Das, M. L. Grilli, E. Di Bartolomeo, E. Traversa, and D. Chakravorty, "Preparation of Sol-Gel Nano-Composites Containing Copper Oxide and Their Gas Sensing Properties," *Journal of Sol-Gel Science and Technology,* 26 [1-3] 1085-1089 (2003).

27. A. Dutta and T. Ishihara, "Amperometric NOX Sensor Based on Oxygen Pumping Current by Using LaGaO3-Based Solid Electrolyte for Monitoring Exhaust Gas," *Sensors and Actuators B-Chemical,* 108 [1-2] 309-313 (2005).

28. P. Elumalai, J. Wang, S. Zhuiykov, D. Terada, M. Hasei, and N. Miura, "Sensing Characteristics of YSZ-Based Mixed-Potential-Type Planar NO_X Sensors Using NiO Sensing Electrodes Sintered at Different Temperatures," *Journal of the Electrochemical Society,* 152 [7] H95-H101 (2005).

29. P. Elumalai and N. Miura, "Performances of Planar NO_2 Sensor Using Stabilized Zirconia and NiO Sensing Electrode at High Temperature," *Solid State Ionics,* 176 [31-34] 2517-2522 (2005).

30. F. H. Garzon, R. Mukundan, R. Lujan, and E. L. Brosha, "Solid State Ionic Devices for Combustion Gas Sensing," *Solid State Ionics,* 175 [1-4] 487-490 (2004).

31. W. Gopel, G. Reinhardt, and M. Rosch, "Trends in the Development of Solid State Amperometric and Potentiometric High Temperature Sensors," *Solid State Ionics,* 136 519-531 (2000).

32. M. L. Grilli, E. Di Bartolomeo, and E. Traversa, "Electrochemical NO_X Sensors Based on Interfacing Nanosized $LaFeO_3$ Perovskite-Type Oxide and Ionic Conductors," *Journal of the Electrochemical Society,* 148 [9] H98-H102 (2001).

33. M. L. Grilli, N. Kaabbuathong, A. Dutta, E. Di Bartolomeo, and E. Traversa, "Electrochemical NO_2 Sensors With WO_3 Electrodes for High Temperature Applications," *Journal of the Ceramic Society of Japan,* 110 [3] 159-162 (2002).

34. M. L. Grilli, E. Di Bartolomeo, and E. Traversa, "NO_X Sensors Based on Interfacing Yttria Stabilized Zirconia With P and N-Type Semiconducting Oxides," *Euro Ceramics Vii, Pt 1-3,* 206-2 1243-1246 (2002).

35. M. L. Grilli, E. Di Bartolomeo, A. Lunardi, L. Chevallier, S. Cordiner, and E. Traversa, "Planar Non-Nernstian Electrochemical Sensors: Field Test in the Exhaust of a Spark Ignition Engine," *Sensors and Actuators B-Chemical,* 108 [1-2] 319-325 (2005).

36. H. Kaneko, H. Taimatsu, Y. Miyoshi, K. Kawanaka, and T. Kusano, "YSZ/Ag Potentiometric Sensor for Reducing Gas-Detection," *Sensors and Actuators B-Chemical,* 13 [1-3] 151-154 (1993).

37. G. Y. Lu, N. Miura, and N. Yamazoe, "High-Temperature Hydrogen Sensor Based on Stabilized Zirconia and a Metal Oxide Electrode," *Sensors and Actuators B-Chemical,* 35 [1-3] 130-135 (1996).

38. G. Y. Lu, N. Miura, and N. Yamazoe, "Mixed Potential Hydrogen Sensor Combining Oxide Ion Conductor With Oxide Electrode," *Journal of the Electrochemical Society,* 143 [7] L154-L155 (1996).

39. C. M. Mari, "Non-Nernstian Solid State Gas Sensors: Operating Principles and Materials," *Ionics,* 9 [5-6] 365-369 (2003).

40. N. Miura, S. Yao, Y. Shimizu, and N. Yamazoe, "Development of High-Performance Solid-Electrolyte Sensors for NO and NO_2," *Sensors and Actuators B-Chemical,* 13 [1-3] 387-390 (1993).

41. N. Miura, H. Kurosawa, M. Hasei, G. Y. Lu, and N. Yamazoe, "Stabilized Zirconia-Based Sensor Using Oxide Electrode for Detection of NO_X in High-Temperature Combustion-Exhausts," *Solid State Ionics,* 86-8 1069-1073 (1996).

42. N. Miura, G. Y. Lu, N. Yamazoe, H. Kurosawa, and M. Hasei, "Mixed Potential Type NO_X Sensor Based on Stabilized Zirconia and Oxide Electrode," *Journal of the Electrochemical Society,* 143 [2] L33-L35 (1996).

43. N. Miura, G. Y. Lu, and N. Yamazoe, "High-Temperature Potentiometric/Amperometric NO_X Sensors Combining Stabilized Zirconia With Mixed-Metal Oxide Electrode," *Sensors and Actuators B-Chemical,* 52 [1-2] 169-178 (1998).

44. N. Miura, M. Ono, K. Shimanoe, and N. Yamazoe, "A Compact Solid-State Amperometric Sensor for Detection of NO_2 in Ppb Range," *Sensors and Actuators B-Chemical,* 49 [1-2] 101-109 (1998).

45. N. Miura, G. Y. Lu, and N. Yamazoe, "Progress in Mixed-Potential Type Devices Based on Solid Electrolyte for Sensing Redox Gases," *Solid State Ionics,* 136 533-542 (2000).

46. N. Miura, S. Zhuiykov, T. Ono, M. Hasei, and N. Yamazoe, "Mixed Potential Type Sensor Using Stabilized Zirconia and $ZnFe_2O_4$ Sensing Electrode for NO_X Detection at High Temperature," *Sensors and Actuators B-Chemical,* 83 [1-3] 222-229 (2002).

47. N. Miura, J. Wang, M. Nakatou, P. Elumalai, S. Zhuiykov, and M. Hasei, "High-Temperature Operating Characteristics of Mixed-Potential-Type NO_2 Sensor Based on Stabilized-Zirconia Tube and NiO Sensing Electrode," *Sensors and Actuators B-Chemical,* 114 [2] 903-909 (2006).

48. J. Mizusaki, K. Yashiro, T. Kawada, and H. Ohama, "A Concept of Chemical Potential Pumping Effect With the NO_x Sensing Mechanism of Perovskite-Type Oxide Mixed Conductors" pp 236. in Proceedings of the 202nd Meeting of The Electrochemical Society, Vol. 2002-26, *Solid State Ionic Devices III.* Edited by E. D. Wachsman, K. Swider-Lyons, M. F. Carolan, F. H. Garzon, M. Liu, and J. R. Stetter. The Electrochemical Society, Pennington, NJ, 2003.

49. R. Moos, "A Brief Overview on Automotive Exhaust Gas Sensors Based on Electroceramics," *International Journal of Applied Ceramic Technology,* 2 [5] 401-413 (2005).

50. R. Mukundan, E. L. Brosha, D. R. Brown, and F. H. Garzon, "A Mixed-Potential Sensor Based on a $Ce_{0.8}Gd_{0.2}O_{1.9}$ Electrolyte and Platinum and Gold Electrodes," *Journal of the Electrochemical Society,* 147 [4] 1583-1588 (2000).

51. R. Mukundan, K. Teranishi, E. L. Brosha, and F. H. Garzon, "Nitrogen Oxide Sensors Based on Yttria-Stabilized Zirconia Electrolyte and Oxide Electrodes," *Electrochemical and Solid State Letters,* 10 [2] J26-J29 (2007).

52. M. Ono, K. Shimanoe, N. Miura, and N. Yamazoe, "Amperometric Sensor Based on NASICON and NO Oxidation Catalysts for Detection of Total NOx in Atmospheric Environment," *Solid State Ionics,* 136 583-588 (2000).

53. M. Ono, K. Shimanoe, N. Miura, and N. Yamazoe, "Reaction Analysis on Sensing Electrode of Amperometric NO_2 Sensor Based on Sodium Ion Conductor by Using Chronopotentiometry," *Sensors and Actuators B-Chemical,* 77 [1-2] 78-83 (2001).

54. T. Ono, M. Hasei, A. Kunimoto, and N. Miura, "Improvement of Sensing Performances of Zirconia-Based Total NO_X Sensor by Attachment of Oxidation-Catalyst Electrode," *Solid State Ionics,* 175 [1-4] 503-506 (2004).

55. C. O. Park, S. A. Akbar, and W. Weppner, "Ceramic Electrolytes and Electrochemical Sensors," *Journal of Materials Science,* 38 [23] 4639-4660 (2003).

56. C. O. Park and N. Miura, "Absolute Potential Analysis of the Mixed Potential Occurring at the Oxide/YSZ Electrode at High Temperature in NO_X-Containing Air," *Sensors and Actuators B-Chemical,* 113 [1] 316-319 (2006).

57. Park, J. Solid-State Electrochemical Properties of Oxygen-Ion Conducting Ceramic Materials And Their Applications. Ph.D. Dissertation, University of Florida, 2004.

58. P. Schmidt-Zhang, K. P. Sandow, F. Adolf, W. Gopel, and U. Guth, "A Novel Thick Film Sensor for Simultaneous O_2 and NO Monitoring in Exhaust Gases," *Sensors and Actuators B-Chemical,* 70 [1-3] 25-29 (2000).

59. Y. Shimizu and K. Maeda, "Solid Electrolyte-Based NO_X Sensor Using Auxiliary Phase of Metal Oxide," *Chemistry Letters,* [2] 117-118 (1996).

60. Y. Shimizu and K. Maeda, "Solid Electrolyte NO_X Sensor Using Pyrochlore-Type Oxide Electrode," *Sensors and Actuators B-Chemical,* 52 [1-2] 84-89 (1998).

61. Y. Shimizu, H. Nishi, H. Suzuki, and K. Maeda, "Solid-State NO_x Sensor Combined With NASICON and Pb-Ru-Based Pyrochlore-Type Oxide Electrode," *Sensors and Actuators B-Chemical,* 65 [1-3] 141-143 (2000).

62. Y. Shimizu, N. Nakashima, T. Hyodo, and M. Egashira, "NOx Sensing Properties of Varistor-Type Gas Sensors Consisting of Micro P-n Junctions," *Journal of Electroceramics,* 6 [3] 209-217 (2001).

63. E. D. Wachsman and P. Jayaweera, "Selective Detection of NO_X by Differential Electrode Equilibria" pp 298-304. in Proceedings of the 202nd Meeting of The Electrochemical Society, Vol. 2000-32, *Solid State Ionic Devices II - Ceramic Sensors.* Edited by E. D. Wachsman, W. Weppner, E. Traversa, M. Liu, P. Vanysek, and N. Yamazoe. The Electrochemical Society, Pennington, NJ, 2001.

64. E. D. Wachsman, "Selective Potentiometric Detection of NO_X by Differential Electrode Equilibria" pp 215. in Proceedings of the 202nd Meeting of The Electrochemical Society, Vol. 2002-26, *Solid State Ionic Devices III.* Edited by E. D. Wachsman, K. Swider-Lyons, M. F. Carolan, F. H. Garzon, M. Liu, and J. R. Stetter. The Electrochemical Society, Pennington, NJ, 2003.

65. D. L. West, F. C. Montgomery, and T. R. Armstrong, ""NO-Selective" NO_X Sensing Elements for Combustion Exhausts," *Sensors and Actuators B-Chemical,* 111 84-90 (2005).

66. J. Yoo, S. Chatterjee, F. M. Van Assche, and E. D. Wachsman, "Influence of Adsorption and Catalytic Reaction on Sensing Properties of a Potentiometric La_2CuO_4/YSZ/Pt Sensor," *Journal of the Electrochemical Society,* 154 [7] J190-J195 (2007).

67. J. Yoo, H. Yoon, and E. D. Wachsman, "Sensing Properties of MO_X/YSZ/Pt (MO_X = Cr_2O_3, SnO_2, CeO_2) Potentiometric Sensor for NO_2 Detection," *Journal of the Electrochemical Society,* 153 [11] H217-H221 (2006).

68. J. Yoo, F. M. Van Assche, and E. D. Wachsman, "Temperature-Programmed Reaction and Desorption of the Sensor Elements of a WO_3/YSZ/Pt Potentiometric Sensor," *Journal of the Electrochemical Society,* 153 [6] H115-H121 (2006).

69. J. Yoo, S. Chatterjee, F. M. Van Assche, and E. D. Wachsman, "Influence of Adsorption and Catalytic Reaction on Sensing Properties of a Potentiometric La_2CuO_4/YSZ/Pt Sensor," *Journal of the Electrochemical Society (accepted),* (2007).

70. J. Yoo and E. D. Wachsman, "NO_2/NO Response of Cr_2O_3- and SnO_2-Based Potentiometric Sensors and Temperature-Programmed Reaction Evaluation of the Sensor Elements," *Sensors and Actuators B: Chemical,* In Press, Corrected Proof (2007).

71. J. W. Yoon, M. L. Grilli, E. Di Bartolomeo, R. Polini, and E. Traversa, "The NO_2 Response of Solid Electrolyte Sensors Made Using Nano-Sized $LaFeO_3$ Electrodes," *Sensors and Actuators B-Chemical,* 76 [1-3] 483-488 (2001).

72. S. Benard, L. Retailleau, F. Gaillard, P. Vernoux, and A. Giroir-Fendler, "Supported Platinum Catalysts for Nitrogen Oxide Sensors," *Applied Catalysis B: Environmental,* 55 [1] 11-21 (2005).

73. N. Imanaka, A. Oda, S. Tamura, and G. y. Adachi, "Total Nitrogen Oxides Gas Sensor Based on Solid Electrolytes With Refractory Oxide-Based Auxiliary Electrode," *Journal of The Electrochemical Society,* 151 [5] H113-H116 (2004).

74. J. Tamaki, A. Hayashi, Y. Yamamoto, and M. Matsuoka, "Detection of Dilute Nitrogen Dioxide and Thickness Effect of Tungsten Oxide Thin Film Sensors," *Sensors and Actuators B: Chemical,* 95 [1-3] 111-115 (2003).

75. W. Xiong and G. M. Kale, "Novel High-Selectivity NO_2 Sensor Incorporating Mixed-Oxide Electrode," *Sensors and Actuators B: Chemical,* 114 [1] 101-108 (2006).

76. S. Yao and J. R. Stetter, "Modification of NASICON Solid Electrolyte for NO_x Measurements," *Journal of The Electrochemical Society,* 151 [4] H75-H80 (2004).

77. S. Zhuiykov, T. Nakano, A. Kunimoto, N. Yamazoe, and N. Miura, "Potentiometric NO_x Sensor Based on Stabilized Zirconia and $NiCr_2O_4$ Sensing Electrode Operating at High Temperatures," *Electrochemistry Communications,* 3 [2] 97-101 (2001).

78. S. Zhuiykov, "Mathematical Modelling of YSZ-Based Potentiometric Gas Sensors With Oxide Sensing Electrodes: Part I: Model of Interactions of Measuring Gas With Sensor," *Sensors and Actuators B: Chemical,* 119 [2] 456-465 (2006).

79. S. Zhuiykov and N. Miura, "Development of Zirconia-Based Potentiometric NO_x Sensors for Automotive and Energy Industries in the Early 21st Century: What Are the Prospects for Sensors?," *Sensors and Actuators B: Chemical,* 121 [2] 639-651 (2007).

80. E. L. Brosha, R. Mukundan, D. R. Brown, F. H. Garzon, J. H. Visser, M. Zanini, Z. Zhou, and E. M. Logothetis, "CO/HC Sensors Based on Thin Films of LaCoO3 and La0.8Sr0.2CoO3-[Delta] Metal Oxides," *Sensors and Actuators B: Chemical,* 69 [1-2] 171-182 (2000).

81. E. L. Brosha, R. Mukundan, D. R. Brown, and F. H. Garzon, "Mixed Potential Sensors Using Lanthanum Manganate and Terbium Yttrium Zirconium Oxide Electrodes," *Sensors and Actuators B-Chemical,* 87 [1] 47-57 (2002).

82. E. L. Brosha, R. Mukundan, D. R. Brown, F. H. Garzon, and J. H. Visser, "Development of Ceramic Mixed Potential Sensors for Automotive Applications," *Solid State Ionics,* 148 [1-2] 61-69 (2002).

83. T. Hibino, Y. Kuwahara, S. Q. Wang, S. Kakimoto, and M. Sano, "Nonideal Electromotive Force of Zirconia Sensors for Unsaturated Hydrocarbon Gases," *Electrochemical and Solid State Letters,* 1 [4] 197-199 (1998).

84. T. Hibino, S. Tanimoto, S. Kakimoto, and M. Sano, "High-Temperature Hydrocarbon Sensors Based on a Stabilized Zirconia Electrolyte and Metal Oxide Electrodes," *Electrochemical and Solid State Letters,* 2 [12] 651-653 (1999).

85. T. Hibino, S. Kakimoto, and M. Sano, "Non-Nernstian Behavior at Modified Au Electrodes for Hydrocarbon Gas Sensing," *Journal of the Electrochemical Society,* 146 [9] 3361-3366 (1999).

86. T. Hibino, A. Hashimoto, S. Kakimoto, and M. Sano, "Zirconia-Based Potentiometric Sensors Using Metal Oxide Electrodes for Detection of Hydrocarbons," *Journal of the Electrochemical Society,* 148 [1] H1-H5 (2001).

87. R. Mukundan, E. L. Brosha, D. R. Brown, and F. H. Garzon, "Ceria-Electrolyte-Based Mixed Potential Sensors for the Detection of Hydrocarbons and Carbon Monoxide," *Electrochemical and Solid State Letters,* 2 [8] 412-414 (1999).

88. N. Miura, Y. T. Yan, G. Y. Lu, and N. Yamazoe, "Sensing Characteristics and Mechanism of Hydrogen Sulfide Sensor Using Stabilized Zirconia and Oxide Sensing Electrode," *Sensors and Actuators B-Chemical,* 34 [1-3] 367-372 (1996).

89. Y. Yan, N. Miura, and N. Yamazoe, "Construction and Working Mechanism of Sulfur Dioxide Sensor Utilizing Stabilized Zirconia and Metal Sulfate," *Journal of the Electrochemical Society,* 143 [2] 609-613 (1996).

90. Y. T. Yan, Y. Shimizu, N. Miura, and N. Yamazoe, "Characteristics and Sensing Mechanism of SO_X Sensor Using Stabilized Zirconia and Metal Sulfate," *Sensors and Actuators B-Chemical,* 12 [2] 77-81 (1993).

91. Y. T. Yan, Y. Shimizu, N. Miura, and N. Yamazoe, "High-Performance Solid-Electrolyte SO_X Sensor Using MgO-Stabilized Zirconia Tube and Li_2SO_4-$CaSO_4$-SiO_2 Auxiliary Phase," *Sensors and Actuators B-Chemical,* 20 [2-3] 81-87 (1994).

92. A. Vogel, G. Baier, and V. Schule, "Non-Nernstian Potentiometric Zirconia Sensors - Screening of Potential Working Electrode Materials," *Sensors and Actuators B-Chemical,* 15 [1-3] 147-150 (1993).

93. E. Kanazawa, G. Sakai, K. Shimanoe, Y. Kanmura, Y. Teraoka, N. Miura, and N. Yamazoe, "Semiconductor Gas Sensor Using SrO-Modified SnO_2 for the Detection of N_2O in Air," *Electrochemical and Solid State Letters,* 3 [12] 572-574 (2000).

94. E. Kanazawa, G. Sakai, K. Shimanoe, Y. Kanmura, Y. Teraoka, N. Miura, and N. Yamazoe, "Metal Oxide Semiconductor N_2O Sensor for Medical Use," *Sensors and Actuators B-Chemical,* 77 [1-2] 72-77 (2001).

95. E. Kanazawa, M. Kugishima, K. Shimanoe, Y. Kanmura, Y. Teraoka, N. Miura, and N. Yamazoe, "Mixed-Potential Type N_2O Sensor Using Stabilized Zirconia- and SnO_2-Based Sensing Electrode," *Sensors and Actuators B-Chemical,* 75 [1-2] 121-124 (2001).

96. K. Tanaka, S. Morimoto, S. Sonoda, S. Matsuura, K. Moriya, and M. Egashira, "Combustion Monitoring Sensor Using Tin Dioxide Semiconductor," *Sensors and Actuators B-Chemical,* 3 [4] 247-253 (1991).

97. D. E. Williams, P. McGehin, and B. C. Tolfiled, "Solid Electrolyte Mixed Potential Phenomena" pp 275. in Solid State Chemistry, 1982 proceedings of the Second European Conference, 1982.

98. F. H. Garzon, R. Mukundan, and E. L. Brosha, "Solid-State Mixed Potential Gas Sensors: Theory, Experiments and Challenges," *Solid State Ionics,* 136-137 633-638 (2000).

99. N. Miura, S. Zhuiykov, T. Ono, M. Hasei, and N. Yamazoe, "Mixed Potential Type Sensor Using Stabilized Zirconia and ZnFe2O4 Sensing Electrode for NOx

Detection at High Temperature," *Sensors and Actuators B: Chemical,* 83 [1-3] 222-229 (2002).

100. F. Menil, V. Coillard, and C. Lucat, "Critical Review of Nitrogen Monoxide Sensors for Exhaust Gases of Lean Burn Engines," *Sensors and Actuators B-Chemical,* 67 1 (2000).

101. B. K. Narayanan, S. A. Akbar, and P. K. Dutta, "A Phosphate-Based Proton Conducting Solid Electrolyte Hydrocarbon Gas Sensor," *Sensors and Actuators B: Chemical,* 87 [3] 480-486 (2002).

102. E. D. Wachsman, P. Jayaweera, G. Krishnan, and A. Sanjurjo, "Electrocatalytic Reduction of NO_x on $La_{(1-x)}A_{(x)}B_{(1-y)}B_{(y)}O_{(3-\delta)}$: Evidence of Electrically Enhanced Activity," *Solid State Ionics,* 136 775-782 (2000).

103. E. Di Bartolomeo, N. Kaabbuathong, M. L. Grilli, and E. Traversa, "Planar Electrochemical Sensors Based on Tape-Cast YSZ Layers and Oxide Electrodes," *Solid State Ionics,* 171 [3-4] 173-181 (2004).

104. V. V. Kharton, E. V. Tsipis, A. A. Yaremchenko, and J. R. Frade, "Surface-Limited Oxygen Transport and Electrode Properties of $La_2Ni_{0.8}Cu_{0.2}O_{4+\delta}$," *Solid State Ionics,* 166 [3-4] 327-337 (2004).

105. J. Mizsei, "How Can Sensitive and Selective Semiconductor Gas Sensors Be Made?," *Sensors and Actuators B: Chemical,* 23 [2-3] 173-176 (1995).

106. N. S. Baik, G. Sakai, K. Shimanoe, N. Miura, and N. Yamazoe, "Hydrothermal Treatment of Tin Oxide Sol Solution for Preparation of Thin-Film Sensor With Enhanced Thermal Stability and Gas Sensitivity," *Sensors and Actuators B-Chemical,* 65 [1-3] 97-100 (2000).

107. C. Xu, J. Tamaki, N. Miura, and N. Yamazoe, "Grain-Size Effects on Gas Sensitivity of Porous SnO_2-Based Elements," *Sensors and Actuators B-Chemical,* 3 [2] 147-155 (1991).

108. T. Anukunprasert, C. Saiwan, and E. Traversa, "The Development of Gas Sensor for Carbon Monoxide Monitoring Using Nanostructure of Nb-TiO_2," *Science and Technology of Advanced Materials,* 6 [3-4] 359-363 (2005).

109. J. Tamaki, Z. Zhang, K. Fujimori, M. Akiyama, T. Harada, N. Miura, and N. Yamazoe, "Grain-Size Effects in Tungsten Oxide-Based Sensor for Nitrogen-Oxides," *Journal of the Electrochemical Society,* 141 [8] 2207-2210 (1994).

110. A. Bielanski, and J. Haber, *Oxygen in Catalysis* Marcel Dekker, New York, 1991.

111. E. Traversa, G. Gnappi, A. Montenero, and G. Gusmano, "Ceramic Thin Films by Sol-Gel Processing As Novel Materials for Integrated Humidity Sensors," *Sensors and Actuators B-Chemical,* 31 [1-2] 59-70 (1996).

112. Nowotny, J. Interface Electrical Phenomena in Ionic Solids. In *CRC Handbook of Solid State Ionics*, Gellings, P. J., Bouwmeester, H. J. M., Eds.; CRC Press: Boca Raton, 1997; pp 121-169.

113. P. B. Weisz, "Effects of Electronic Charge Transfer Between Adsorbate and Solid on Chemisorption and Catalysis," *The Journal of Chemical Physics,* 11 [9] (1953).

114. Z. Y. Can, H. Narita, J. Mizusaki, and H. Tagawa, "Detection of Carbon-Monoxide by Using Zirconia Oxygen Sensor," *Solid State Ionics,* 79 344-348 (1995).

115. A. Dutta, N. Kaabbuathong, M. L. Grilli, E. Di Bartolomeo, and E. Traversa, "Study of YSZ-Based Electrochemical Sensors With Oxide Electrodes for High Temperature Applications," *Bulletin of Materials Science,* 25 [6] 451-453 (2002).

116. N. Miura, G. Lu, and N. Yamazoe, "Progress in Mixed-Potential Type Devices Based on Solid Electrolyte for Sensing Redox Gases," *Solid State Ionics,* 136-137 533-542 (2000).

117. N. Barsan, J. R. Stetter, M. Findlay, and W. Gopel, "High Performance Gas Sensing of CO: Comparative Tests for Semiconducting (SnO_2-Based) and for Amperometric Gas Sensors," *Analytical Chemistry,* 71 [13] 2512-2517 (1999).

118. J. Yoo, S. Chatterjee, and E. D. Wachsman, "Sensing Properties and Selectivities of a WO3/YSZ/Pt Potentiometric NOx Sensor," *Sensors and Actuators B: Chemical,* 122 644-652 (2007).

119. J. E. Anderson and Y. B. Graves, "Steady-State Characteristics of Oxygen Concentration Cell Sensors Subjected to Non-Equilibrium Gas-Mixtures," *Journal of the Electrochemical Society,* 128 [2] 294-300 (1981).

120. A. Dutta, T. Ishihara, and H. Nishiguchi, "An Amperometric Solid-State Gas Sensor Using a $LaGaO_3$-Based Perovskite Oxide Electrolyte for Detecting Hydrocarbon in Exhaust Gas. A Bimetallic Anode for Improving Sensitivity at Low Temperature," *Chemistry of Materials,* 16 [24] 5198-5204 (2004).

121. T. Hyodo, Y. Tominaga, T. Yamaguchi, A. Kawahara, H. Katsuki, Y. Shimizu, and M. Egashira, "NO_X Sensing Properties of WO_3-Based Semiconductor Gas Sensors Fabricated by Slide-Off Transfer Printing," *Electrochemistry,* 71 [6] 481-484 (2003).

122. T. Ishihara, H. Fujita, H. Nishiguchi, and Y. Takita, "$SrSnO_3$-WO_3 As Capacitive-Type Nitrogen Oxide Sensor for Monitoring at High Temperature," *Sensors and Actuators B-Chemical,* 65 [1-3] 319-324 (2000).

123. T. Maekawa, J. Tamaki, N. Miura, N. Yamazoe, and S. Matsushima, "Development of SnO_2-Based Ethanol Gas Sensor," *Sensors and Actuators B-Chemical,* 9 [1] 63-69 (1992).

124. J. Mizusaki, H. Tagawa, Y. Miyaki, S. Yamauchi, K. Fueki, I. Koshiro, and K. Hirano, "Kinetics of the Electrode-Reaction at the CO-CO_2, Porous Pt/Stabilized Zirconia Interface," *Solid State Ionics,* 53-6 126-134 (1992).

125. B. M. White, F. M. Van Assche, E. Traversa, and E. D. Wachsman, "Electrical Characterization of Semiconducting La_2CuO_4 For Potentiometric Gas Sensor Applications" pp 109. in Proceedings of the 208th Meeting of The Electrochemical Society, Vol. 1, *Solid State Ionic Devices IV, ECS Transactions.* Edited by E. D. Wachsman, V. Birss, F. H. Garzon, R. Mukundan, and E. Traversa. The Electrochemical Society, Pennington, NJ, 2006.

126. J. W. Yoon, T. Sasaki, N. Koshizaki, and E. Traversa, "Preparation and Characterization of M/TiO_2 (M = Ag, Au, Pt) Nanocomposite Thin Films," *Scripta Materialia,* 44 [8-9] 1865-1868 (2001).

127. S. Zurek, M. Mosialek, P. Tomczyk, and D. Oblakowska, "Investigation of the Partial Oxidation of Methane at the Interface Metal (Pt, Au)Vertical Bar YSZ," *Journal of Electroceramics,* 15 [1] 83-93 (2005).

128. E. L. Brosha, R. Mukundan, D. R. Brown, F. H. Garzon, J. H. Visser, M. Zanini, Z. Zhou, and E. M. Logothetis, "CO/HC Sensors Based on Thin Films of $LaCoO_3$ and $La_{0.8}Sr_{0.2}CoO_{3-\delta}$ Metal Oxides," *Sensors and Actuators B-Chemical,* 69 [1-2] 171-182 (2000).

129. Bhattacharjee, S. The Expert System for Thermodynamics (TEST). Bhattacharjee, S. 2007. San Diego State University.
Ref Type: Data File

130. S. Bhattacharjee, "TEST - The Expert System for Thermodynamics" in Proceedings of the 2003 American Society for Engineering Education Annual Conference & Exposition,*American Society for Engineering Education*, 2003.

131. D. C. Johnston, J. P. Stokes, D. P. Goshorn, and J. T. Lewandowski, "Influence of Oxygen Defects on the Physical-Properties of La_2CuO_{4-y}," *Physical Review B,* 36 [7] 4007-4010 (1987).

132. J. D. Jorgensen, H. B. Schuttler, D. G. Hinks, D. W. Capone, K. Zhang, M. B. Brodsky, and D. J. Scalapino, "Lattice Instability and High-Tc Superconductivity in $La_{2-x}Ba_xCuO_4$," *Physical Review Letters,* 58 [10] 1024-1027 (1987).

133. J. D. Jorgensen, B. Dabrowski, S. Y. Pei, D. G. Hinks, L. Soderholm, B. Morosin, J. E. Schirber, E. L. Venturini, and D. S. Ginley, "Superconducting Phase of $La_2CuO_{4+\delta}$ - A Superconducting Composition Resulting From Phase-Separation," *Physical Review B,* 38 [16] 11337-11345 (1988).

134. H. Kanai, J. Mizusaki, H. Tagawa, S. Hoshiyama, K. Hirano, K. Fujita, M. Tezuka, and T. Hashimoto, "Defect Chemistry of $La_{(2-x)}Sr_xCuO_4$: Oxygen Nonstoichiometry

and Thermodynamic Stability," *Journal of Solid State Chemistry,* 131 150-159 (1997).

135. J. Maier and G. Pfundtner, "Defect Chemistry of the High-Tc Superconductors," *Advanced Materials,* 3 [6] 292-297 (1991).

136. G. Cao, J. W. O'Reilly, J. E. Crow, and L. R. Testardi, "Enhanced Electric Polarizability at the Magnetic Ordering Temperature of La_2CuO_{4+x}," *Physical Review B,* 47 [17] 11510-11511 (1993).

137. A. Lappas and K. Prassides, "Layered Cuprates With the T* Structure: Structural and Conducting Properties," *Journal of Solid State Chemistry,* 115 [2] 332-346 (1995).

138. J. M. Longo and P. M. Raccah, "The Structure of La_2CuO_4 and $LaSrVO_4$," *Journal of Solid State Chemistry,* 6 [4] 526-531 (1973).

139. A. Shukla, M. Calandra, M. Taguchi, A. Kotani, G. Vanko, and S. W. Cheong, "Polarized Resonant Inelastic X-Ray Scattering As an Ultrafine Probe of Excited States of La_2CuO_4," *Physical Review Letters,* 96 [7] 077006 (2006).

140. J. C. Bennett, M. Olfert, G. A. Scholz, and F. W. Boswell, "Synthesis of Bulk Superconducting La_2CuO_4 in an Electrochemical Cell," *Physical Review B,* 44 [6] 2727-2731 (1991).

141. Y. F. Zhu, R. Q. Tan, T. Yi, S. Gao, C. H. Yan, and L. L. Cao, "Preparation of Nanosized La_2CuO_4 Perovskite Oxide Using an Amorphous Heteronuclear Complex As a Precursor at Low-Temperature," *Journal of Alloys and Compounds,* 311 [1] 16-21 (2000).

142. L. Bapat, G. N. Natu, J. Kher, and M. Bhide, "Reactivity of Binary Mixture of La(III) Oxide and Cu(II) Oxalate or Nitrate and Synthesis of La(III) Cuprate," *Journal of Thermal Analysis and Calorimetry,* 62 285-294 (2000).

143. J. Mahia, J. L. Martinez-Lorenzo, M. C. Blanco, and J. Lopez-Quintela, "Structural Characterization of Electrochemically Oxidized $La_2CuO_{4+\delta}$ Particles Prepared by a Sol-Gel Method," *Journal of Solid State Chemistry,* 131 246-251 (1997).

144. L. M. Gan, L. H. Zhang, H. S. O. Chan, C. H. Chew, and B. H. Loo, "A Novel Method for the Synthesis of Perovskite-Type Mixed Metal Oxides by the Inverse Microemulsion Technique," *Journal of Materials Science,* 31 1071-1079 (1996).

145. A. A. Galkin, B. G. Kostyuk, V. V. Lunin, and M. Poliakoff, "Continuous Reactions in Supercritical Water: A New Route to La_2CuO_4 With a High Surface Area and Enhanced Oxygen Mobility," *Angewandte Chemie-International Edition,* 39 [15] 2738-2740 (2000).

146. B. L. Kirkwood, T. S. Luhman, R. R. Stephenson, and M. M. Strasik, Method for Producing Superconducting Oxide Compounds. USA 6,559,103, May 6, 2003.

147. Vayenas, C. G.; Bebelis, S. I.; Yentekakis, I. V.; Neophytides, S. N. Electrocatalysis and Electrochemical Reactors. In *CRC Handbook of Solid State Ionics*, Gellings, P. J., Bouwmeester, H. J. M., Eds.; CRC Press: Boca Raton, 1997; pp 445-480.

148. M. Akiyama, Z. Zhang, J. Tamaki, N. Miura, N. Yamazoe, and T. Harada, "Tungsten Oxide-Based Semiconductor Sensor for Detection of Nitrogen-Oxides in Combustion Exhaust," *Sensors and Actuators B-Chemical,* 14 [1-3] 619-620 (1993).

149. Y. G. Choi, G. Sakai, K. Shimanoe, N. Miura, and N. Yamazoe, "Wet Process-Prepared Thick Films of WO_3 for NO_2 Sensing," *Sensors and Actuators B-Chemical,* 95 [1-3] 258-265 (2003).

150. Y. G. Choi, G. Sakai, K. Shimanoe, Y. Teraoka, N. Miura, and N. Yamazoe, "Preparation of Size and Habit-Controlled Nano Crystallites of Tungsten Oxide," *Sensors and Actuators B-Chemical,* 93 [1-3] 486-494 (2003).

151. T. Hyodo, T. Mori, A. Kawahara, H. Katsuki, Y. Shimizu, and M. Egashira, "Gas Sensing Properties of Semiconductor Heterolayer Sensors Fabricated by Slide-Off Transfer Printing," *Sensors and Actuators B-Chemical,* 77 [1-2] 41-47 (2001).

152. X. S. Wang, G. Sakai, K. Shimanoe, N. Miura, and N. Yamazoe, "Spin-Coated Thin Films of SiO_2-WO_3 Composites for Detection of Sub-Ppm NO_2," *Sensors and Actuators B-Chemical,* 45 [2] 141-146 (1997).

153. X. S. Wang, N. Miura, and N. Yamazoe, "Study of WO_3-Based Sensing Materials for NH_3 and NO Detection," *Sensors and Actuators B-Chemical,* 66 [1-3] 74-76 (2000).

154. C. N. Xu, N. Miura, Y. Ishida, K. Matsuda, and N. Yamazoe, "Selective Detection of NH_3 Over NO in Combustion Exhausts by Using Au and MoO_3 Doubly Promoted WO_3 Element," *Sensors and Actuators B-Chemical,* 65 [1-3] 163-165 (2000).

155. G. Lu, N. Miura, and N. Yamazoe, "Stabilized Zirconia-Based Sensors Using WO_3 Electrode for Detection of NO or NO_2," *Sensors and Actuators B-Chemical,* 65 [1-3] 125-127 (2000).

156. M. C. Carotta, G. Martinelli, L. Crema, M. Gallana, M. Merli, G. Ghiotti, and E. Traversa, "Array of Thick Film Sensors for Atmospheric Pollutant Monitoring," *Sensors and Actuators B-Chemical,* 68 [1-3] 1-8 (2000).

157. M. C. Carotta, C. Martinelli, L. Crema, C. Malagu, M. Merli, G. Ghiotti, and E. Traversa, "Nanostructured Thick-Film Gas Sensors for Atmospheric Pollutant Monitoring: Quantitative Analysis on Field Tests," *Sensors and Actuators B-Chemical,* 76 [1-3] 336-342 (2001).

158. M. C. Carotta, M. Ferroni, S. Gherardi, V. Guidi, C. Malagu, G. Martinelli, M. Sacerdoti, M. L. Di Vona, S. Licoccia, and E. Traversa, "Thick-Film Gas Sensors Based on Vanadium-Titanium Oxide Powders Prepared by Sol-Gel Synthesis," *Journal of the European Ceramic Society,* 24 [6] 1409-1413 (2004).

159. M. C. Carotta, V. Guidi, C. Malagu, B. Vendemiati, A. Zanni, G. Martinelli, M. Sacerdoti, S. Licoccia, M. L. Di Vona, and E. Traversa, "Vanadium and Tantalum-Doped Titanium Oxide (TiTaV): a Novel Material for Gas Sensing," *Sensors and Actuators B-Chemical,* 108 [1-2] 89-96 (2005).

160. M. Ferroni, M. C. Carotta, V. Guidi, G. Martinelli, F. Ronconi, M. Sacerdoti, and E. Traversa, "Preparation and Characterization of Nanosized Titania Sensing Film," *Sensors and Actuators B-Chemical,* 77 [1-2] 163-166 (2001).

161. M. L. Frank, M. D. Fulkerson, B. R. Patton, and P. K. Dutta, "TiO_2-Based Sensor Arrays Modeled With Nonlinear Regression Analysis for Simultaneously Determining CO and O_2 Concentrations at High Temperatures," *Sensors and Actuators B-Chemical,* 87 [3] 471-479 (2002).

162. N. O. Savage, S. A. Akbar, and P. K. Dutta, "Titanium Dioxide Based High Temperature Carbon Monoxide Selective Sensor," *Sensors and Actuators B-Chemical,* 72 239-248 (2001).

163. E. Traversa, G. Gusmano, and A. Montenero, "Innovative Humidity Sensitive Electrical-Properties of Sol-Gel Processed Ceramic Thin-Films," *European Journal of Solid State and Inorganic Chemistry,* 32 [7-8] 719-729 (1995).

164. E. Traversa, M. L. Di Vona, S. Licoccia, M. Sacerdoti, M. C. Carotta, M. Gallana, and G. Martinelli, "Sol-Gel Nanosized Semiconducting Titania-Based Powders for Thick-Film Gas Sensors," *Journal of Sol-Gel Science and Technology,* 19 [1-3] 193-196 (2000).

165. E. Traversa, Y. Sadaoka, M. C. Carotta, and G. Martinelli, "Environmental Monitoring Field Tests Using Screen-Printed Thick-Film Sensors Based on Semiconducting Oxides," *Sensors and Actuators B-Chemical,* 65 [1-3] 181-185 (2000).

166. E. Traversa, M. L. Di Vona, S. Licoccia, M. Sacerdoti, M. C. Carotta, L. Crema, and G. Martinelli, "Sol-Gel Processed TiO_2-Based Nano-Sized Powders for Use in Thick-Film Gas Sensors for Atmospheric Pollutant Monitoring," *Journal of Sol-Gel Science and Technology,* 22 [1-2] 167-179 (2001).

167. J. Wu, K. Mobley, and R. L. McCreery, "Electronic Characteristics of Fluorene/TiO_2 Molecular Heterojunctions," *Journal of Chemical Physics,* 126 [2] 024704 (2007).

168. C. Y. Yu, T. Hyodo, Y. Shimizu, and M. Egashira, "Preparation of Thermally Stable Mesoporous TiO_2 Powder and Its Gas Sensor Application," *Electrochemistry,* 71 [6] 475-480 (2003).

169. N. S. Baik, G. Sakai, N. Miura, and N. Yamazoe, "Hydrothermally Treated Sol Solution of Tin Oxide for Thin-Film Gas Sensor," *Sensors and Actuators B-Chemical,* 63 [1-2] 74-79 (2000).

170. N. Barsan, M. Schweizer-Berberich, and W. Gopel, "Fundamental and Practical Aspects in the Design of Nanoscaled SnO_2 Gas Sensors: A Status Report," *Fresenius Journal of Analytical Chemistry,* 365 [4] 287-304 (1999).

171. S. C. Chang, "Thin-Film Semiconductor NO_x Sensor," *IEEE Transactions on Electron Devices,* 26 [12] 1875-1880 (1979).

172. W. Gopel and K. D. Schierbaum, "SnO_2 Sensors - Current Status and Future-Prospects," *Sensors and Actuators B-Chemical,* 26 [1-3] 1-12 (1995).

173. T. Sahm, A. Gurlo, N. Barsan, and U. Weimar, "Basics of Oxygen and SnO_2 Interaction; Work Function Change and Conductivity Measurements," *Sensors and Actuators B-Chemical,* 118 [1-2] 78-83 (2006).

174. G. Sakai, N. S. Baik, N. Miura, and N. Yamazoe, "Gas Sensing Properties of Tin Oxide Thin Films Fabricated From Hydrothermally Treated Nanoparticles - Dependence of CO and H_2 Response on Film Thickness," *Sensors and Actuators B-Chemical,* 77 [1-2] 116-121 (2001).

175. G. Sberveglieri, S. Groppelli, and P. Nelli, "Highly Sensitive and Selective NO_X and NO_2 Sensor Based on Cd-Doped SnO_2 Thin-Films," *Sensors and Actuators B-Chemical,* 4 [3-4] 457-461 (1991).

176. G. Sberveglieri, G. Faglia, S. Groppelli, and P. Nelli, "Methods for the Preparation of NO, NO_2 and H_2 Sensors Based on Tin Oxide Thin-Films, Grown by Means of the RF Magnetron Sputtering Technique," *Sensors and Actuators B-Chemical,* 8 [1] 79-88 (1992).

177. K. D. Schierbaum, U. Weimar, W. Gopel, and R. Kowalkowski, "Conductance, Work Function and Catalytic Activity of SnO_2-Based Gas Sensors," *Sensors and Actuators B-Chemical,* 3 [3] 205-214 (1991).

178. Y. Shimizu, A. Jono, T. Hyodo, and M. Egashira, "Preparation of Large Mesoporous SnO_2 Powder for Gas Sensor Application," *Sensors and Actuators B-Chemical,* 108 [1-2] 56-61 (2005).

179. J. Tamaki, T. Maekawa, N. Miura, and N. Yamazoe, "CuO-SnO_2 Element for Highly Sensitive and Selective Detection of H_2S," *Sensors and Actuators B-Chemical,* 9 [3] 197-203 (1992).

180. H. Yamaura, T. Jinkawa, J. Tamaki, K. Moriya, N. Miura, and N. Yamazoe, "Indium Oxide-Based Gas Sensor for Selective Detection of CO," *Sensors and Actuators B-Chemical,* 36 [1-3] 325-332 (1996).

181. X. Zhou, Q. Cao, Y. Hu, J. Gao, and Y. Xu, "Sensing Behavior and Mechanism of La_2CuO_4-SnO_2 Gas Sensors," *Sensors and Actuators B-Chemical,* 77 443-446 (2001).

182. S. Bredikhin, J. Liu, and W. Weppner, "Solid Ionic Conductor Semiconductor Junctions for Chemical Sensors," *Applied Physics A-Materials Science & Processing,* 57 [1] 37-43 (1993).

183. H. Aono, E. Traversa, M. Sakamoto, and Y. Sadaoka, "Crystallographic Characterization and NO_2 Gas Sensing Property of $LnFeO_3$ Prepared by Thermal Decomposition of Ln-Fe Hexacyanocomplexes, $Ln[Fe(CN)_6]\bullet NH_2O$, Ln = La, Nd, Sm, Gd, and Dy," *Sensors and Actuators B-Chemical,* 94 [2] 132-139 (2003).

184. M. C. Carotta, M. A. Butturi, G. Martinelli, Y. Sadaoka, P. Nunziante, and E. Traversa, "Microstructural Evolution of Nanosized $LaFeO_3$ Powders From the Thermal Decomposition of a Cyano-Complex for Thick Film Gas Sensors," *Sensors and Actuators B-Chemical,* 44 [1-3] 590-594 (1997).

185. E. Traversa, S. Matsushima, G. Okada, Y. Sadaoka, Y. Sakai, and K. Watanabe, "NO_2 Sensitive $LaFeO_3$ Thin-Films Prepared by RF-Sputtering," *Sensors and Actuators B-Chemical,* 25 [1-3] 661-664 (1995).

186. H. Aono, M. Sato, E. Traversa, M. Sakamoto, and Y. Sadaoka, "Design of Ceramic Materials for Chemical Sensors: Effect of $SmFeO_3$ Processing on Surface and Electrical Properties," *Journal of the American Ceramic Society,* 84 [2] 341-347 (2001).

187. M. C. Carotta, G. Martinelli, Y. Sadaoka, P. Nunziante, and E. Traversa, "Gas-Sensitive Electrical Properties of Perovskite-Type $SmFeO_3$ Thick Films," *Sensors and Actuators B-Chemical,* 48 [1-3] 270-276 (1998).

188. E. Traversa, S. Villanti, G. Gusmano, H. Aono, and Y. Sadaoka, "Design of Ceramic Materials for Chemical Sensors: $SmFeO_3$ Thick Films Sensitive to NO_2," *Journal of the American Ceramic Society,* 82 [9] 2442-2450 (1999).

189. E. L. Brosha, R. Mukundan, D. R. Brown, F. H. Garzon, J. H. Visser, M. Zanini, Z. Zhou, and E. M. Logothetis, "CO/HC Sensors Based on Thin Films of $LaCoO_3$ and $La_{0.8}Sr_{0.2}CoO_{3-\delta}$ Metal Oxides," *Sensors and Actuators B: Chemical,* 69 [1-2] 171-182 (2000).

190. C. Baratto, G. Sberveglieri, A. Onischuk, B. Caruso, and S. di Stasio, "Low Temperature Selective NO_2 Sensors by Nanostructured Fibres of ZnO," *Sensors and Actuators B-Chemical,* 100 [1-2] 261-265 (2004).

191. T. Ishihara, S. Sato, and Y. Takita, "Capacitive-Type Sensors for the Selective Detection of Nitrogen-Oxides," *Sensors and Actuators B-Chemical,* 25 [1-3] 392-395 (1995).

192. E. Traversa, M. Miyayama, and H. Yanagida, "Gas Sensitivity of ZnO/La_2CuO_4 Heterocontacts," *Sensors and Actuators B-Chemical,* 17 [3] 257-261 (1994).

193. E. Traversa, A. Bearzotti, M. Miyayama, and H. Yanagida, "The Electrical-Properties of La_2CuO_4/ZnO Heterocontacts at Different Relative Humidities," *Journal of Materials Research,* 10 [9] 2286-2294 (1995).

194. E. Traversa, A. Bearzotti, M. Miyayama, and H. Yanagida, "Study of the Conduction Mechanism of La_2CuO_4-ZnO Heterocontacts at Different Relative Humidities," *Sensors and Actuators B-Chemical,* 25 [1-3] 714-718 (1995).

195. E. Traversa, A. Bearzotti, M. Miyayama, and H. Yanagida, "Influence of the Electrode Materials on the Electrical Response of ZnO-Based Contact Sensors," *Journal of the European Ceramic Society,* 18 [6] 621-631 (1998).

196. N. Q. Wu, M. H. Zhao, J. G. Zheng, C. B. Jiang, B. Myers, S. X. Li, M. Chyu, and S. X. Mao, "Porous CuO-ZnO Nanocomposite for Sensing Electrode of High-Temperature CO Solid-State Electrochemical Sensor," *Nanotechnology,* 16 [12] 2878-2881 (2005).

197. W. Y. Chung, G. Sakai, K. Shimanoe, N. Miura, D. D. Lee, and N. Yamazoe, "Preparation of Indium Oxide Thin Film by Spin-Coating Method and Its Gas-Sensing Properties," *Sensors and Actuators B-Chemical,* 46 [2] 139-145 (1998).

198. W. Y. Chung, G. Sakai, K. Shimanoe, N. Miura, D. D. Lee, and N. Yamazoe, "Spin-Coated Indium Oxide Thin Film on Alumina and Silicon Substrates and Their Gas Sensing Properties," *Sensors and Actuators B-Chemical,* 65 [1-3] 312-315 (2000).

199. H. Yamaura, J. Tamaki, K. Moriya, N. Miura, and N. Yamazoe, "Selective CO Detection by Using Indium Oxide-Based Semiconductor Gas Sensor," *Journal of the Electrochemical Society,* 143 [2] L36-L37 (1996).

200. K. Obata, S. Kumazawa, K. Shimanoe, N. Miura, and N. Yamazoe, "Potentiometric Sensor Based on NASICON and In_2O_3 for Detection of CO_2 at Room Temperature - Modification With Foreign Substances," *Sensors and Actuators B-Chemical,* 76 [1-3] 639-643 (2001).

201. J. Zosel, D. Westphal, S. Jakobs, R. Mueller, and U. Guth, "Au-Oxide Composites As HC-Sensitive Electrode Material for Mixed Potential Gas Sensors," *Solid State Ionics,* 152 525-529 (2002).

202. A. Kohli, C. C. Wang, and S. A. Akbar, "Niobium Pentoxide As a Lean-Range Sensor," *Sensors and Actuators B-Chemical,* 56 121 (1999).

203. J. Zosel, K. Ahlborn, R. Mueller, D. Westphal, V. Vashook, and U. Guth, "Response Behavior of Perovskites and Au/Oxide Composites As HC-Electrodes in Different Combustibles," *Solid State Ionics,* 169 115-119 (2004).

204. E. R. Macam, F. M. Van Assche, J. Yoo, and E. D. Wachsman, "Optimization of La_2CuO_4 Sensing Electrodes for a NO_x Potentiometric Sensor," *ECS Transactions,* 1 [7] 121 (2006).

205. F. M. Van Assche, J. Yoo, S. Chatterjee, and E. D. Wachsman, "Heterogeneous Catalytic Evaluation of Potentiometric La_2CuO_4 Sensor Electrodes" pp 185. in Proceedings of the 208th Meeting of The Electrochemical Society, Vol. 1, *Solid State Ionic Devices IV, ECS Transactions.* Edited by E. D. Wachsman, V. Birss, F. H. Garzon, R. Mukundan, and E. Traversa. The Electrochemical Society, Pennington, NJ, 2006.

206. N. A. Besley, "Theoretical Study of the Electronic Spectroscopy of CO Adsorbed on Pt(111)," *Journal of Chemical Physics,* 122 [18] 184706 (2005).

207. P. Hu, D. A. King, M. H. Lee, and M. C. Payne, "Orbital Mixing in Co Chemisorption on Transition-Metal Surfaces," *Chemical Physics Letters,* 246 [1-2] 73-78 (1995).

208. G. A. Somorjai, K. M. Bratlie, M. O. Montano, and J. Y. Park, "Dynamics of Surface Catalyzed Reactions; the Roles of Surface Defects, Surface Diffusion, and Hot Electrons," *Journal of Physical Chemistry B: Condensed Matter,* 110 [40] 20014-20022 (2006).

209. A. R. Balkenende, J. W. Geus, A. J. H. M. Kock, and R. J. van der Pas, "The Effect of a Coverage-Dependent Heat of Adsorption on Temperature-Programmed Desorption and Adsorption in Porous Catalysts," *Journal of Catalysis,* 115 [2] 365-375 (1989).

210. J. M. Kanervo, K. M. Reinikainen, and A. O. I. Krause, "Kinetic Analysis of Temperature-Programmed Desorption," *Applied Catalysis A: General,* 258 [2] 135-144 (2004).

211. J. M. Kanervo, T. J. Keskitalo, R. I. Slioor, and A. O. I. Krause, "Temperature-Programmed Desorption As a Tool to Extract Quantitative Kinetic or Energetic Information for Porous Catalysts," *Journal of Catalysis,* 238 [2] 382-393 (2006).

212. H. E. Kissinger, "Reaction Kinetics in Differential Thermal Analysis," *Analytical Chemistry,* 29 [11] 1702-1706 (1957).

213. L. Olsson, B. Westerberg, H. Persson, E. Fridell, M. Skoglundh, and B. Andersson, "A Kinetic Study of Oxygen Adsorption/Desorption and NO Oxidation Over Pt/Al_2O_3 Catalysts," *Journal of Physical Chemistry B,* 103 [47] 10433-10439 (1999).

214. L. Olsson, H. Persson, E. Fridell, M. Skoglundh, and B. Andersson, "Kinetic Study of NO Oxidation and NO_x Storage on Pt/Al_2O_3 and $Pt/BaO/Al_2O_3$," *Journal of Physical Chemistry B,* 105 [29] 6895-6906 (2001).

215. A. C. van Veen, D. Farrusseng, M. Rebeilleau, T. Decamp, A. Holzwarth, Y. Schuurman, and C. Mirodatos, "Acceleration in Catalyst Development by Fast Transient Kinetic Investigation," *Journal of Catalysis,* 216 [1-2] 135-143 (2003).

216. O. J. Wimmers, "Analytical Expressions for Temperature Programmed Reduction Patterns Using Solid-State Kinetics," *Thermochimica Acta,* 95 [1] 67-72 (1985).

217. O. J. Wimmers, P. Arnoldy, and J. A. Moulijn, "Determination of the Reduction-Mechanism by Temperature-Programmed Reduction - Application to Small Fe_2O_3 Particles," *Journal of Physical Chemistry,* 90 [7] 1331-1337 (1986).

218. J. Baltrusaitis and V. H. Grassian, "Surface Reactions of Carbon Dioxide at the Adsorbed Water-Iron Oxide Interface," *Journal of Physical Chemistry B: Condensed Matter,* 109 [25] 12227-12230 (2005).

219. D. Duprez, "Study of Surface Reaction Mechanisms by $^{16}O/^{18}O$ and H/D Isotopic Exchange," *Catalysis Today,* 112 [1-4] 17-22 (2006).

220. P. S. Lambrou and A. M. Efstathiou, "The Effects of Fe on the Oxygen Storage and Release Properties of Model Pd-Rh/CeO_2-Al_2O_3 Three-Way Catalyst," *Journal of Catalysis,* 240 [2] 182-193 (2006).

221. S. Roy, W. Sigmund, and F. Aldinger, "Nanostructured Yttria Powders Via Gel Combustion," *Journal of Materials Research,* 14 [4] 1524-1531 (1999).

222. D. Bhattacharya, L. C. Pathak, S. K. Mishra, D. Sen, and K. L. Chopra, "Pyrophoric Synthesis Technique for Multicomponent High-Temperature Superconductors," *Applied Physics Letters,* 57 [20] 2145-2147 (1990).

223. White, B. M. Solid-State Potentriometric NO_x/CO Sensors and Differential Electrode Equilibria. Ph.D. Dissertation, University of Florida, 2007.

224. P. A. Redhead, "Thermal Desorption of Gases," *Vacuum,* 12 [4] 203-211 (1962).

225. A. A. Davydov, *Infrared Spectroscopy of Adsorbed Species on the Surface of Transition Metal Oxides* John Wiley and Sons, Chichester, 1990.

226. J. A. Rodriguez, T. Jirsak, G. Liu, J. Hrbek, J. Dvorak, and A. Maiti, "Chemistry of NO_2 on Oxide Surfaces: Formation of NO_3 on TiO_2(110) and NO_2<-->O Vacancy Interactions," *Journal of the American Chemical Society,* 123 [39] 9597-9605 (2001).

227. D. L. S. Nieskens, A. P. van Bavel, and J. W. Niemantsverdriet, "The Analysis of Temperature Programmed Desorption Experiments of Systems With Lateral Interactions; Implications of the Compensation Effect," *Surface Science,* 546 [2-3] 159-169 (2003).

228. F. H. Garzon, R. Mukundan, and E. L. Brosha, "Solid-State Mixed Potential Gas Sensors: Theory, Experiments and Challenges," *Solid State Ionics,* 136-137 633-638 (2000).

229. W. Gopel, G. Reinhardt, and M. Rosch, "Trends in the Development of Solid State Amperometric and Potentiometric High Temperature Sensors," *Solid State Ionics,* 136-137 519-531 (2000).

230. N. Miura, G. Lu, and N. Yamazoe, "Progress in Mixed-Potential Type Devices Based on Solid Electrolyte for Sensing Redox Gases," *Solid State Ionics,* 136-137 533-542 (2000).

231. N. Miura, S. Zhuiykov, T. Ono, M. Hasei, and N. Yamazoe, "Mixed Potential Type Sensor Using Stabilized Zirconia and $ZnFe_2O_4$ Sensing Electrode for NOx Detection at High Temperature," *Sensors and Actuators B: Chemical,* 83 [1-3] 222-229 (2002).

232. E. Di Bartolomeo, N. Kaabbuathong, M. L. Grilli, and E. Traversa, "Planar Electrochemical Sensors Based on Tape-Cast YSZ Layers and Oxide Electrodes," *Solid State Ionics,* 171 [3-4] 173-181 (2004).

233. K. Hadjiivanov and L. Dimitrov, "IR Spectroscopy Study of CO and NO_x Adsorption on a Cu/Zr-HMS Catalyst," *Microporous and Mesoporous Materials,* 27 [1] 49-56 (1999).

234. C. Drouet, P. Alphonse, J. L. G. Fierro, and A. Rousset, "Adsorption of Nitric Oxide and Temperature Programmed Desorption on Nonstoichiometric Nickel-Copper Manganites," *Applied Surface Science,* 174 [3-4] 289-295 (2001).

235. B. M. White, F. M. Van Assche, IV, E. Traversa, and E. D. Wachsman, "Electrical Characterization of Semiconducting La_2CuO_4 for Potentiometric Gas Sensor Applications," *ECS Transactions,* 1 [7] 109 (2006).

236. N. J. Crane, E. G. Bartick, R. S. Perlman, and S. Huffman, "Infrared Spectroscopic Imaging for Noninvasive Detection of Latent Fingerprints," *Journal of Forensic Science,* 52 [1] 48-53 (2007).

237. D. G. Lumsdon and A. R. Fraser, "Infrared Spectroscopic Evidence Supporting Heterogeneous Site Binding Models for Humic Substances," *Environmental Science and Technology,* 39 [17] 6624-6631 (2005).

238. L. Cho, J. A. Reffner, B. M. Gatewood, and D. L. Wetzel, "Single Fiber Analysis by Internal Reflection Infrared Microspectroscopy," *Journal of Forensic Science,* 46 [6] 1309-1314 (2001).

239. F. M. Van Assche, J. Yoo, S. Chatterjee, and E. D. Wachsman, "Heterogeneous Catalytic Evaluation of Potentiometric La_2CuO_4 Sensor Electrodes," *ECS Transactions,* 1 [7] 185 (2007).

240. Potassium Bromide MSDS. 2007. Mallinckrodt Baker.
Ref Type: Data File

241. B. Stuart, *Infrared Spectroscopy : Fundamentals and Applications* John Wiley & Sons, Ltd.., Chichester, England, 2004.

242. A. V. Bazhenov, T. N. Fursova, V. B. Timofeev, A. S. Cooper, J. P. Remeika, and Z. Fisk, "Infrared Reflectivity Spectra of Single Crystals of La_2CuO_4," *Physical Review B. Condensed Matter,* 40 [7] 4413-4418 (1989).

243. Ch. Sedlmair, K. Seshanc, A. Jentys, and J. A. Lercher, "Elementary Steps of NO_x Adsorption and Surface Reaction an a Commercial Storage-Reduction Catalyst," *Journal of Catalysis,* 214 308-316 (2003).

244. G. Busca and V. Lorenzelli, "Infrared Study of the Adsorption of Nitrogen Dioxide, Nitric Oxide and Nitrous Oxide on Hematite," *Journal of Catalysis,* 72 [2] 303-313 (1981).

245. K. Nakamoto, *Infrared and Raman Spectra of Inorganic Coordination Compounds*, 5th ed. Wiley, New York, 1997.

246. M. Schraml-Marth, A. Wokaun, and A. Baikert, "Surface Structure of Crystalline and Amorphous Chromia Catalysts for the Selective Catalytic Reduction of Nitric Oxide IV. Diffuse Reflectance FTIR Study of NO Adsorption and Reaction," *Journal of Catalysis,* 138 [1] 306-321 (1992).

247. G. Ghiotti and A. Chiorino, "An IR Study of NO Adsorption on a CrO_x/ZrO_2 Catalyst," *Spectrochimica Acta Part A: Molecular Spectroscopy,* 49 [9] 1345-1359 (1993).

248. M. J. D. Low and R. T. Yang, "Reactions of Gaseous Pollutants With Solids : V. Infrared Study of the Sorption of NO on CaO," *Journal of Catalysis,* 34 [3] 479-489 (1974).

249. L. Cerruti, E. Modone, E. Guglielm, and E. Borello, "Infrared Study of Nitric-Oxide Adsorption on Magnesium-Oxide," *Journal of the Chemical Society-Faraday Transactions I,* 70 [4] 729-739 (1974).

250. L. H. Little, *Infrared Spectra of Adsorbed Species,* Academic Press, London, 1966.

251. M. Shelef and J. T. Kummer, *Chemical Engineering Progress Symposium Series,* 67 [74] (1971).

252. A. Martinezarias, J. Soria, J. C. Conesa, X. L. Seoane, A. Arcoya, and R. Cataluna, "NO Reaction at Surface Oxygen Vacancies Generated in Cerium Oxide," *Journal of the Chemical Society-Faraday Transactions,* 91 [11] 1679-1687 (1995).

253. J. Laane and J. R. Ohlsen, *Progress in Inorganic Chemistry,* 27 465 (1980).

254. A. Snis and I. Panas, "Surface Complexes of Nitric Oxide: Adsorption of Anionic NO and N_2O_2 on CaO," *Surface Science,* 413 477-488 (1998).

255. L. M. Roev, and A. V. Alekseev, *Elementary Photoprocesses in Molecules* Consultants Bureau, New York, 1968.

256. Miscellaneous. In *CRC Handbook of Chemistry and Physics*, 57 ed.; CRC Press, Cleveland, 1976; p F-245-F-264.

257. S.-J. Huang, A. B. Walters, and M. A. Vannice, "Adsorption and Decomposition of NO on Lanthanum Oxide," *Journal of Catalysis,* 192 [1] 29-47 (2000).

258. F. M. Capece, V. Dicastro, C. Furlani, G. Mattogno, C. Fragale, M. Gargano, and M. Rossi, *Journal of Electron Spectroscopy Related Phenomenon,* 27 119 (1982).

259. N. S. Mcintyre and M. G. Cook, "X-Ray Photoelectron Studies on Some Oxides and Hydroxides of Cobalt, Nickel, and Copper," *Analytical Chemistry,* 47 [13] 2208-2213 (1975).

260. C. D. Wagner, W. M. Riggs, L. E. Davis, J. F. Moulder, and G. E. Muilenberg, *Handbook of X-Ray Photoelectron Spectroscopy* Perkin-Elmer Corporation, Physical Electronics Division, Eden Prairie, Minnesota, 1979.

261. Y. Uwamino, Y. Ishizuka, and H. Yamatera, *Journal of Electron Spectroscopy Related Phenomenon,* 34 69 (1984).

262. Kaufmann R., Klewe-Nebenius H., Moers H., Pfennig G., Jenett H., and Ache H.J., *Surface Interface Analysis,* 11 502 (1988).

263. Johansson G., Hedman J., Berndtsson A., Klasson M., and Nilsson R., *Journal of Electron Spectroscopy Related Phenomenon,* 2 [295] (1973).

264. Y.S.Meng Combining Ab Initio Computation with Experiments for Designing/ Understanding High Energy Density Electrode Materials for Advanced Lithium Batteries. Ph.D Massachusetts Institute of Technology, 2005.

265. B. Glorieux, R. Berjoan, M. Matecki, A. Kammouni, and D. Perarnau, "XPS Analyses of Lanthanides Phosphates," *Applied Surface Science,* 253 [6] 3349-3359 (2007).

266. N. Mizuno, "Supported Perovskites," *Catalysis Today,* 8 221-230 (1990).

267. J. Zhu, Z. Zhao, D. Xiao, J. Li, X. Yang, and Y. Wu, "Effect of Valence of Copper in $La_{2-X}Th_xCuO_4$ on NO Decomposition Reaction," *Catalysis Communications,* 7 [1] 29-32 (2006).

268. B. Lesiak, J. Zemek, P. Jiricek, and A. Jozwik, "Investigation of CoPd Alloys by XPS and EPES Using the Pattern Recognition Method," *Journal of Alloys and Compounds,* 428 [1-2] 190-196 (2007).

269. S. Lizzit, A. Baraldi, D. Cocco, G. Comelli, G. Paolucci, R. Rosei, and M. Kiskinova, "NO Adsorption on the Rh(110) Surface: Kinetics and Composition of the Adlayer Studied by Fast XPS," *Surface Science,* 410 [2-3] 228-236 (1998).

270. J. F. Zhu, M. Kinne, T. Fuhrmann, R. Denecke, and H.-P. Steinruck, "In Situ High-Resolution XPS Studies on Adsorption of NO on Pt(1 1 1)," *Surface Science,* 529 [3] 384-396 (2003).

271. E. R. Macam, F. M. Van Assche, J. Yoo, and E. D. Wachsman, "Optimization of La_2CuO_4 Sensing Electrodes for a NO_x Potentiometric Sensor," *ECS Transactions,* 1 [7] 121 (2006).

272. J. A. Connor, *Handbook of X-Ray and Ultraviolet Photoelectron Spectroscopy*, 2nd ed. Heyden, 1978.

273. S. Hüfner, *Photoelectron Spectroscopy*, 2nd ed. Springer-Verlag Berlin Heidelberg, Berlin, 1996.

274. N. Nucker, J. Fink, B. Renker, D. Ewert, C. Politis, P. J. W. Weijs, and J. C. Fuggle, "Experimental Electronic-Structure Studies of $La_{2-X}Sr_xCuO_4$," *Zeitschrift fur Physik B-Condensed Matter,* 67 [1] 9-14 (1987).

275. H. Romberg, N. Nucker, M. Alexander, J. Fink, D. Hahn, T. Zetterer, H. H. Otto, and K. F. Renk, "Density and Symmetry of Unoccupied Electronic States of $Ti_2Ba_2CaCu_2O_8$," *Physical Review B,* 41 [4] 2609-2611 (1990).

276. T. Horita, K. Yamaji, N. Sakai, Y. Xiong, T. Kato, H. Yokokawa, and T. Kawada, "Determination of Proton and Oxygen Movements in Solid Oxides by the Tracer Gases Exchange Technique and Secondary Ion Mass Spectrometry," *Applied Surface Science,* 203-204 634-638 (2003).

277. T. Kawada, M. Sase, M. Kudo, K. Yashiro, K. Sato, J. Mizusaki, N. Sakai, T. Horita, K. Yamaji, and H. Yokokawa, "Microscopic Observation of Oxygen Reaction Pathway on High Temperature Electrode Materials," *Solid State Ionics,* 177 [35-36] 3081-3086 (2006).

278. R. A. De Souza and R. J. Chater, "Oxygen Exchange and Diffusion Measurements: The Importance of Extracting the Correct Initial and Boundary Conditions," *Solid State Ionics,* 176 [23-24] 1915-1920 (2005).

279. N. Sakai, K. Yamaji, T. Horita, H. Kishimoto, M. E. Brito, H. Yokokawa, and Y. Uchimoto, "Application of SIMS Analyses on Oxygen Transport in SOFC Materials," *Applied Surface Science,* 252 [19] 7045-7047 (2006).

280. J. M. Bassat, M. Petitjean, J. Fouletier, C. Lalanne, G. Caboche, F. Mauvy, and J. C. Grenier, "Oxygen Isotopic Exchange: A Useful Tool for Characterizing Oxygen Conducting Oxides," *Applied Catalysis A: General,* 289 [1] 84-89 (2005).

281. H. Wang, R. G. Tobin, G. B. Fisher, C. L. DiMaggio, and D. K. Lambert, "Oxygen Exchange Between NO Gas and Adsorbed Atomic Oxygen on Pt(335)," *Surface Science,* 440 [3] 429-437 (1999).

282. A. Danon, A. Saig, Y. Finkelstein, and J. E. Koresh, "A New Route of Oxygen Isotope Exchange in the Solid Phase: Demonstration in $CuSO_{4.5}H_2O$," *Journal of Physical Chemistry B: Condensed Matter,* 109 [44] 21197-21201 (2005).

283. K. Krau[ss], A. Drochner, M. Fehlings, J. Kunert, and H. Vogel, "Oxygen Exchange at Mo/V Mixed Oxides: A Transient and ^{18}O Isotope Study Under Technical Conditions," *Journal of Molecular Catalysis A: Chemical,* 177 [2] 237-245 (2002).

284. A. J. Fletcher, Y. Yuzak, and K. M. Thomas, "Adsorption and Desorption Kinetics for Hydrophilic and Hydrophobic Vapors on Activated Carbon," *Carbon,* 44 [5] 989-1004 (2006).

285. E. Boehm, J. M. Bassat, P. Dordor, F. Mauvy, J. C. Grenier, and P. Stevens, "Oxygen Diffusion and Transport Properties in Non-Stoichiometric $Ln_{2-X}NiO_{4+\delta}$ Oxides," *Solid State Ionics,* 176 [37-38] 2717-2725 (2005).

286. F. M. Van Assche, J. C. Nino, and E. D. Wachsman, "Adsorbate Studies on La_2CuO_4 Using Infrared Spectroscopy and X-Ray Photoemisson Spectroscopy to Determine Potentiometric NO_x Sensor Response Mechanism," *J. Electrochemical Society, accepted* (2008).

287. L. Pauling, *The Nature of the Chemical Bond and the Structure of Molecules and Crystals*, Second ed. Oxford University Press, Ithica, NY, 1948.

288. O'Haver, T. Interactive Peak Fitter, version 1.6. 2007.
Ref Type: Data File

289. E. Foldes, Z. Szabo, A. Janecska, G. Nagy, and B. Pukanszky, "Quantitative Analysis of Functional Groups in HDPE Powder by DRIFT Spectroscopy," *Macromolecular Symposia,* 202 97-115 (2003).

290. S.-J. Huang, A. B. Walters, and M. A. Vannice, "Adsorption and Decomposition of NO on Lanthanum Oxide," *Journal of Catalysis,* 192 [1] 29-47 (2000).

291. M. Bhattacharya, W. G. Devi, and P. S. Mazumdar, "Determination of Kinetic Parameters From Temperature Programmed Desorption Curves," *Applied Surface Science,* 218 [1-4] 1-6 (2003).

292. P. Garcia, A. Molina, and F. Mondragon, "Desorption Activation Energy Distribution Function of Nitric Oxide Chemisorbed on Carbonaceous Materials at 373 K," *Carbon,* 43 [7] 1445-1452 (2005).

293. T. Ishihara, M. Ando, K. Sada, K. Takiishi, K. Yamada, H. Nishiguchi, and Y. Takita, "Direct Decomposition of NO into N_2 and O_2 Over La(Ba)Mn(In)O_3 Perovskite Oxide," *Journal of Catalysis,* 220 [1] 104-114 (2003).

294. A. Kotsifa, D. I. Kondarides, and X. E. Verykios, "Comparative Study of the Chemisorptive and Catalytic Properties of Supported Pt Catalysts Related to the Selective Catalytic Reduction of NO by Propylene," *Applied Catalysis B: Environmental,* In Press, Corrected Proof.

295. R. Zhang, A. Villanueva, H. Alamdari, and S. Kaliaguine, "SCR of NO by Propene Over Nanoscale $LaMn_{1-X}Cu_xO_3$ Perovskites," *Applied Catalysis A: General,* 307 [1] 85-97 (2006).

296. R. W. Odom, S. E. Buttrill, R. H. Fleming, M. Rossi, L. N. Goeller, and W. Gohl, "Pulsed Field Desorption Mass Spectrometry: A Technique for Investigating Field Desorption Ion Formation Mechanisms," *International Journal or Mass Spectrometry and Ion Physics,* 49 [3] 319-335 (1983).

297. T. Wilhelm and G. Wittstock, "Patterns of Functional Proteins Formed by Local Electrochemical Desorption of Self-Assembled Monolayers," *Electrochimica Acta,* 47 [1-2] 275-281 (2001).

298. C. A. Widrig, C. Chung, and M. D. Porter, "The Electrochemical Desorption of N-Alkanethiol Monolayers From Polycrystalline Au and Ag Electrodes," *Journal of Electroanalytical Chemistry,* 310 [1-2] 335-359 (1991).

299. Blackburn, B. 2007.

300. C. Carretti, P. Manini, and G. L. Grotto, "Mass Spectrometric Evaluation of the Desorption Properties of Some Glasses Under High Applied Voltage Conditions," *Vacuum,* 46 [8-10] 769-772 (1995).

301. N. Mingo and F. Flores, "Lateral Forces and Atomic Desorption Induced by the Electric Field Created by STM Tips on Metal Surfaces," *Surface Science,* 395 [2-3] 342-355 (1998).

302. D. Sengupta, "Effect of External Field on Bond Energy and Activation Barrier for Surface Diffusion," *Journal of Crystal Growth,* 286 [1] 91-95 (2006).

303. C. Tang, L. Feller, P. Rossbach, B. Keller, J. Voros, S. Tosatti, and M. Textor, "Adsorption and Electrically Stimulated Desorption of the Triblock Copolymer Poly(Propylene Sulfide-Bl-Ethylene Glycol) (PPS-PEG) From Indium Tin Oxide (ITO) Surfaces," *Surface Science,* 600 [7] 1510-1517 (2006).

304. M. Zembala, "Electrokinetics of Heterogeneous Interfaces," *Advances in Colloid and Interface Science,* 112 [1-3] 59-92 (2004).

305. R. W. O'Brian and L. R. White, "Electrophoretic Mobility of a Spherical Colloidal Particle," *Jourtnal of the Chemical Society, Faraday Transactions,* 2 [74] 1607-1626 (1978).

306. N. Golovan and V. Smyntyna, "The Sensitization of Semiconductor Gas Sensors," *Sensors and Actuators B: Chemical,* 6 [1-3] 289-292 (1992).

307. S. Gonzalez, C. Sousa, and F. Illas, "Electric Field Effects in the Chemisorption of CO on Bimetallic RhCu Surface Models," *Surface Science,* 548 [1-3] 209-219 (2004).

308. W. Hellmich, G. Muller, C. Braunmuhl, T. Doll, and I. Eisele, "Field-Effect-Induced Gas Sensitivity Changes in Metal Oxides," *Sensors and Actuators B: Chemical,* 43 [1-3] 132-139 (1997).

309. Blackburn, B. Rendered image of PPD experimental reactor setup. 2007.
Ref Type: Data File

310. Blackburn, B. Sensor Automation Protocol. [3]. 2007.
Ref Type: Data File

311. Blackburn, B. HP Voltage Step Automation Protocol. [1.01]. 2007.
Ref Type: Data File

312. M. Matsuda, M. Fujita, and K. Yamada, "Static Spin Correlations in Lightly-Doped La2CuO4+[Delta]," *Physica C: Superconductivity,* 408-410 810-811 (2004).

313. A. Du, G. Z. Wei, Q. L. Hu, and Z. Xianyu, "Neel Temperature of Orthorhombic La2CuO4," *Journal of Magnetism and Magnetic Materials,* 146 [1-2] 201-202 (1995).

314. J. Shimizu, M. Nakagawa, and Y. Oda, "The Normal State Magnetic Susceptibility of La2CuO4+[Delta] With Excess Oxygen," *Physica C: Superconductivity,* 388-389 263-264 (2003).

315. N. Shah, M. A. Green, and D. A. Neumann, "Phase Stability in the LnCa2Mn2O7 (Ln=Pr, Nd, Sm and Gd) Ruddlesden-Popper Series," *Journal of Physics and Chemistry of Solids,* 63 [9] 1779-1786 (2002).

316. D. di Caprio, J. Stafiej, and J. P. Badiali, "Field Theory for Ionic Systems. From Fluctuations and Structure at a Hard Wall to Thermodynamics," *Electrochimica Acta,* 48 [20-22] 2967-2974 (2003).

317. J. C. Maxwell, *A Treatise on Electricity and Magnetism*, 3rd ed. Dover Publications, New York, 1891.

318. S. S. Atwood, *Electric and Magnetic Fields*, 3rd ed. New York, 1932.

319. S. Capone, M. Epifani, L. Francioso, S. Kaciulis, A. Mezzi, P. Siciliano, and A. M. Taurino, "Influence of Electrodes Ageing on the Properties of the Gas Sensors Based on SnO_2," *Sensors and Actuators B: Chemical,* 115 [1] 396-402 (2006).

320. J. Nowotny, T. Bak, and C. C. Sorrell, "Charge Transfer at Oxygen/Zirconia Interface at Elevated Temperatures - Part 7: Effect of Surface Processing," *Advances in Applied Ceramics,* 104 [4] 195-199 (2005).

321. J. J. Sprague, O. Porat, and H. L. Tuller, "Mixed Conducting Gas Sensors: Atmosphere Dependent Electrode Impedance," *Sensors and Actuators B: Chemical,* 36 [1-3] 348-352 (1996).

322. D. Kuscer, J. Holc, M. Hrovat, S. Bernik, Z. Samardzija, and D. Kolar, "Interactions Between a Thick Film LaMnO3 Cathode and YSZ SOFC Electrolyte During High Temperature Ageing," *Solid State Ionics,* 78 [1-2] 79-85 (1995).

323. J. Nowotny, T. Bak, M. K. Nowotny, and C. C. Sorrell, "Charge Transfer at Oxygen/Zirconia Interface at Elevated Temperatures - Part 3: Segregation Induced Interface Properties," *Advances in Applied Ceramics,* 104 [4] 165-173 (2005).

324. J. Nowotny, T. Bak, and C. C. Sorrell, "Charge Transfer at Oxygen/Zirconia Interface at Elevated Temperatures - Part 5: Reactivity Models," *Advances in Applied Ceramics,* 104 [4] 181-187 (2005).

325. M. M. Viitanen, R. G. Welzenis, H. H. Brongersma, and F. P. F. van Berkel, "Silica Poisoning of Oxygen Membranes," *Solid State Ionics,* 150 [3-4] 223-228 (2002

BIOGRAPHICAL SKETCH

Frederick Martin Van Assche IV was born on September 26, 1980 in Winter Park, Florida. After a short and fulfilling stint as an enfant terrible, he progressed through Winter Park High School, garnering a reputation for dogged (almost ludicrous) persistence in academics and athletics, winning four state championships in rowing before graduating with honors in 1998. He was accepted to the chemical engineering program at the University of Florida, and following five years of late nights, early mornings, and the occasional injury, was awarded his undergraduate degree in the spring of 2003. During his undergraduate tenure, he studied the Diels-Alder reactions of tetrachlorocyclopropene under the direction of Dr. Merle Battiste in the Chemistry department. His research experience in chemistry convinced him to further his education through graduate study, though in a slightly less flammable concentration.

Following graduation, he was accepted into the University of Florida graduate school in both materials science and civil engineering. As he was never properly informed about the civil engineering admission, he accepted a position in Dr. Eric Wachsman's sensor group in materials. His initial work in mass spectrometry with La_2CuO_4, WO_3, and other sensor materials inspired him to further work in the subject following his masters in 2005. In the final two years of doctoral pursuit, Martin has presented at conferences in Los Angeles, Daytona Beach, and Washington DC, and served as the Student Chapter President of the Electrochemical Society at the University of Florida. At time of writing, he eagerly awaits the next opportunity to apply his can-do spirit and ridiculously exuberant character.